

PHENOMENOLOGICAL ASPECTS  
OF AN ANISOTROPIC  
QUARK-GLUON PLASMA

Dissertation  
zur Erlangung des Doktorgrades  
der Naturwissenschaften

vorgelegt beim Fachbereich Physik  
der Johann Wolfgang Goethe-Universität  
in Frankfurt am Main

von  
Mauricio Martínez Guerrero  
aus Socorro, Kolumbien

Frankfurt am Main 2009  
(D30)

vom Fachbereich Physik (13) der Johann Wolfgang Goethe-Universität  
als Dissertation angenommen.

Dekan: Prof. Dr. D. H. Rischke

Gutachter: Pr. Dr. C. Greiner, Dr. Michael Strickland

Datum der Disputation: 30.04.2010

*In the memory of the little child, Amira Martínez G.*

Un camino que no solamente nadie conocía sino que  
probablemente ni siquiera existía.

---

*Vida de Anne Moore*  
Roberto Bolaño.

# Zusammenfassung

Die folgende Arbeit baut sich auf den folgenden Publikationen auf:

- Mauricio Martinez and Michael Strickland, *Measuring QGP thermalization time with dileptons*, Phys. Rev. Lett. **100**: 102301, 2008.
- Mauricio Martinez and Michael Strickland, *Pre-equilibrium dilepton production from an anisotropic quark-gluon plasma*, Phys. Rev. C **78**: 034917, 2008.
- Mauricio Martinez and Michael Strickland, *Suppression of forward dilepton production from an anisotropic quark-gluon plasma*, Eur. Phys. J. C **61**: 905-913, 2009.
- Mauricio Martinez and Michael Strickland, *Constraining relativistic viscous hydrodynamical evolution*, Phys. Rev. C **79**: 044903, 2009.
- Mauricio Martinez and Michael Strickland, *Matching pre-equilibrium dynamics and viscous hydrodynamics*, arXiv:0909.0264 [hep-ph].

## Abstract

### 0.1. Zusammenfassung

In der folgenden Arbeit werden die Auswirkungen von Impuls-Raum Anisotropien im Quark-Gluonen untersucht. Es wird erwartet, dass Impuls-Raum Anisotropien im Frühstadium einer Schwerionenkollision aufgrund der Unterschiedlichkeit der Ausdehnungsraten in longitudinaler und transversaler Richtung auftreten.

Im ersten Teil der Arbeit werden zwei Modelle, die beide von einer Beschreibung einer anfangszeitlichen 0+1 dimensionalen Vor-Gleichgewichts Expansion hin zu einer hydrodynamischen Beschreibung der zentralen Rapiditätszone interpolieren, beschrieben. Die Modelle beinhalten die Auswirkungen der Impuls-Raum Anisotropien indem sowohl die Eigenzeitabhängigkeit **Proper time dependence** auf der Impulsskala der harten Partonen,  $p_{\text{hard}}$ , als auch der Parameter,  $\xi$ , der die Anisotropien misst, mitberücksichtigt wird. Das erste Modell beschreibt die Interpolation zwischen einem anfangszeitlichen 0+1 dimensionalen freien Fluss, und einer 0+1 dimensionalen Expansion, beschrieben durch ideale Hydrodynamik. Im zweiten Modell wird zusätzlich die, durch Kollisionen verursachte, Verbreiterung der Partonen-Verteilungsfunktion, im Vergleichgewichtszustand des Plasmas berücksichtigt. Es zeigt sich in beiden Modellen, dass, bei gleichen Anfangsbedingungen, die Dileptonenproduktionsrate durch Abstrahlung im Vergleichgewicht vergrößert wird. Wenn in den Modellen die Einschränkung angenommen wird, dass die Pionen Multiplizitäten am Ende der Kollision fixiert sind, so ergibt sich, dass die Abhängigkeit der resultierenden Spektren von der angenommenen Isotropisierung des Plasmas abnimmt. Wenn das realistischere Beschreibungsmodell, welches Effekte durch Kollisionen miteinbezieht, verwendet wird, ergibt sich, bei einer Thermalisierungszeit von 2 fm/c, dass die Produktion von Dileptonen mit einem hohen transversalen Impuls um 40% am RHIC und um 50% am LHC vergrößert würde. Des Weiteren wird eine, nach vorne gerichtete Dileptonenabstrahlung beobachtet, wenn die Rapiditätsabhängigkeit der harten Impuls Skala der Partonen,  $p_{\text{hard}}$ , berücksichtigt wird. Daher geben die Rechnungen Grund zur Annahme, dass die nach vorne gerichteten Dileptonen, bei LHC Energien unterdrückt sind.

Im zweiten Teil der Arbeit wird die Beschreibung der Dynamik des Impuls-Raumes Anisotropien des gebildeten Feuerballs weiter verfeinert. Dissipative Korrekturen, die durch den viskosen **shear tensor** verursacht werden, bewirken, dass sich die transversalen und longitudinalen Drücke des Feuerballs zeitlich verändern. Zur Lösung dieses neuen hydrodynamischen Gleichungssystems werden zwei physikalische Beschränkungen auf die Eingabewerte der viskosen hydrodynamischen Gleichungen vorgenommen.: (a) Die Forderung nach positiven Werten des longitudinalen Druckes zu allen Zeiten (b) Die Beschränkung auf kleine Werte des viskosen **shear tensors** verglichen mit dem Gleichgewichtsdruck, d.h.  $|\Pi^{\mu\nu}| \leq \alpha \mathcal{P}$  wobei hier  $\alpha \in \{0, 1\}$ . Wenn nun diese zwei Beschränkungen auf 0+1 dimensionale konforme viskose Hydrodynamik in 2ter Ordnung angewendet werden, so ergeben sich nicht triviale Zusammenhänge, zwischen den Anfangswerten der Komponenten des **shear tensors**, der Energie, dem Druck und der Anfangszeit der numerischen Simulation. Es wird im Laufe dieser Arbeit erklärt, wie diese Beschränkungen auch auf höhere Ordnungen in der Störungsreihe erweitert werden können. Abschließend wird eine Methode entwickelt, mit welcher die 0+1 dimensionale Vor-Gleichgewichts Expansion in Zusammenhang gebracht werden kann, mit der 0+1 dimensionale viskosen Hydrodynamik in zweiter Ordnung Störungstheorie. Die Anfangswerte des viskosen **shear tensors** und der Energiedichte werden dabei gegen die Lebenszeit der Vor-Equilibrierten Phase des QGP aufgetragen. Des Weiteren werden die Auswirkungen der Vor-Equilibrierten Dynamik auf die Entropieproduktion untersucht und eine genaue Definition dieser neuen Nicht-Gleichgewichts Entropie gegeben.

## Einleitung

Bei geringen Temperaturen und kleinen Dichten ist Materie aufgebaut aus Elektronen, Protonen und Neutronen. Wird nun ein System dieser Bestandteile erhitzt, so beginnen thermische Anregungen einen wichtigen Einfluss auf die Dynamik dieses Systems auszuüben. Es ist bekannt, dass Protonen und Neutronen aus Quarks und Gluonen aufgebaut sind. Wird nun das oben beschriebene System weiter erhitzt, so überlappen die Wellenfunktionen der Protonen und Neutronen und die Quarks und Gluonen, welchen in jenen enthalten sind können sich frei bewegen. Ab einer bestimmten Temperatur verhält sich das System wie ein Plasma aufgebaut aus Quarks und Gluonen. Dieses Plasma wird daher ein QGP, d.h. ein Quark Gluonen Plasma genannt. Gitterrechnungen sagen voraus, dass sich eine scharfe Übergangstemperatur von der hadronischen Phase zur QGP Phase bei  $175 - 200 \text{ GeV}$  befindet. Die zu dieser für diesen Übergang notwendige Energiedichte beträgt  $\mathcal{E} \gtrsim 1 \text{ GeV}/\text{fm}^3$ . In der Natur können solche Dichten zum Beispiel in den Zentren von Neutronensternen oder bei Supernovae Explosionen detektiert werden. Um ähnliche Dichten im Labor zu erzeugen, werden schwere Kerne mit sehr hohen Energien aufeinander geschossen. Die daraus entstehende Kernmaterie entsteht, da Kerne bei solch hohen Geschwindigkeiten stark längenkontrahiert in longitudinaler Richtung sind, wodurch die Materie sehr heiß und dicht wird. Experimente dieser Art wurden bisweilen schon am RHIC in Brookhaven New York durchgeführt und sollen am LHC des CERN in Genf zu noch höheren Energien ausgeweitet werden. Bei den Experimenten am RHIC wurde ein großes Spektrum an verschiedenen Kollisionen untersucht. Es wurden hierbei p+p, d+Au und Au+Au Kollisionen bei Schwerpunktsenergien  $(\sqrt{s})$  von 20 bis 200 GeV durchgeführt. Am LHC soll sich die Stahlergie um eine Größenordnung, gegenüber der am RHIC, auf  $\sqrt{5,5} \text{ TeV}$  pro Nukleon, vergrößern. Eine der größten Herausforderungen der in der modernen Schwerionenphysik ist es eine genaue thermodynamische Beschreibung der Transporteigenschaften dieses Materiezustandes zu finden. Alleine das Auffinden eines eindeutigen Signals, welches das Entstehen eines QGP bestätigt ist schwierig. Anstelle weiter nach einem direkten Signal zu suchen, werden daher Datensätze verschiedener Observablen auf Spuren einer freien Quark Gluon Phase untersucht. Dabei kommen viele Observablen, wie z.B. elektromagnetische Proben, der elliptische Fluss-Koeffizient, die Lösung schwerer Quarks aus Quarkonium Zuständen usw., in Frage. Diese Arbeit wird sich vornehmlich mit Dileptonen Ausbeuten, die eine sehr wichtige Observable bei ultra-relativistischen Schwerionenkollisionen darstellen, beschäftigen.

Ein sehr interessantes und bisweilen ungelöstes Problem ist dabei, ob das QGP thermalisiert oder nicht. Die Resultate der ersten Versuchsreihe am RHIC konnten allesamt durch ideale Hydrodynamik erklärt werden, mit welcher sämtliche transversalen Spektren von zentralen und halbzentralen Stößen, einschließlich der Anisotropien in nicht zentralen Stößen, die durch den elliptischen Flusskoeffizienten  $v_2$  quantifiziert werden, erklärt werden. Modelle der idealen Hydrodynamik konnten dabei erfolgreich die Abhängigkeit von  $v_2$  von der Ruhemasse der Hadronen bei transversalen Impulsen von  $\langle p_L^2 \rangle \ll \langle p_T^2 \rangle$  erklären. Dabei mussten die idealen Hydrodynamikrechnungen schon bei frühen Zeiten, d.h.  $\tau_{hydro} = 1 \text{ fm}/c$  gestartet werden, um zu funktionieren. Aufgrund dieser Ergebnisse wurde angenommen, dass die Materie, die bei der Kollision geschaffen wurde eine geringe Thermalisierungszeit hat und sich daher fast wie eine perfekte Flüssigkeit verhält. Wenn nun aber die dissipativen Korrekturen bis zur 2ten Ordnung in der Gradientenentwicklung mit in die Rechnung einbezogen werden, so ist es nicht mehr notwendig, die hydrodynamische Rechnung von solch frühen Zeiten aus zu starten, um die Messdaten zu beschreiben. Die Abschätzungen der Thermalisierungszeiten, die aus den hydrodynamischen Rechnungen folgen sind sehr ungenau, da die genauen Eingabewerten der Rechnung, sowie eine genaue Beschreibung der Hadronisierung und der Plasmadyamik nicht gegeben ist. Eine, vor kurzer Zeit durchgeführte Rechnung, bei der 2-Ordnung konforme viskose Hydrodynamik verwendet wurde, gibt Anlass zu der Annahme, dass Thermalisierungszeiten von über  $2 \text{ fm}/c$  nicht in der Lage sind RHIC Daten [1] zu beschreiben.

Aus theoretischer Sicht gesehen, ist es sogar noch schwerer zu Erklären, wie das QGP thermalisiert, wenn sich Partronen des heranfliegenden Kerns abspalten. Ausgehend von einem umgedrehten Szenario kann die Thermalisierungszeit des QGP auf  $\sim 2,7 \text{ fm}/c$  für RHIC Energien geschätzt werden. Bei dieser Abschätzung werden  $2 \leftrightarrow 3$  Kollisionen betrachtet. Leider werden in diesem Szenario die Anisotropien, die sich in den Anfangszeiten der Kollision bilden, vernachlässigt. Diese Anisotropien werden durch die rasche longitudinale Ausbreitung des QGPs verursacht, welche das System stärker in longitudinaler Richtung abkühlen lässt als in transversaler. Daher ist zu dieser Zeit die Ausbreitungs Rate größer als die Kollisions Rate und es bildet sich eine lokale Impuls-Raum Anisotropie. Wenn das System in die Nähe eines lokalen Gleichgewichts kommen soll, so muss zu einem bestimmten Zeitpunkt die Kollisionsrate größer als die Expansionsrate sein. Sobald dies passiert kann ein hydrodynamisches Verhalten des Systems angenommen werden. Es ist bekannt, dass Anisotropien im Impulsraum mit Plasmainstabilitäten korreliert sind. Diese lokalen Anisotropien des QGP können als chromo-Weibel Instabilitäten beschrieben werden [2]. Chromo Weibel Instabilitäten verursachen ein rasches Wachstum der weichen Feldmoden die wiederum die Isotropisierung des Plasmas zu restaurieren versuchen, wobei diese rasche Restaurierung auf viel kleineren Zeitskalen als denen der Kollisionen stattfindet. Die meisten Fortschritte in der theoretischen und numerischen Beschreibung eines QGP mit chromo Weibel Instabilitäten wurden bis jetzt in einem asymptotischen Energiebereich gewonnen, in dem Vergleiche zu Störungsrechnungen möglich waren. Daher konnte bis jetzt die Isotropisierung am RHIC und LHC noch nicht bewiesen werden.

Solange eine eindeutige physikalische Beschreibung des Thermalisierungsprozesses fehlt, ist ein möglicher Beschreibungsweg, durch die phänomenologische Beschreibung der von  $v_2$  unabhängigen Variablen gegeben. Diese Observablen sollten Auskunft über das Frühstadium des Plasmas geben. In dieser Arbeit werden die phänomenologischen Konsequenzen von Impuls Raum Anisotropien in Schwerionenkollisionen erforscht und beschrieben.

## Dileptonenproduktion aus einem anisotropen QGP

Eine sehr wichtige Art von Signalen des QGP sind elektromagnetische Signale, wie hoch energetische Photonen und Dileptonen. Da diese Teilchen an die stark wechselwirkende Materie nur über die elektromagnetische Kraft ankoppeln können, haben sie eine große freie Weglänge und können somit aus der starkwechselwirkenden Zone entweichen. Aus diesem Grunde tragen Teilchen dieser Art wichtige Informationen über die Anfangszeiten der Kollision. Im ersten Abschnitt dieser Arbeit werde Dileptonen berechnet, die im Medium entstehen und aus der Strahlung des Mediums hervorgehen, die vor dem Gleichgewichtszustand abgestrahlt wurde. Um die Dileptonen Spektren zu ermitteln ist

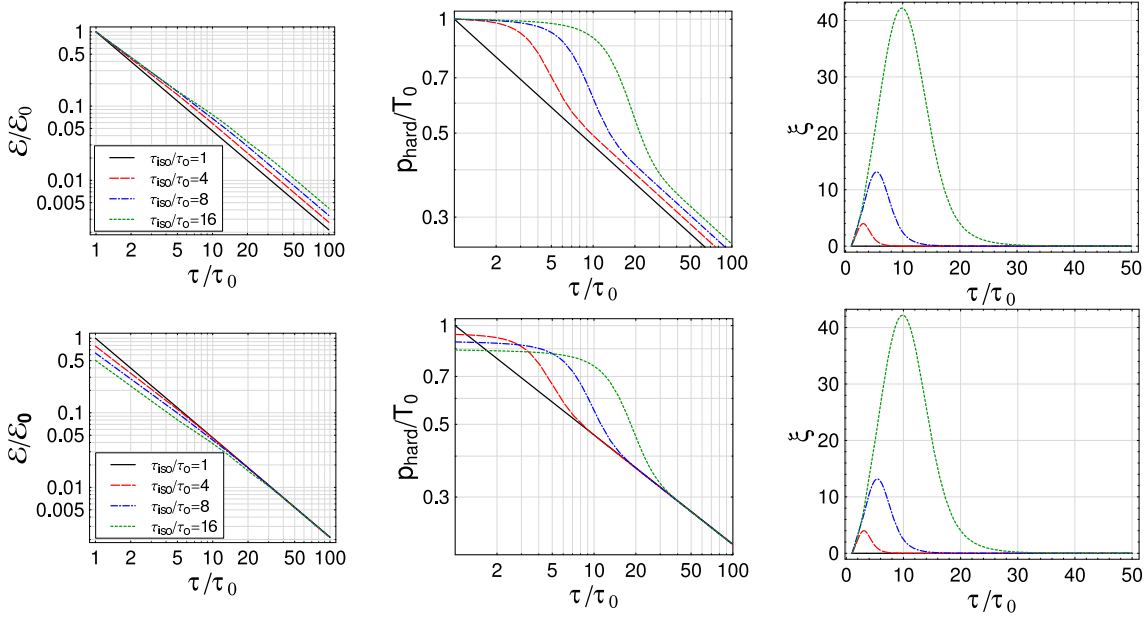


Figure 0.1.: Zeitliche Entwicklung der Energiedichte (linke Seite), des harten Impulses und des Anisotropie Parameters (rechte Seite) wobei ein Modell mit kollisionaler Verbreiterung einbezogen wurde. Es wurden vier verschiedene Isotropisierungszeiten verwendet  $\tau_{\text{iso}} \in \{1, 4, 6, 18\} \tau_0$ . Die Übergangsbreite ist  $\gamma = 2$ . Um sie in physikalischen Einheiten umzurechnen wird  $\tau_0 \sim 0.3 \text{ fm}/c$  für RHIC und  $\tau_0 \sim 0.1 \text{ fm}/c$  für LHC Daten. Die obere Reihe ist für das Interpolationsmodell mit festen Anfangsbedingungen und die untere für feste Endbedingungen.

es wichtig, zuerst die differentielle Dileptonen Rate zu berechnen. Diese differentielle Dileptonen Rate ist aus der kinetischen Theorie gegeben als:

$$\frac{dR^{l^+l^-}}{d^4P} = \int \frac{d^3\mathbf{p}_1}{(2\pi)^3} \frac{d^3\mathbf{p}_2}{(2\pi)^3} f_q(\mathbf{p}_1) f_{\bar{q}}(\mathbf{p}_2) v_{q\bar{q}} \sigma_{q\bar{q}}^{l^+l^-} \delta^{(4)}(P - p_1 - p_2), \quad (0.1)$$

Wobei hier  $f_{q,\bar{q}}$  die Phasenraumverteilungsfunktion der Mediumquarks (Antiquarks),  $v_{q,\bar{q}}$  die Relativgeschwindigkeit zwischen Quarks und Antiquarks und  $\sigma_{q\bar{q}}^{l^+l^-}$  der totale Wirkungsquerschnitt des Vernichtungsprozesses  $q + \bar{q} \rightarrow l^+ + l^-$  ist. Um Impuls-Raum Anisotropien in der Verteilungsfunktion mitzuberechnen, wird eine azimuthale Symmetrie der Materie im Impulsraum angenommen, so dass die anisotropen Quark/Antiquark Phasenraumverteilungen aus einer beliebigen isotropen Phasenraumverteilungsfunktion durch Stauchung  $\xi > 0$  oder Strecken  $\xi < 0$  relativ zu einer Richtung im Impulsraum ermittelt werden kann, als

$$f_{q,\bar{q}}(\mathbf{p}, \xi, p_{\text{hard}}) = f_{q,\bar{q}}^{\text{iso}}(\sqrt{\mathbf{p}^2 + \xi(\mathbf{p} \cdot \hat{\mathbf{n}})^2}, p_{\text{hard}}), \quad (0.2)$$

Hierbei ist  $p_{\text{hard}}$  die Skala des harten Impulses,  $\mathbf{n}$  die Richtung der Anisotropie und  $\xi > -1$  ein Parameter der Auskunft über die Stärke und Art der Anisotropie gibt. Es ist bekannt, dass es für eine gute Beschreibung nicht ausreicht, nur die Dileptonenrate mit den Experimenten zu vergleichen. Zusätzlich muss eine Beschreibung der zeitlichen Entwicklung des Feuerballs im Ortsraum gegeben werden. Dazu ist es wiederum notwendig, über den gesamten Raum zu integrieren, was mit einem Entwicklungsmodell für den harten Impuls geschehen kann. Dabei sind die Dileptonen Ausbeuten



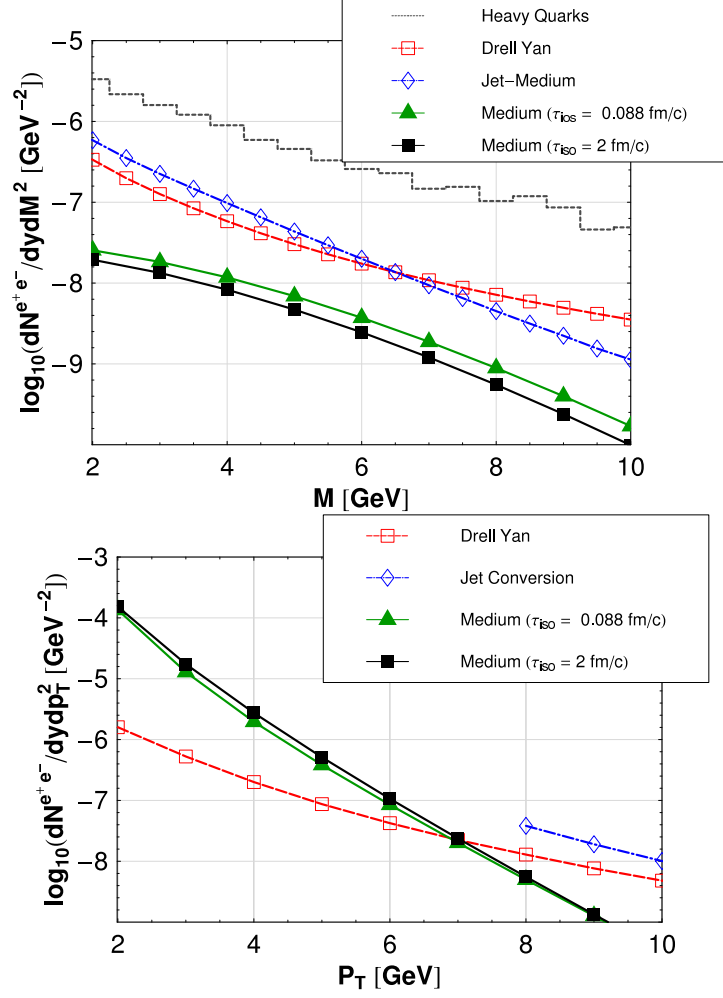


Figure 0.2.: Dileptonen Ausbeute simuliert mit einem kollisionsberücksichtigendem Modells aufgetragen gegen die invariante Masse bei Au+Au Kollisionen bei LHC Daten mit Rapidität  $y=0$  und fester Endmultiplizität.

gegeben als.:

$$\frac{dN^{l^+l^-}}{dM^2 dy} = \pi R_T^2 \int d^2 p_T \int_{\tau_0}^{\tau_f} \int_{-\infty}^{\infty} \frac{dR^{l^+l^-}}{d^4 P} \tau d\tau d\eta, \quad (0.3)$$

$$\frac{dN^{l^+l^-}}{d^2 p_T dy} = \pi R_T^2 \int dM^2 \int_{\tau_0}^{\tau_f} \int_{-\infty}^{\infty} \frac{dR^{l^+l^-}}{d^4 P} \tau d\tau d\eta \quad (0.4)$$

$$\frac{dN^{l^+l^-}}{dy} = \pi R_T^2 \int dM^2 d^2 p_T \int_{\tau_0}^{\tau_f} \int_{-\infty}^{\infty} \frac{dR^{l^+l^-}}{d^4 P} \tau d\tau d\eta, \quad (0.5)$$

Wobei  $dR^{l^+l^-}/d^4 P$  die differenzielle Dileptonenrate und  $R_T$  der transversale Radius des Kerns ist. Die ersten beiden Ausdrücke werden dabei in der zentralen Rapiditätszone ausgewertet und die Letzte in der nach vorne gerichteten Rapiditätszone.

Das Hauptinteresse liegt bei Impulsraumanisotropien, die sich zu Beginn der Kollision entwickeln. Diese Entwicklung der anfänglichen Anisotropien wird in das Gesamtmodell miteinbezogen,

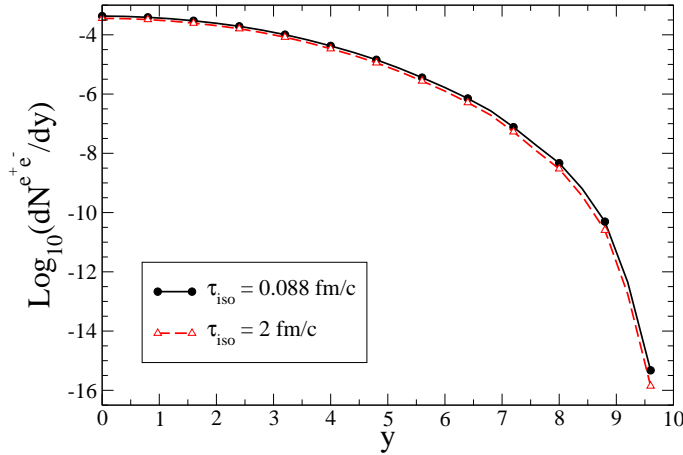


Figure 0.3.: Dileptonen Ausbeuten simuliert mit dem kollisionsintegrierten Modell bei festgehaltener Endmultiplizität und einem Schnitt bei  $M \geq 2$  GeV und  $P_T \geq 100$  MeV. Für Dileptonen im Medium wird entweder mit  $\gamma = 2$  und  $\tau_{\text{iso}}$  entweder 0.088 oder 2 fm/c für LHC Energien benutzt.

welches nun die Entwicklung der Energiedichte, des harten Impulses  $p_{\text{hard}}$  und die des Anisotropieparameters  $\xi$  beschreibt. Es werden zwei phenomenologische Modelle vorgestellt, die diese Entwicklung beschreiben. Zuerst wird ein Modell vorgestellt, in dem von einem, 0+1 dimensionalen frei strömenden System zur Anfangszeit, hin zu einem 0+1 dimensionalen idealen hydrodynamischen System interpoliert wird. Im zweiten Modell wird von einem sich verbreiternden 0+1 dimensional System mit Kollisionen hin zu einem idealen hydrodynamischen System interpoliert. In beiden Modellen werden drei Parameter benutzt. Der erste  $\tau_0$  ist die Zeit die vergeht, bis sich die Partonen von den Kernen abspalten. Der zweite,  $\tau_{\text{iso}}$  ist die Zeitspanne, bis das System isotrop im Impulsraum wird. Und der dritte  $\gamma$  beschreibt die Weite des Übergangs von der Vor Gleichgewichtsphase zur ideal hydrodynamischen Phase. Bei passend gewählten asymptotischen Grenzen, sind diese Interpolationsmodelle in der Lage, instantan ideale Hydrodynamik und ideales freies Strömen als spezielle Fälle einer Expansion darzustellen. Dabei werden die Rechnungen dadurch beschränkt, dass entweder die Anfangsbedingungen oder die Pionen Multiplizität am Ende festgehalten werden. In Abbildung 0.1 wird die Eigenzeitabhängigkeit der Energiedichte, der harten Impulsskala und des Anisotropieparameters für eine frei strömende Expansion mit festgehaltenen Anfangsbedingungen (oben) und festgehaltener finaler Pionenmultiplizität (unten) gezeigt. Anhand der Abbildung ist zu erkennen, dass bei festgehaltenen Anfangsbedingungen die Energiedichte immer größer ist im Falle eines Systems, das instantan zu einem hydrodynamischen Verhalten thermalisiert. Daher ist die Dileptonenausbeute in diesem Falle größer, als wenn die finale Pionenmultiplizität festgehalten würde.

Aus Abbildung 0.2 ist zu entnehmen, dass die Dileptonenausbeute als eine Funktion der invarianten Masse und des transversalen Impulses empfindlich auf die Wahl der Isotropisierungszeit  $\tau_{\text{iso}}$  reagiert. Die Abhängigkeit von der invarianten Masse ist keine geeignete Observable für Experimentalphysiker, da die Dileptonenproduktion im Medium von gleicher Größenordnung oder sogar kleiner als andere Dileptonenquellen sein kann. Im Falle hoher harter Impulse  $p_T$  sieht die Lage vielversprechender aus. Die beste Möglichkeit, um Informationen über  $\tau_{\text{iso}}$  und den Grad der Anisotropisierung zu erhalten, liegt darin hohe transversale Impulse in den Dileptonen Spektren am RHIC ( $1 < p_T < 6$  GeV) und am LHC ( $2 < p_T < 8$  GeV) zu analysieren.

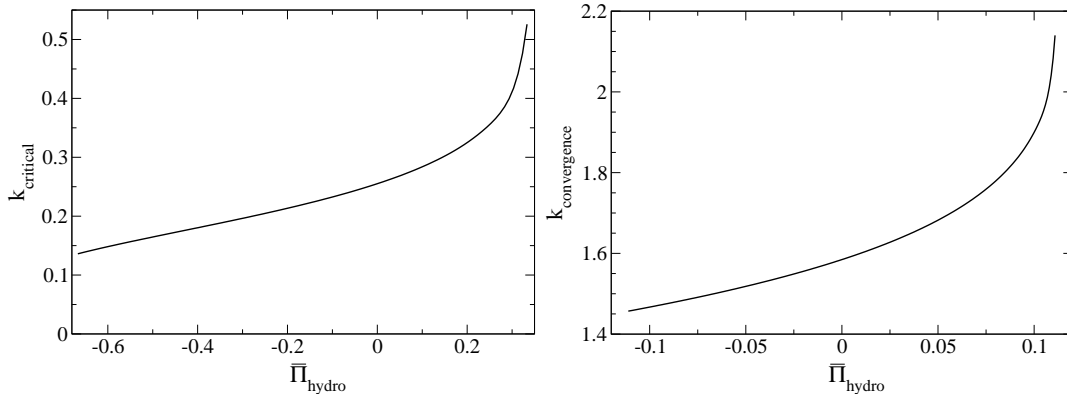


Figure 0.4.: Kritischer (links) und konvergierender (rechts) Grenzfall bei  $k = \tau_{\text{hydro}}(\mathcal{E}(\tau = \tau_{\text{hydro}}))^{1/4}$  als Funktion der Anfangsshear,  $\bar{\Pi}_{\text{hydro}} = \Pi(\tau = \tau_{\text{hydro}})/\mathcal{E}(\tau = \tau_{\text{hydro}})$ . Die Transportkoeffizienten in diesem Fall haben typische starke Kopplungswerte.

Die zuvor beschriebenen Interpolationsmodelle werden auf die nach vorne gerichtete Region der Kollision ausgeweitet, indem die Rapiditätsabhängigkeit des harten Impulses einbezogen wird. In Abbildung 0.3 sind die Resultate der berechneten Dileptonen Produktion gegen die Rapidität geplottet. Es zeigt sich, dass die nach vorne gerichteten Dileptonen bei einer Isotropisierungszeit von 2 fm/c um einen Faktor 3 unterdrückt sind.

## Wahl der Anfangsbedingungen für viskose Hydrodynamik

Eine Hauptidee, die aus der Analyse der RHIC Daten mit Hilfe eines viskosen Hydrodynamik Modells in 2ter Ordnung gewonnen werden kann, ist, dass ein Mangel an Methoden zur Bestimmung der Anfangsbedingungen für eine viskose hydrodynamische Simulation besteht. Insbesondere ist es nicht klar, wann überhaupt ein Hydrodynamikmodell zur Beschreibung von ultrarelativistischen Schwerionenkollisionen verwendet werden darf. Es wäre daher wünschenswert, eine Methode zu finden, die die Wahl der passenden Anfangsbedingungen ermöglicht. Der zweite Teil dieser Arbeit wird genau diesen Punkt focussieren. Zunächst seien zwei Notwendigkeiten für die Berechnung von Lösungen der viskosen Hydrodynamik zu nennen: (1) Der longitudinale Druck muss positiv sein (2) Die Komponenten des **viscous shear tensors** müssen kleiner als der hydrostatische Druck sein. Die erste Bedingung, auch kritische Beschränkung genannt, ist die minimale Bedingung, um überhaupt numerischen Simulationen von viskos hydrodynamischen Systemen zu trauen. Sollten negative Werte des effektiven longitudinalen Druckes auftreten, so heißt das, dass dissipative Korrekturen größer als der Gleichgewichtsteil des Energie-Impuls tensors ist, was Hydrodynamik als Modell unbrauchbar macht. Einen effektiven longitudinalen Druck zu kennen reicht nicht aus, um die Gradientenentwicklung durchzuführen, die für die Hydrodynamik essentiell ist, da die viskosen **shear** Korrekturen von der gleichen Größenordnung sein könnten, wie die Gleichgewichtskomponenten des Energie-Impuls Tensors. In dem zu letzt genannten Fall wäre es notwendig eine stärkere Bedingung zu fordern mit der die Gradientenentwicklung besser durchgeführt werden kann. Diese Bedingung ergibt sich als  $\alpha \Pi$  wobei  $\alpha$  eine Nummer zwischen [0,1] ist. Im Laufe der Arbeit wird gezeigt werden, wie sich diese physikalischen Bedingungen im Kontext von Schwerionenkollisionen auswirken werden, indem sie auf eine 0+1 dimensionale viskos hydrodynamische Rechnung in 2 Ordnung Störungstheorie angewendet werden. Dabei werden sowohl starke als auch schwache Kop-

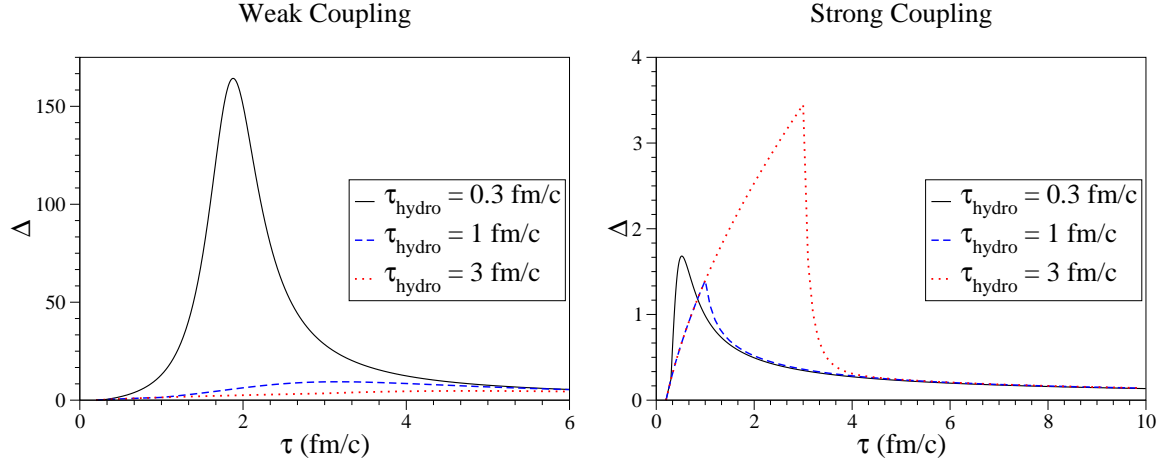


Figure 0.5.: Zeitliche Entwicklung der Druckanisotropieparameters  $\Delta$  für drei verschiedene Werte von  $\tau_{\text{hydro}} \in \{0.3, 1, 3\}$  fm/c. Es wird  $\tau_0 = 0.3$  fm/c und alle Anfangs Temperaturen bei einer Partonenformationszeit  $p_{\text{hard}} = T_{\text{hydro}} = 0.35$  GeV benutzt. Alle Plots benutzen das Kollisionsintegrierte Modell und die transport Koeffizienten sind ungefähr die des schwachen Kopplungsfall (linke Seite) und des starken Kopplungsfall (rechte Seite).

plungen betrachtet. Durch die Untersuchung des Phasenraumes werden physikalischen nicht triviale Beziehungen zwischen den Anfangsbedingungen der Energiedichte, des **shear viscous tensor** und der Anfangszeit gefunden. Diese Untersuchung ermöglicht es, immer niedrigere Grenzen der Anfangszeit  $\tau_{\text{hydro}}$  zu finden. Die linke Seite von Abbildung zeigt die Lösungen, welche  $P > 0$  erfüllen. Auf der rechten Seite erfüllen die Lösungen nicht nur Positivität, sondern auch die Bedingung IIY3.

Mit diesen Erkenntnissen ist es möglich die 0+1 dimensionale Expansion an 0+1 dimensionale viskose Hydrodynamik, in 2 Ordnung der Störungsreihe, anzupassen, indem die Abhängigkeit des Anisotropieparameters  $\xi$  vom Anisotropiedruck  $\Delta$  untersucht wird. Damit ist es möglich, im Rahmen der viskosen Hydrodynamik, die Anfangswerte der Energiedichte und des **shear viscous tensors** also Funktion der Lebenszeit der Vergleichgewichtsphase zu finden. Dabei werden zwei Fälle betrachtet.: Das freie Strömen des Systems und der Fall eines sich durch Kollisionen weitenden Systems. Folglich werden zwei Zeitskalen verwendet.: Die Zeit die vergeht, bis die Partonen sich ablösen  $\tau_0$  und die Zeit bei der das System anfängt sich viskos hydrodynamisch zu verhalten. Die Anfangsbedingungen hängen dabei nicht von der Art der Kopplungskonstante ab, da diese nicht in der ersten Ordnung vorkommt. In Abbildung 0.4 ist die zeitliche Entwicklung des Anisotropiedruckes  $\Delta$  aufgetragen, wobei eine Expansion aus dem Vergleichgewichtszustand mit kollisionsbedingter Systemverbreiterung angenommen wurde. Wird dieses Modell benutzt, kann untersucht werden, wie sich die Entropieproduktion verhält, wenn die Anfangsbedingungen verändert werden. Des Weiteren können Grenzfälle entwickelt  $\sim 0.5$  werden.

# Abstract

In this work we investigate phenomenological aspects of an anisotropic quark-gluon plasma. In the first part of this thesis, we formulate phenomenological models that take into account the momentum-space anisotropy of the system developed during the expansion of the fireball at early-times. By including the proper-time dependence of the parton hard momentum scale,  $p_{\text{hard}}(\tau)$ , and the plasma anisotropy parameter,  $\xi(\tau)$ , the proposed models allow us to interpolate from 0+1 pre-equilibrated expansion at early-times to 0+1 ideal hydrodynamics at late times. We study dilepton production as a valuable observable to experimentally determine the isotropization time of the system as well as the degree of anisotropy developed at early-times. We generalize our interpolating models to include the rapidity dependence of  $p_{\text{hard}}$  and consider its impact on forward dileptons.

Next, we discuss how to constrain the onset of hydrodynamics by demanding two requirements of the solutions to the equations of motion of viscous hydrodynamics. We show this explicitly for 0+1 dimensional 2nd-order conformal viscous hydrodynamics and find that the initial conditions are non-trivially constrained. Finally, we demonstrate how to match the initial conditions for 0+1 dimensional viscous hydrodynamics from pre-equilibrated expansion. We analyze the dependence of the entropy production on the pre-equilibrium phase and discuss limitations of the standard definitions of the non-equilibrium entropy in kinetic theory.



# Contents

0.1. Zusammenfassung . . . . .	v
<b>1. Introduction</b>	<b>1</b>
1.1. Basics of Quantum Chromodynamics . . . . .	1
1.2. Nuclear matter at extreme conditions . . . . .	2
1.3. Thermalization of the QGP and anisotropic plasmas . . . . .	5
1.4. Electromagnetic probes . . . . .	6
1.5. Notation of this thesis . . . . .	7
1.6. Outline of this thesis . . . . .	8
<b>2. Physics of the anisotropic quark-gluon plasma</b>	<b>9</b>
2.1. Review of bottom-up scenario . . . . .	9
2.1.1. a) $1 < Q_s \tau < \alpha^{-3/2}$ . . . . .	10
2.1.2. b) $\alpha^{-3/2} < Q_s \tau < \alpha^{-5/2}$ . . . . .	11
2.1.3. c) $\alpha^{-5/2} < Q_s \tau < \alpha^{-13/5}$ . . . . .	11
2.2. Plasma instabilities in QCD . . . . .	12
2.2.1. Physical origin of plasma instabilities . . . . .	12
2.2.2. Collective modes of an anisotropic plasma . . . . .	13
2.3. Impact of plasma instabilities on the thermalization process of the QGP . . . . .	19
<b>3. Hydrodynamics and Ultrarelativistic Heavy Ion Collisions</b>	<b>23</b>
3.1. Relativistic hydrodynamics . . . . .	23
3.1.1. Tensor decomposition . . . . .	24
3.1.2. Choosing the reference frame . . . . .	25
3.2. Fluid dynamics from kinetic theory . . . . .	25
3.2.1. Ideal relativistic hydrodynamics . . . . .	27
3.2.2. Dissipative relativistic hydrodynamics . . . . .	28
3.2.3. Conformal viscous hydrodynamics . . . . .	33
<b>4. Dileptons in ultrarelativistic heavy ion collisions</b>	<b>37</b>
4.1. Medium dilepton production rate from finite temperature field theory . . . . .	38
4.2. Medium dilepton production rate from kinetic theory . . . . .	41
4.3. Sources of high-energy dileptons . . . . .	42
4.3.1. Drell-Yan dileptons . . . . .	42
4.3.2. Heavy flavour decays . . . . .	43
4.3.3. Jet conversion . . . . .	43
<b>5. Dilepton production from an anisotropic quark-gluon plasma</b>	<b>45</b>
5.1. Differential dilepton rate . . . . .	46
5.2. Dilepton yields from the pre-equilibrated stage: central rapidity region . . . . .	47
5.2.1. Space-Time Models . . . . .	49
5.2.2. Asymptotic Limits of the Anisotropic Phase Space Distribution . . . . .	50
5.2.3. Momentum-space Broadening in an Expanding Plasma . . . . .	53
5.2.4. Space-Time Interpolating Models with Fixed Initial Conditions . . . . .	55
5.2.5. Space-Time Interpolating Models with Fixed Final Multiplicity . . . . .	58

5.2.6.	Results of high energy dileptons in the central rapidity region . . . . .	60
5.2.7.	Dilepton production with fixed initial conditions . . . . .	61
5.2.8.	Dilepton production with fixed final multiplicity . . . . .	67
5.2.9.	Summary of Results . . . . .	71
5.3.	Dilepton yields from the pre-equilibrated stage: forward rapidity region . . . . .	75
5.3.1.	Space-time interpolating models with the rapidity dependence . . . . .	75
5.3.2.	Results of high-energy dileptons in the forward rapidity region . . . . .	76
5.4.	Conclusions . . . . .	80
<b>6.</b>	<b>Constraining the onset of relativistic viscous hydrodynamics</b>	<b>83</b>
6.1.	0+1 Dimensional Conformal 2nd-Order Viscous Hydrodynamics . . . . .	84
6.1.1.	Specification of equation of state and dimensionless variables . . . . .	85
6.1.2.	Strong coupling estimates of the transport coefficients . . . . .	87
6.1.3.	Weak coupling estimates of the transport coefficients . . . . .	87
6.1.4.	Momentum space anisotropy . . . . .	88
6.1.5.	Approximate Analytic Solution of 0+1 Conformal Hydrodynamics . . . . .	89
6.2.	Lower bounds on the initial time from the viscous hydrodynamical equations . . . . .	90
6.2.1.	Time Evolution of $\Delta$ . . . . .	90
6.2.2.	Negativity of Longitudinal Pressure . . . . .	93
6.2.3.	Determining the critical line in initial condition space . . . . .	94
6.2.4.	Determining the convergence line in initial condition space . . . . .	95
6.2.5.	Implications for higher dimensional hydrodynamical simulations . . . . .	97
6.3.	Matching pre-equilibrium dynamics and viscous hydrodynamics . . . . .	100
6.3.1.	0+1 dimensional model for a pre-equilibrium QGP . . . . .	101
6.3.2.	Temporal evolution including pre-equilibrium dynamics . . . . .	104
6.4.	Entropy and kinetic theory . . . . .	108
6.4.1.	Entropy from 14th Grad's Method . . . . .	108
6.4.2.	Entropy from the anisotropic distribution ansatz . . . . .	109
6.5.	Entropy generation . . . . .	110
6.5.1.	Free streaming model . . . . .	111
6.5.2.	Collisionally broadened model . . . . .	111
6.5.3.	Including initial anisotropies at the formation time . . . . .	114
6.6.	Summary of results . . . . .	115
<b>7.</b>	<b>Conclusions and outlook</b>	<b>117</b>
	<b>Appendices</b>	<b>121</b>
<b>A.</b>	<b>Useful relations of the moments of the Boltzmann distribution function</b>	<b>123</b>
<b>B.</b>	<b>2nd order conformal relativistic hydrodynamics for a 0+1 dimensional expansion</b>	<b>127</b>
B.1.	0+1 viscous hydrodynamical equations . . . . .	127
<b>C.</b>	<b>Useful relations in thermal field theory</b>	<b>131</b>
C.1.	Relation between thermal Green functions . . . . .	131
C.2.	Fermionic summation formula . . . . .	133
C.3.	Evaluation of $\tilde{C}_{\mu\nu}(P)$ using imaginary time formalism . . . . .	134
C.3.1.	Reinterpretation of $\tilde{C}^{<}(p^0)$ in terms of kinetic theory . . . . .	136
C.4.	Transversality of the free current-current correlator . . . . .	138
	<b>Bibliography</b>	<b>139</b>



# 1. Introduction

And my story. It began.

---

*I haven't dreamed of flying for a while*  
Taichi Yamada.

## 1.1. Basics of Quantum Chromodynamics

Quantum Chromodynamics (QCD) is at present universally accepted as the theory of the strong interaction. The fundamental degrees of freedom in the theory are the quarks and gluons that carry color charges. These particles cannot be directly seen in Nature, because confinement binds them into color-neutral bound states known as baryons and mesons. QCD has been thoroughly tested in experiment and is known to possess the expected properties: the coupling constant weakens as the energy increases (celebrated ‘asymptotic freedom’ [3, 4]), the quarks and gluons manifest themselves through the production of jets, the partonic constituents of matter are seen in Deep Inelastic Scattering and the corresponding structure functions exhibit scaling violation, etc.

QCD is formulated as a gauge theory, in analogy with QED. The structure of QED is entirely fixed by the requirement of invariance under local gauge transformations, that is invariance with respect to the phase rotation of the electron field  $\Psi(x) \rightarrow e^{i\alpha(x)}\Psi(x)$ , where the phase factor  $\alpha$  depends on the space-time coordinates. In the case of QCD, we have the constituent quarks that come in three different colors,  $N_c = 3$ . The local gauge invariance with respect to the  $SU(N_c)$  rotations in color space introduces  $N_c^2 - 1 = 8$  gauge bosons, the gluons. Quarks are spin 1/2 particles that belong to the fundamental representation of  $SU(3)$  whereas gluons are spin 1 particles defined in the adjoint representation of  $SU(3)$ . Quarks have three different colors say, red, green and blue, hence a quark state vector can be expressed as a color multiplet of three components. Interactions with gluons rotate the colors of the quarks, however the non-abelian nature of the gauge group  $SU(3)$  implies that gluons can also interact with each other.

The QCD lagrangian reads as <sup>1</sup>

$$\mathcal{L}_{\text{QCD}} = \sum_q \bar{q}(x) (i \gamma_\mu D^\mu - m_q) q(x) - \frac{1}{4g^2} \text{tr} G^{\mu\nu}(x) G_{\mu\nu}(x) \quad (1.1)$$

where the sum is extended over the number of colors and flavors.  $q(x)$ ,  $\bar{q}(x)$  are the quark and antiquark fields,  $D_\mu = \partial_\mu - i g A_\mu^a t^a$  is the covariant derivative,  $g$  is the coupling constant and  $G^{\mu\nu}(x)$  is the field strength tensor given in terms of the gauge field  $A_\mu^a$

$$G_a^{\mu\nu}(x) = \partial^\mu A_\nu^a(x) - \partial^\nu A_\mu^a(x) + f_{abc} A_b^\mu(x) A_c^\nu(x). \quad (1.2)$$

To ensure gauge invariance of the QCD lagrangian, the quark and gauge fields transform under the gauge group in the fundamental and adjoint representation

$$q(x) \rightarrow U(x) q(x), \quad (1.3a)$$

$$A^\mu(x) \rightarrow U(x) A^\mu(x) U^\dagger(x) + \frac{i}{g} U(x) \partial^\mu U^\dagger(x). \quad (1.3b)$$

---

<sup>1</sup>We omit the sum over color indices explicitly.

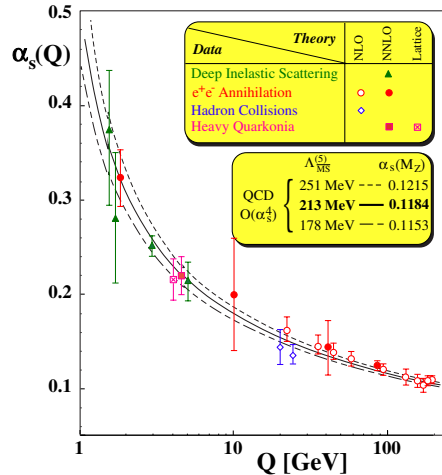


Figure 1.1.: The running coupling constant  $\alpha_s(Q^2)$  as a function of momentum transfer  $Q^2$  determined from a variety of processes. Figure taken from Ref. [9].

where  $U(x) = \exp(-i \phi_a(x) T^a)$  is a unitary complex valued matrix and  $T^a$  are the generators of  $SU(3)$ .

One of the most remarkable properties of QCD is related to the fact that at large energies the coupling constant is small, i.e. perturbation theory is applicable. Because of the gluon self-interactions, we have *anti*-screening [3, 4] and the constant coupling becomes small at short distances (high energies) but large at large distances (low energies). In Coulomb gauge, the anti-screening stems from the diagram in which the exchange of a Coulomb gluon excites from the vacuum zero modes of the transverse gluons [5, 6, 7]; for review see [8]. This diagram is purely real and leads to a Coulomb interaction that strengthens as the distance grows. Finally, the dependence of the coupling in momentum space can be expressed as a function of the virtuality of the photon  $Q^2$ . To one loop order the scale dependence is

$$\alpha_s(Q^2) = \frac{\alpha_s(Q_0^2)}{1 + \frac{\alpha_s(Q_0^2)}{12\pi} (11 N_c - 2 N_f) \log(Q^2/Q_0^2)}. \quad (1.4)$$

In Fig. 1.1 we show the experimental verification of this prediction. Formally speaking, the fact that the coupling constant is small at high energies is related to the negative value of the so-called  $\beta$ -function. However, in spite of these successes the behavior of the theory at low energies or large distances and the structure of its vacuum state are still poorly understood due to confinement. Confinement means that at large distances we do not observe single quarks but instead we observe hadrons which are colorless particles. One may hope that progress can be achieved through the studies of thermodynamics of quarks and gluons at high temperatures and densities. Understanding collective behavior may appear simpler than understanding the dynamics of the individual constituents. At temperatures accessible experimentally, the typical distances between the quarks and gluons in the ‘Quark-Gluon Plasma’ (QGP) can be quite large and the coupling becomes strong during that stage. Achieving progress in the understanding of QGP thus requires methods that apply in both the weak and strong coupling domains.

## 1.2. Nuclear matter at extreme conditions

After the great success of asymptotic freedom of non-abelian gauge theories and its applications to high-energy scattering processes, a new paradigm came out and up to now it has not been

understood completely: *confinement*. In scattering processes described by QED, we can have that the initial and final states can be either photons or leptons. In QCD the situation turns out to be a bit more complicated since at large distances the coupling constant becomes large, and hence, quarks and gluons cannot be considered as asymptotically free particles and the hadrons observed in nature are colorless when these are measured. To understand confinement one should deal with non-perturbative physics and the best available tool is to examine the system on a discrete lattice of space and time or better known as QCD lattice.

Nevertheless, one can get great physical insight by simplifying the complex structure of hadrons by considering these as containers or bags of quarks and gluons. In this phenomenological model, quarks are considered as massless particles inside a bag of finite dimension, and are infinitely massive outside the bag. The gluons are also contained within the bag. Confinement in the model is the result of the balance of the bag pressure  $B$ , which is directed inward, and the stress arising from the kinetic energy of the quarks. The total color charge of the matter inside of the bag is zero, implying that the only allowed hadronic bags would be baryons ( $qqq$ ), antibaryons ( $\bar{q}\bar{q}\bar{q}$ ) and mesons ( $q\bar{q}$ ). When the pressure of the strong matter inside the bag is increased, there will be a point when the pressure directed outward is greater than the inward bag pressure. In this case, the bag pressure cannot be balanced and the bag cannot contain the matter inside. Therefore, a new state of matter composed of quarks and gluons in an unconfined state is then possible. The main condition for such state of matter is the occurrence of a large pressure exceeding the bag pressure  $B$ . The large pressure of this deconfined state of QCD matter arises when the temperature is large or when the baryon number density is large. New phases of QCD matter are then expected. More refined models that take into account another effects such as chiral symmetry have been done. In principal, the simple bag model can predict some of the phases of QCD matter excepting color superconductivity and most recently the quarkyonic phase [10, 11, 12]. Nevertheless, its simplicity allows us to understand qualitatively asymptotic limits, say large temperatures or high baryon number density. The complete description of the QCD phase diagram is an incomplete program; however, much progress have been made in the last 30 years.

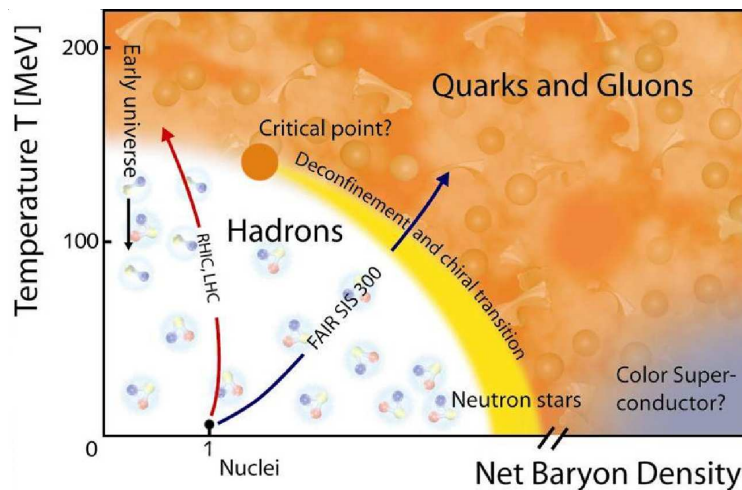


Figure 1.2.: Sketch of the contemporary view of the QCD phase diagram.

In Fig. 1.2, we show a sketch of the contemporary version of the QCD phase diagram in the  $(\mu_B, T)$  plane.<sup>2</sup> At low temperature  $T$  and low values of the baryo-chemical potential  $\mu_B$  the chiral symmetry of the QCD lagrangian is broken [13] and the system is in the hadronic phase.

<sup>2</sup>Figure taken from <http://www.gsi.de/fair/experiments/CBM/1intro.html>.

As one increases  $\mu_B$  but keeping low temperatures, QCD matter enters in the phase described by color superconductivity [14]. In the opposite limit, i.e., high temperatures but low values of  $\mu_B$ , the quarks and gluons are in a deconfined plasma phase (QGP) and the chiral symmetry is restored.

When we consider QCD matter in the limit of high temperatures and low baryochemical potential  $\mu_B \approx 0$ , lattice QCD can help to quantify more precisely the emerging picture of deconfinement. As a matter of fact, lattice calculations indicate that there is a transition from deconfined to confined phase [15, 16, 17]. In Fig. 1.3 we show the energy density scaled by  $T^4$  as a function of the temperature predicted by lattice QCD for different types of QCD matter. This computation shows an increase of the energy density when the temperature of the system  $T \approx T_C = 160\text{-}180$  MeV. Indeed, the energy density changes by up to one order of magnitude around  $T_C$ . Since the energy density and the other thermodynamical variables are proportional to the degrees of freedom of the system, this increase of the energy density can be interpreted as a change of the degrees of freedom between a confined and a deconfined phase. Above  $T_C$ , QCD matter behaves as a plasma of quarks and gluons whereas below  $T_C$  the system is a confined system composed of hadrons.

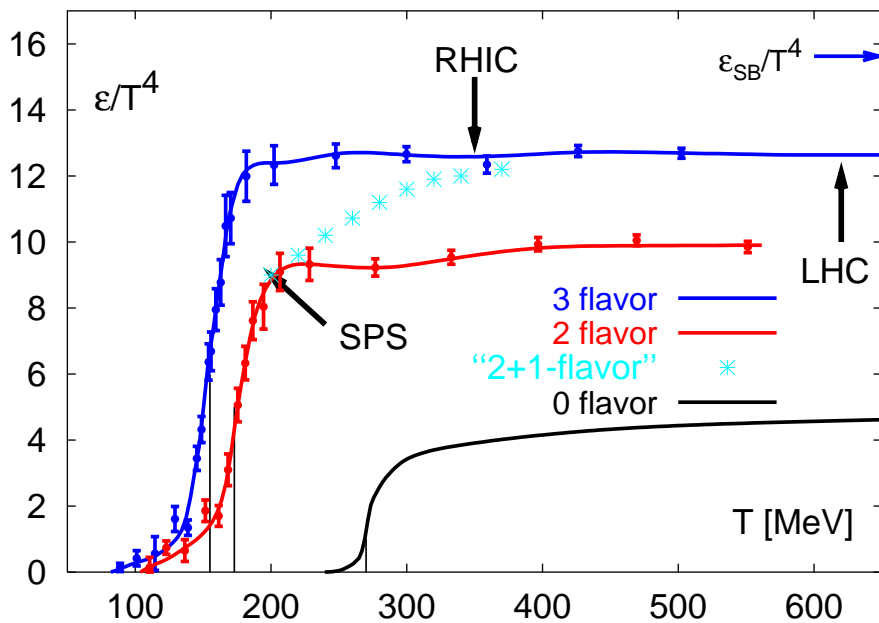


Figure 1.3.: The energy density as a function of the temperature for different content of flavors from lattice QCD. Figure taken from [18].

From the experimental point of view, high temperatures and low values of baryochemical potential can be studied by colliding nuclei at high energies. Due to the Lorentz contraction along the longitudinal beam axis of the collision and large size of the nuclei along the transverse plane, a very hot and dense system of nuclear matter can be formed in the central region [19]. The main goal of the experiments that perform ultrarelativistic heavy-ion collisions is to produce and study the properties of a deconfined plasma of quarks and gluons. This program has been underway for nearly a decade at the Relativistic Heavy Ion Collider (RHIC) and in the future experiments are scheduled at the Large Hadron Collider (LHC).

### 1.3. Thermalization of the QGP and anisotropic plasmas

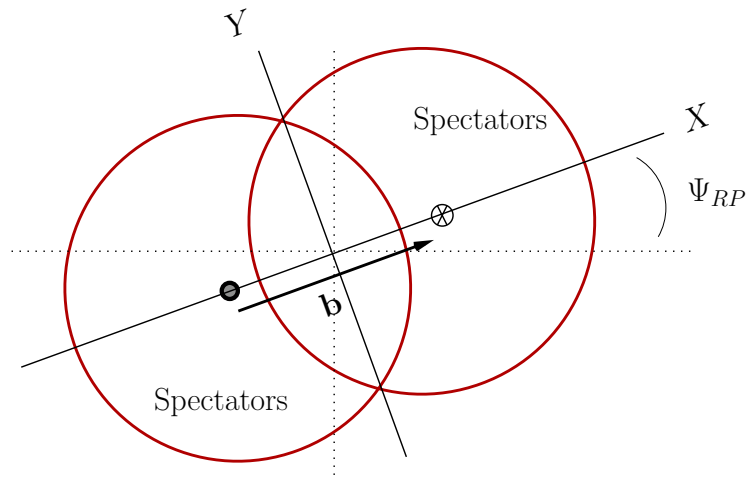


Figure 1.4.: A schematic of the transverse plane in a heavy ion event. The impact parameter is a transverse vector  $\mathbf{b} = (b_x, b_y)$  pointing from the center of one nucleus to the center of the other one.  $\Psi_{RP}$  is known as the reaction plane angle, which is the angle respect to the lab axes as shown in the figure. Figure taken from [20].

When two nuclei collide, they usually do so at impact parameter  $\mathbf{b}$  and oriented at an angle  $\Psi_{RP}$  with respect to the lab axes as shown in Fig. 1.4. As a result of this, the initial profile of energy density of the nuclear matter is azimuthally anisotropic. Because of this initial configuration, there are higher pressure gradients along the shortest overlap region than in the largest overlap region (in-plane and out-of plane) and therefore, the emission of particles produced after the collision will carry this information. Experimentalists quantify the flow of matter by expanding the differential yield of particles in a Fourier series

$$\frac{1}{p_T} \frac{dN}{dy dp_T d\phi} = \frac{1}{2\pi p_T} \frac{dN}{dy dp_T} (1 + 2v_2(p_T) \cos 2(\phi - \Psi_{RP}) + \dots), \quad (1.5)$$

where  $v_2$  is second Fourier coefficient of the azimuthal distribution  $\langle \cos(2(\phi - \Psi_{RP})) \rangle$ . This coefficient is defined as

$$v_2 \equiv \left\langle \frac{p_X^2 - p_Y^2}{p_X^2 + p_Y^2} \right\rangle. \quad (1.6)$$

Notice that in Eq. (1.5), higher harmonics such as  $v_4, v_6$  and so on can also contribute to the produced particles. The typical way to model is hydrodynamics where one should ensure that the energy-momentum tensor of the system is not far from equilibrium. In the case of ideal hydrodynamics, the energy-momentum tensor should be at least, isotropic in momentum-space [21]. The first results of RHIC demonstrated that ideal hydrodynamics was able to fit the low  $p_T$  dependence of the elliptic flow  $v_2$  if the hydro simulations were initialized at early times  $\tau_0 \lesssim 1$  fm/c [22, 23, 24, 25]. This lead to the initial statements concerning ‘early thermalization’ of the QGP. However, once viscous corrections are included, the matching of hydrodynamics to data does not require a short thermalization time. Indeed, recent analysis of RHIC data show that even thermalization times of  $\tau_0 \sim 2$  fm/c can describe the dependence of  $v_2$  on the hadron rest mass  $p_T$  [1].

From first principles calculations based on pQCD, thermalization of the QGP is achieved due to parton-parton collisions. In the bottom-up scenario [26] where binary and  $2 \leftrightarrow 3$  collisions are

included, it is estimated that the thermalization time for RHIC energies is  $\tau_0 \sim$  is 2.7 fm/c [27]. Numerical simulations based on parton cascade models for 3+1 dimensions which also include binary and  $2 \leftrightarrow 3$  parton interactions show that the estimated time for the thermalization of a gluonic system is  $\sim 1.5$  fm/c [28, 29]. These calculations have ignored an important issue related with non-equilibrium field theory, namely the formation of plasma instabilities [30, 31]. This mechanism turns out to be important in the isotropization process of the QGP. At the earliest times after the collision, the system expands almost entirely along the longitudinal beam axis. Immediately after the collision, the partons are produced from the incoming colliding nuclei at  $\tau = \tau_0$ , at which time the partonic momentum distributions can be assumed to be isotropic.<sup>3</sup> The subsequent rapid longitudinal expansion of the matter (along the beam line) causes it to become much colder in the longitudinal direction than in the transverse direction [26]. Longitudinal cooling occurs because initially the longitudinal expansion rate is larger than the parton interaction rate and, as a result, a local momentum-space anisotropy is induced with  $\langle p_L^2 \rangle \ll \langle p_T^2 \rangle$  in the local rest frame. If the system is to return to an isotropic state it is necessary that at some later time the interaction rate overcomes the expansion rate with the system finally isotropizing and remaining isotropic for  $\tau \geq \tau_{\text{iso}}$ . Once isotropy is achieved (and maintained by parton interactions) the use of hydrodynamic simulations can be justified. The study of anisotropic plasmas has received much interest recently due to the fact that a quark-gluon plasma which has a local momentum-space anisotropy,  $2\langle p_L^2 \rangle \neq \langle p_T^2 \rangle$ , is subject to the chromo-Weibel instability [21, 33, 34, 35, 2, 36, 37, 38, 39, 40, 41, 42, 43, 44, 45, 46, 47, 48, 49, 50, 51]. The chromo-Weibel instability causes rapid growth of soft gauge fields which preferentially work to restore the isotropy of the quark-gluon plasma on time scales much shorter than the collisional time scale. However, most of the theoretical and numerical developments in describing the time-evolution of a QGP subject to the chromo-Weibel instability have been restricted to asymptotic energies at which perturbative resummations can be applied and hence the presence of the instability-driven isotropization at RHIC and LHC energies is not yet proven. In addition, numerical studies of the chromo-Weibel instability in an one-dimensionally expanding system show that there is a time delay before the effects of plasma instabilities become important to the system's dynamics [48, 51]. In this work we study phenomenological consequences of anisotropies in momentum-space and attempt to model the effect of collisions, instabilities, etc.

## 1.4. Electromagnetic probes

In general, it is difficult to have an unequivocal identification of the quark-gluon plasma phase. What can be achieved is to have a broad set of data from different observables which, taken together, allows us to identify the presence of the deconfined phase. Electromagnetic probes such as high-energy photons and dileptons have been proposed as one of the most clear signals of the QGP phase [52, 53]. These particles interact only electromagnetically, thus their mean free path is larger than the typical system size ( $\sim 10$  fm) and as a result, they do not suffer further interaction with the medium ( $\alpha \ll \alpha_s$ ) and carry undistorted information about the circumstances of their production to the detector [52, 53]. Unlike hadrons, which are emitted from the freeze-out surface after undergoing intense re-scatterings, the observed photon and dilepton spectrum are the result of the convolution of the emissions from the entire history of the nuclear collision. To calculate the spectra of electromagnetic probes it is necessary to know how to get their production rates from the underlying theory and a model for the evolution of the fireball. Thermal photon yields and dilepton production have been studied exhaustively in ultrarelativistic heavy ion collisions.<sup>4</sup>

From the experimental point of view, in the case of high-energy medium photon production it is difficult to subtract the large backgrounds coming from  $\pi^0$  decays from other sources of photons,

<sup>3</sup>See Ref. [32] for an alternative view of the early times after the initial collision wherein the authors find that the distribution may be prolate for longer than usual assumptions.

<sup>4</sup>For a more extensive discussion of electromagnetic radiation from relativistic nuclear collisions, we refer to the reader to Refs. [54, 55].

making it hard to measure a clean high-energy medium photon production signal. In the case of high-energy dileptons, the experimental situation is dramatically improved.

When hydrodynamical predictions of  $v_2$  are confronted with experiments there are many theoretical uncertainties. Due to this, it is not clear what is the initial time when the system reaches its hydrodynamical behaviour. One possible way to remove many of these uncertainties is to find observables which are sensitive to the earliest times after the collision and are relatively unaffected by the later stages of plasma evolution. One obvious candidate to consider is high-energy dilepton production. In this work we propose space-time models for the pre-equilibrium phase of the QGP that take into account momentum-space anisotropies and study their impact on dilepton production.

## 1.5. Notation of this thesis

We summarize the conventions and notation we use along this thesis:

- We use natural units:  $\hbar = c = k_B = 1$ .
- The metric in Minkowski space  $g_{\mu\nu}$  is

$$g_{\mu\nu} = \text{diag.}(1, -1, -1, -1). \quad (1.7)$$

- The projector onto the 3-space orthogonal to the fluid velocity  $u^\mu$ :

$$\Delta^{\mu\nu} = g^{\mu\nu} - u^\mu u^\nu, \quad u_\mu \Delta^{\mu\nu} = 0. \quad (1.8)$$

- The geometric covariant derivative acting over any tensor  $T^{\mu_1\mu_2\cdots\mu_k}_{\nu_1\nu_2\cdots\nu_l}$  is [56]

$$\begin{aligned} D_\sigma T^{\mu_1\mu_2\cdots\mu_k}_{\nu_1\nu_2\cdots\nu_l} &= \partial_\sigma T^{\mu_1\mu_2\cdots\mu_k}_{\nu_1\nu_2\cdots\nu_l} \\ &+ \Gamma_{\sigma\lambda}^{\mu_1} T^{\lambda\mu_2\cdots\mu_k}_{\nu_1\nu_2\cdots\nu_l} + \Gamma_{\sigma\lambda}^{\mu_2} T^{\mu_1\lambda\cdots\mu_k}_{\nu_1\nu_2\cdots\nu_l} + \cdots \\ &- \Gamma_{\sigma\nu_1}^\lambda T^{\mu_1\mu_2\cdots\mu_k}_{\lambda\nu_2\cdots\nu_l} - \Gamma_{\sigma\nu_2}^\lambda T^{\mu_1\mu_2\cdots\mu_k}_{\nu_1\lambda\cdots\nu_l} - \cdots, \end{aligned} \quad (1.9)$$

where  $\Gamma_{\mu\nu}^\sigma$  is the associated Christoffel symbol

$$\Gamma_{\mu\nu}^\sigma = \frac{1}{2} g^{\sigma\rho} (\partial_\mu g_{\nu\rho} + \partial_\nu g_{\mu\rho} - \partial_\rho g_{\mu\nu}). \quad (1.10)$$

As a particular example of the last expression, the action of the covariant derivative for any vector  $V^\nu$  give us

$$D_\mu V^\nu = \partial_\mu V^\nu + \Gamma_{\mu\lambda}^\nu V^\lambda. \quad (1.11)$$

- The comoving time derivative  $D$

$$D \equiv u^\alpha D_\alpha. \quad (1.12)$$

- The comoving space derivative  $\nabla_\mu$

$$\nabla^\mu \equiv \Delta^{\mu\alpha} D_\alpha. \quad (1.13)$$

- The brackets  $\langle \rangle$  denote an operator that is symmetric, traceless, and orthogonal to the fluid velocity:

$$A_{\langle\mu} B_{\nu\rangle} = \left( \Delta_\mu^\alpha \Delta_\nu^\beta + \Delta_\nu^\alpha \Delta_\mu^\beta - \frac{2}{3} \Delta^{\alpha\beta} \Delta_{\mu\nu} \right) A_\alpha B_\beta. \quad (1.14)$$

- The symmetric and anti-symmetric operators:

$$A_{(\mu} B_{\nu)} = \frac{1}{2} (A_\mu B_\nu + A_\nu B_\mu), \quad (1.15)$$

$$A_{[\mu} B_{\nu]} = \frac{1}{2} (A_\mu B_\nu - A_\nu B_\mu). \quad (1.16)$$

- Phase space integral:

$$\int d\Gamma \equiv \int \frac{d^3\mathbf{p}}{(2\pi)^3 E_{\mathbf{p}}}. \quad (1.17)$$

## 1.6. Outline of this thesis

This thesis is organized as follows: in Chapter 2 we review the basic physics of anisotropic plasmas and discuss in detail the appearance of unstable modes and its relation with isotropization of the QGP. We also comment about recent numerical simulations of plasma instabilities in non-abelian gauge field theories. In Chapter 7 we present the formulation of hydrodynamics from kinetic theory; we emphasize the derivation of the 2nd-order viscous hydrodynamical equations and the recent advances for conformal plasmas. In Chapter 4 we present the theoretical methods necessary to calculate the differential dilepton rate. Moreover, we include a short review of dilepton production, its sources and experimental methods to measure it.

In Chapter 5 we investigate the impact of the early-time momentum-space anisotropies on dilepton production in the central and forward rapidity region. In the central region, we formulate two interpolating models from early-time 0+1 dimensional expansion (free streaming or collisionally-broadening) to late-time 0+1 ideal hydrodynamics. The models include the proper-time dependence of the parton hard momentum scale,  $p_{\text{hard}}$ , and the plasma anisotropy parameter,  $\xi$ . We conclude that in both cases, dilepton production is affected by pre-equilibrated emission. In the forward region, we generalize these models by including the rapidity dependence of  $p_{\text{hard}}$ . Our calculations allow us to conclude that dilepton production in the forward rapidity region is suppressed due to pre-equilibrium effects.

In Chapter 6 we extend our studies of the non-equilibrium phase of the QGP by constraining the initial conditions of viscous hydrodynamics. We present two requirements for the solutions of viscous hydrodynamical equations: (1) by imposing positivity of the effective longitudinal pressure of the solutions of viscous hydrodynamical equations and (2) by demanding that dissipative corrections coming from shear viscous effects are small compared with the hydrostatic pressure. We apply these requirements to the 0+1 dimensional 2nd-order conformal viscous hydrodynamical equations. We find that the initial conditions for the energy density, the initial shear viscous tensor and the initial time are non-trivially correlated. Additionally, we present a method that allows us to match pre-equilibrium dynamics of a 0+1 dimensional quark gluon plasma to 2nd-order viscous hydrodynamical evolution. Based on this interpolating model, we study the impact of the pre-equilibrated phase on the entropy generation and discuss the limitations of the usual definitions of entropy from kinetic theory. The conclusions of this work are presented in Chapter 7.



## 2. Physics of the anisotropic quark-gluon plasma

Thermalization of quark-gluon plasmas in heavy-ion collisions is a very difficult question. One theoretical approach to understand the physics of thermalization has been to explore two extreme cases, when the plasma is strongly coupled [57] or in a relatively simplifying limit of high-energy collisions, say when the running coupling constant is arbitrarily small [26]. For the strongly coupled case, the plasma has a short thermalization time  $\tau_{\text{therm.}} \sim 0.5 \text{ fm}/c$  [58]. In the opposite limit, it is not clear how to determine the thermalization time from weakly coupled plasma, the first estimates provided a significantly longer thermalization time with  $\tau_{\text{therm.}} \sim 2.7 \text{ fm}/c$  [26].

From pQCD, parton-parton collisions are responsible for the thermalization. The calculations performed within the ‘bottom-up’ thermalization scenario [26], where the binary and  $2 \leftrightarrow 3$  processes are taken into account, give an equilibration time of at least approximately  $2.7 \text{ fm}/c$  [27]. To thermalize the system one needs either a few hard collisions of momentum transfer of order of the characteristic hard parton momentum, which is denoted here as  $p_{\text{hard}}$  (which corresponds, in the case of a equilibrium situation, to the temperature  $T$  of a thermalized system), or many collisions of smaller transfer. For an equilibrated QGP at a given temperature  $T$ , the inverse equilibration time is of order  $g^4 \log(1/g) T$  (with  $g$  being the QCD coupling constant) when the binary collisions are responsible for the system’s thermalization [59, 60]. However, the equilibration is sped up by instabilities generated in an anisotropic quark-gluon plasma [21, 30, 31, 36, 2], as growth of the unstable modes is associated with the system’s isotropization. Up to now, the effect of plasma instabilities on  $\tau_{\text{therm}}$  has not been fully quantified.

In this chapter we review the physics of the anisotropic QGP. We start by reviewing the bottom-up scenario. Next, we discuss the effect of plasma instabilities in the thermalization of the QGP, focusing on the so-called chromo-Weibel instability which turns out to be the most relevant one at early times of the expansion of the fireball.

### 2.1. Review of bottom-up scenario

In the McLerran-Venugopalan model of the color glass condensate [61, 62, 63], small- $x$  gluons with transverse momentum below a certain saturation scale  $Q_s$  are at their maximum density. When applied to a nucleus-nucleus collision at impact parameter  $b$ , this scale is given by [64]

$$Q_s^2 = \frac{8\pi^2\alpha N_c}{N_c^2 - 1} \sqrt{R_A^2 - b^2} \rho x G_p(x, Q_s^2), \quad (2.1)$$

and its value is  $Q_s \sim 1 \text{ GeV}$  at the Relativistic Heavy Ion Collider (RHIC). Here  $R_A$  is the nuclear radius,  $\rho$  is the nuclear number density,  $N_c$  is the number of colors,  $\alpha$  is the coupling and  $G_p$  is the gluon distribution of a proton. In a nuclear collision these gluons have a typical momentum of  $Q_s$  and are freed at a time around  $1/Q_s$  after the initial impact.

The bottom-up scenario pointed out for first time how thermalization can be achieved from first principles. One of the most important aspects of this calculation was to show that inelastic processes are no less important than elastic processes for thermalization and that equilibration is driven by these hard gluons and goes through three distinct stages [26]. The stages of the bottom up are (a) the early times  $1 < Q_s\tau < \alpha^{-3/2}$ , (b) the intermediate times  $\alpha^{-3/2} < Q_s\tau < \alpha^{-5/2}$  and (c) the final

stage  $\alpha^{-5/2} < Q_s \tau < \alpha^{-13/5}$ . The description of every stage is presented below. In Fig. ?? we show a cartoon picture of how thermalization is achieved in the QGP according with bottom-up scenario.

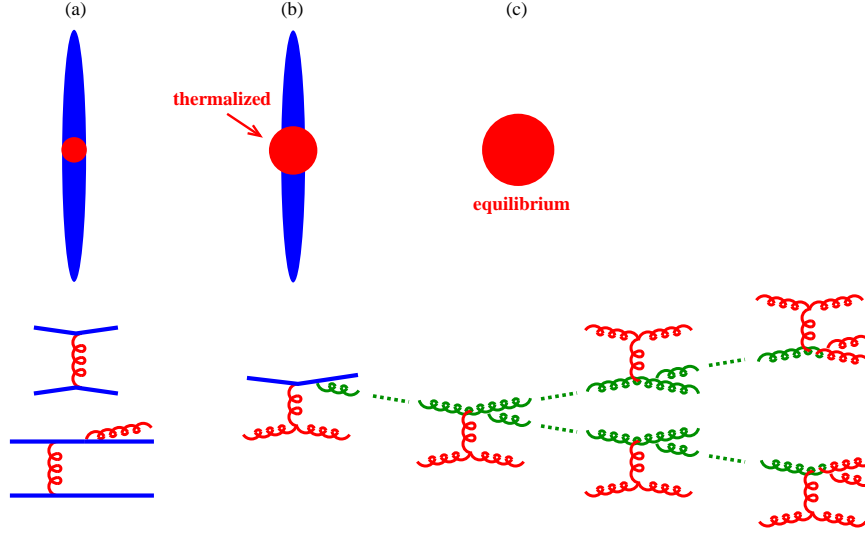


Figure 2.1.: Qualitative picture of the three stages of the bottom-up thermalization scenario. See the text for the description. Figure taken from Ref. [60].

### 2.1.1. a) $1 < Q_s \tau < \alpha^{-3/2}$

At early times hard gluons dominate and due to longitudinal expansion, the density decreases as

$$N_h \sim \frac{Q_s^3}{\alpha(Q_s \tau)}. \quad (2.2)$$

In the central collision region most of the gluons have small longitudinal momentum,  $p_z \ll p_T$ . Nevertheless, the longitudinal momentum cannot be zero because of the broadening due to multiple scattering. Indeed,  $p_z$  follows a random walk in momentum space due to the random kicks by other hard gluons so

$$p_z^2 \sim N_{\text{col}} m_D^2 \sim \frac{\alpha N_h}{p_z}, \quad (2.3)$$

where  $N_{\text{col}}$  is the number of collisions a hard gluon typically has encountered at the time  $\tau$  and  $m_D^2$  is the Debye mass square defined as

$$m_D^2 \sim \alpha \int d^3 p \frac{f_h(p)}{p} \sim \frac{\alpha N_h}{Q_s} \sim \frac{Q_s^2}{Q_s \tau}. \quad (2.4)$$

Effectively, the Debye mass acts as the minimum transfer of momentum for each kick due to frequent small angle collisions. Solving for  $p_z$  one obtains

$$p_z \sim (\alpha N_h)^{1/3} \sim \frac{Q_s}{(Q_s \tau)^{1/3}}. \quad (2.5)$$

Soft gluons with momentum  $k_s$  are produced during these times via the Bethe-Heitler radiation [65]. The parametric form for the density of the soft gluons  $N_s$  is estimated as

$$N_s \sim \tau \frac{\partial N_s}{\partial \tau} \sim \frac{Q_s^3}{\alpha(Q_s \tau)^{4/3}}. \quad (2.6)$$

Once produced, random scattering by other gluons increases the energy of the soft gluons so that their momenta would be around  $k_s \sim p_z$ . Therefore, the soft gluon distribution is

$$f_s \sim \frac{N_s}{k_s^3} \sim \frac{1}{\alpha(Q_s\tau)^{1/3}}. \quad (2.7)$$

### 2.1.2. b) $\alpha^{-3/2} < Q_s\tau < \alpha^{-5/2}$

In the intermediate times hard gluons still dominate the occupation number of particles but now  $f_h < 1$ . This changes the scattering rate with the hard gluons so that

$$k_s^2 \sim N_{\text{col}} m_D^2 \sim \alpha Q_s^2, \quad (2.8)$$

is now approximately constant. If one assumes that the screening is mainly due to the soft gluons, then

$$m_D^2 \sim \frac{\alpha N_s}{k_s} \gg \frac{\alpha N_h}{Q_s}, \quad (2.9)$$

and self-consistently, it is found that during this stage the the density of the soft gluons is

$$N_s \sim \frac{\alpha^{1/4} Q_s^3}{(Q_s\tau)^{1/2}}. \quad (2.10)$$

### 2.1.3. c) $\alpha^{-5/2} < Q_s\tau < \alpha^{-13/5}$

In the final stage, the system has diluted in such a way that most gluons are soft  $N_s \gg N_h$ . Soft gluons reach thermal equilibrium basically due to the collisions between themselves. The remaining hard gluons will scatter with the soft gluons and lose energy via successive gluon splitting. Whereas in the previous stages gluon production via the Bethe-Heitler radiation is unaffected by multiple scattering, this is no longer true as the branching gluon momenta fall within the range of the Landau-Pomeranchuk-Migdal suppression [66]. Specifically gluon emission with momentum larger than  $k_{\text{LPM}} = m_D^2/N_{\text{scatt}}\sigma$  is suppressed [67].  $N_{\text{scatt}}$  is the number density of the particles that is responsible for most of the scatterings. In this case the formation time of the branching gluon is  $t_f \sim k_{\text{br}}/k_t^2$  where  $k_t$  is the transverse momentum picked up by the branching gluon through the random kicks by the soft gluons. It can be estimated similarly as the momentum broadening during the first stage but the number of collisions is now restricted by the formation time  $t_f$  and the mean free path  $\lambda$ , so

$$k_t^2 \sim m_D^2 t_f/\lambda. \quad (2.11)$$

The rate of branching is roughly related to the formation time via  $1/t_{\text{br}} \sim \alpha/t_f$ . By identifying  $t_{\text{br}}$  with  $\tau$  and requiring that the soft gluon now be in a thermal bath  $N_s \sim T^3$ , one finds the branching momentum to be

$$k_{\text{br}} \sim \alpha^4 T^3 \tau^2. \quad (2.12)$$

The number of  $k_{\text{br}}$ -gluons produced per unit time per unit volume is

$$\frac{dN(k_{\text{br}})}{d\tau} \sim \frac{N_h}{t_{\text{br}}} \sim \frac{\alpha^2 N_s^{1/2} N_h}{k_{\text{br}}^{1/2}} \sim \frac{Q_s^2}{\alpha\tau^2}. \quad (2.13)$$

Subsequently, the rate of energy flow from the hard gluons to the soft thermal bath is

$$k_{\text{br}} \frac{dN(k_{\text{br}})}{d\tau} \sim \alpha^3 Q_s^2 T^3. \quad (2.14)$$

This energy flow increases the energy in the thermal bath, and thus must be proportional to  $d(T^4)/d\tau$ . Therefore one finds

$$T \sim \alpha^3 Q_s^2 \tau. \quad (2.15)$$

The linear growth of  $T$  terminates when the hard gluons lose all of their energy. This happens when  $k_{\text{br}} \sim Q_s$ , or  $\tau \sim \alpha^{-13/5} Q_s^{-1}$ , when the temperature achieves a maximal value of order  $\alpha^{2/5} Q_s$ , which is larger than the initial temperature only by a factor of  $\alpha^{-1/10}$ . Subsequently the temperature decreases as it is usually known in the Bjorken model, i.e.,  $T \sim \tau^{-1/3}$  [19].

The bottom-up scenario includes binary and  $2 \leftrightarrow 3$  collisions to achieve thermalization. Nevertheless, at the first stage of this scenario, one of the assumptions of the model is not correct. It is implicitly assumed that the behaviour of the soft gauge modes behaves the same in an anisotropic plasma as in an isotropic one which is not true since  $p_z \ll p_T$ . If one wants to be self consistent, one should determine the collective modes for an anisotropic system and use those. This collective behavior is overlooked by the bottom-up scenario and is related to the appearance of plasma instabilities in the analysis of the equilibration of the QGP [21, 30, 31, 36, 2].

## 2.2. Plasma instabilities in QCD

### 2.2.1. Physical origin of plasma instabilities

Consider two dense homogeneous streams of charged hard particles, one going up (say along  $+\hat{z}$ ) and other one going down ( $-\hat{z}$ ). Notice that this configuration establishes that the velocity distribution of the particles for the described system is anisotropic in momentum-space.

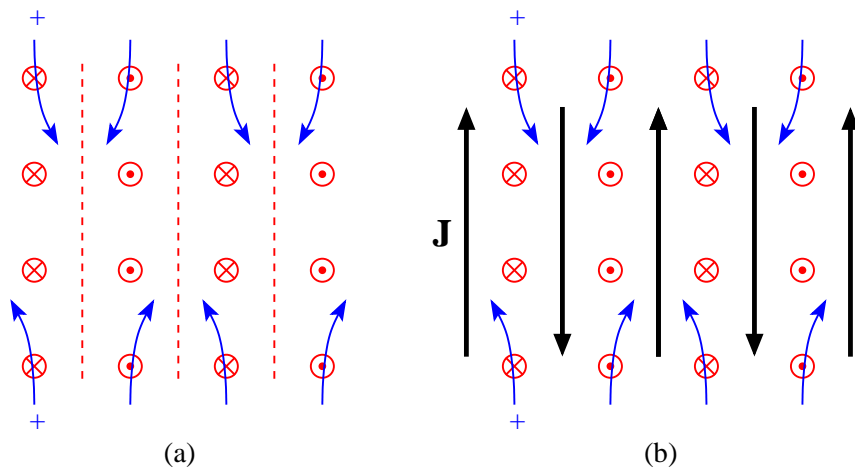


Figure 2.2.: Origin of Weibel instability. Here, crosses denote magnetic fields pointing into the page, and dots fields pointing out of the page. See description in the text. Figure is taken from Ref. [60].

Because every stream is a highly populated system of particles, there can be fluctuations in the distribution of the particle velocities which causes a very tiny seed magnetic field of the form  $\mathbf{B} = B \cos(kz) \hat{e}_y$ , as shown in Fig. 2.2a. Due to the Lorentz force, one concludes that the magnetic fields bend the trajectories of positively charged particles in the directions shown. This focuses the downward and upward currents like filaments, as shown in Fig. 2.2b. Due to the Biot-Savart law, one finds that the currents in turn create magnetic fields that add to the original seed field. With bigger fields, the effect becomes more pronounced, and the fields continue to grow through this mechanism. This is the Weibel instability. The instability is driven by the energy transferred from the particles to fields.

### 2.2.2. Collective modes of an anisotropic plasma

The theoretical framework to describe the physics of gauge theories at high temperatures is provided by the Hard Thermal Loop (HTL) effective theory. If a plasma of massless particles is in thermal equilibrium, the only scale that appears in the theory is the temperature  $T$ , corresponding to the mean energy of particles in the plasma. The Debye screening mass is determined in turn by the scale  $gT \ll T$ , where  $g$  is the self-interaction coupling for plasma particles. There are no propagating modes in plasma below the Debye scale. The term ‘hard thermal loops’ takes its origin from the fact that Debye screening is given by loop contributions with the highest power of loop momentum. The latter is cut off by the temperature  $T$ , i.e., these loops are hard thermal loops. If we want to determine what happens at scales softer than  $gT$  (and time scales longer than  $(gT)^{-1}$ ), we have to correspondingly resum propagators and vertices; this resummation gives rise to the HTL effective field theory [68, 69]. There are other important scales in the theory where not only naive perturbation theory, but also the resummed HTL effective QFT cease to work. One such scale is  $g^2T$ , where magnetostatic sector becomes involved, and another is  $g^4T$ , the scale related to inverse shear viscosity  $T^4/\eta$ . Nevertheless, HTL analysis may be sufficient if one considers dynamics of plasma near to equilibrium.

One can also implement HTL effective field theory to study anisotropic plasmas [38]. Nevertheless, it is simpler to do so by using semi-classical kinetic theory. Within this description partons are described by their phase-space densities and their time evolution is given by Vlasov-type transport equations [70]. This framework is equivalent to the HTL effective theory to leading order in the coupling constant  $g$  [71, 72].

Here we show the linearized analysis of the Vlasov-type transport theory for abelian theories. For non-abelian theories there is no fundamental difference within this approximation [36]. The Vlasov equation describes the space-time evolution of the hard particle distribution function  $f(x, p)$  and the Maxwell equations for the soft fields

$$p^\mu \partial_\mu f(x, p) + g p_\mu F^{\mu\nu} \partial_\nu^{(p)} f(x, p) = 0, \quad (2.16a)$$

$$\partial_\mu F^{\mu\nu}(x) = J^\nu(x) = \int \frac{d^3\mathbf{p}}{(2\pi)^3} v^\mu f(x, p), \quad (2.16b)$$

where  $F^{\mu\nu}(x) = \partial^\mu A^\nu(x) - \partial^\nu A^\mu(x)$  is the electromagnetic stress tensor and  $v^\mu = (1, \mathbf{v})$  the four-velocity of the hard particle. In the right hand side of Eqn. (2.16b), there is an implicit sum over the different particle species that compose the system. In the absence of external fields, the gauge field is small and the distribution function can be approximated to first order as  $f(x, p) = f_0(\mathbf{p}) + \delta f(x, \mathbf{p})$ ,  $\delta f$  is a fluctuation around the homogeneous distribution function  $f_0(\mathbf{p})$ . We consider the case where the homogeneous distribution function does not contribute to the current  $J^\mu$ , i.e.,  $f_0(\mathbf{p})$  does not carry net charge or current. By inserting this ansatz in Eqs. (2.16), we obtain

$$p^\mu \partial_\mu \delta f(x, p) = -g p_\mu F^{\mu\nu} \partial_\nu^{(p)} f_0(\mathbf{p}), \quad (2.17a)$$

$$\partial_\mu F^{\mu\nu}(x) = \int \frac{d^3\mathbf{p}}{(2\pi)^3} v^\mu \delta f(x, p). \quad (2.17b)$$

Next, we apply the Fourier transform to  $\delta f(x, p)$  and the stress tensor  $F^{\mu\nu}(x)$

$$\delta f(x, p) = \int \frac{d^4k}{(2\pi)^4} e^{ik \cdot x} \delta f(k, p), \quad (2.18a)$$

$$F^{\mu\nu}(x) = i \int d^4k e^{ik \cdot x} \tilde{F}_{\mu\nu}(k). \quad (2.18b)$$

By inserting the previous expressions into the linearized Vlasov-Maxwell equations (2.17), one solves

for  $\delta f(k, \mathbf{p})$  and finds the induced current caused by the soft fields

$$\begin{aligned} J_{ind}^\mu(k) &= g^2 \int \frac{d^3 \mathbf{p}}{(2\pi)^3} v^\mu \partial_\lambda^{(\mathbf{p})} f_{iso}(\mathbf{p}) \frac{v_\alpha \tilde{F}^{\alpha\lambda}(k)}{v \cdot k + i\epsilon}, \\ &= g^2 \int \frac{d^3 \mathbf{p}}{(2\pi)^3} v^\mu \partial_\lambda^{(\mathbf{p})} f_{iso}(\mathbf{p}) \left( g^{\lambda\nu} - \frac{v^\nu k^\lambda}{v \cdot k + i\epsilon} \right) A_\nu. \end{aligned} \quad (2.19)$$

where  $\epsilon$  is a small parameter that has to be sent to zero in the end. From this expression of the induced current, the self-energy is obtained via

$$\Pi^{\mu\nu}(k) = \frac{\delta J_{ind}^\mu(k)}{\delta A_\nu(k)}, \quad (2.20)$$

which gives us

$$\Pi^{\mu\nu}(k) = g^2 \int \frac{d^3 \mathbf{p}}{(2\pi)^3} v^\mu \partial_\lambda^{(\mathbf{p})} f_{iso}(\mathbf{p}) \left( g^{\lambda\nu} - \frac{v^\nu k^\lambda}{v \cdot k + i\epsilon} \right). \quad (2.21)$$

Plugging the self-energy into the Fourier transform of the Maxwell's equation

$$-ik_\mu F^{\mu\nu}(k) = J_{ind}^\nu(k), \quad (2.22)$$

we obtain

$$[k^2 g^{\mu\nu} - k^\mu k^\nu + \Pi^{\mu\nu}(k)] A_\nu(k) = -J_{ext}^\nu(k), \quad (2.23)$$

where  $J_{ext}^\nu$  is an external current. Because the self-energy is a gauge invariant, it is possible to rewrite in a more appropriate way in terms of a physical electric field by specifying a particular gauge. In the temporal axial gauge defined by  $A_0 = 0$  we obtain

$$[(k^2 - \omega^2)\delta^{ij} - k^i k^j + \Pi^{ij}(k)] E^j(k) = (\Delta^{-1}(k))^{ij} E^j(k) = i\omega J_{ext}^i(k). \quad (2.24)$$

By solving in the last expression for the propagator, this allows us to determine the response of the system to the external source

$$E^i(k) = i\omega \Delta^{ij}(k) J_{ext}^j(k). \quad (2.25)$$

The dispersion relations for the collective modes can be obtained by finding the poles in the propagator  $\Delta^{ij}(k)$ .

### Dispersion relations for an anisotropic plasma

In order to show the instability, we use the ansatz for the anisotropic distribution function which was used for first time by Romatschke and Strickland [2]. The anisotropic distribution function is obtained by stretching or squeezing an isotropic distribution along a certain direction in momentum-space defined by an unit vector  $\hat{\mathbf{n}}$

$$f(\mathbf{p}) = f_{iso}(\sqrt{p^2 + \xi(\mathbf{p} \cdot \hat{\mathbf{n}})^2}). \quad (2.26)$$

This particular class of distribution functions preserves the azimuthal symmetry in momentum-space. We show this procedure in Fig. 2.3.  $f_{iso}$  is not necessarily a distribution function that describes a system in thermal equilibrium. The strength of the anisotropy is measured by the parameter  $\xi$

$$\xi = \frac{\langle p_T^2 \rangle}{2\langle p_L^2 \rangle} - 1, \quad (2.27)$$

where  $\langle p_{T(L)} \rangle$  is the average transverse (longitudinal) momentum of the hard particles. When  $0 < \xi < \infty$  the distribution function has an oblate shape along  $\hat{\mathbf{n}}$  whereas for  $-1 < \xi \leq 0$  has

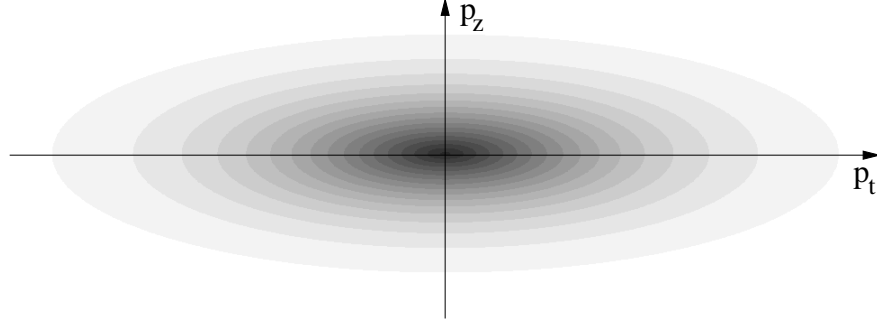


Figure 2.3.: Contour plot of a squeezed Fermi-Dirac distribution with anisotropy parameter  $\xi = 10$ . The anisotropy vector  $\hat{\mathbf{n}}$  is taken to be along the  $p_z$  direction. Figure taken from Ref. [73].

a prolate profile along  $\hat{\mathbf{n}}$ . In general, for an expanding system such as the QGP, the anisotropy parameter will have temporal dependence.

By inserting the ansatz of the anisotropic distribution Eq. (2.26) into Eqn. (2.21), one calculates the spatial components of the retarded self-energy for an anisotropic plasma which results in

$$\Pi^{ij}(k) = m_D^2 \int \frac{d\Omega}{4\pi} v^i \frac{v^l + \xi(\mathbf{v} \cdot \mathbf{n})n^l}{(1 + \xi(\mathbf{v} \cdot \mathbf{n})^2)^2} \left( \delta^{jl} + \frac{v^j k^l}{k \cdot v + i\epsilon} \right) \quad (2.28)$$

with

$$m_D^2 \equiv -\frac{g^2}{2\pi^2} \int_0^\infty dp p^2 \frac{df_{\text{iso}}(p^2)}{dp}. \quad (2.29)$$

The fact that in the presence of an anisotropic distribution function there is a preferred direction introduces an additional complication. In this case, the self-energy cannot be decomposed into only transverse and longitudinal components as is the case for an isotropic distribution function [74, 75]. Nevertheless, one can show that the usual isotropic dispersion relations can be obtained in the limit when  $\xi \rightarrow 0$  [2].

In the anisotropic case,  $\Pi^{\mu\nu}$  is symmetric and  $\Pi^{0\nu}$  is fixed by transversality  $k_\mu \Pi^{\mu\nu} = 0$  which would lead to six structure functions in general. In heavy ion collisions, the most important configuration is when the anisotropy is directed along the beam axis  $\hat{\mathbf{n}} = (0, 0, 1)$  and there is axial symmetry around the  $z$ -axis. Assuming this as the only direction of momentum space anisotropy, one can define four symmetric basis tensors for  $\Pi^{ij}$ , corresponding to 4 independent structure functions defined as [2]

$$A^{ij} = \delta^{ij} - k^i k^j / k^2, \quad B^{ij} = k^i k^j / k^2, \quad C^{ij} = \tilde{n}^i \tilde{n}^j / \tilde{n}^2, \quad D^{ij} = k^i \tilde{n}^j + k^j \tilde{n}^i, \quad (2.30)$$

with  $\tilde{n}^i = A^{ij} n^j$ . With these four linearly independent structure functions, the spatial components of the self-energy can be expressed as

$$\Pi^{ij} = \alpha A^{ij} + \beta B^{ij} + \gamma C^{ij} + \delta D^{ij}, \quad (2.31)$$

where the coefficients  $\alpha, \beta, \gamma$  and  $\delta$  are determined, for any value of  $\xi$ , by the contractions listed below

$$\begin{aligned} k^i \Pi^{ij} k^j &= k^2 \beta, \\ \tilde{n}^i \Pi^{ij} k^j &= \tilde{n}^2 k^2 \delta, \\ \tilde{n}^i \Pi^{ij} \tilde{n}^j &= \tilde{n}^2 (\alpha + \gamma), \\ \text{Tr } \Pi^{ij} &= 2\alpha + \beta + \gamma. \end{aligned} \quad (2.32)$$

Using this, one can find the gluon propagator in the temporal axial gauge [2]

$$\Delta(k) = \Delta_T \mathbf{A} + (\mathbf{k}^2 - \omega^2 + \alpha + \gamma) \Delta_{\mathcal{L}} \mathbf{B} + [(\beta - \omega^2) \Delta_{\mathcal{L}} - \Delta_T] \mathbf{C} - \delta \Delta_{\mathcal{L}} \mathbf{D}, \quad (2.33)$$

with

$$\Delta_T(k) = [\mathbf{k}^2 - \omega^2 + \alpha]^{-1} \quad (2.34a)$$

$$\Delta_{\mathcal{L}}(k) = [(\mathbf{k}^2 - \omega^2 + \alpha + \gamma)(\beta - \omega^2) - \mathbf{k}^2 \tilde{n}^2 \delta^2]^{-1}. \quad (2.34b)$$

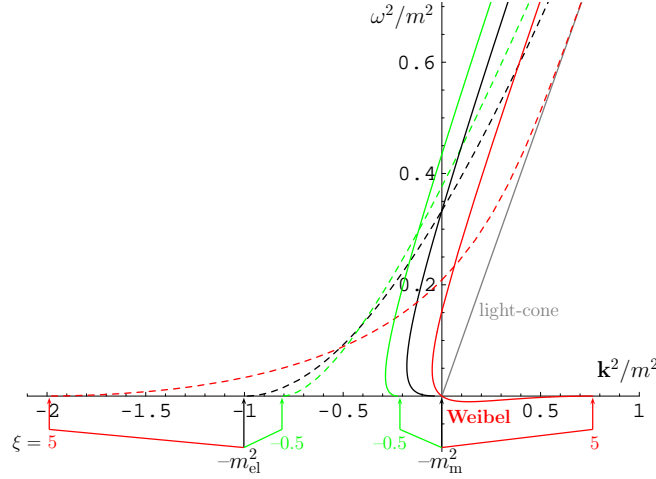


Figure 2.4.: Anisotropic dispersion relations for  $\mathbf{k} \parallel \hat{\mathbf{n}}$  for a distribution function which in momentum space is: isotropic ( $\xi=0$ ), prolate ( $\xi=-0.5$ ) and oblate ( $\xi=5$ ). Full and dashed lines represent poles of  $\Delta_T$  and  $\Delta_{\mathcal{L}}$ , respectively. The magnetic Weibel instability corresponds to the poles for negative  $\omega^2$  and positive  $\mathbf{k}^2$  that appear for positive  $\xi$ . Figure taken from Ref. [76].

Let's consider the structure function  $\alpha(k)$  for the case that  $\mathbf{k} \parallel \hat{\mathbf{n}}$  and in the static limit where  $\alpha(\omega = 0) = \Pi^{ii}(\omega = 0)/2 = m_m^2$  which has the interpretation of the square of the magnetostatic screening mass. For finite values of  $\xi$  one can find

$$\left. \frac{m_m^2}{m_D^2} \right|_{\mathbf{k} \parallel \hat{\mathbf{n}}} = \begin{cases} \frac{1}{4} [(1 - \xi)(-\xi)^{-1/2} \operatorname{atanh}(-\xi)^{1/2} - 1] & \text{for } \xi < 0 \\ \frac{1}{4} [(1 - \xi)\xi^{-1/2} \arctan \xi^{1/2} - 1] & \text{for } \xi > 0 \end{cases} \quad (2.35)$$

In the limit when  $\xi = 0$ , the magnetostatic screening mass vanishes exactly as it is known in the isotropic case. Nevertheless, once the system develops an anisotropy measured by  $\xi$ , the isotropic result is no longer valid as one can see from Eqn. (2.35). In particular, when  $\xi \in (-1, 0)$ , the magnetostatic mass takes a non-vanishing value whereas for  $\xi \in (0, \infty)$ , the magnetostatic mass turns out to be imaginary which signals the presence of the chromomagnetic Weibel instability [2]. Notice that this is valid for the case when  $\mathbf{k} \parallel \mathbf{n}$ . However, one can show that for a prolate distribution function [ $\xi \in (0, \infty)$ ] when the wave vectors are perpendicular to the  $z$  axis, the magnetostatic mass also has an imaginary value. The corresponding instability for this case is known as the electric (Buneman) instability [36].

Returning to the case of an oblate distribution function [ $\xi \in (0, \infty)$ ] and restricting to the configuration  $\mathbf{p} \parallel \mathbf{n}$ , we consider the dependence of the frequency on the momentum in order to determine



the dispersion relations. By defining the parameter  $\eta = \omega/|\mathbf{k}|$  one finds [37]

$$\alpha(\eta) = \frac{m_D^2}{4\sqrt{\xi}(1+\xi\eta^2)^2} \left[ (1+\eta^2 + \xi(-1 + (6+\xi)\eta^2 - (1-\xi)\eta^4)) \arctan \sqrt{\xi} \right. \\ \left. + \sqrt{\xi}(\eta^2 - 1) \left( 1 + \xi\eta^2 - (1+\xi)\eta \ln \left[ \frac{\eta+1+i\epsilon}{\eta-1+i\epsilon} \right] \right) \right], \quad (2.36a)$$

$$\beta(\eta) = -\frac{\eta^2 m_D^2}{2\sqrt{\xi}(1+\xi\eta^2)^2} \left[ (1+\xi)(1-\xi\eta^2) \arctan \sqrt{\xi} \right. \\ \left. + \sqrt{\xi} \left( (1+\xi\eta^2) - (1+\xi)\eta \ln \frac{\eta+1+i\epsilon}{\eta-1+i\epsilon} \right) \right]. \quad (2.36b)$$

The resulting poles for the propagators  $\Delta_T$  and  $\Delta_L$  defined by Eqs. (2.34) are shown in Fig. 2.4 for the different values of  $\xi = \{0, -0.5, 5\}$ .

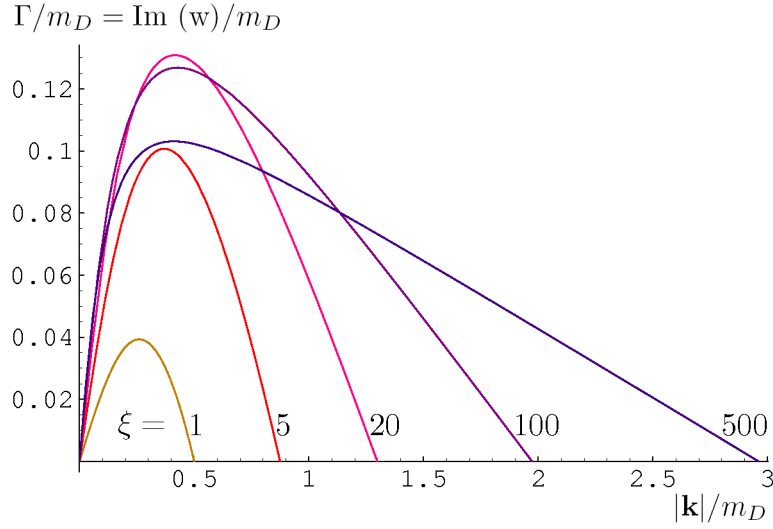


Figure 2.5.: Growth rate  $\Gamma$  of the unstable modes for a Weibel instability as function of the wave vector for different values of anisotropy parameter  $\xi$  and for the configuration  $\mathbf{k} \parallel \hat{\mathbf{n}}$ . Figure taken from Ref. [76].

The imaginary value of the frequency gives the momentum-dependent growth rate of the unstable magnetic modes. The resulting growth rates are shown in Fig. 2.5. From the plot, one can also see that the growth rate  $\Gamma$  and the maximal value of the instability wavenumber  $\mathbf{k}$  for the unstable modes changes as one increases the anisotropy parameter.

### Instabilities in the presence of collisions

In the above treatment of anisotropic plasmas, we considered the case where there were no collisions. As was pointed out in the bottom-up scenario [26], collisions are needed to drive the system towards thermal equilibrium. The equilibration due to instabilities only happens indirectly, shaping the parton momenta distribution. One would expect that the inclusion of collisions will decrease the instability growth rate. Schenke et. al [43] made the first quantitative calculation to estimate more precisely how the collisions affect the dispersion relations and the growth of instabilities. Here we follow their argument and present their main results. The details of such calculations can be found in Ref. [43].

The analysis of collisions is based on the Vlasov equations for QCD combined with a Bhatnagar-Gross-Krook (BGK)-type collision term [43]

$$p^\mu \partial_\mu f(x, p) + g p_\mu F^{\mu\nu} \partial_\nu^{(p)} f(x, p) = \mathcal{C}(p, X), \quad (2.37)$$

with

$$\mathcal{C}(p, X) = -\nu \left[ f(p, X) - \frac{N(X)}{N_{\text{eq}}} f_{\text{eq}}(|\mathbf{p}|) \right], \quad (2.38)$$

where  $f(p, X) = f(\mathbf{p}) + \delta f(p, X)$ . This term describes how collisions equilibrate the system within a time proportional to  $\nu^{-1}$ , so one interprets  $\nu$  as the collisional frequency. Note that these collisions are not color-rotating. The particle numbers are given by

$$N(X) = \int_{\mathbf{p}} f(p, X), \quad N_{\text{eq}} = \int_{\mathbf{p}} f_{\text{eq}}(|\mathbf{p}|) = \int_{\mathbf{p}} f(\mathbf{p}). \quad (2.39)$$

By studying the poles of the gluon propagator and using as an ansatz for the anisotropic distribution function of the hard particles Eq. (2.26), one can analyze the dispersion relations in a similar manner as we presented in Sect. 2.2.2. As a result, the structure functions which determine the poles of the gluon propagator will not only be a function of the anisotropy parameter  $\xi$  but will also depend on the collisional frequency  $\nu$  [43].

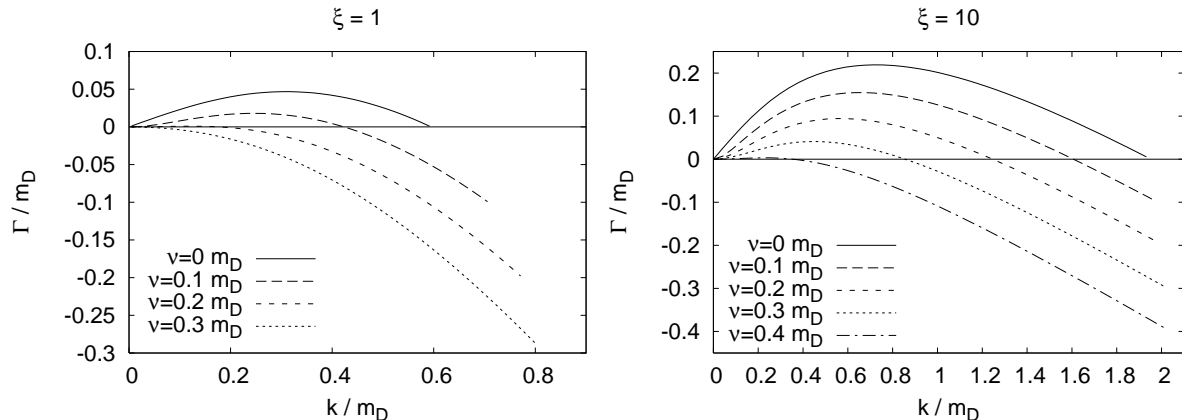


Figure 2.6.: Dependence of the growth rate  $\Gamma$  of the unstable transverse mode on the collision rate  $\nu$ , for an anisotropy parameter  $\xi = 1$  (left panel) and  $\xi = 10$  (right panel). Figures taken from Ref. [43].

In Fig. 2.6, we show the momentum dependent growth rate  $\Gamma$  of the unstable magnetic modes ( $\mathbf{p} \parallel \mathbf{n}$ ) for an anisotropy parameter  $\xi = 1$  (left panel) and  $\xi = 10$  (right panel) and different values of the collision rate  $\nu$ . This plot confirms the physical expectations, the growth rate decreases with an increasing collision rate as does the maximal wave number for an unstable mode.

Notice that within this approach  $\nu$  is a small parameter so implicitly it is assumed that perturbation theory is valid. Nevertheless, this procedure is highly nontrivial due to the fact that in non-abelian theories there are at least two collisional frequencies [77]: (a) the frequency for the hard-hard scatterings which is parametrically estimated as  $\nu_{\text{hard}} \sim \alpha_s^2 \log \alpha_s^{-1}$  and (b) the frequency for hard-soft scatterings which is parametrically estimated as  $\nu_{\text{soft}} \sim \alpha_s \log \alpha_s^{-1}$ .

The hard-hard scatterings correspond to interactions which change the momentum of a hard particle by  $\mathcal{O}(p_{\text{hard}})$  whereas the hard-soft scatterings correspond to changes in momentum which are order  $\mathcal{O}(g p_{\text{hard}})$ . These small angle scatterings occur frequently and it turns out that after traversing one hard scattering mean free path,  $\lambda_{\text{hard}} \sim \nu_{\text{hard}}^{-1}$ , the typical deflection of the particle is also  $\mathcal{O}(1)$ . The physics of small-angle scattering by the soft-background is precisely what is captured

by the HTL treatment. However, the form of the BGK scattering kernel (2.38) does not mix color channels and in that sense cannot be used to describe the physics of color-rotation of the hard particles. For this reason one is lead to the conclusion that when using the BGK kernel (2.38) the appropriate damping rate is  $\nu \sim \nu_{\text{hard}} \sim \alpha_s^2 \log \alpha_s^{-1}$ .

Recent real-time numerical simulations which solve the Wong-Yang-Mills equations by including binary collisions [73, 78, 79] have shown that the instability growth is reduced when collisions are present, but small enough for the instabilities to still play an important role in isotropization and equilibration of the QGP.

### 2.3. Impact of plasma instabilities on the thermalization process of the QGP

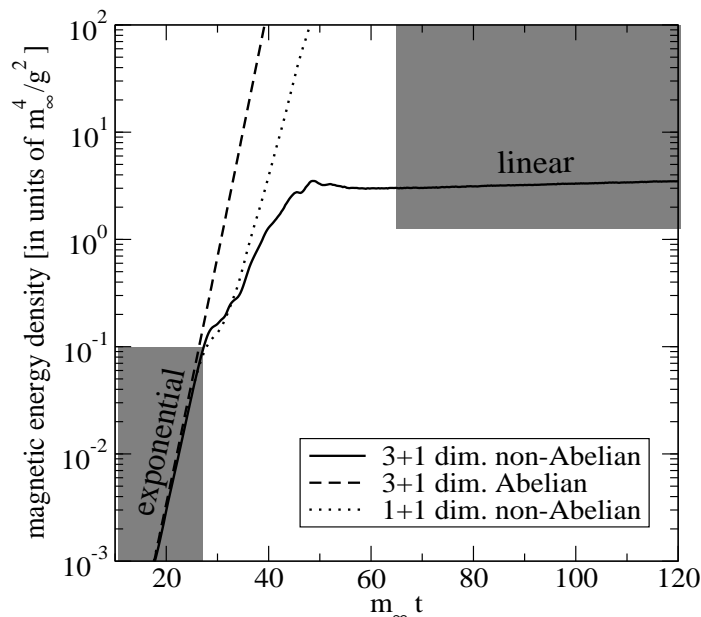


Figure 2.7.: Time-evolution of the chromo-magnetic energy density in the 1+3 dimensional simulation. The abelian result and that of 1+1 dimensions are also shown. Figure taken from Ref. [40].

In the last section we have shown that the unstable modes of an anisotropic plasma play an important role during the first stage of the bottom-up scenario. To extract information about the degree of anisotropy of the plasma as well as the development of instabilities is a non-trivial issue. Some phenomenological proposals to extract information about these aspects have been already published in the scientific literature [35, 73, 80, 81, 82, 83, 84, 85, 86, 79, 78, 87]. One of the most difficult problems associated with plasma instabilities in anisotropic plasma is to quantify precisely their effect on the momentum broadening of a hard particle as the QGP expands. Up to now, there is no complete answer to this question. Here we present the general arguments based on the different attempts to solve this problem [88, 89, 90]. The main results presented here will be used when we discuss the effect of plasma instabilities on dilepton production in Chapter 5.

In the treatment of the Vlasov-Maxwell equations in the last section, we assumed that the gauge fields were small. Nevertheless, the perturbative treatment of plasma instabilities breaks down in

the presence of instabilities.<sup>1</sup> Perturbation theory can be used to study the growth of instabilities from small seed fields. In Fig. 2.6 we show the time-evolution of the chromo-magnetic energy density from a 1+3 dimensional simulation. From this plot one sees clearly that during certain stage, the chromomagnetic fields increases exponentially and afterwards the growth stops and behaves almost linear. Similar results have been found by different groups using different numerical simulation methods [39, 40, 41, 42, 46, 47, 48, 49, 50, 51, 89, 90, 93, 94, 95, 96].

We define the density of the particles as

$$n = \int \frac{d^3p}{(2\pi)^3} f_0(\mathbf{p}), \quad (2.40)$$

where  $f_0(\mathbf{p})$  is the phase-space distribution of the particles in the plasma. We also need to define a scale that becomes important when the soft gauge fields amplitudes are large [77]

$$m_\infty^2 \sim g^2 \int \frac{d^3p}{(2\pi)^3} \frac{f_0(\mathbf{p})}{p}. \quad (2.41)$$

If  $p_{\text{hard}}$  is the momentum scale of the particle, then  $m_\infty \sim g p_{\text{hard}}$ .

The amount of anisotropy becomes a problem when  $\xi \gg 0$ . This will be the situation of the first stage of the bottom up scenario since  $p_z \ll p_T \sim Q_s$ . We define the parameter  $\theta$  as the ratio between the average longitudinal momentum of the hard particles and the hard momentum scale

$$\theta \equiv \frac{|p_z|}{p_{\text{hard}}} \approx |v_z|. \quad (2.42)$$

By analyzing how  $\theta$  scales parametrically with the chromomagnetic field associated with the unstable modes, it is possible to understand the impact of plasma instabilities on the broadening of the hard particles as the QGP expands.

The perturbative analysis of the instability has shown that the typical unstable modes have wave numbers  $\mathbf{k}$  and growth rates  $\gamma$  are of order [36]

$$(k_\perp, k_z) \sim (m_\infty, k_{\text{max}}), \quad \text{and} \quad \gamma \sim m_\infty. \quad (2.43)$$

where  $k_{\text{max}}$  is the maximum value of  $k$  for unstable modes. It is a non-trivial issue to determine its functional behavior analytically. This topic has been studied by different authors without complete solution [88, 89, 90]. Nevertheless, these studies have shown that  $k_{\text{max}}$  depends on  $m_\infty$  and  $\theta$  as

$$k_{\text{max}} \sim \frac{m_\infty}{\theta^\nu}, \quad (2.44)$$

where  $\nu$  is some number to be determined. In the approach of Bödeker [88] and Arnold & Moore [89, 90], different values for the exponent  $\nu$  have been found as listed below

$$\nu = \begin{cases} 0, & \text{Ref. [88];} \\ 1, & \text{Ref. [89];} \\ 2, & \text{Nielsen-Olesen limit [90].} \end{cases} \quad (2.45)$$

Soft covariant derivatives  $D_z = \partial_z - igA_z$  and  $D_\perp = \partial_\perp - igA_\perp$  will become non-perturbative when

$$A_z \sim \frac{k_z}{g} \sim \frac{k_{\text{max}}}{g} \quad \text{and} \quad A_\perp \sim \frac{k_\perp}{g} \sim \frac{m_\infty}{g}, \quad (2.46)$$

which allow us to determine the corresponding transverse and magnetic fields

$$B_\perp \sim (k_\perp A_z \text{ or } k_z A_\perp) \sim \frac{k_{\text{max}} m_\infty}{g} \quad \text{and} \quad B_z \sim k_\perp A_\perp \sim \frac{m_\infty^2}{g}. \quad (2.47)$$

---

<sup>1</sup>There has been some recent advances to extend the perturbative approach in the presence of instabilities [91, 92].

From the last expression, one sees that the transverse magnetic field receives a larger contribution due to unstable modes since  $k_{\max} > m_\infty$  as  $\xi \rightarrow \infty$  and its maximum value is given by

$$B_{\max} \sim \frac{k_{\max} m_\infty}{g} \sim \frac{m_\infty^2}{\theta^\nu g}. \quad (2.48)$$

By determining the maximum value of the magnetic field caused by the unstable modes, we are able to estimate the impact on the broadening of the hard particles as the QGP expands. When a particle crosses the spatial region where there is a chromomagnetic field associated with the unstable modes, there will be a change in the direction of the longitudinal momentum due to the Lorentz force. The particle will feel the bending due to the magnetic field during a time  $\delta t \sim 1/m_\infty$  which is the typical size of the magnetic domains. The change of the momentum at that time along the  $z$  direction is estimated as

$$\delta p_z \sim F_z t \sim g B_{\max} l_\perp \sim g B_{\max} / m_\infty, \quad (2.49)$$

where  $l_\perp$  is the coherence length.<sup>2</sup>

After a finite amount of time  $\tau$ , the particles will follow a random walk through  $N \sim \tau/l_\perp$  such changes, giving a total change of order

$$\Delta p_z \sim N^{1/2} \delta p_z \sim (m_\infty \tau)^{1/2} \frac{g B_{\max}}{m_\infty} \sim \frac{(m_\infty^3 \tau)^{1/2}}{\theta^\nu}. \quad (2.50)$$

This will broaden the particle distribution to

$$\theta \sim \frac{\Delta p_z}{p_{\text{hard}}} \sim \frac{(m_\infty^3 \tau)^{1/2}}{\theta^\nu Q_s}. \quad (2.51)$$

Solving self-consistently for  $\theta$ ,

$$\theta \sim \left( \frac{(m_\infty^3 \tau)^{1/2}}{Q_s} \right)^{1/(1+\nu)}. \quad (2.52)$$

Now we just need to know how  $m_\infty$  depends on time. This was determined for the first stage of bottom-up thermalization by very simple arguments in the original work of Baier et al. [26]. Their result does not change in the presence of plasma instabilities. Comparing (2.40) and (2.41), one sees that  $m_\infty^2 \sim g^2 n/p \sim g^2 n/Q_s$ . Initially, at saturation,  $n \sim Q_s^3/g^2$ . In the first stage of bottom-up, there is no significant change in the number of hard particles, and so hard particle number density  $n$  dilutes from this initial value by the scale factor  $Q_s \tau$  of one-dimensional expansion, so that  $n \sim Q_s^3/g^2(Q_s \tau)$ . Putting everything together,

$$m_\infty \sim \tau^{-1/2} Q_s^{1/2}. \quad (2.53)$$

Inserting this into (2.52), we get

$$\theta = (Q_s \tau)^{1/(1+\nu)}. \quad (2.54)$$

From this result one can determine the effect of broadening due to unstable modes.

<sup>2</sup> The coherence length of the unstable magnetic fields will be of order their wavelength, so

$$l_\perp \sim \frac{1}{k_\perp} \sim \frac{1}{m_\infty} \quad \text{and} \quad l_z \sim \frac{1}{k_z} \sim \frac{\theta^\nu}{m_\infty}$$



### 3. Hydrodynamics and Ultrarelativistic Heavy Ion Collisions

Mirar el río hecho de tiempo y agua  
y recordar que el tiempo es otro río,  
saber que nos perdemos como el río  
y que los rostros pasan como el agua.

---

*Arte Poética*  
Jorge Luis Borges.

The original description of the expansion of the strongly interacting matter created during high-energy nuclear collisions based on hydrodynamics was formulated years ago by Landau [97]. Models based on fluid hydrodynamics have been applied to describe colliding systems over a broad range of beam energies. For the description of nuclear matter by fluid hydrodynamics to be valid, it is necessary that the microscopic interaction time scale be much shorter than the macroscopic evolution time scale. However, the hot and dense matter created in these experiments expands very rapidly, causing the range of validity of hydrodynamics to be limited. The recent experimental results from the Relativistic Heavy Ion Collider (RHIC) [98, 99, 100, 101] show, for the first time, that collective expansion of nuclear matter is in good quantitative agreement with hydrodynamical predictions, at least for the largest collision systems (e.g. Au+Au) at the highest collision energies ( $\sqrt{s}=200$  GeV per nucleon pair) near midrapidity and at small to moderate impact parameters. Because of this, important improvements to hydrodynamics of ultrarelativistic nucleus-nucleus collisions have been discovered during the last decade. Nevertheless, many aspects have not been totally clarified, making relativistic fluid hydrodynamics one of the most relevant research areas nowadays.

In this chapter we will make a review of the most important technical details in the derivation of 2nd. order relativistic fluid hydrodynamics based on kinetic theory [102]. We review the basics of ideal hydrodynamics, Israel-Stewart (IS) theory and we briefly describe the recent approach of 2nd order conformal viscous hydrodynamics based on AdS/CFT methods [103, 104]. The equations derived from this formalism will be explicitly used in Chapter 6. Extensions of hydrodynamics to non-conformal regimes [105, 106] is also briefly discussed. More details of theoretical and phenomenological aspects of relativistic fluid hydrodynamics and applications to ultrarelativistic heavy-ion collisions can be found in Refs. [102, 107, 108, 109, 110, 20].

#### 3.1. Relativistic hydrodynamics

Fluid dynamics equations are derived from the basic requirements of energy and momentum conservation and any conserved charges. Mathematically, the last statement is established by two equations

$$\partial_\mu T^{\mu\nu} = 0, \tag{3.1a}$$

$$\partial_\mu N_i^\mu = 0, \quad i = 1, 2, \dots, k \tag{3.1b}$$

where  $T^{\mu\nu}$  is the energy-momentum tensor and  $N_i^\mu$  is the  $i$ -th conserved net charge current. Any physical theory described by hydrodynamics should satisfy the second law of thermodynamics and

one should ensure that this condition is satisfied

$$\partial_\mu \mathcal{S}^\mu \geq 0, \quad (3.2)$$

where  $\mathcal{S}^\mu$  is the entropy current. In the absence of shock discontinuities, the equations of motion of ideal hydrodynamics exactly preserve the entropy, i.e.,  $\partial_\mu \mathcal{S}^\mu = 0$  [108]. In the presence of dissipative corrections, the four-divergence of the entropy current should be semi-positive.

In addition to the hydrodynamical equations of motion (3.1) that describe the dynamics of the expansion of the system, it is necessary to know the equation of state that relates the pressure to other independent thermodynamic variables, i.e.,  $\mathcal{P} = \mathcal{P}(\mathcal{E}, n)$ . For the case of ultrarelativistic heavy ion collisions, the equation of state can be inferred from lattice QCD (See Refs. [111, 112] and references therein). The information about the nature of the particles contained in the fluid and the interaction between them is contained in the equation of state. In general, the equation of state is chosen to be the *thermodynamic* one, i.e. as computed for a system in thermodynamical equilibrium. Therefore, by closing the equations of motion of hydrodynamics, Eqs. (3.1), it is implicitly assumed that the fluid is at least, in local thermal equilibrium. Additional knowledge of the microscopical dynamics related with deconfinement or hadronization processes is not necessary at all until the moment of the freeze-out. If the equation of state and appropriate initial conditions are known, it is possible to have a good description of the evolution of the fireball created after the collisions.

### 3.1.1. Tensor decomposition

For simplicity and without losing generality, hereafter, we will consider just one particle species, i.e.,  $k = 1$ . Moreover, we will neglect the effect of the bulk viscosity, so that when we refer to dissipative corrections, these arise due just to the presence of the shear stress (see below). Fluid hydrodynamical equations follow from the above conservation laws. To proceed, we perform a tensor decomposition of  $T^{\mu\nu}$  and  $N^\mu$  as it follows

$$T^{\mu\nu} = \mathcal{E} u^\mu u^\nu - \mathcal{P} \Delta^{\mu\nu} + q^\mu u^\nu + q^\nu u^\mu + \Pi^{\mu\nu}, \quad (3.3a)$$

$$N^\mu = n u^\mu + \nu^\mu. \quad (3.3b)$$

Before explaining the physical meaning of some of the quantities indicated on the right hand side (RHS) of the last equations, it is necessary to define an arbitrary normalized time-like 4-vector  $u^\mu$ ,  $u^\mu u_\mu = 1$ . The projector orthogonal to this vector, denoted by  $\Delta^{\mu\nu}$  is defined as  $\Delta^{\mu\nu} = g^{\mu\nu} - u^\mu u^\nu$ . Next, we define the local rest frame (LRF) as the coordinate system where the 4-vector  $u^\mu$  has vanishing spatial components, i.e.  $u_{\text{LRF}}^\mu = (1, 0, 0, 0)$ . In this rest frame the projector  $\Delta_{\text{LRF}}^{\mu\nu} = (0, -1, -1, -1)$ . From these definitions, it is straightforward to conclude that any Lorentz vector/tensor projected over  $u^\mu$  ( $\Delta^{\mu\nu}$ ) will pick-up the time-(space-)like components.

With these definitions, the physical meaning of the new quantities that appears in the RHS of the Eqs. (3.3) becomes clear. In the LRF, the decomposition of the energy-momentum tensor and the conserved net charge current is

$$n = u_\mu N^\mu \quad (\text{net density of particles}), \quad (3.4a)$$

$$\nu^\mu = \Delta_\nu^\mu N^\nu \quad (\text{net flow of charge}), \quad (3.4b)$$

$$\mathcal{E} = u_\mu T^{\mu\nu} u_\nu \quad (\text{energy density}), \quad (3.4c)$$

$$\mathcal{P} = -\frac{1}{3} \Delta_{\mu\nu} T^{\mu\nu} \quad (\text{hydrostatic pressure}), \quad (3.4d)$$

$$q^\mu = \Delta^{\mu\alpha} T_{\alpha\beta} u^\beta \quad (\text{heat flow}), \quad (3.4e)$$

$$\Pi^{\mu\nu} = \left( \Delta_\alpha^\mu \Delta_\beta^\nu + \Delta_\alpha^\nu \Delta_\beta^\mu - \frac{2}{3} \Delta_{\alpha\beta} \Delta^{\mu\nu} \right) T^{\alpha\beta} = T^{\langle\mu\nu\rangle} \quad (\text{shear stress tensor}). \quad (3.4f)$$



### 3.1.2. Choosing the reference frame

Up to now in our discussion the 4-vector  $u^\mu$  has no physical meaning and it is completely arbitrary. We identify it as the 4-velocity of the fluid in a particular reference frame. In the scientific literature, two standard frames for  $u^\mu$  are used: the Landau reference frame or the Eckart reference frame. In what follows we discuss these definitions. Other definitions for the velocity of flow  $u^\mu$  can also be considered [102].

#### Landau reference frame

In this reference frame, the flow velocity  $u^\mu$  is defined as

$$u_L^\mu = \frac{T^\mu{}_\nu u^\nu}{\sqrt{u_L^\alpha T^\beta{}_\alpha T_{\beta\delta} u_L^\delta}}. \quad (3.5)$$

Notice that this definition is itself an equation with respect  $u_L^\mu$ . One may solve the eigenvalue problem for a given energy-momentum tensor  $T^{\mu\nu}$ . In the LRF, the corresponding positive eigenvalue is precisely the energy density  $\mathcal{E}$ . Therefore,  $u_L^\mu$  is the physical 4-velocity of the energy flow. In this frame,  $q^\mu = 0$ .

#### Eckart reference frame

In this reference frame, the flow velocity is given by the following

$$u_E^\mu = \frac{N^\mu}{\sqrt{N_\mu N^\mu}}. \quad (3.6)$$

This choice means that  $u_E^\mu$  is the physical 4-velocity of the net charge. From this definition it follows that in the Eckart reference frame,  $\nu^\mu = 0$ . In the LRF,  $N^\mu = nu^\mu \equiv (N_{(0)}, \mathbf{0})$ . For a system with vanishing net baryon number, as is approximately the case at RHIC and LHC energies, the Eckart frame is ill-defined [108, 113] and Landau frame is more suitable for this physical situation. We shall use this reference frame in the main body of the text.

For more general systems that include conserved charges, the freedom of choosing a particular definition of  $u^\mu$  reflects the freedom of defining the LRF as the frame where either the energy density (Landau) or the charge density (Eckart) is at rest. The physics must be independent of the chosen frame. It is possible to show that charge diffusion in one frame is related to heat flow in the other one, see the Appendix of Ref. [114]. The procedure for choosing the reference frame is similar to the case of the gauge fixing condition of gauge theories to eliminate unphysical/redundant degrees of freedom. As in gauge theories, one chooses the most convenient ‘gauge’ for practical calculations.

## 3.2. Fluid dynamics from kinetic theory

Kinetic theory deals with the description of the macroscopic observables of certain system based on microscopical interactions between its components. To do this, the system will be described in terms of phase-space of the canonical variables of the system  $(x, p)$ ; sometimes one can identify the canonical variables of the system as the position and momentum of the particle, however, it is not the general case [115]. In principal, one can think that if one knows the Hamiltonian  $\mathcal{H}$  that describes the dynamics of  $n$  particles, it is possible to know completely the macroscopical properties of the system by solving the  $2n$  Hamilton equations. However, this task becomes complicated as the number of particles increases. Rather, it is better to consider a phase-space distribution function  $f(x, \mathbf{p})$  defined over the phase space of the canonical variables  $(X, P)$ . One defines

$$f(x, \mathbf{p}) d^3\mathbf{x} d^3\mathbf{p}, \quad (3.7)$$

as the number of particles which at time  $t$ , have positions lying within a volume  $d^3\mathbf{x}$  around  $\mathbf{x}$  and momenta lying within a momentum-space volume  $d^3\mathbf{p}$  around  $\mathbf{p}$  [116, 117]. Of course, it is implicitly assumed that the volume elements  $d^3\mathbf{x}$  and  $d^3\mathbf{p}$  are finite volume elements which are large enough to contain a very larger number of particles and yet small enough compared with the macroscopical scales of the system so they look essentially as simple points.

The temporal evolution of  $f^a(x, p)$  is dictated by the integro-differential Boltzmann equation which in its covariant form is written as [116, 117, 102]<sup>1</sup>

$$\begin{aligned} p^\mu \partial_\mu f^a(x, \mathbf{p}) &= -\mathcal{C}[f(x, \mathbf{p})], \\ &= -\sum_{a_i, b_j} \frac{1}{n_i! n_j!} \int d\Gamma_i d\Gamma_j (2\pi)^4 \delta^4 \left( P - \sum K_i + \sum K'_j \right) \\ &\quad |\mathcal{M}|_{a_i, b_j}^2(\mathbf{p}, \mathbf{k}_i, \mathbf{k}'_j) \times \left( f^a(\mathbf{p}) \prod_{i,j} f^{a_i}(\mathbf{k}_i) [1 \pm f^{b_j}(\mathbf{k}'_j)] \right. \\ &\quad \left. - [1 \pm f^a(\mathbf{p})] \prod_{i,j} [1 \pm f^{a_i}(\mathbf{k}_i)] f^{b_j}(\mathbf{k}'_j) \right), \end{aligned} \quad (3.8)$$

where  $\mathcal{C}[f(x, \mathbf{p})]$  is the collisional kernel which is a functional of  $f(x, \mathbf{p})$ . The LHS of 3.8 describes the free propagation of particles; the time rate of change of the occupancy  $E\partial_t f$  is determined by the particles' momentum  $p^i$  times the spatial variation of the distribution function  $\partial_i f(x, \mathbf{p})$ . The RHS describes the change in occupancy due to collisions, which are approximated as spacetime-local (so all  $f$ 's on the RHS are evaluated at the point  $x$ ). The first product of distribution functions represents the rate at which particles of momentum  $\mathbf{p}$  are scattered out of that momentum state;  $[1 \pm f(\mathbf{k}')]_+$  is a Bose stimulation (+) or Pauli blocking (−) final state factor. The second product of distribution functions is the rate for the reverse process, producing a particle of momentum  $\mathbf{p}$ . In equilibrium and in the local rest frame,  $[1 \pm f_{\text{eq}}(\mathbf{k})] = f(k)e^{k/T}$  and so the two terms cancel by energy conservation, ensuring detailed balance, i.e.,  $\mathcal{C}[f_{\text{eq}}(\mathbf{p})] = 0$ .<sup>2</sup> The Boltzmann equation rests on several approximations, such as the separation of scales between the distance between collisions and the physical extent of the particle states or deBroglie wavelengths of excitations. It is not clear how to incorporate systematic corrections to these approximations. It is also problematic to evaluate the collision operator to high order in the coupling and its general form depends on the kind of interactions between particles. In QCD, the relevant terms that contribute to the leading order in the coupling constant are presented in Ref. [77].

According with the definition (3.7), the phase-space distribution is associated with the number of on-shell particles per unit phase space, for a system composed by particles and antiparticles with charge  $q$ , one can interpret the number density and the energy-momentum tensor as moments of  $f(x, \mathbf{p})$ <sup>3</sup> [102]

$$N^\mu(x) = q \int d\Gamma p^\mu (f(x, \mathbf{p}) - \bar{f}(x, p)), \quad (3.9a)$$

$$T^{\mu\nu}(x) = \int d\Gamma p^\mu p^\nu (f(x, \mathbf{p}) + \bar{f}(x, p)), \quad (3.9b)$$

<sup>1</sup>The index  $a$  denotes internal degrees of freedom such as spin or color. In the rest of the text we won't use it.

<sup>2</sup>We point out that by neglecting the collisional kernel in the Boltzmann equation does not imply that the system is already in global equilibrium. There are solutions to the Boltzmann equation which describe far from equilibrium physical situations when  $\mathcal{C}[f(x, \mathbf{p})] = 0$ . For example, one known solution used very often to model early-time dynamics in relativistic heavy-ion collisions is the 'simple' 0+1 dimensional free streaming expansion. In this expansion model, every particle of the system follows a straight line trajectory without any interaction (hence,  $\mathcal{C}[f(x, \mathbf{p})] = 0$ ) along the beam axis. The fastest partons will leave the midrapidity region and therefore, in every fluid cell the longitudinal momentum  $p_L$  of the particle will be smaller than its transverse momentum  $p_T$  ( $\langle p_L^2 \rangle \ll \langle p_T^2 \rangle$ ). The system is colder in the longitudinal direction than in the transverse one and there is no global equilibrium. In Sect. 5.2.2 we will give more details about this particular model of expansion.

<sup>3</sup>The single particle phase-space distribution of the antiparticles is denoted by  $\bar{f}$ . In the presence of a non-vanishing chemical potential  $\mu$ ,  $\bar{f}(x, p, \bar{\mu}) = f(x, p, -\mu)$ .

where  $\int d\Gamma \equiv \int d^3\mathbf{p}/((2\pi)^3 E_{\mathbf{p}})$ . In Eqs. (3.9) there is no assumption about the functional form of the distribution function of the distribution function, i.e.  $f(x, \mathbf{p})$  does not correspond necessarily with the distribution function that maximizes the entropy.

If one interprets the definition given in Eq. (3.9b) as the energy-momentum tensor of the system, one can get the conservation laws of hydrodynamics by taking moments of the Boltzmann equation (3.8). Consider the first two moments of the Boltzmann equation (3.8)

$$\int d\Gamma p^\mu \partial_\mu f(x, \mathbf{p}) = \partial_\mu N^\mu(x) = \int d\Gamma \mathcal{C}[f(x, \mathbf{p})] = 0, \quad (3.10a)$$

$$\int d\Gamma p^\nu p^\mu \partial_\mu f(x, \mathbf{p}) = \partial_\mu T^{\mu\nu}(x) = \int d\Gamma p^\nu \mathcal{C}[f(x, \mathbf{p})] = 0, \quad (3.10b)$$

The left hand side (LHS) of the last two equations vanishes due to conservation of the particle number and energy-momentum conservation in microscopic collisions between particles [102, 118].

### 3.2.1. Ideal relativistic hydrodynamics

Ideal hydrodynamics follows from kinetic theory under the assumption of local thermal equilibrium, i.e., the distribution function  $f(x, \mathbf{p})$  relaxes almost instantaneously to the local equilibrium form,  $f_{\text{eq}}(x, p)$ . The distribution  $f_{\text{eq}}(x, p)$  should be an invariant scalar under Lorentz transformations. We introduce the ‘Jüttner’ distribution function of particle momenta  $p^\mu$  for a system in local thermal equilibrium which is moving with velocity  $u^\mu$  [102, 118]<sup>4</sup>

$$f_{\text{eq}}(x, \mathbf{p}) = f_{\text{eq}}\left(\frac{u^\mu(x) p_\mu}{T(x)}\right) = \frac{1}{e^{[u^\mu(x) p_\mu]/T(x)} + a}, \quad (3.11)$$

where  $a = \pm 1$  for fermions/bosons or  $a = 0$  for a Boltzmann distribution. In the LRF, it follows that  $u^\mu(x) p_\mu = E_{\mathbf{p}} = p$  and because  $u^\mu(x) p_\mu$  is Lorentz invariant scalar, it is the same for any reference frame.  $T(x)$  is identified with the temperature at the space-time point  $x$ . The derivation of relativistic fluid hydrodynamics from kinetic theory will be based on the moment expansion of the phase-space distribution function [102]. The  $n$ -th moment of the equilibrated distribution function is defined as the  $n$  rank tensor

$$I^{\mu_1 \mu_2 \dots \mu_n}(x) = \int d\Gamma p^{\mu_1} p^{\mu_2} \dots p^{\mu_n} f_{\text{eq}}(x, \mathbf{p}). \quad (3.12)$$

It is possible to show that one can expand this  $n$  rank tensor as follows [119, 120]

$$I^{\mu_1 \mu_2 \dots \mu_n} = \sum_{k=0}^{(n/2)} a_{nk} \Delta^{(2k)} u^{n-2k}, \quad (3.13)$$

where

$$\Delta^{(2k)} u^{n-2k} = \frac{2^k! k! (n-2k)!}{n!} \times \sum_{\text{permutations}} \Delta^{\mu_1 \mu_2} \dots \Delta^{\mu_{2k-1} \mu_{2k}} u^{\mu_{2k+1}} \dots u^{\mu_n}, \quad (3.14)$$

with  $\Delta^{\mu\nu} = g^{\mu\nu} - u^\mu u^\nu$  and  $u^\mu$  being the flow velocity of the fluid. The coefficients  $a_{nk}$  are found by contracting both sides of Eq. (3.13) with a tensor of the form (3.14).

With these definitions, the energy-momentum tensor of an ideal gas can be seen as the second moment of an equilibrated particle distribution function  $f_{\text{eq}}(x, \mathbf{p})$  given by Eq. (3.11)

$$T_{(0)}^{\mu\nu} = \int d\Gamma p^\mu p^\nu f_{\text{eq}}(x, \mathbf{p}) = a_{20} u^\mu u^\nu + a_{21} \Delta^{\mu\nu}, \quad (3.15)$$

<sup>4</sup>We are interested in systems with vanishing net baryon number, so  $\mu_B = 0$ . Generalizations for systems with  $\mu_B \neq 0$  are straightforward [102, 118].

where we use explicitly the tensor decomposition (3.13) when  $n = 2$ . The coefficients  $a_{20}$  and  $a_{21}$  can be easily evaluated by contracting (3.15) with  $u^\mu u^\nu$  and  $\Delta^{\mu\nu}$ , respectively

$$a_{20} = \int d\Gamma (u_\mu p^\mu)^2 f_{\text{eq}}(x, \mathbf{p}), \quad (3.16a)$$

$$a_{21} = \frac{1}{3} \int d\Gamma (p^\mu p_\mu - (u_\mu p^\mu)^2) f_{\text{eq}}(x, \mathbf{p}). \quad (3.16b)$$

Since  $f_{\text{eq}}$  is a Lorentz scalar, the values of the integrals do not depend on the chosen rest frame, so we evaluate them in the LRF. It is possible to show that for ultrarelativistic particles described by a Boltzmann distribution function, the last integrals give as a result

$$a_{20} = \int d\Gamma p^2 e^{-p/T} = \frac{3}{\pi^2} T^4, \equiv \mathcal{E}(T) \quad (3.17a)$$

$$a_{21} = -\frac{1}{3} \int d\Gamma p^2 e^{-p/T} = -\frac{1}{\pi^2} T^4 = -\frac{a_{20}}{3} \equiv -\mathcal{P}(T). \quad (3.17b)$$

The LHS of both expressions are the well known results of an ideal massless Boltzmann gas and therefore, we identify  $a_{20}$  as the energy density  $\mathcal{E}$  of the system and  $a_{21}$  as the pressure  $\mathcal{P}$  of the system. For particles obeying Bose-Einstein or Fermi-Dirac statistics the relation between  $a_{20}$  ( $a_{21}$ ) and the energy density (pressure) is also satisfied. Using these relations between the coefficients of the expansion and the thermodynamical variables of the system, the energy-momentum tensor  $T_{(0)}^{\mu\nu}$  (3.15) is identified with the energy-momentum tensor of an ideal fluid.

The equations of motion of ideal hydrodynamics for the energy density and fluid velocity can be obtained from conservation law (3.1a) by projecting it with  $u^\mu$  and  $\Delta^{\mu\nu}$ , respectively

$$u_\mu \partial_\mu T_{(0)}^{\mu\nu} = D\mathcal{E} + (\mathcal{E} + \mathcal{P}) \partial_\mu u^\mu = 0, \quad (3.18a)$$

$$\Delta_\mu^\alpha \partial_\mu T_{(0)}^{\mu\nu} = (\mathcal{E} + \mathcal{P}) Du^\alpha - \nabla^\alpha \mathcal{P} = 0, \quad (3.18b)$$

where  $D = u^\mu \partial_\mu$  and  $\nabla^\mu = \Delta^{\mu\alpha} \partial_\alpha$ . Notice that in order to completely solve the last equations we need to specify the initial conditions and the equation of state, i.e.  $\mathcal{P} = \mathcal{P}(\mathcal{E})$ .

### 3.2.2. Dissipative relativistic hydrodynamics

In this section we briefly describe the derivation of dissipative relativistic hydrodynamics from kinetic theory. Before doing this, we derive the equations of motion of the energy density and fluid velocity in the presence of the shear viscous tensor.

For a system with vanishing net baryon number and in the Landau frame, the energy-momentum tensor  $T^{\mu\nu}$  is written as:

$$T^{\mu\nu} = \mathcal{E} u^\mu u^\nu - \mathcal{P} \Delta^{\mu\nu} + \Pi^{\mu\nu}, \quad (3.19)$$

where  $\Pi^{\mu\nu}$  is the shear viscous tensor. The equations of motion for the energy density and flow velocity in the presence of shear viscosity can be obtained in a similar manner as in ideal hydrodynamical Eqs. (3.18)

$$u_\mu \partial_\mu T^{\mu\nu} = D\mathcal{E} + (\mathcal{E} + \mathcal{P}) \partial_\mu u^\mu - \Pi^{\mu\nu} \nabla_{(\mu} u_{\nu)} = 0, \quad (3.20a)$$

$$\Delta_\mu^\alpha \partial_\mu T^{\mu\nu} = (\mathcal{E} + \mathcal{P}) Du^\alpha - \nabla^\alpha \mathcal{P} + \Delta_\mu^\alpha \partial_\nu \Pi^{\mu\nu} = 0, \quad (3.20b)$$

where  $T^{\mu\nu}$  is given by (3.19). Notice that in the last equations we not only need appropriate initial conditions for  $\mathcal{E}$ ,  $u^\mu$  and equation of state, but it is also necessary to specify the evolution equation for the shear viscous tensor  $\Pi^{\mu\nu}$ . This implies an additional problem, to specify the initial conditions of the different components of  $\Pi^{\mu\nu}$ . As we will show in Chapter 6, an incorrect choice of the initial conditions for the shear tensor could allow the development of unphysical behaviour of the solutions of viscous hydrodynamics [121, 122].

### Navier-Stokes theory

The simplest way to introduce the first order corrections in the gradient expansion of the fluid velocity is by considering the dissipative corrections to the entropy current based on the second law of thermodynamics (3.2). In the LRF, the entropy density  $\mathcal{S} = u_\mu \mathcal{S}^\mu$ . This variable is related with the energy density, pressure and temperature by the fundamental relation of thermodynamics

$$T \mathcal{S} = \mathcal{E} + \mathcal{P}, \quad \text{or} \quad T d\mathcal{S} = d\mathcal{E}. \quad (3.21)$$

For the entropy current  $\mathcal{S}^\mu = \mathcal{S} u^\mu$ , the second law of the thermodynamics  $\partial_\mu \mathcal{S}^\mu \geq 0$ , gives us

$$\partial_\mu \mathcal{S}^\mu = \frac{D\mathcal{E}}{T} + \frac{(\mathcal{E} + \mathcal{P})}{T} \partial_\mu u^\mu = \frac{1}{T} \Pi^{\mu\nu} \nabla_{\langle\mu} u_{\nu\rangle} \geq 0. \quad (3.22)$$

In the derivation of this relation we used explicitly the fundamental relation of thermodynamics (3.21) and the viscous hydrodynamical equations (3.20). The simplest way is satisfy the last inequality is to assume that

$$\Pi_{\text{NS}}^{\mu\nu} = \eta \nabla^{\langle\mu} u^{\nu\rangle}. \quad (3.23)$$

We recognize the proportionality factor  $\eta$  in the last expression as the shear viscosity transport coefficient ( $\eta \geq 0$ ). Eq. (3.23) is known as the relativistic generalization of the Navier-Stokes (NS) equation for the shear viscosity tensor. From this expression, one recognizes that  $\Pi_{\text{NS}}^{\mu\nu}$  is proportional to first order gradients in the velocity. Therefore, one can guess that second order corrections would be  $\sim \mathcal{O}((\partial_\mu u^\mu)^2)$ . The set of equations (3.20), together with the NS viscous tensor (3.23), form the complete first order viscous hydrodynamical equations.

Even though Navier-Stokes theory is simple and beautiful, it turns out that relativistic NS equations do not preserve causality [123, 124]. To cure this problem it is necessary to go up to, at least, 2nd-order in the gradient expansion of the flow velocity. We describe in the next section how to include these corrections from kinetic theory approach.

### Linearizing the Boltzmann equation: moment method

In the last section, we derived the relativistic NS equation for the shear viscosity tensor based on the second law thermodynamics. It is possible to implement the same procedure to include the 2nd-order corrections in the gradient expansion to the shear viscous tensor.<sup>5</sup> However, this method doesn't include the coupling with the fluid vorticity, which is an important contribution at second order in the gradient expansion of the fluid velocity. Fluid vorticity does not contribute to the entropy production, so there is no violation of the second law of thermodynamics if one adds by hand its contribution to the evolution equation of  $\Pi^{\mu\nu}$  [128]. The main advantage of the derivation of the equation of motion for the shear viscous tensor from kinetic theory relies on the fact that it captures almost all of the contributions to 2nd-order in the gradient expansion of the fluid velocity. However, the last statement is valid as far as one knows the complete form of the collisional kernel of the Boltzmann equation to second order in the gradient expansion.

To consider dissipative corrections, we consider off-equilibrium departures from the equilibrated distribution function  $f_{eq}(x, \mathbf{p})$  (3.11)

$$f(x, \mathbf{p}) = f_{eq}(x, \mathbf{p})(1 + \delta f(x, \mathbf{p})), \quad (3.24)$$

where  $\delta f(x, \mathbf{p})$  is the fluctuation of the equilibrated phase-space distribution function and it is assumed that the departures from equilibrium are small, i.e.,  $|\delta f(x, \mathbf{p})| \ll 1$ . An alternative approach to include viscous corrections to ideal hydrodynamics is based on the Grmela-Öttinger formalism [129, 129, 130] whose relativistic generalization and numerical implementation was performed by Dusling and Teaney [131].

<sup>5</sup>An explicit derivation of the 2nd-order equation for the shear viscous tensor based on the second law of thermodynamics is presented in Refs. [125, 109, 126, 127].

If one replaces the distribution function given by Eq. (3.24) in the kinetic theory definition of the energy-momentum tensor  $T^{\mu\nu}$  (3.9b), we have

$$\begin{aligned} T^{\mu\nu} &= \int d\Gamma p^\mu p^\nu f_{eq}(x, \mathbf{p})(1 + \delta f(x, \mathbf{p})), \\ &= \int d\Gamma p^\mu p^\nu f_{eq}(x, \mathbf{p}) + \int d\Gamma p^\mu p^\nu f_{eq}(x, \mathbf{p}) \delta f(x, \mathbf{p}) \equiv T_{(0)}^{\mu\nu} + \delta T^{\mu\nu}. \end{aligned} \quad (3.25)$$

By demanding that the last expression correspond to the same energy-momentum tensor for a system with vanishing net baryon number given by Eq. (3.19), we conclude that

$$\delta T^{\mu\nu} \equiv \Pi^{\mu\nu} = \int d\Gamma p^\mu p^\nu f_{eq}(x, \mathbf{p}) \delta f(x, \mathbf{p}). \quad (3.26)$$

It is possible to calculate  $\delta f(x, \mathbf{p})$  by linearizing the Boltzmann equation [102]. Here we follow the moment expansion method [102]. In this method, the momentum dependence of the fluctuating part of the distribution function is approximated as a truncated Taylor series

$$\delta f(x, \mathbf{p}) = \epsilon(x) + \epsilon_\mu(x) p^\mu + \epsilon_{\mu\nu}(x) p^\mu p^\nu + \mathcal{O}(p^3). \quad (3.27)$$

The coefficients  $\epsilon(x)$ ,  $\epsilon_\mu(x)$  and  $\epsilon_{\mu\nu}(x)$  are determined a posteriori. It is possible to show that for systems where the dissipative effects come only in the presence of the shear viscous tensor, the coefficients  $\epsilon(x)$  and  $\epsilon_\mu(x)$  vanish [119, 126]. Therefore, for the case we are studying  $\delta f(x, \mathbf{p}) = \epsilon_{\mu\nu}(x) p^\mu p^\nu$ . Replacing this into the shear viscous tensor (3.26), we have the relation

$$\Pi^{\mu\nu}(x) = \epsilon_{\alpha\beta}(x) \int d\Gamma p^\mu p^\nu p^\alpha p^\beta f_{eq}(x, \mathbf{p}) \equiv \epsilon_{\alpha\beta}(x) I^{\alpha\beta\mu\nu}(x), \quad (3.28)$$

with  $I^{\alpha\beta\mu\nu}(x)$  being the 4th moment of the equilibrated distribution function according with the definition (3.12). The last expression suggests that  $\epsilon_{\alpha\beta}(x) = c_2 \Pi_{\alpha\beta}(x)$  where  $c_2$  is an unknown function of  $\mathcal{E}$  and  $\mathcal{P}$ . Hence

$$\Pi^{\mu\nu}(x) = c_2 \Pi_{\alpha\beta}(x) I^{\alpha\beta\mu\nu}(x). \quad (3.29)$$

The 4th moment  $I^{\alpha\beta\mu\nu}(x)$  can be decomposed in a tensorial basis following Eq. (3.13). Doing that we find that the previous last expression leads to

$$\Pi^{\mu\nu}(x) = 2 c_2 a_{42} \Pi^{\mu\nu}, \quad \implies \quad c_2 = \frac{1}{2 a_{42}}. \quad (3.30)$$

The coefficient  $a_{42}$  can be calculated in a similar manner as the coefficients  $a_{20}$  and  $a_{21}$ . For a Boltzmann gas,  $a_{42} = T^2 (\mathcal{E} + \mathcal{P})$  (see explicit calculation in Appendix A). Once we have specified the coefficient  $c_2$ , the fluctuating part of the Jüttner distribution function can be expressed as

$$\begin{aligned} \delta f(x, \mathbf{p}) &= \frac{1}{2 a_{42}} p^\mu p^\nu \Pi_{\mu\nu}, \\ &= \frac{1}{2 T^2 (\mathcal{E} + \mathcal{P})} p^\mu p^\nu \Pi_{\mu\nu}. \end{aligned} \quad (3.31)$$

The last relation strongly suggests the relation between  $\delta f(x, \mathbf{p})$  and the gradient expansion. For example, using the NS value of  $\Pi^{\mu\nu}$  (3.23), Eq. (3.31) results into  $\delta f(x, \mathbf{p}) \sim \nabla^{\langle\mu} u^{\nu\rangle}$ . Therefore, the magnitude of  $\delta f$  is identified with the size of gradients of the hydrodynamics degrees of freedom. Keeping in mind this equivalence, the collisional kernel can be approximated to first order in gradients by inserting the form of the distribution function (3.24) in the Boltzmann equation (3.8). Before doing that, we need to find an approximate form of the equations of viscous hydrodynamics for the

energy density and fluid velocity (Eqs. (3.20)). To first order in gradients, these equations can be approximated as

$$D\mathcal{E} = -(\mathcal{E} + \mathcal{P}) \partial_\mu u^\mu + \mathcal{O}(\Pi \partial \cdot u \sim \delta^2), \quad (3.32a)$$

$$Du^\alpha = \frac{\nabla^\alpha \mathcal{P}}{\mathcal{E} + \mathcal{P}} + \mathcal{O}(\Pi \partial \cdot u \sim \delta^2). \quad (3.32b)$$

For a Boltzmann distribution function,  $\mathcal{E} = 3T^4/\pi^2$ , hence

$$\frac{D\mathcal{E}}{\mathcal{E}} = 4 \frac{DT}{T}. \quad (3.33)$$

If one uses the ideal equation of state and the last expression in the approximated equation of motion for the energy density (3.32a), we get the identity

$$\frac{DT}{T} = -\frac{1}{3} \partial_\mu u^\mu. \quad (3.34)$$

Using the ideal equation of state in the approximated equation of motion for the fluid velocity

$$Du^\mu = \frac{\nabla^\mu T}{T}. \quad (3.35)$$

Now, by expanding the Boltzmann equation for the distribution function (3.24) we get

$$\begin{aligned} \mathcal{C}[f] &= -p^\mu \partial_\mu (f_{eq}(x, \mathbf{p})(1 + \delta f(x, \mathbf{p}))), \\ &\approx -p^\mu \partial_\mu f_{eq}(x, \mathbf{p}) + \mathcal{O}((\delta f)^2), \quad f_{eq}(x, \mathbf{p}) = e^{-u^\mu p_\mu/T} \\ &\approx p^\mu p^\nu f_{eq}(x, \mathbf{p}) \left( \frac{u_\mu}{T} Du^\mu - \frac{1}{T^2} u_\mu u_\nu DT + \frac{\nabla_\mu u_\nu}{T} - \frac{u_\nu}{T^2} \nabla_\mu T \right) \\ &+ \mathcal{O}((\delta f)^2), \end{aligned} \quad (3.36)$$

where we use the identity  $\partial_\mu = u_\mu D + \nabla_\nu$ . Using the relations (3.34) and (3.35) and the fact that the tensor  $p^\mu p^\nu$  is symmetric, the last expression is finally written as

$$\begin{aligned} \mathcal{C}[f] &= \frac{p^\mu p^\nu}{2T} f_{eq}(x, \mathbf{p}) (\nabla_{\langle \mu} u_{\nu \rangle} - \Delta_{\mu\nu} \partial_\alpha u^\alpha) + \mathcal{O}((\delta f)^2), \\ &= \frac{p^\mu p^\nu}{2T} f_{eq}(x, \mathbf{p}) \nabla_{\langle \mu} u_{\nu \rangle} + \mathcal{O}((\delta f)^2). \end{aligned} \quad (3.37)$$

For the NS theory, the collisional kernel is calculated exactly from the last expression if one uses Eq. (3.23) giving

$$\mathcal{C}[f]_{\text{NS}} = \frac{p^\mu p^\nu}{2\eta T} \Pi_{\mu\nu} f_{eq}(x, \mathbf{p}) + \mathcal{O}((\delta f)^2). \quad (3.38)$$

### Israel-Stewart theory

In the last section, we showed how to linearize the Boltzmann equation using the moment method to determine the fluctuation around equilibrium  $\delta f(x, \mathbf{p})$  (Eqn. 3.31). Using this result, we determined in the NS theory the exact form of the collisional kernel  $\mathcal{C}[f]_{\text{NS}}$ . We will use these results to derive the equation of motion of the shear viscous tensor to 2nd order in the gradient expansion from kinetic theory. To accomplish this, we use the third moment of the Boltzmann equation for the fluctuation around equilibrium  $\delta f(x, \mathbf{p})$  (3.31)

$$\int d\Gamma p^\alpha p^\beta p^\mu \partial_\mu \left( e^{-u^\mu p_\mu/T} \left( 1 + \frac{1}{2a_{42}} p^\delta p^\gamma \Pi_{\delta\gamma} \right) \right) = \int d\Gamma p^\alpha p^\beta \mathcal{C}[f]. \quad (3.39)$$

By reorganizing the terms on the LHS of the last expression, one identifies them as the third and fifth moment of the Boltzmann distribution function, so the last expression can be expressed as

$$\partial_\mu \left( I^{\alpha\beta\mu} + \frac{\Pi_{\gamma\delta}}{2a_{42}} I^{\alpha\beta\mu\gamma\delta} \right) = \int d\Gamma p^\alpha p^\beta \mathcal{C}[f]. \quad (3.40)$$

In general, the RHS of this relation doesn't vanish. One can in principle try to perform all the required integrals that appear in the last expression. Nevertheless, one can avoid this long and lengthy calculation by projecting Eq. (3.40) by the operator  $P_{\alpha\beta}^{\mu\nu}$

$$P_{\alpha\beta}^{\mu\nu} \partial_\mu \left( I^{\alpha\beta\mu} + \frac{\Pi_{\gamma\delta}}{2a_{42}} I^{\alpha\beta\mu\gamma\delta} \right) = P_{\alpha\beta}^{\mu\nu} \int d\Gamma p^\alpha p^\beta \mathcal{C}[f], \quad (3.41)$$

where  $P_{\alpha\beta}^{\mu\nu}$  is defined by

$$P_{\alpha\beta}^{\mu\nu} = \Delta_\alpha^\mu \Delta_\beta^\nu + \Delta_\beta^\mu \Delta_\alpha^\nu - \frac{2}{3} \Delta^{\mu\nu} \Delta_{\alpha\beta}. \quad (3.42)$$

$P_{\alpha\beta}^{\mu\nu}$  has three interesting properties:  $u^\alpha P_{\alpha\beta}^{\mu\nu} = u^\beta P_{\alpha\beta}^{\mu\nu} = 0$ ,  $\Delta^{\alpha\beta} P_{\alpha\beta}^{\mu\nu} = 0$  and  $\Pi^{\alpha\beta} P_{\alpha\beta}^{\mu\nu} = 2\Pi^{\mu\nu}$ . From the projection of  $I^{\alpha\beta\mu}$ ,  $I^{\alpha\beta\mu\gamma\delta}$  and the NS value of the collisional kernel  $\mathcal{C}_{\text{NS}}[f]$  over  $P_{\alpha\beta}^{\mu\nu}$ , we obtain

$$P_{\alpha\beta}^{\mu\nu} \partial_\phi I^{\phi\beta\mu} = 2a_{31} \nabla^{\langle\mu} u^{\nu\rangle}, \quad (3.43a)$$

$$\begin{aligned} P_{\alpha\beta}^{\mu\nu} \partial_\phi \left( \frac{\Pi_{\gamma\delta}}{2a_{42}} I^{\phi\alpha\beta\gamma\delta} \right) &= 2\Pi^{\mu\nu} D \left( \frac{a_{52}}{a_{42}} \right) \\ &+ 2 \frac{a_{52}}{a_{42}} \left( \Pi^{\mu\nu} \partial_\phi u^\phi + \Delta_\alpha^\mu \Delta_\beta^\nu D \Pi^{\alpha\beta} + P_{\alpha\beta}^{\mu\nu} \Pi^{\phi\beta} \partial_\phi u^\alpha \right), \end{aligned} \quad (3.43b)$$

$$\begin{aligned} P_{\alpha\beta}^{\mu\nu} \int d\Gamma p^\alpha p^\beta \mathcal{C}_{\text{NS}}[f] &= \frac{1}{2\eta T} P_{\alpha\beta}^{\mu\nu} \int d\Gamma p^\alpha p^\beta p^\gamma p^\delta \Pi_{\gamma\delta} e^{-u^\mu p_\mu/T}, \\ &= \frac{1}{2\eta T} \Pi_{\gamma\delta} P_{\alpha\beta}^{\mu\nu} I^{\alpha\beta\gamma\delta}, \\ &= 2 \frac{a_{42}}{T\eta} \Pi^{\alpha\beta}. \end{aligned} \quad (3.43c)$$

For a Boltzmann distribution function, the calculation of these coefficients gives us (See App. B for details)

$$a_{31} = -4 \frac{T^5}{\pi^2}, \quad a_{42} = 4 \frac{T^6}{\pi^2}, \quad a_{52} = 24 \frac{T^7}{\pi^2}, \quad (3.44)$$

By collecting Eqs. (3.43) and (3.44) into Eq. (3.41), we get the evolution equation of  $\Pi^{\mu\nu}$

$$\Pi^{\mu\nu} + \frac{a_{52}}{a_{42}} T \eta \left( \Delta_\alpha^\mu \Delta_\beta^\nu D \Pi^{\alpha\beta} + P_{\alpha\beta}^{\mu\nu} \Pi^{\phi\beta} \nabla_\phi u^\alpha + \Pi^{\mu\nu} \partial_\alpha u^\alpha + \Pi^{\mu\nu} D \log T \right) = \eta \nabla^{\langle\mu} u^{\nu\rangle}. \quad (3.45)$$

By introducing the antisymmetric tensor  $\Omega_{\alpha\beta} \equiv \nabla_{[\alpha} u_{\beta]}$  (which we identify with the fluid vorticity), the term  $P_{\alpha\beta}^{\mu\nu} \Pi^{\phi\beta} \nabla_\phi u^\alpha$  is rewritten after some algebra

$$\begin{aligned} P_{\alpha\beta}^{\mu\nu} \Pi^{\phi\beta} \nabla_\phi u^\alpha &= P_{\alpha\beta}^{\mu\nu} \Delta^{\alpha\gamma} \Pi^{\phi\beta} \left[ \Omega_{\phi\gamma} + \frac{1}{2} \nabla_{\langle\phi} u_{\gamma\rangle} + \frac{1}{3} \Delta_{\phi\gamma} \nabla_\delta u^\delta \right] \\ &= -2\Pi^{\phi(\mu} \Omega_{\phi}^{\nu)} + \frac{\Pi^{\phi\langle\mu} \Pi_{\phi}^{\nu\rangle}}{2\eta} + \frac{2}{3} \Pi^{\mu\nu} \nabla_\delta u^\delta + \mathcal{O}(\delta^3), \end{aligned} \quad (3.46)$$



In the last relation, we explicitly use the NS value of  $\Pi^{\mu\nu}$  in order to write  $\nabla_{\langle\phi}u_{\gamma\rangle}$  to first order in gradients. Using the truncated versions of the viscous equations for the energy density and the fluid viscosity (3.32), one can replace the term  $D \log T = -\nabla_\alpha u^\alpha/3$ . By doing this, Eq. (3.45) becomes

$$\Pi^{\mu\nu} + \tau_\pi \left[ \Delta_\alpha^\mu \Delta_\beta^\nu D \Pi^{\alpha\beta} + \frac{4}{3} \Pi^{\mu\nu} \nabla_\alpha u^\alpha - 2 \Pi^{\phi(\mu} \Omega^{\nu)}_\phi + \frac{\Pi^{\phi < \mu} \Pi^{\nu >}_\phi}{2\eta} \right] = \eta \nabla^{<\mu} u^{\nu>} + \mathcal{O}(\delta^2), \quad (3.47)$$

where we define  $\tau_\pi \equiv (a_{52}/a_{42}^2)T\eta$ . From this definition of  $\tau_\pi$  and after replacing the values of  $a_{52}$  and  $a_{42}$  (Eq. (3.44)), we find the well known relation for a Boltzmann gas

$$\frac{\eta}{\tau_\pi} = \frac{2T^4}{3\pi^2} = \frac{2}{3}p. \quad (3.48)$$

Eq. (3.47) is an evolution equation for  $\Pi^{\mu\nu}$  derived from kinetic theory using the moment method up to 2nd order using the gradient expansion. Notice that not all the terms  $\mathcal{O}((\delta f)^2)$  are included in this equation because we approximated the complete collisional kernel to its NS value. To have a self consistent approach, one has to solve the Boltzmann equation by including all the terms  $\mathcal{O}((\delta f)^2)$  in the collisional kernel. This issue indicates to us that there is a need to develop a new theory that keeps all the 2nd-order structures in the gradient expansion in order to obtain the evolution equation of the hydrodynamical degrees of freedom. In the next section, we review the recent developed theory for conformal fluids [103, 104].

### 3.2.3. Conformal viscous hydrodynamics

As we mentioned at the end of the last section, in the derivation of the equation of motion for the shear viscous tensor, we explicitly used the NS value of the collisional kernel  $\mathcal{C}_{\text{NS}}[f]$ . By doing that, we are neglecting unknown second order corrections of  $\mathcal{O}((\delta f)^2)$  which, in principal, shouldn't be ignored if one desires a consistent derivation. In general, there is no precise way to determine self-consistently the collisional kernel  $\mathcal{C}[f]$  to all the orders of the gradient expansion for any field theory, just a few exceptions can be calculated. Therefore, a better theory that includes completely all the 2nd order structures of the gradient expansion should be developed. Based on AdS/CFT methods, Baier et. al [103] and the Tata group [104] completed this task for conformal fluids up to 2nd order. The main idea of this approach is to classify all the possible 2nd order structures in the gradient expansion that are invariant under conformal transformations. By conformal symmetry, we mean, a symmetry that allows the system to be invariant under dilation (scale invariance) and under special conformal transformations. When we say that some theory is conformal, it means that its action  $S(\phi, g^{\mu\nu})$ , as a functional of the metric  $g^{\mu\nu}$  is invariant under the Weyl rescaling

$$g^{\mu\nu} \rightarrow \bar{g}^{\mu\nu} = e^{-2w(x)} g^{\mu\nu}, \quad (3.49)$$

where  $w(x)$  is an arbitrary function of the space-time point  $x$ . If the theory is said to be conformal, the trace of the energy-momentum tensor of the system vanishes exactly, i.e.  $T^\mu_\mu=0$ . As a consequence of the Weyl transformation of the metric, the energy-momentum tensor transforms as

$$T^{\mu\nu} \rightarrow \bar{T}^{\mu\nu} = e^{6w(x)} T^{\mu\nu}. \quad (3.50)$$

For the energy-momentum tensor of a system with vanishing net baryon number given by Eq. (3.19), the last expression implies that under Weyl transformations the shear viscous tensor transforms as [103]

$$\Pi^{\mu\nu} \rightarrow \bar{\Pi}^{\mu\nu} = e^{\delta w(x)} \Pi^{\mu\nu} \quad (3.51)$$

This scaling of  $\Pi^{\mu\nu}$  imposes a constraint on the possible terms that contribute at all orders to its evolution equation if one demands that the theory is conformal. The NS value of  $\Pi^{\mu\nu} = \eta \nabla^{<\mu} u^{\nu>}$

satisfies this constraint since under the transformation (3.49) the shear viscosity  $\eta$  and the velocity tensor  $\nabla^{\langle\mu}u^{\nu\rangle}$  transform like [103]

$$\eta \rightarrow \bar{\eta} = e^{3w(x)}\eta, \quad \nabla^{\langle\mu}u^{\nu\rangle} \rightarrow \overline{\nabla^{\langle\mu}u^{\nu\rangle}} = e^{3w(x)}\nabla^{\langle\mu}u^{\nu\rangle}. \quad (3.52)$$

Additionally, all the mathematical structures of the gradient expansion should satisfy  $u_\mu\Pi^{\mu\nu}=0=\Pi_\nu^\mu$ . At 2nd order it is found that for a general curved space-time, there are only 8 structures that satisfy the last two conditions [103, 104]<sup>6</sup>

$$D^{\langle\mu} \ln \mathcal{E} D^{\nu\rangle} \ln \mathcal{E}, \quad D^{\langle\mu} D^{\nu\rangle} \ln \mathcal{E} \quad \nabla^{\langle\mu}u^{\nu\rangle} (\nabla_\alpha u^\alpha), \quad P_{\alpha\beta}^{\mu\nu} \nabla^{\langle\alpha}u^{\gamma\rangle} g_{\gamma\delta} \nabla^{\langle\delta}u^{\beta\rangle} \\ P_{\alpha\beta}^{\mu\nu} \nabla^{\langle\alpha}u^{\gamma\rangle} g_{\gamma\delta} \Omega^{\beta\delta}, \quad P_{\alpha\beta}^{\mu\nu} \Omega^{\alpha\gamma} g_{\gamma\delta} \Omega^{\beta\delta}, \quad u_\gamma R^{\gamma\langle\mu\nu\rangle\delta} u_\delta, \quad R^{\langle\mu\nu\rangle}, \quad (3.53)$$

where  $\mathcal{E}$  is the energy density,  $R^{\alpha\mu\nu\beta}$  and  $R^{\mu\nu}$  are the Riemann and Ricci tensor respectively. But only 5 combinations of the above terms satisfy the Weyl invariance. By regrouping in a proper way, the 2nd-order evolution equation for the shear tensor is [103, 104]

$$\Pi^{\mu\nu} = \eta \nabla^{\langle\mu}u^{\nu\rangle} - \tau_\pi \left[ \Delta_\alpha^\mu \Delta_\beta^\nu D \Pi^{\alpha\beta} + \frac{4}{3} \Pi^{\mu\nu} (\nabla_\alpha u^\alpha) \right] \\ + \frac{\kappa}{2} [R^{\langle\mu\nu\rangle} + 2u_\alpha R^{\alpha\langle\mu\nu\rangle\beta} u_\beta] \\ - \frac{\lambda_1}{2\eta^2} \Pi^{\langle\mu}{}_\lambda \Pi^{\nu\rangle\lambda} - \frac{\lambda_2}{2\eta} \Pi^{\langle\mu}{}_\lambda \Omega^{\nu\rangle\lambda} - \frac{\lambda_3}{2} \Omega^{\langle\mu}{}_\lambda \Omega^{\nu\rangle\lambda}, \quad (3.54)$$

Comparing with the equation derived from kinetic theory discussed in the last section, we have not only  $\eta$  and  $\tau_\pi$  but also there are four new transport coefficients  $\kappa, \lambda_1, \lambda_2$  and  $\lambda_3$ . The conformal symmetry constraint (3.51) doesn't tell us how to obtain the values of these transport coefficients. Such calculations have been performed explicitly for two distinct theories,  $\mathcal{N}=4$  SYM at strong coupling and weakly coupled QCD at finite temperature. In the  $\mathcal{N}=4$  SYM theory, one should make use of the AdS/CFT correspondence [132] to determine the correspondent Green functions. For  $\mathcal{N}=4$  SYM, the values of the transport coefficients in the large  $N_c$  limit are listed below

$$\frac{\eta}{\mathcal{S}} = \frac{1}{4\pi}, \quad \tau_\pi = \frac{2 - \ln 2}{2\pi T}, \\ \kappa = \frac{\eta}{\pi T}, \quad \lambda_1 = \frac{\eta}{2\pi T}, \quad \lambda_2 = -\ln 2 \frac{\eta}{\pi T}, \quad \lambda_3 = 0 \quad (3.55)$$

Based on weakly coupled QCD [133, 134, 77, 135, 136, 137], York and Moore [138] found that for weakly coupled QCD theory, these transport coefficients also emerged once the collisional kernel is taken into account properly up to 2nd order in the gradient expansion. Their results are given by

$$\tau_\pi = \frac{5.0 \dots 5.9}{T} \frac{\eta}{\mathcal{S}}, \quad \lambda_1 = \frac{4.1 \dots 5.2}{T} \frac{\eta^2}{\mathcal{S}}, \quad \lambda_2 = -2\eta\tau_\pi, \quad \lambda_3 = 0, \quad \kappa = \frac{5}{8\pi^2 T} \mathcal{S}. \quad (3.56)$$

Parametrically,  $\eta/\mathcal{S} \sim 1/(g^4 \log g^{-1})$  where  $g$  is the coupling constant of the field theory and the proportionality factor depends on the content of matter [135, 136].

When one applies this formalism to ultrarelativistic heavy ion collisions, it is assumed that the created matter after collision is approximately conformal, which can be a reasonable assumption at high energies. Nevertheless, lattice gauge theory calculations have suggested that the bulk viscosity plays an important role around the critical temperature  $T_C$  when the QGP transforms into a hadron gas [139, 140], so a theory for non-conformal fluids is required to describe this stage of the dynamical evolution of the fireball. This program has been already started by Betz et. al. [105]. Based on consistent expansions to second order in Knudsen number, these authors deduce the complete IS

<sup>6</sup>For a Minkowski space there are just 6 of these structures.

---

equations for the Boltzmann equation for the bulk pressure  $\Pi$ , shear viscous tensor  $\Pi^{\mu\nu}$  and the heat flow  $q^\mu$  via 14's Grads method [102]. An alternative approach to the same problem has been recently proposed by Romatschke [106]; in this work the author classified the possible 2nd-order terms that contribute to the entropy production for conformal and non-conformal fluids.

In Chapter 6, our calculations are based on conformal viscous hydrodynamics formalism. This is due to the fact that we are interested in the early stages of the collision where bulk viscosity/heat flow effects can be neglected and the fluid is almost conformal.



## 4. Dileptons in ultrarelativistic heavy ion collisions

Dilepton yields are one of the key observables to study the dynamics of ultrarelativistic heavy ion collisions. Dileptons are indicators of every stage of heavy ion collisions, so their experimental and theoretical analysis helps to elucidate the properties of the evolving medium created in collisions between heavy nuclei. One of the main advantages of dileptons is the fact that they possess finite pair mass and therefore, there are two kinematic variables that characterize dilepton spectra, the invariant mass  $M$  and transverse momentum  $p_T$ . These two parameters can be varied to investigate the different stages of the collisions.

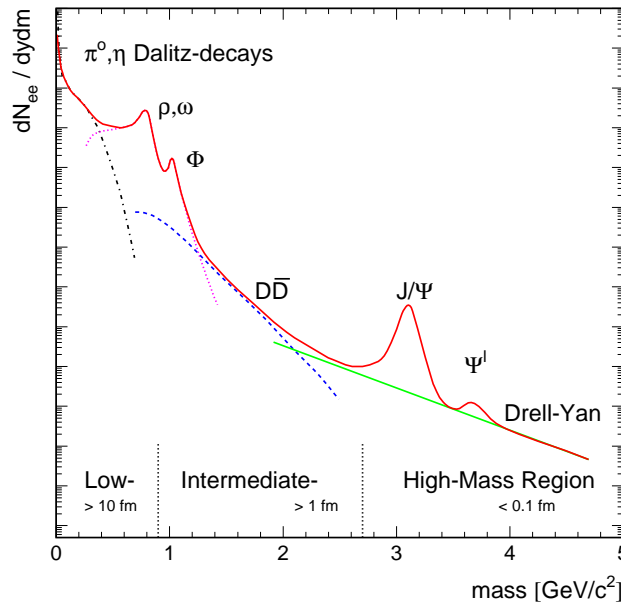


Figure 4.1.: A schematic view of dilepton production as a function of the invariant mass in ultrarelativistic heavy ion collisions. Figure taken from Ref. [141].

In Fig. 4.1 we show a schematic view of characteristic dilepton sources in ultrarelativistic heavy ion collisions as a function of the invariant mass of the dilepton pair. From this figure, we can roughly distinguish three kinematic regions that characterize dilepton spectra:

1. Low mass region (LMR): is the region below and around the  $\phi$  meson, i.e.,  $M \lesssim M_\phi = 1.024$  GeV. This region is governed by the light quark sector of  $u, d$  and  $s$  quarks. The spectrum is dominated by  $\pi^0$  and  $\eta$  decays and there are two additional peaks due to the vector meson decay of  $\rho, \omega$  and  $\phi$ . Many studies indicate that low mass region of medium dilepton production gives signals of chiral symmetry restoration which can be inferred in terms of medium modification of light hadrons.<sup>1</sup> Dileptons with lower invariant mass are produced at the late-times of the collision.

<sup>1</sup>It is known that in the limit of vanishing current quark masses, the order parameter of the QCD phase transition associated with chiral symmetry restoration, (i.e., the chiral condensate) is most likely of first order for three flavors.

2. Intermediate mass region (IMR): this region is located between  $M_\phi < M < M_{J/\Psi} = 3.1$  GeV. This has been one of the most studied regions since continuum radiation coming from QGP dominates the dilepton mass spectrum. In the QGP phase at leading order, dilepton pairs arise from the annihilation process between quarks,  $q + \bar{q} \rightarrow \gamma^* \rightarrow l^+ + l^-$  for large invariant masses. However, most of the background in this regime arise from decays of open-charms, i.e., pairwise produced from  $D\bar{D}$  mesons followed by semileptonic decays which may obscure signals from QGP. This also holds true for the lower-mass tail of Drell-Yan production.
3. High mass region (HMR): this kinematic region lies above  $M \geq M_{J/\Psi}$ . Drell-Yan production is one of the most prominent sources of dilepton pairs. Primordial emission and heavy quarkonia like  $J/\Psi$  and  $\Upsilon$  suppression are the most important phenomenon to study medium effects.

As can be seen from the above discussion, high-energy dileptons are sensitive to early-time dynamics of the collision. Therefore, one can expect that information about emission of dileptons from an anisotropic QGP can be obtained from the intermediate and high mass region. In this work we explore pre-equilibrium production of high-energy dileptons as a function of the transverse momentum and invariant mass in the range  $1 \lesssim M, p_T \lesssim 10$  GeV.

## 4.1. Medium dilepton production rate from finite temperature field theory

To access physical properties of thermal systems is not an easy task in many experimental situations. Instead, one can assume that the system is composed of some particles that behave like a thermal reservoir, i.e., particles that interact so strongly as to remain in thermal equilibrium, while other particles interact weakly with the thermal system and cannot follow thermal equilibrium. One can imagine that these particles can escape the region either explicitly (they leave a thermal system of finite size) or in the abstract sense (they remain in the thermal reservoir but the interaction is so small that they behave as free particles). Familiar examples of these systems have been observed in nature, for example in the decoupling of weakly interacting dark matter particles in cosmology [142], the electromagnetic radiation from the QCD plasma generated in heavy ion collisions and the neutrino emissivity of neutron stars. These are all examples of thermal particle production. In this section, we briefly discuss the basics of thermal particle production for the case of dileptons. More general details of thermal particle production can be found in Refs. [74, 75].

It can be shown that at leading order in the electromagnetic coupling constant  $\mathcal{O}(\alpha^2)$  and all orders of the strong coupling constant, the differential dilepton rate can be expressed in terms of the correlation function of the hadronic electromagnetic current [143, 144, 145]. Here, we will show the results of the differential dilepton rate to  $\mathcal{O}(\alpha^2)$  without including HTL resummation of the bare propagators.<sup>2</sup> At high temperatures, the dominant medium contribution comes from the annihilation process  $q + \bar{q} \rightarrow \gamma^* \rightarrow l^+ + l^-$ .

The differential dilepton rate is defined as <sup>3</sup>

$$\frac{dN^{l^+l^-}}{d^4x d^3\mathbf{p}_1 d^3\mathbf{p}_2} = \lim_{t, V \rightarrow \infty} \frac{1}{Vt} \sum_{f,i} \frac{e^{-\beta E_i}}{Z_{sys}} |T_{fi}|^2, \quad (4.1)$$

<sup>2</sup>Details of a calculation that includes such corrections to the bare propagators can be found in Ref. [146].

<sup>3</sup>Notice that in principle one can make use of a more formal definition:

$$\frac{dN^{l^+l^-}}{d^4x d^3\mathbf{p}_1 d^3\mathbf{p}_2} = \frac{d}{dt} \left( \text{Tr.} \left[ \frac{d\hat{N}^{l^+l^-}}{d^3\mathbf{x} d^3\mathbf{p}_1 d^3\mathbf{p}_2} \hat{\rho}_I(t) \right] \right),$$

where  $\frac{d\hat{N}^{l^+l^-}}{d^3\mathbf{x} d^3\mathbf{p}} = \frac{1}{V} \hat{a}_{\mathbf{p}}^\dagger \hat{a}_{\mathbf{p}}$  is the number operator of particles per space and momentum volume and  $\hat{\rho}_I(t)$  is the density matrix of the system in the interaction picture. The result obtained from this definition is the same as the one presented in the main text.

where  $t$  is the observation time,  $V$  is the volume of the system,  $Z_{sys}$  is the partition function of the system and  $T_{fi}$  is the scattering amplitude which indicates the transition  $i \rightarrow f + l^+ + l^-$ , i.e., from some initial hadronic state to some final hadronic state plus a dilepton pair of momenta  $\mathbf{p}_1$  and  $\mathbf{p}_2$ . Notice that the last definition involves a statistical average and this is why we sum over every initial state weighed with the Boltzmann factor  $e^{-E_i/T}/Z_{sys}$ ,  $Z_{sys} = \sum_j e^{-\beta \hat{H}_j}$ .<sup>4</sup>

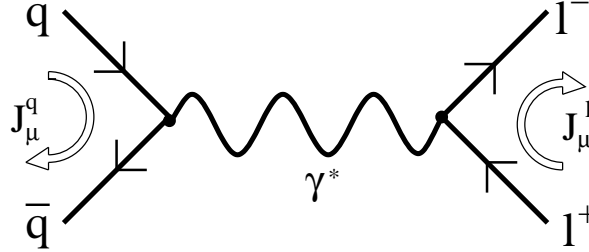


Figure 4.2.: Feynman diagram for the process  $q + \bar{q} \rightarrow \gamma^* \rightarrow l^+ + l^-$  to leading order  $\mathcal{O}(\alpha)$ . The figure also shows the quark current  $\hat{J}_\mu^q(x)$  and leptonic current  $\hat{J}_\mu^l(x) = \hat{l}(x)\gamma_\mu\hat{l}(x)$ .

In the interaction picture, the hamiltonian that describes the local interactions between the coupling of the photon field  $A_\mu(x)$  and the electromagnetic currents of the quark fields  $\hat{J}_\mu^q(x)$  and the lepton fields  $\hat{J}_\mu^l(x) = \hat{l}(x)\gamma_\mu\hat{l}(x)$  (see Fig. 4.2) is

$$\hat{H} = \int d^3x (e\tilde{e}\hat{A}^\mu(x)\hat{J}_\mu^q(x) + e\hat{A}_\mu(x)\hat{l}(x)\gamma^\mu\hat{l}(x)), \quad (4.2)$$

where  $e$  is the electric charge,  $\tilde{e} = e_q/e$  is the proportional value of the quark electric charge and  $\hat{l}(x)$  is the lepton field which, expressed in terms of the annihilation and creation operators, is [147]

$$\hat{l}(x) = \int \frac{d^3\mathbf{p}_1}{\sqrt{(2\pi)^3 2E_{\mathbf{p}_1}}} \sum_{s_1=\pm 1} \left( \hat{a}_{\mathbf{p}_1}^{\dagger(s_1)} \bar{u}(\mathbf{p}_1, s_1) e^{i p_1 \cdot x} + \hat{b}_{\mathbf{p}_1}^{(s_1)} \bar{v}(\mathbf{p}_1, s_1) e^{-i p_1 \cdot x} \right), \quad (4.3a)$$

$$\hat{l}(x) = \int \frac{d^3\mathbf{p}_2}{\sqrt{(2\pi)^3 2E_{\mathbf{p}_2}}} \sum_{s_2=\pm 1} \left( \hat{a}_{\mathbf{p}_2}^{(s_2)} u(\mathbf{p}_2, s_2) e^{-i p_2 \cdot x} + \hat{b}_{\mathbf{p}_2}^{\dagger(s_2)} v(\mathbf{p}_2, s_2) e^{i p_2 \cdot x} \right) \quad (4.3b)$$

where  $u(\mathbf{p}_i, s_i)$ ,  $\bar{u}(\mathbf{p}_i, s_i)$ ,  $v(\mathbf{p}_i, s_i)$  and  $\bar{v}(\mathbf{p}_i, s_i)$  are the usual plane wave solutions to the Dirac equation [147] which satisfy the relations

$$\sum_{s=\pm 1} u(\mathbf{p}, s)\bar{u}(\mathbf{p}, s) = \not{p} + m, \quad \sum_{s=\pm 1} v(\mathbf{p}, s)\bar{v}(\mathbf{p}, s) = \not{p} - m. \quad (4.4)$$

Because we are assuming that the system is composed of a thermal reservoir and an ensemble of weakly interacting particles, one can assume that the initial state  $|I\rangle$  and the final state  $|F\rangle$  are

$$|I\rangle \equiv |i\rangle \otimes |0\rangle \otimes |0\rangle, \quad (4.5a)$$

$$|F\rangle \equiv |f\rangle \otimes |l(\mathbf{p}_1, s_1)\rangle \otimes |\bar{l}(\mathbf{p}_2, s_2)\rangle, \quad (4.5b)$$

<sup>4</sup>We are not considering non-vanishing chemical potential but this definition can be extended to that case.

<sup>4</sup>Strictly speaking, this factorization of the final and initial states is based on the fact that the Hilbert space for this quantum system is the direct product of the Hilbert space of the thermal reservoir times the Hilbert space of the weakly interacting particles, i.e.,  $\mathcal{H} = \mathcal{H}_{\text{therm.res.}} \otimes \mathcal{H}_{\text{weak part.}}$ .

where  $|l(\mathbf{p}_1, s_1)\rangle = \hat{a}_{\mathbf{p}_1}^{\dagger(s_1)}|0\rangle$  and  $|\bar{l}(\mathbf{p}_2, s_2)\rangle = \hat{b}_{\mathbf{p}_2}^{\dagger(s_2)}|0\rangle$ . The leading order contribution to the scattering amplitude  $T_{\text{fi}}$  comes from the ‘cross term’ at  $\mathcal{O}(e^2)$  and is

$$\begin{aligned}
T_{\text{fi}} &= \langle F | \int dt \hat{H}_I(t) | I \rangle, \\
&= \langle F | \int d^4y eQ \hat{A}_\mu(y) J_q^\mu(y) \int d^4x e \hat{A}_\mu(x) \hat{l}(x) \gamma^\mu \hat{l}(x) | I \rangle, \\
&= e^2 \tilde{e} \int d^4x \frac{e^{i(p_1+p_2)\cdot x}}{\sqrt{(2\pi)^3} 2E_{\mathbf{p}_1} (2\pi)^3 2E_{\mathbf{p}_2}} \bar{u}(\mathbf{p}_1, s_1) \gamma^\mu v(\mathbf{p}_2, s_2), \\
&\quad \times \int d^4y \int \frac{d^4R}{(2\pi)^4} \frac{e^{iR\cdot(x-y)}}{R^2} \langle f | \hat{J}_\mu^q(y) | i \rangle \\
&= e^2 \tilde{e} \frac{\bar{u}(\mathbf{p}_1, s_1) \gamma^\mu v(\mathbf{p}_2, s_2)}{\sqrt{(2\pi)^3} 2E_{\mathbf{p}_1} (2\pi)^3 2E_{\mathbf{p}_2}} \int d^4y \frac{e^{i(p_1+p_2)\cdot y}}{(p_1+p_2)^2} \langle f | \hat{J}_\mu^q(y) | i \rangle. \tag{4.6}
\end{aligned}$$

In the last expression, we explicitly use the propagator of the gauge field  $A_\mu(x)$  given by

$$\langle 0 | \mathcal{T} \{ A^\mu(x) A^\nu(y) \} | 0 \rangle = \int \frac{d^4R}{(2\pi)^4} e^{iR\cdot(x-y)} \frac{(-i)}{R^2} g^{\mu\nu},$$

where  $\mathcal{T}$  is the time-ordering symbol. Using Eq. (4.6), it is straightforward to calculate  $|T_{\text{fi}}|^2$

$$\begin{aligned}
|T_{\text{fi}}|^2 &= e^4 \tilde{e}^2 \frac{1}{(2\pi)^3 2E_{\mathbf{p}_1} (2\pi)^3 2E_{\mathbf{p}_2}} \bar{u}(\mathbf{p}_1, s_1) \gamma^\mu v(\mathbf{p}_2, s_2) \bar{v}(\mathbf{p}_2, s_2) \gamma^\nu u(\mathbf{p}_1, s_1) \\
&\quad \times \int d^4x \int d^4y \frac{e^{i(p_1+p_2)\cdot(y-x)}}{(p_1+p_2)^4} \langle f | \hat{J}_\mu^q(y) | i \rangle \langle i | \hat{J}_\nu^q(x) | f \rangle, \\
&= e^4 \tilde{e}^2 \frac{1}{(2\pi)^3 2E_{\mathbf{p}_1} (2\pi)^3 2E_{\mathbf{p}_2}} \bar{u}(\mathbf{p}_1, s_1) \gamma^\mu v(\mathbf{p}_2, s_2) \bar{v}(\mathbf{p}_2, s_2) \gamma^\nu u(\mathbf{p}_1, s_1) \\
&\quad Vt \int d^4y \frac{e^{iy\cdot(p_1+p_2)}}{(p_1+p_2)^4} \langle f | \hat{J}_\mu^q(0) | i \rangle \langle i | \hat{J}_\nu^q(y) | f \rangle. \tag{4.7}
\end{aligned}$$

By inserting the last expression into the definition of the differential dilepton rate (4.1) and summing over lepton spins  $s_1$  and  $s_2$ , we have <sup>5</sup>

$$\begin{aligned}
\frac{dN^{l^+l^-}}{d^4x d^3\mathbf{p}_1 d^3\mathbf{p}_2} &= \frac{4e^4 \tilde{e}^2}{(2\pi)^3 2E_{\mathbf{p}_1} (2\pi)^3 2E_{\mathbf{p}_2}} \frac{1}{(p_1+p_2)^4} [p_1^\mu p_2^\nu + p_1^\nu p_2^\mu - g^{\mu\nu}(p_1 \cdot p_2 + m^2)] \\
&\quad \times \int d^4y e^{iy\cdot(p_1+p_2)} \left( \sum_{i,f} \frac{1}{Z_{\text{sys}}} e^{-\beta E_i} \langle f | \hat{J}_\mu^q(0) | i \rangle \langle i | \hat{J}_\nu^q(y) | f \rangle \right), \\
&= \frac{4e^4 \tilde{e}^2}{(2\pi)^3 2E_{\mathbf{p}_1} (2\pi)^3 2E_{\mathbf{p}_2}} \frac{1}{(p_1+p_2)^4} [p_1^\mu p_2^\nu + p_1^\nu p_2^\mu - g^{\mu\nu}(p_1 \cdot p_2 + m^2)] \\
&\quad \times \int d^4y e^{iy\cdot(p_1+p_2)} \langle \hat{J}_\mu^q(0) \hat{J}_\nu^q(y) \rangle, \\
&= \frac{4e^4 \tilde{e}^2}{(2\pi)^3 2E_{\mathbf{p}_1} (2\pi)^3 2E_{\mathbf{p}_2}} \frac{1}{(p_1+p_2)^4} \\
&\quad \times [p_1^\mu p_2^\nu + p_1^\nu p_2^\mu - g^{\mu\nu}(p_1 \cdot p_2 + m^2)] \tilde{C}_{\mu\nu}^<(p_1+p_2), \tag{4.8}
\end{aligned}$$

<sup>5</sup>To get this result, we use this property

$$\begin{aligned}
\sum_{s_1, s_2} \bar{u}(\mathbf{p}_1, s_1) \gamma^\mu v(\mathbf{p}_2, s_2) \bar{v}(\mathbf{p}_2, s_2) \gamma^\nu u(\mathbf{p}_1, s_1) &= \text{Tr}[(\not{p}_1 + m) \gamma^\mu (\not{p}_2 - m) \gamma^\nu] \\
&= 4[p_1^\mu p_2^\nu + p_1^\nu p_2^\mu - g^{\mu\nu}(p_1 \cdot p_2 + m^2)].
\end{aligned}$$



where we identify the retarded current-current correlation function

$$\begin{aligned}\tilde{C}_{\mu\nu}^<(p_1 + p_2) &\equiv \int d^4y e^{iy \cdot (p_1 + p_2)} \langle \hat{J}_\mu^q(0) \hat{J}_\nu^q(y) \rangle \\ &= \int d^4y e^{iy \cdot (p_1 + p_2)} \left( \sum_{i,f} \frac{1}{Z_{\text{sys.}}} e^{-\beta E_i} \langle f | \hat{J}_\mu^q(0) | i \rangle \langle i | \hat{J}_\nu^q(y) | f \rangle \right).\end{aligned}\quad (4.9)$$

We will need to know the dependence of the differential dilepton rate on the total momentum of the lepton pairs,  $P = p_1 + p_2$ . To do that, we insert in the right side of Eq. (4.8)  $1 = \int d^4P \delta(P - p_1 - p_2)$  and integrate over  $p_1$  and  $p_2$ . By doing this procedure the final result for the differential dilepton rate is ( $\alpha = e^2/(4\pi)$ )

$$\begin{aligned}\frac{dN^{l^+l^-}}{d^4x d^4P} &= \frac{4\alpha^2 \tilde{e}^2}{3(2\pi)^3} \frac{\Theta(P^2 - 4m^2)}{P^4} \left(1 + \frac{2m^2}{P^2}\right) \left(1 - \frac{4m^2}{P^2}\right)^{1/2} (P^\mu P^\nu - P^2 g^{\mu\nu}) \tilde{C}_{\mu\nu}^<(P) \\ &= \frac{4\alpha^2 \tilde{e}^2}{3(2\pi)^3} L^{\mu\nu}(P) \tilde{C}_{\mu\nu}^<(P)\end{aligned}\quad (4.10)$$

where  $L_{\mu\nu}(P)$  is defined as

$$L^{\mu\nu}(P) = \Theta(P^2 - 4m^2) \left(1 + \frac{2m^2}{P^2}\right) \left(1 - \frac{4m^2}{P^2}\right)^{1/2} (P^\mu P^\nu - P^2 g^{\mu\nu}).\quad (4.11)$$

To obtain a more useful expression for the dilepton rate at leading order in  $\mathcal{O}(\alpha^2)$ , it is necessary to obtain the current-current correlation  $\tilde{C}_{\mu\nu}^<(P)$  from thermal field theory. In App. C.3 a more detailed calculation of  $\tilde{C}_{\mu\nu}^<(P)$  based on the imaginary time formalism is presented. The final result of the differential dilepton rate at leading order, after calculating the retarded current-current correlator  $\tilde{C}_{\mu\nu}^<(P)$ , is

$$\begin{aligned}\frac{dN^{l^+l^-}}{d^4x d^4P} &= \frac{4\alpha^2}{3(2\pi)^3} N_C \tilde{e}^2 \left(1 - \frac{4m^2}{P^2}\right)^{1/2} \left(1 + \frac{2m^2}{P^2}\right) \left(1 + \frac{2M^2}{P^2}\right) \\ &\quad \times \int \frac{d^3\mathbf{q}}{(2\pi)^3 2E_{\mathbf{q}}} \frac{d^3\bar{\mathbf{q}}}{(2\pi)^3 2E_{\bar{\mathbf{q}}}} (2\pi)^4 \delta^{(4)}(P - Q - \bar{Q}) n_F(E_{\mathbf{q}}) n_F(E_{\bar{\mathbf{q}}}).\end{aligned}\quad (4.12)$$

In the next section we show that at leading order this expression coincides with the result obtained using kinetic theory.

## 4.2. Medium dilepton production rate from kinetic theory

To compute corrections associated with the collective dynamics of the medium to observables one should make use of HTL effective theory [148, 69, 68]. Nowadays the connection between hard thermal loops and classical kinetic theory is well known [71, 72]. This connection basically establishes that at leading order in the coupling constant, the effective action obtained from hard thermal loops is exactly the same one calculated from classical kinetic theory. In practical terms, this equivalence indicates that medium corrections to observables computed by either hard thermal loop techniques or classical kinetic theory are the same. In App. C.3, we present the equivalence between the two treatments when there are no corrections to the internal lines of the propagators. A more complete and detailed calculation where this equivalence is proven for the case of dilepton production including HTL corrections to the internal lines of the propagators can be found in Ref. [146]. In this work dilepton yields are calculated based on the kinetic theory approach.

For simplicity we are going to consider a highly dense plasma with non-vanishing baryon number. Under this assumption, the content of quarks (antiquarks) in the system is described by a distribution function  $f_{q(\bar{q})}(x, p)$ . We assume that the distribution function of the quarks is the same as the antiquarks.<sup>6</sup> In the kinetic theory language, the dilepton production rate is roughly the square of the density of quarks times the cross section times the relative velocity. From this approach, the dilepton emission rate is given by

$$\frac{dN^{l^+l^-}}{d^4x d^4P} = \int \frac{d^3q}{(2\pi)^3 2E_{\mathbf{q}}} \frac{d^3\bar{q}}{(2\pi)^3 2E_{\bar{\mathbf{q}}}} \frac{d^3p_{l^+}}{(2\pi)^3 2E_{\mathbf{p}_{l^+}}} \frac{d^3p_{l^-}}{(2\pi)^3 2E_{\mathbf{p}_{l^-}}} n_F(E_{\mathbf{q}}) n_F(E_{\bar{\mathbf{q}}}) \times |\mathcal{M}|_{q\bar{q} \rightarrow l^+l^-}^2 (2\pi)^4 \delta^{(4)}(q + \bar{q} - p_{l^+} - p_{l^-}) \delta^{(4)}(P - Q - \bar{Q}), \quad (4.13)$$

where  $n_F(E_{\mathbf{p}}) = (e^{\beta E_{\mathbf{p}}} + 1)^{-1}$  is the occupation probability for fermions. The Pauli blocking factor of the dilepton pair has been neglected in the above equation, this is because we are interested at high energies where the quantum nature of the outgoing lepton pair is not important. The cross section of the quark annihilation process  $q + \bar{q} \rightarrow \gamma^* \rightarrow l^+ + l^-$  can be expressed in terms of the scattering amplitude  $\mathcal{M}$  [147]

$$\sigma_{q\bar{q}}^{l^+l^-} = \frac{1}{v_{q\bar{q}}} \int \frac{d^3p_{l^+}}{(2\pi)^3 2E_{\mathbf{p}_{l^+}}} \frac{d^3p_{l^-}}{(2\pi)^3 2E_{\mathbf{p}_{l^-}}} |\mathcal{M}|_{q\bar{q} \rightarrow l^+l^-}^2 (2\pi)^4 \delta^{(4)}(q + \bar{q} - p_{l^+} - p_{l^-}), \quad (4.14)$$

where  $v_{q\bar{q}}$  is the relative velocity of the dilepton pair defined as

$$v_{q\bar{q}} = \frac{((q \cdot \bar{q})^2 - m_q^4)^{1/2}}{E_q E_{\bar{\mathbf{q}}}}. \quad (4.15)$$

This allows us to rewrite Eq. (4.13) as

$$\frac{dN^{l^+l^-}}{d^4x d^4P} = \int \frac{d^3q}{(2\pi)^3 2E_{\mathbf{q}}} \frac{d^3\bar{q}}{(2\pi)^3 2E_{\bar{\mathbf{q}}}} n_F(E_{\mathbf{q}}) n_F(E_{\bar{\mathbf{q}}}) v_{q\bar{q}} \sigma_{q\bar{q}}^{l^+l^-} \delta^{(4)}(P - Q - \bar{Q}). \quad (4.16)$$

To observe the equivalence of this expression with the dilepton rate obtained from thermal field theory (Eq. (4.12)) one should replace the leading order value of  $\sigma_{q\bar{q}}^{l^+l^-}$  and evaluate  $v_{q\bar{q}}$  in the center of mass frame where the total momentum of the dilepton pair vanishes  $\mathbf{p} = 0$ .

### 4.3. Sources of high-energy dileptons

To disentangle a QGP signal from total experimental dilepton production is a non-trivial issue. Lepton pairs are also produced in the high  $p_T, M$  region from the Drell-Yan process, jet conversion and heavy flavour decay.

#### 4.3.1. Drell-Yan dileptons

In the region of large invariant mass dilepton yields have a significant contribution coming from the Drell-Yan process  $A + A \rightarrow l^+l^- + X$  and thus form one of principal background sources to dileptons emitted from QGP. The Drell-Yan process consists of the annihilation of a quark from one of the incoming nucleus  $A$  and an antiquark from the other incoming nucleus, this produces a virtual photon which subsequently decays into a lepton pair. The differential yield of such lepton pairs produced in  $A + A$  collisions is obtained by an incoherent sum of the contributions from independent nucleon-nucleon collisions. The total Drell-Yan yield is the sum of the direct (which is the Compton

<sup>6</sup>This is an assumption based on chemical equilibrium between quarks and antiquarks which we consider valid in our work. However, it is possible to have situations where the distribution functions of quarks and antiquarks is unequal and this issue plays an important role in the description of the physics. See Sect. 18.2 of Ref. [149].

and annihilation process of two incoming partons) and the Bremsstrahlung contributions,  $\sigma_{\text{DY}} = \sigma_{\text{direct}} + \sigma_{\text{frag}}$  [146, 150, 151]. The final yield from Drell-Yan is given by [146]

$$\begin{aligned} \frac{dN_{\text{DY}}}{dM^2 dy_d} &= \frac{2\langle N_{\text{coll}} \rangle}{\sigma_{\text{in}}} \int_{p_{T\text{cut}}}^{\infty} dp_T p_T \left[ K_{\text{dir}} \frac{d\sigma_{\text{direct}}}{dM^2 dy_d dp_T^2} + K_{\text{frag}} \frac{d\sigma_{\text{frag}}}{dM^2 dy_d dp_T^2} \right] \\ &\times P(|y_{e^\pm}| \leq y_{\text{cut}}, p_T). \end{aligned} \quad (4.17)$$

where  $\frac{d\sigma_{\text{direct}}}{dM^2 dy_d dp_T^2}$  is the direct contribution of two nuclei and  $\frac{d\sigma_{\text{frag}}}{dM^2 dy_d dp_T^2}$  is the fragmentation contribution. Their explicit functional forms are given in Ref. [146].  $K_{\text{dir}}$  and  $K_{\text{frag}}$  are phenomenological factors introduced with the goal to take into account higher order corrections. The function  $P(|y_{e^\pm}| \leq y_{\text{cut}}, p_T)$  accounts for the probability for a virtual photon with momentum  $p_T$  at midrapidity to emit two leptons with rapidities  $|y_{e^\pm}| \leq y_{\text{cut}}$ ; in practical terms, this probability helps to constrain the phase space distribution of the dilepton pairs in accordance with the experimental arrangement.

### 4.3.2. Heavy flavour decays

One of the most difficult significant background sources that obscures medium dilepton production from the QGP is the decay of open charm and bottom mesons. During the initial hard scattering  $c\bar{c}(b\bar{b})$  pairs are produced which fragment into  $D(B)$  and  $\bar{D}(\bar{B})$  mesons. In phenomenological studies, only correlated decay is considered, which occurs when a positron coming from the semileptonic decay of a  $D(B)$  is measured together with the electron from the semileptonic decay of a  $\bar{D}(\bar{B})$ , i.e., one calculates the rate for the reaction  $D\bar{D} \rightarrow e^+e^- + \nu\bar{\nu} + X$ . Details of how to perform such calculations from perturbative QCD are found in Ref. [152].

### 4.3.3. Jet conversion

One of the great discoveries at RHIC is the large production of high energy quark and gluon jets which lose energy due to the interactions with the QGP. This is the celebrated phenomenon of jet-quenching. Quark jets can be formed over a scale of time which is even smaller than the QGP formation time for large values of transverse momentum. This quark (antiquark) jet has the probability to annihilate with other thermal antiquark (quark) while is passing the medium or undergo a Compton scattering with a thermal gluon and lead to a production of a high energy virtual photon which decays into a lepton pair. This calculation involves the evolution of the thermal distribution of the jets, which can be calculated using the perturbative formalism of Arnold, Moore and Yaffe [134, 137, 153].



## 5. Dilepton production from an anisotropic quark-gluon plasma

Many of us were worried about how difficult it seemed to make progress in the state that physics was in then. Some people thought that the path to understanding the strong interactions led through the study of the analytic structure of scattering amplitudes as functions of several kinematic variables. That approach really depressed me because I knew that I could never understand the theory of more than one complex variable. So I was pretty worried about how I could do research working in this mess. So the moral of my tale is not to despair at the formidable difficulties that you face in getting started in today's research... You'll have a hard time, but you'll do OK.

---

*To the Postdocs, Physics Today* **60**: 58, 2007.  
Steven Weinberg.

In this chapter we calculate leading-order dilepton yields from a quark-gluon plasma which has a time-dependent anisotropy in momentum space in the central and forward rapidity region. In the central region ( $y = 0$ ), two phenomenological models are constructed for the proper time dependence of the parton hard momentum scale,  $p_{\text{hard}}$ , and the plasma anisotropy parameter,  $\xi$ . The models describe the transition of the plasma from its initial non-equilibrium state to an isotropic thermalized state. We find for both cases that by fixing either the initial conditions or final pion multiplicity, high-energy dilepton production is modified by pre-equilibrium emission. For the later case, the dependence of the resulting spectra on the assumed plasma isotropization time is reduced.

We extend the calculation of the dilepton yields to the forward rapidity region ( $y \neq 0$ ). In addition to the temporal evolution of the plasma anisotropy parameter,  $\xi$ , and the hard momentum scale,  $p_{\text{hard}}$ , we include the rapidity dependence of  $p_{\text{hard}}$ . The model interpolates between 0+1 dimensional collisionally-broadened expansion at early times and 0+1 dimensional ideal hydrodynamic expansion at late times. Using this model, we find that at LHC energies, forward high-energy medium dilepton production would be suppressed by up to a factor of 3 if one assumes an isotropization/thermalization time of 2 fm/c.

Given sufficiently precise experimental data, it may be possible to use dilepton yields in the forward and central rapidity region to experimentally determine the time of onset of locally isotropic hydrodynamic expansion of the quark-gluon plasma as produced in ultrarelativistic heavy-ion collisions.

The results presented in this chapter are based on the publications:

1. Mauricio Martinez and Michael Strickland, *Measuring QGP thermalization time with dileptons*, Phys. Rev. Lett. **100**: 102301, 2008 [82].
2. Mauricio Martinez and Michael Strickland, *Pre-equilibrium dilepton production from an anisotropic quark-gluon plasma*, Phys. Rev. C **78**: 034917, 2008 [83].
3. Mauricio Martinez and Michael Strickland, *Suppression of forward dilepton production from an anisotropic quark-gluon plasma*, Eur. Phys. J. C **61**: 905-913, 2009 [84].

## 5.1. Differential dilepton rate

From relativistic kinetic theory, the differential dilepton rate  $dN^{l^+l^-}/d^4Xd^4P \equiv dR^{l^+l^-}/d^4P$  (i.e. the number of dileptons produced per space-time volume and four dimensional momentum-space volume) at leading order in the electromagnetic coupling,  $\alpha$ , is given by [154, 155, 156]

$$\frac{dR^{l^+l^-}}{d^4P} = \int \frac{d^3\mathbf{p}_1}{(2\pi)^3} \frac{d^3\mathbf{p}_2}{(2\pi)^3} f_q(\mathbf{p}_1) f_{\bar{q}}(\mathbf{p}_2) v_{q\bar{q}} \sigma_{q\bar{q}}^{l^+l^-} \delta^{(4)}(P - p_1 - p_2), \quad (5.1)$$

where  $f_{q,\bar{q}}$  is the phase space distribution function of the medium quarks (anti-quarks),  $v_{q\bar{q}}$  is the relative velocity between quark and anti-quark and  $\sigma_{q\bar{q}}^{l^+l^-}$  is the total cross section

$$\sigma_{q\bar{q}}^{l^+l^-} = \frac{4\pi}{3} \frac{\alpha^2}{M^2} \left(1 + \frac{2m_l^2}{M^2}\right) \left(1 - \frac{4m_l^2}{M^2}\right)^{1/2}, \quad (5.2)$$

with  $m_l$  and  $M$  being the lepton mass and the center-of-mass energy respectively. Since we will be considering high-energy dilepton pairs with center-of-mass energies much greater than the dilepton mass we can safely ignore the finite dilepton mass corrections and use simply  $\sigma_{q\bar{q}}^{l^+l^-} = 4\pi\alpha^2/3M^2$ . In addition, to very good approximation, we can assume that the distribution function of quarks and anti-quarks is the same,  $f_{\bar{q}} = f_q$ .

In this work we will assume azimuthal symmetry of the matter in momentum-space so that the anisotropic quark/anti-quark phase distributions can be obtained from an arbitrary isotropic phase space distribution by squeezing ( $\xi > 0$ ) or stretching ( $\xi < 0$ ) along one direction in the momentum space using the ansatz

$$f_{q,\bar{q}}(\mathbf{p}, \xi, p_{\text{hard}}) = f_{q,\bar{q}}^{\text{iso}}(\sqrt{\mathbf{p}^2 + \xi(\mathbf{p} \cdot \hat{\mathbf{n}})^2}, p_{\text{hard}}), \quad (5.3)$$

where  $p_{\text{hard}}$  is the hard momentum scale,  $\hat{\mathbf{n}}$  is the direction of the anisotropy and  $\xi > -1$  is a parameter that reflects the strength and type of anisotropy. In general,  $p_{\text{hard}}$  is related to the average momentum in the partonic distribution function. In isotropic equilibrium, where  $\xi=0$ ,  $p_{\text{hard}}$  can be identified with the plasma temperature  $T$ . To give another specific example, in the case of 0+1 dimensional free-streaming discussed in Sec. 5.2.2  $p_{\text{hard}}$  is given by the initial ‘‘temperature’’  $T_0$ .

For general  $\xi$  we split the delta function in Eq. (5.1) such that we can perform the  $\mathbf{p}_2$  integration

$$\begin{aligned} \frac{dR^{l^+l^-}}{d^4P} &= \frac{5\alpha^2}{72\pi^5} \int \frac{d^3\mathbf{p}_1}{E_{\mathbf{p}_1}} \frac{d^3\mathbf{p}_2}{E_{\mathbf{p}_2}} f_q(\mathbf{p}_1, p_{\text{hard}}, \xi) f_{\bar{q}}(\mathbf{p}_2, p_{\text{hard}}, \xi) \delta^{(4)}(P - p_1 - p_2), \\ &= \frac{5\alpha^2}{72\pi^5} \int \frac{d^3\mathbf{p}_1}{E_{\mathbf{p}_1} E_{\mathbf{p}_2}} f_q(\mathbf{p}_1, p_{\text{hard}}, \xi) f_{\bar{q}}(\mathbf{P} - \mathbf{p}_1, p_{\text{hard}}, \xi) \delta(E - E_{\mathbf{p}_1} - E_{\mathbf{p}_2}) \Big|_{\mathbf{p}_2=\mathbf{P}-\mathbf{p}_1} \end{aligned} \quad (5.4)$$

Choosing spherical coordinates with the anisotropy vector  $\hat{\mathbf{n}}$  defining the  $z$  axis, we can write

$$\begin{aligned} \mathbf{p}_1 &= p_1(\sin\theta_{p_1} \cos\phi_{p_1}, \sin\theta_{p_1} \sin\phi_{p_1}, \cos\theta_{p_1}), \\ \mathbf{P} &= P(\sin\theta_P \cos\phi_P, \sin\theta_P \sin\phi_P, \cos\theta_P). \end{aligned} \quad (5.5)$$

It is then possible to reexpress the remaining delta function as

$$\delta(E - E_{\mathbf{p}_1} - E_{\mathbf{p}_2}) = 2(E - p_1) \chi^{-1/2} \Theta(\chi) \sum_i^2 \delta(\phi_i - \phi_{p_1}), \quad (5.6)$$

with  $\chi \equiv 4P^2 p_1^2 \sin^2\theta_P \sin^2\theta_{p_1} - (2p_1(E - P \cos\theta_P \cos\theta_{p_1}) - M^2)^2$ . The angles  $\phi_i$  are defined as the solutions to the following transcendental equation

$$\cos(\phi_i - \phi_{p_1}) = \frac{2 p_1 (E - P \cos \theta_P \cos \theta_{p_1}) - M^2}{2 P p_1 \sin \theta_P \sin \theta_{p_1}}. \quad (5.7)$$

We point out that there are two solutions to Eq. (5.7) when  $\chi > 0$ . After these substitutions and expanding out the phase space integrals, we obtain

$$\begin{aligned} \frac{dR^{l^+l^-}}{d^4P} &= \frac{5\alpha^2}{18\pi^5} \int_{-1}^1 d(\cos \theta_{p_1}) \int_{a_+}^{a_-} \frac{dp_1}{\sqrt{\chi}} p_1 f_q \left( \sqrt{\mathbf{p}_1^2 (1 + \xi \cos^2 \theta_{p_1})}, p_{\text{hard}} \right) \\ &\times f_{\bar{q}} \left( \sqrt{(\mathbf{E} - \mathbf{p}_1)^2 + \xi (\mathbf{p}_1 \cos \theta_{p_1} - \mathbf{P} \cos \theta_P)^2}, p_{\text{hard}} \right), \end{aligned} \quad (5.8)$$

with

$$a_{\pm} = \frac{M^2}{2(E - P \cos(\theta_P \pm \theta_{p_1}))}. \quad (5.9)$$

Note that when  $\xi = 0$ , the limit of isotropic dilepton production is recovered trivially. Also note that as  $\xi$  increases we expect the differential dilepton rate to decrease since for fixed  $p_{\text{hard}}$  the increasing oblateness of the parton distribution functions causes the effective parton density to decrease

$$\begin{aligned} n(\xi, p_{\text{hard}}) &= \int \frac{d^3p}{(2\pi)^3} f_q(\sqrt{\mathbf{p}^2 + \xi (\mathbf{p} \cdot \hat{\mathbf{n}})^2}, p_{\text{hard}}), \\ &= \frac{n(\xi = 0, p_{\text{hard}})}{\sqrt{1 + \xi}} \propto \frac{p_{\text{hard}}^3}{\sqrt{1 + \xi}}. \end{aligned} \quad (5.10)$$

In order to evaluate the anisotropic dilepton rate it is necessary to perform the remaining two integrations in Eq. (5.8) numerically. In Fig. 5.1 we plot the resulting differential dilepton rate as a function of transverse momentum and invariant mass for  $\xi \in \{0, 1, 10, 100\}$ . One can see the effect of increasing  $\xi$  for fixed  $p_{\text{hard}}$ , namely that the dilepton production rate decreases due, primarily, to the density effect mentioned above.

## 5.2. Dilepton yields from the pre-equilibrated stage: central rapidity region

In this section we calculate high-energy dilepton yields in the central rapidity region as a function of the invariant mass and transverse momentum from an anisotropic QGP. Knowing the differential dilepton rate (5.8) is not enough to make a phenomenological prediction for the expected dilepton yields, it is still required to model the space-time evolution of  $p_{\text{hard}}$  and  $\xi$ . Once this is done, one can obtain the dileptons yields integrating Eq. (5.8) over the space-time volume.

The dilepton production as a function of the invariant mass and transverse momentum is given by, respectively

$$\frac{dN^{l^+l^-}}{dM^2 dy} = \pi R_T^2 \int d^2p_T \int_{\tau_0}^{\tau_f} \int_{-\infty}^{\infty} \frac{dR^{l^+l^-}}{d^4P} \tau d\tau d\eta, \quad (5.11a)$$

$$\frac{dN^{l^+l^-}}{d^2p_T dy} = \pi R_T^2 \int dM^2 \int_{\tau_0}^{\tau_f} \int_{-\infty}^{\infty} \frac{dR^{l^+l^-}}{d^4P} \tau d\tau d\eta, \quad (5.11b)$$

where  $R_T = 1.2 A^{1/3}$  fm is the radius of the nucleus in the transverse plane. These expressions are evaluated in the center-of-mass (CM) frame while the differential dilepton rate is calculated in the

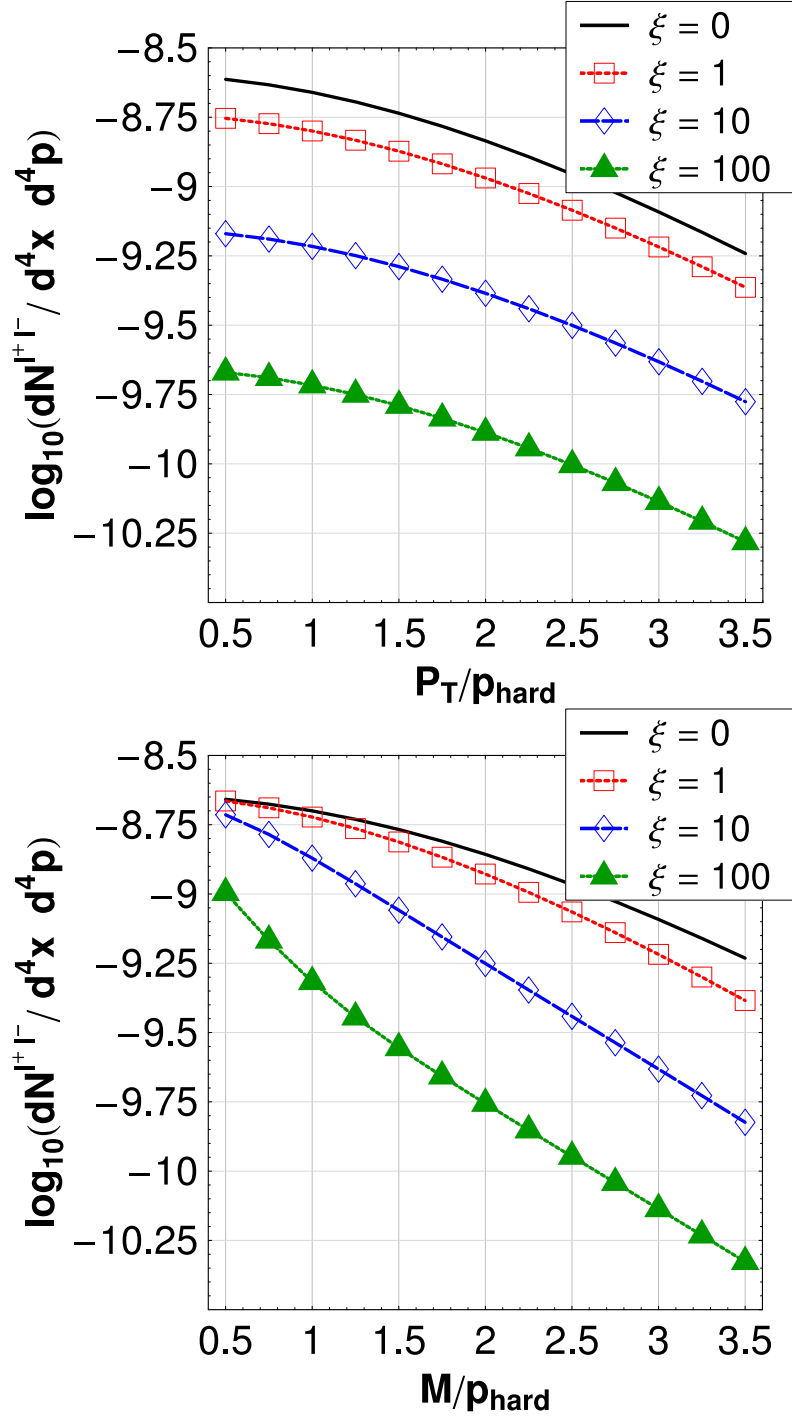


Figure 5.1.: The differential dilepton rate as a function of transverse momentum (left) and invariant mass (right). For the invariant mass dependence (left) we fixed  $p_T = 3$  GeV and for the transverse momentum dependence (right) we fixed  $M = 3$  GeV. In both cases  $p_{\text{hard}} = 1$  GeV and rapidity  $y = 0$ .



local rest frame (LR) of the emitting region. Taking this into account, the dilepton pair energy has to be understood as  $E_{LR} = p_T \cosh(y-\eta)$  in the differential dilepton rate  $dR/d^4P$ . Additionally, in Eqs. (5.11) we have assumed that there is only longitudinal expansion of the system. Since at early times the transverse expansion is small compared to the longitudinal expansion, one can ignore it. Some studies have suggested that the influence of the transverse expansion on the space-time evolution becomes phenomenologically important around 2.7 fm/c [157], therefore, our approximation is valid for describing the early-time behaviour we are interested in. Substituting Eq. (5.8) into Eqs. (5.11) we obtain the dilepton spectrum including the effect of a time-dependent momentum anisotropy.

Note that we have not included the next-to-leading order (NLO) corrections to the dilepton rate due to the complexity of these contributions for finite  $\xi$ . These affect dilepton production for isotropic systems for  $E/T \lesssim 1$  [158, 137, 159, 146]. In the regions of phase space where there are large NLO corrections, we will apply  $K$ -factors to our results as indicated. These  $K$ -factors are determined by taking the ratio between NLO and LO calculation for an isotropic plasma, therefore, in this work we are implicitly assuming that the  $K$ -factor will be the same for an anisotropic plasma.

### 5.2.1. Space-Time Models

In this section we present two new models for 0+1 dimensional non-equilibrium time-evolution of the QGP and review the cases of 0+1 dimensional free-streaming and 0+1 dimensional hydrodynamic expansion. In all cases considered below the number density will obey  $n(\tau) \propto (\tau_0/\tau)$  in its asymptotic regions.<sup>1</sup> This results in all cases from the assumption that the total particle number is fixed while the size of the box containing the plasma is expanding at the speed of light in the longitudinal direction (1d expansion).

In each case below we will be required to specify a proper time dependence of the hard-momentum scale,  $p_{\text{hard}}$ , and anisotropy parameter,  $\xi$ , which is consistent with this scaling for  $\tau \ll \tau_{\text{iso}}$  and  $\tau \gg \tau_{\text{iso}}$ . Before proceeding, however, it is useful to note some general relations. Firstly we remind the reader that the plasma anisotropy parameter is related to the average longitudinal and transverse momentum of the plasma partons via the relation

$$\xi = \frac{\langle p_T^2 \rangle}{2\langle p_L^2 \rangle} - 1. \quad (5.12)$$

Therefore, we can immediately see that for an isotropic plasma that  $\xi = 0$ , and for an oblate plasma which has  $\langle p_T^2 \rangle > 2\langle p_L^2 \rangle$  that  $\xi > 0$ .

Secondly we note that given any anisotropic phase space distribution of the form specified in Eq. (6.26) the local energy density can be factorized via a change of variables to give

$$\begin{aligned} \mathcal{E}(p_{\text{hard}}, \xi) &= \int \frac{d^3\mathbf{p}}{(2\pi)^3} p f_{\text{iso}}(\sqrt{\mathbf{p}^2 + \xi(\mathbf{p} \cdot \hat{\mathbf{n}}^2)}, p_{\text{hard}}), \\ &= \mathcal{E}_0(p_{\text{hard}}) \mathcal{R}(\xi), \end{aligned} \quad (5.13)$$

where  $\mathcal{E}_0$  is the initial local energy density deposited in the medium at  $\tau_0$  and

$$\mathcal{R}(\xi) \equiv \frac{1}{2} \left( \frac{1}{1+\xi} + \frac{\arctan \sqrt{\xi}}{\sqrt{\xi}} \right). \quad (5.14)$$

We note that  $\lim_{\xi \rightarrow 0} \mathcal{R}(\xi) = 1$  and  $\lim_{\xi \rightarrow \infty} \mathcal{R}(\xi) = 1/\sqrt{\xi}$ .

<sup>1</sup>The interpolating models will only obey this relation outside of a region of order  $\gamma^{-1}\tau_{\text{iso}}$  around  $\tau_{\text{iso}}$  where the transition between different types of expansion takes place. In the transition region  $n$  will increase due to non-equilibrium effects as we discuss later in the text.

### 5.2.2. Asymptotic Limits of the Anisotropic Phase Space Distribution

Before presenting our proposed interpolating models we review previous calculations for the free streaming and hydrodynamic expansion cases [154, 160, 161] and show how to determine our anisotropic phase space distribution function parameters,  $p_{\text{hard}}$  and  $\xi$ , in these two cases.

#### 0+1 Dimensional Ideal Hydrodynamical Expansion Limit

We first consider the limiting case that  $\tau_{\text{iso}} = \tau_0$  so that the plasma is assumed to be “instantaneously” thermal and isotropic and undergoes ideal 0+1 dimensional hydrodynamical expansion throughout its evolution. In ideal hydrodynamical evolution using the boost-invariant 0+1 Bjorken model [19] we can identify  $p_{\text{hard}}$  with the temperature and the anisotropy parameter vanishes by assumption,  $\xi = 0$ . Due to the fact that  $\xi = 0$  the distribution function for highly relativistic particles will depend only on the ratio between the energy and temperature,  $f_{\text{hydro}}(p, x) = f(E/T(\tau))$  with  $E = (p_T^2 + p_L^2)^{1/2}$ . In this case the number density, hard scale (temperature), energy density, and anisotropy parameter obey the following

$$n(\tau) = n_0 \left( \frac{\tau_0}{\tau} \right), \quad (5.15a)$$

$$p_{\text{hard}}(\tau) = T(\tau) = T_0 \left( \frac{\tau_0}{\tau} \right)^{\frac{1}{3}}, \quad (5.15b)$$

$$\mathcal{E}(\tau) = \mathcal{E}_0 \left( \frac{\tau_0}{\tau} \right)^{\frac{4}{3}}, \quad (5.15c)$$

$$\xi(\tau) = 0. \quad (5.15d)$$

In order to obtain an analytic result for the differential dilepton rate which is applicable at high energies one can approximate the quark and anti-quark Fermi-Dirac distributions by Boltzmann distributions and integrate Eq. (5.8) analytically. In this case it is also possible to perform the necessary integration of the rate over the plasma space-time evolution analytically [154, 161] to obtain

$$\frac{dN_{\text{hydro}}^{l+l^-}}{dy dM^2} = \frac{5\alpha^2}{6\pi^2} \frac{1}{M^4} R_T^2 T_0^6 \tau_0^2 \left[ H\left(\frac{M}{T_0}\right) - H\left(\frac{M}{T_c}\right) \right], \quad (5.16a)$$

$$\frac{dN_{\text{hydro}}^{l+l^-}}{dM^2 d^2p_T dy} = \frac{5\alpha^2}{24\pi^3} R_T^2 \tau_0^2 \left( \frac{T_0}{m_T} \right)^6 \left[ G\left(\frac{m_T}{T_0}\right) - G\left(\frac{m_T}{T_c}\right) \right], \quad (5.16b)$$

where  $H(z) = z^2(8+z^2)K_0(z) + 4zK_1(z)(4+z^2)$ ,  $G(z) = z^3(8+z^2)K_3(z)$  and  $m_T = \sqrt{M^2 + p_T^2}$ . As a check of our numerics we have verified that numerical integration of our dilepton rate given in Eq. (5.8) over space-time via Eqs. (5.11) reproduces this analytic result in the limit  $\tau_{\text{iso}} \rightarrow \tau_0$  and  $\xi = 0$ .

#### 0+1 Dimensional Free Streaming Limit

As another limiting case we can assume instead that our 0+1 dimensional expanding plasma is non-interacting. If this were true then the system would simply undergo 0+1 dimensional free-streaming expansion [154, 160]. Since, in this case, the system would never become truly thermal or isotropic this corresponds to taking the opposite limit from the one we took in the previous subsection, namely we will now take the limit  $\tau_{\text{iso}} \rightarrow \infty$ .

In the free streaming case, the distribution function is a solution of the collisionless Boltzmann equation

$$p \cdot \partial_x f_{\text{f.s.}}(p, x) = 0, \quad (5.17)$$

where the subscript f.s. indicates that this is the free-streaming solution. In this work we will also assume that the distribution function is isotropic at the formation time,  $\tau = \tau_0$

$$f_{\text{f.s.}}(p, x) \Big|_{\tau=\tau_0} = f \left( \frac{\sqrt{p_T^2 + p_L^2}}{p_{\text{hard}}} \right), \quad (5.18)$$

where  $p_T$  is the transverse momentum,  $p_L$  is the longitudinal momentum and  $p_{\text{hard}}$  is the hard momentum scale at  $\tau_0$ . The typical hard momentum scale of particles undergoing 0+1 dimensional free streaming expansion is constant in time. In the case of indefinite free-streaming expansion the system never reaches thermal equilibrium and so the system strictly cannot have a temperature associated with it; however, since our assumed distribution function is isotropic at  $\tau = \tau_0$ , we can identify the initial ‘‘temperature’’ of the system,  $T_0$ , with the hard momentum scale  $p_{\text{hard}}$  when comparing hydrodynamic and free streaming expansion.

Eq. (5.17) has a family of solutions which are boost invariant along the  $z$  (beam) axis

$$f_{\text{f.s.}}(p, x) = f(p_T, p_L t - E z). \quad (5.19)$$

Therefore, the functional dependence of the distribution function for the free streaming case is of the form

$$f_{\text{f.s.}}(p, x) = f \left( \frac{\sqrt{p_T^2 + (p_L t - E z)^2 / \tau_0^2}}{T_0} \right). \quad (5.20)$$

This distribution function can be simplified if we change to co-moving coordinates

$$p_L = p_T \sinh y, \quad E = p_T \cosh y, \quad (5.21a)$$

$$z = \tau \sinh \eta, \quad t = \tau \cosh \eta, \quad (5.21b)$$

where, as usual,  $y$  is the momentum-space rapidity,  $\tau$  is the proper time, and  $\eta$  is the space-time rapidity. In terms of these variables one obtains

$$f_{\text{f.s.}}(p, x) = f \left( \frac{p_T}{T_0} \sqrt{1 + \frac{\tau^2}{\tau_0^2} \sinh^2(y - \eta)} \right). \quad (5.22)$$

Note that in the case of indefinite free-streaming at late times the quark and anti-quark longitudinal momentum are highly red-shifted reducing late time emission of high-energy dilepton pairs.

As written in Eq. (6.27) the anisotropy parameter is related with the average transverse and longitudinal momenta of the partons. The average momentum-squared values appearing there are defined in the standard way

$$\langle p_{T,L}^2 \rangle \equiv \frac{\int d^3\mathbf{p} p_{T,L}^2 f(p, x)}{\int d^3\mathbf{p} f(p, x)}. \quad (5.23)$$

Using the 0+1 dimensional free streaming distribution given in Eq. (5.22) and transforming to co-moving coordinates defined in (5.21) so that  $d^3\mathbf{p} \rightarrow p_T^2 \cosh y dp_T dy$  we obtain

$$\langle p_T^2 \rangle_{\text{f.s.}} \propto 2 T_0^2, \quad (5.24a)$$

$$\langle p_L^2 \rangle_{\text{f.s.}} \propto T_0^2 \frac{\tau_0^2}{\tau^2}. \quad (5.24b)$$

Inserting these expressions into the general expression for  $\xi$  given in Eq. (6.27) one obtains  $\xi_{\text{f.s.}}(\tau) = \tau^2 / \tau_0^2 - 1$ . With this in hand we can also determine proper time dependence of the energy density in the free-streaming case by substituting this expression for  $\xi$  into Eq. (5.13),  $\mathcal{E}_{\text{f.s.}}(\tau) = \mathcal{E}_0 \mathcal{R}(\xi_{\text{f.s.}}(\tau))$ .

At early times one must use the full expression given by Eq. (5.13); however, at late times one can expand this result to obtain  $\mathcal{E}_{\text{f.s.}}(\tau) \propto \tau_0/\tau$  as expected for a 0+1 free streaming plasma [162].

Summarizing, one finds in the 0+1 free streaming case that in the limit  $\tau \gg \tau_0$

$$n(\tau) = n_0 \left( \frac{\tau_0}{\tau} \right), \quad (5.25a)$$

$$p_{\text{hard}}(\tau) = p_{\text{hard}}(\tau = 0) = T_0, \quad (5.25b)$$

$$\mathcal{E}(\tau) = \mathcal{E}_0 \left( \frac{\tau_0}{\tau} \right), \quad (5.25c)$$

$$\xi(\tau) = \frac{\tau^2}{\tau_0^2} - 1. \quad (5.25d)$$

With the distribution function given by Eq. (5.22), the dilepton spectrum can be calculated. As a function of the invariant mass  $M$ , one obtains [83]

$$\begin{aligned} \frac{dN_{\text{f.s.}}^{l^+l^-}}{dydM^2} &= \frac{5\alpha^2}{72\pi^3} R_T^2 M^2 \tau_0^2 \int x_1 x_2 dx_1 dx_2 dy_1 dy_2 d(\tau/\tau_0)^2 \\ &\times [(x_1 x_2)^2 - (x_1 x_2 \cosh(y_1 - y_2) - 1/2)^2]^{-1/2} \\ &\times f_{\text{f.s.}}^q \left( \frac{M}{T_0} x_1 \sqrt{1 + \left( \frac{\tau}{\tau_0} \right)^2 \sinh^2 y_1} \right) f_{\text{f.s.}}^{\bar{q}} \left( \frac{M}{T_0} x_2 \sqrt{1 + \left( \frac{\tau}{\tau_0} \right)^2 \sinh^2 y_2} \right). \end{aligned} \quad (5.26)$$

In the last expression, the integration is over all  $x_i$  from 0 to  $+\infty$  and over all  $y_i$  from  $-\infty$  to  $\infty$  subject to the constraint

$$\frac{1}{\cosh(y_1 - y_2) + 1} \leq 2x_1 x_2 \leq \frac{1}{\cosh(y_1 - y_2) - 1}.$$

As a function of the transverse momentum,  $p_T$ , the dilepton production using free streaming case we obtain<sup>2</sup>

$$\begin{aligned} \frac{dN_{\text{f.s.}}^{l^+l^-}}{dM^2 d^2 p_T dy} &= \frac{5\alpha^2}{36\pi^4} R_T^2 \tau_0^2 \int_{x_+}^{x_-} x dx dy_1 dy_2 d(\tau/\tau_0)^2 f_{\text{f.s.}}^q \left( \frac{x M}{T_0} \sqrt{1 + \left( \frac{\tau}{\tau_0} \right)^2 \sinh^2 y_1} \right) \\ &\times f_{\text{f.s.}}^{\bar{q}} \left( \frac{M}{T_0} \left( \left( \frac{m_T}{M} \right)^2 + x^2 - 2 \frac{m_T}{M} x \cosh(y_1 - y_2) + \left( \frac{\tau}{\tau_0} \right)^2 \left( \frac{m_T}{M} \sinh y_2 - x \sinh y_1 \right)^2 \right)^{1/2} \right) \\ &\times \left\{ \left( \frac{p_T}{M} x \right)^2 - \left( \frac{m_T}{M} x \cosh(y_1 - y_2) - \frac{1}{2} \right)^2 \right\}^{-1/2}, \end{aligned} \quad (5.27)$$

with

$$x_{\pm} = \frac{M}{2(m_T \cosh(y_1 - y_2) \pm p_T)}. \quad (5.28)$$

We have verified that using the expressions listed in Eq. (5.25) our direct numerical integration of the rate given in Eq. (5.8) over space-time via Eqs. (5.11) reproduces this analytic result in the free-streaming limit.

We note in closing that as a solution of the collisionless (non-interacting) Boltzmann equation, the free-streaming case can be taken as an upper bound on the magnitude of the plasma anisotropy parameter since for fixed  $\langle p_T^2 \rangle$  (no transverse expansion/contraction)  $\xi$  cannot be larger than the free-streaming value by causality.

<sup>2</sup>In the original article by Kapusta et. al [154], the calculation of  $dN^{l^+l^-}/dydM^2 d^2 p_T$  was not presented.

### 5.2.3. Momentum-space Broadening in an Expanding Plasma

In the previous two subsections we presented details of the limiting cases for 0+1 dimensional plasma evolution: 0+1 ideal hydrodynamic expansion and 0+1 dimensional free streaming, with the former arising if there is rapid thermalization of the plasma and the latter arising if the plasma has no interactions. We would now like to extend these models to include the possibility of momentum-space broadening of the plasma partons due to interactions (hard and soft). This can be accomplished mathematically by generalizing our expression for  $\xi(\tau)$  to

$$\xi(\tau, \delta) = \left( \frac{\tau}{\tau_0} \right)^\delta - 1. \quad (5.29)$$

In the limit  $\delta \rightarrow 0$ ,  $\xi \rightarrow 0$  and one recovers the 0+1 hydrodynamical expansion limit and in the limit  $\delta \rightarrow 2$  one recovers the 0+1 dimensional free streaming limit,  $\xi \rightarrow \xi_{f.s.}$ . For general  $\delta$  between these limits one obtains the proper time dependence of the energy density and temperature by substituting (5.29) into the general expression for the factorized energy density (5.13) to obtain  $\mathcal{E}(\tau, \delta) = \mathcal{E}_0 \mathcal{R}(\xi(\tau, \delta))$ . In the limit  $\tau \gg \tau_0$  this gives the following scaling relations for the number density, energy density, and hard momentum scale

$$n(\tau) = n_0 \left( \frac{\tau_0}{\tau} \right), \quad (5.30a)$$

$$p_{\text{hard}}(\tau) = T_0 \left( \frac{\tau_0}{\tau} \right)^{(1-\delta/2)/3}, \quad (5.30b)$$

$$\mathcal{E}(\tau) = \mathcal{E}_0 \left( \frac{\tau_0}{\tau} \right)^{4(1-\delta/8)/3}. \quad (5.30c)$$

Different values of  $\delta$  arise dynamically from the different processes contributing to parton isotropization. Below we list the values of  $\delta$  resulting from processes which are relevant during the earliest times after the initial nuclear impact.

#### Collisional Broadening via Elastic $2 \leftrightarrow 2$ collisions

In the original version of the bottom up scenario [26], it was shown that, even at early times after the nuclear impact, elastic collisions between the liberated partons will cause a broadening of the longitudinal momentum of the particles compared to the non-interacting, free-streaming case. During the first stage of the bottom-up scenario, when  $1 \ll Q_s \tau \ll \alpha_s^{3/2}$ , the initial hard gluons have typical momentum of order  $Q_s$  and occupation number of order  $1/\alpha_s$ . Due to the fact that the system is expanding at the speed of light in the longitudinal direction  $N_g \sim Q_s^3/(\alpha_s Q_s \tau)$ . If there were no interactions this expansion would be equivalent to 0+1 free streaming and the longitudinal momentum  $p_L$  would scale like  $1/\tau$ . However, when elastic  $2 \leftrightarrow 2$  collisions of hard gluons are taken into account [26], the ratio between the longitudinal momentum  $p_L$  and the typical transverse momentum of a hard particle  $p_T$  decreases as

$$\frac{\langle p_L^2 \rangle}{\langle p_T^2 \rangle} \propto (Q_s \tau)^{-2/3}. \quad (5.31)$$

Assuming, as before, isotropy at the formation time,  $\tau_0 = Q_s^{-1}$ , this implies that for a collisionally-broadened plasma  $\delta = 2/3$ . Note that, as obtained in Ref. [26], the derivation of this result makes an implicit assumption that the elastic cross-section is screened at long distances by an isotropic real-valued Debye mass. This is not guaranteed in an anisotropic plasma as the Debye mass can become complex due to the chromo-Weibel instability [2]. However, at times short compared to the time scale where plasma instabilities become important, we expect the isotropic result to hold to good approximation.

### Effect of Plasma Instabilities

Plasma instabilities affect the first stage of bottom-up scenario [36]. These instabilities are characterized by the growing of chromo-electric and -magnetic fields  $E^a$  and  $B^a$ . These fields bend the particles and how much bending occurs will depend on the amplitude and domain size of the induced chromofields. Currently, the precise parametric relations between the amount of plasma anisotropy and amplitude and domain size of the chromofields are not known from first principles. There are three possibilities for how the chromo-Weibel instability will affect isotropization of a QGP proposed in the literature [88, 89, 90]

$$\frac{\langle p_L^2 \rangle}{\langle p_T^2 \rangle} \sim (Q_s \tau)^{-\frac{1}{2} \left( \frac{1}{1+\nu} \right)}, \quad (5.32)$$

where

$$\nu = \begin{cases} 0 & \text{Ref.[88]} \quad , \\ 1 & \text{Ref.[89]} \quad , \\ 2 & \text{Nielsen-Olesen limit, Ref.[90]} \quad . \end{cases} \quad (5.33)$$

These results correspond to  $\delta = 1/2$ ,  $\delta = 1/4$ , and  $\delta = 1/6$ , respectively.

### Summary and Discussion

Summarizing, the coefficient  $\delta$  takes on the following values

$$\delta = \begin{cases} 2 & \text{Free streaming expansion} \quad , \\ 2/3 & \text{Collisional-Broadening, Ref.[26]} \quad , \\ 1/2 & \text{Ref.[88]} \quad , \\ 1/4 & \text{Ref.[89]} \quad , \\ 1/6 & \text{Nielsen-Olesen limit, Ref.[90]} \quad , \\ 0 & \text{Hydrodynamic expansion} \quad . \end{cases} \quad (5.34)$$

The exponents in Eq. (5.34) are a direct consequence of the relation between the anisotropy parameter  $\xi$  and the longitudinal and transverse momentum given in Eq. (6.27). The exponent  $\delta$  indicates which kind of broadening we are considering. Notice that  $\delta=2$  (0) reproduces the behaviour of free streaming (hydrodynamic) expansion.

In Fig. 5.2 we sketch the time-dependence of the plasma anisotropy parameter indicating the time scales at which the various processes become important. At times shorter than the mean time between successive elastic scatterings,  $\tau_{\text{MFP}}$ , the system will undergo 0+1 dimensional free streaming with  $\delta = 2$ . For times long compared to  $\tau_{\text{MFP}}$  but short compared to  $\tau_{\text{Instability}}$  the plasma anisotropy will grow with the collisionally-broadened exponent of  $\delta = 2/3$ . Here  $\tau_{\text{Instability}}$  is the time at which instability-induced soft gauge fields begin to influence the hard particles' motion. When  $\tau_{\text{Instability}} < \tau < \tau_{\text{iso}}$  the plasma anisotropy grows with the slower exponent of  $\delta = 1/6 \dots 1/2$  due to the bending of particle trajectories in the induced soft-field background. At times large compared to  $\tau_{\text{Instability}}$  inelastic processes are expected to drive the system back to isotropy [26]. We note here that for small  $\xi$  and realistic couplings it has been shown [43] that one cannot ignore the effect of collisional-broadening of the distribution functions and that this may completely eliminate unstable modes from the spectrum.

Based on such a sketch one could try to construct a detailed model which includes all of the various time scales and study the dependence of the process under consideration on each. However, due to the current theoretical uncertainties in each of these time scales and their dependences on experimental conditions we choose to use a simpler approach in which we will construct two phenomenological

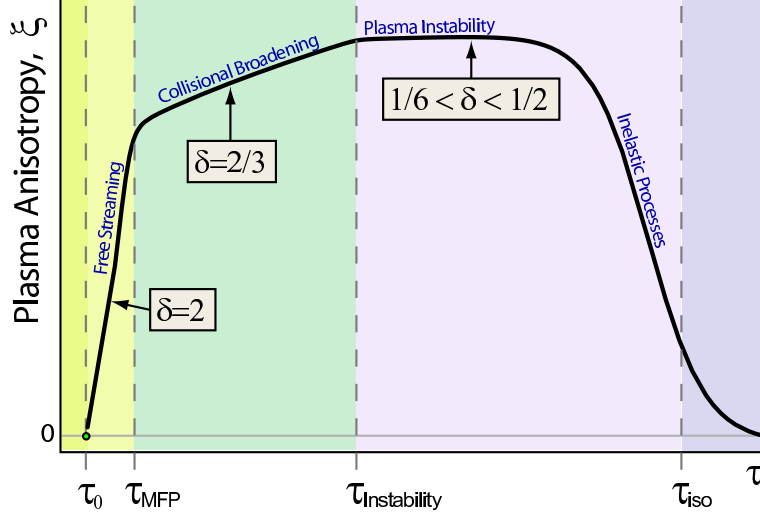


Figure 5.2.: Sketch of the time dependence of the plasma anisotropy indicating the various time-scales and processes taking place. Here  $\tau_{\text{MFP}}$  is the time between elastic collisions (mean-free time) and  $\tau_{\text{Instability}}$  is the time at which plasma-instability induced soft modes have grown large enough to affect hard particle dynamics.

models which smoothly interpolate the coefficient  $\delta$

Free streaming interpolating model :  $2 \geq \delta \geq 0$  ,

Collisionally-broadened interpolating model :  $\frac{2}{3} \geq \delta \geq 0$  .

In both models we introduce a transition width,  $\gamma^{-1}$ , which governs the smoothness of the transition from the initial value of  $\delta \in \{2, 2/3\}$  to  $\delta = 0$  at  $\tau \sim \tau_{\text{iso}}$ . The free streaming interpolating model will serve as an upper-bound on the possible effect of early time momentum-space anisotropies while the collisionally-broadened interpolating model should provide a more realistic estimate of the effect due to the lower anisotropies generated. This will help us gauge our theoretical uncertainties. Note that by using such a smooth interpolation one can achieve a reasonable phenomenological description of the transition from non-equilibrium to equilibrium dynamics which should hopefully capture the essence of the physics. In the next section we will give mathematical definitions for these two models.

#### 5.2.4. Space-Time Interpolating Models with Fixed Initial Conditions

In order to construct our interpolating models, the parameter  $\delta$  should be a function of proper time. To accomplish this, we introduce a smeared step function

$$\lambda(\tau, \tau_{\text{iso}}, \gamma) \equiv \frac{1}{2} \left( \tanh \left[ \frac{\gamma(\tau - \tau_{\text{iso}})}{\tau_{\text{iso}}} \right] + 1 \right) , \quad (5.35)$$

where  $\gamma^{-1}$  sets the width of the transition between non-equilibrium and hydrodynamical evolution in units of  $\tau_{\text{iso}}$ . In the limit when  $\tau \ll \tau_{\text{iso}}$ , we have  $\lambda \rightarrow 0$  and when  $\tau \gg \tau_{\text{iso}}$  we have  $\lambda \rightarrow 1$ .

Physically, the energy density  $\mathcal{E}$  should be continuous as we change from the initial non-equilibrium value of  $\delta$  to the final isotropic  $\delta = 0$  value appropriate for ideal hydrodynamic expansion. Once the energy density is specified this immediately gives us the time dependence of the hard momentum

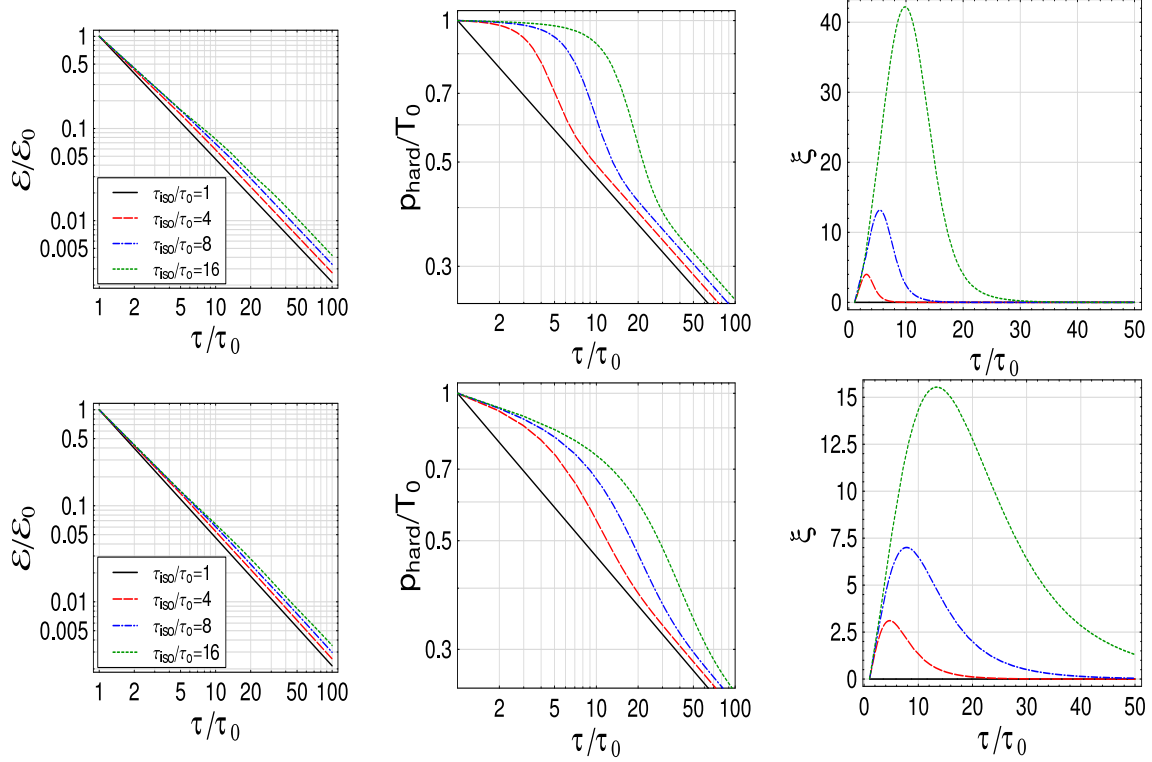


Figure 5.3.: Temporal evolution using our fixed initial condition free-streaming interpolating model ( $\delta = 2$ ) for the energy density (left column), hard momentum scale (middle column), and anisotropy parameter (right column) for four different isotropization times  $\tau_{\text{iso}} \in \{1, 4, 6, 18\} \tau_0$ . The transition width is taken to be (top row)  $\gamma = 2$  and (bottom row)  $\gamma = 0.5$ . To convert to physical scales use  $\tau_0 \sim 0.3$  fm/c for RHIC and  $\tau_0 \sim 0.1$  fm/c for LHC.

scale. We find that for general  $\delta$  this can be accomplished with the following model

$$\xi(\tau, \delta) = (\tau/\tau_0)^{\delta(1-\lambda(\tau))} - 1, \quad (5.36a)$$

$$\mathcal{E}(\tau) = \mathcal{E}_0 \mathcal{R}(\xi) \bar{\mathcal{U}}^{4/3}(\tau), \quad (5.36b)$$

$$p_{\text{hard}}(\tau) = T_0 \bar{\mathcal{U}}^{1/3}(\tau), \quad (5.36c)$$

with  $\mathcal{R}(\xi)$  defined in Eq. (5.14) and for fixed initial conditions

$$\mathcal{U}(\tau) \equiv \left[ \mathcal{R}\left((\tau_{\text{iso}}/\tau_0)^\delta - 1\right) \right]^{3\lambda(\tau)/4} \left( \frac{\tau_{\text{iso}}}{\tau} \right)^{1-\delta(1-\lambda(\tau))/2}, \quad (5.37a)$$

$$\bar{\mathcal{U}}(\tau) \equiv \mathcal{U}(\tau)/\mathcal{U}(\tau_0). \quad (5.37b)$$

The power of  $\mathcal{R}$  in  $\mathcal{U}$  keeps the energy density continuous at  $\tau = \tau_{\text{iso}}$  for all  $\gamma$ . In the following subsections we will briefly discuss the two interpolating models we consider in this work.

### Free streaming interpolating model

Using Eqs. (5.36) and (5.37) we can obtain a model which interpolates between early-time 0+1 dimensional longitudinal free streaming and late-time 0+1 dimensional ideal hydrodynamic expansion



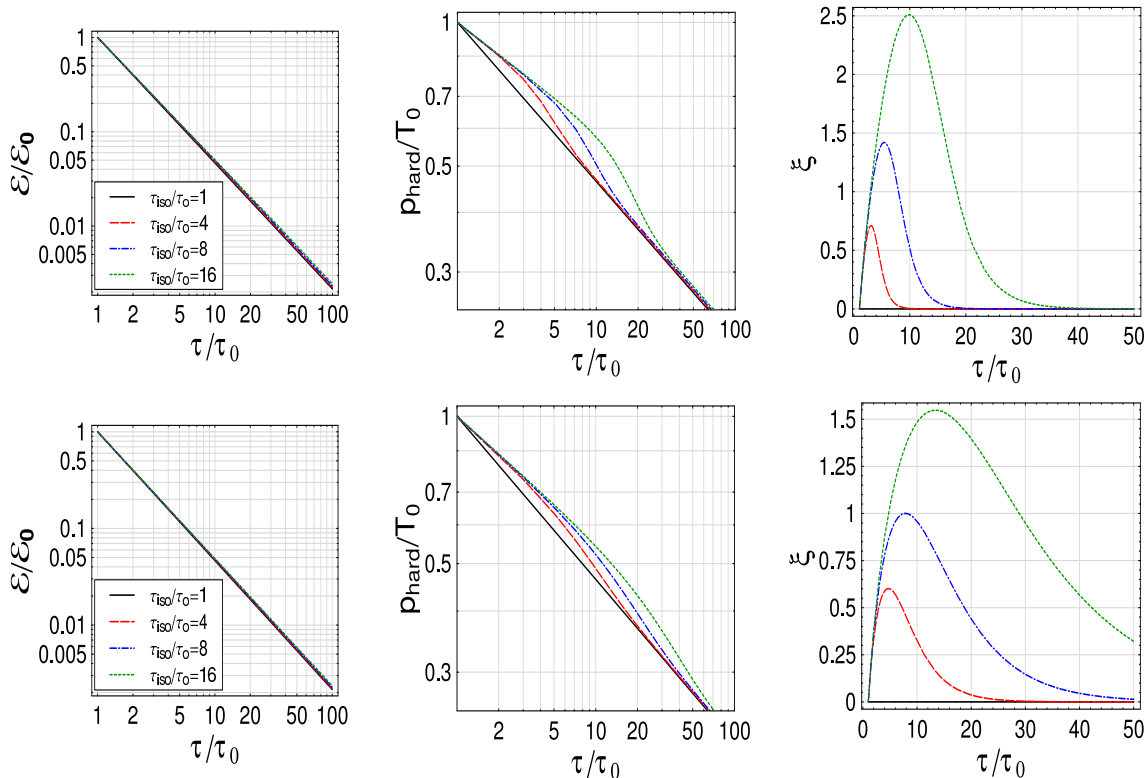


Figure 5.4.: Temporal evolution using our fixed initial condition collisionally-broadened interpolating model ( $\delta = 2/3$ ) for the energy density (left column), hard momentum scale (middle column), and anisotropy parameter (right column) for four different isotropization times  $\tau_{\text{iso}} \in \{1, 4, 6, 18\} \tau_0$ . The transition width is taken to be (top row)  $\gamma = 2$  and (bottom row)  $\gamma = 0.5$ . To convert to physical scales use  $\tau_0 \sim 0.3$  fm/c for RHIC and  $\tau_0 \sim 0.1$  fm/c for LHC.

by choosing  $\delta = 2$ . With this choice and in the limit  $\tau \ll \tau_{\text{iso}}$ , we have  $\lambda \rightarrow 0$  and the system undergoes 0+1 dimensional free streaming. When  $\tau \gg \tau_{\text{iso}}$  then  $\lambda \rightarrow 1$  and the system is expanding hydrodynamically. In the limit  $\gamma \rightarrow \infty$ ,  $\lambda \rightarrow \Theta(\tau - \tau_{\text{iso}})$ , the system makes a theta function transition from free streaming to hydrodynamical evolution with the energy density being continuous during this transition by construction. In Fig. 5.3 we plot the time-dependence of  $\mathcal{E}$ ,  $p_{\text{hard}}$ , and  $\xi$  assuming (top)  $\gamma = 2$  and (bottom)  $\gamma = 0.5$  for different values of  $\tau_{\text{iso}}$ . As can be seen from this figure for fixed initial conditions during the period of free-streaming evolution the system always has a higher effective temperature ( $p_{\text{hard}}$ ) than would be obtained by a system which undergoes only hydrodynamic expansion from the formation time. As we will show in the results section, for fixed initial conditions, this results in a sizable enhancement in high-energy dilepton production.

### Collisionally-broadened interpolating model

Similarly using Eqs. (5.36) and (5.37) we can obtain a model which interpolates between early-time 0+1 dimensional collisionally-broadened expansion and late-time 0+1 dimensional ideal hydrodynamic expansion by choosing  $\delta = 2/3$ . In Fig. 5.4 we plot the time-dependence of  $\mathcal{E}$ ,  $p_{\text{hard}}$ , and  $\xi$  assuming (top)  $\gamma = 2$  and (bottom)  $\gamma = 0.5$  for different values of  $\tau_{\text{iso}}$ . As in the free-streaming interpolating model for fixed initial conditions at early times a collisionally-broadened system always has a higher effective temperature ( $p_{\text{hard}}$ ) than would be obtained by a system which undergoes

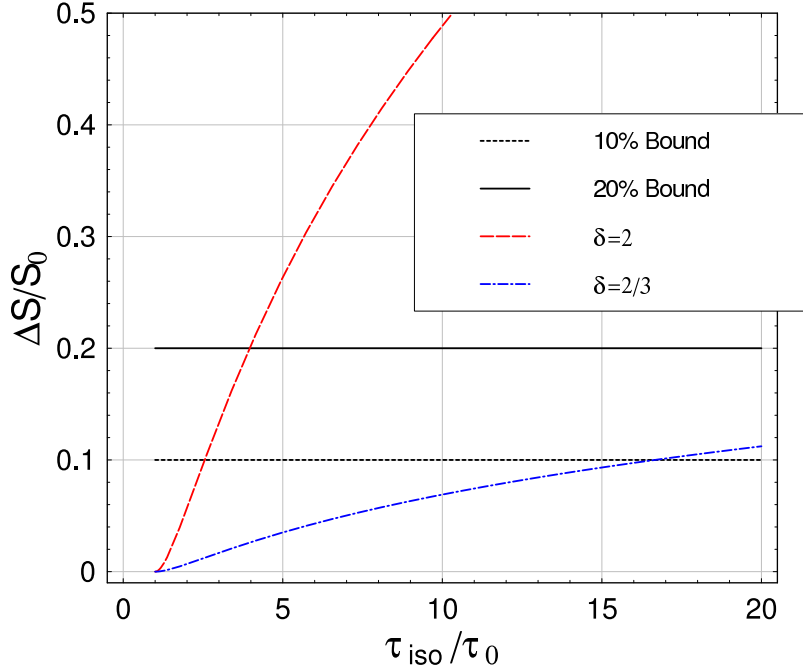


Figure 5.5.: Percentage entropy generation using fixed initial condition interpolating models (5.36) and (5.37) with  $\delta = 2$  and  $\delta = 2/3$ . Horizontal lines show 10% and 20% entropy generation bounds.

Model	RHIC – 10%	RHIC – 20%	LHC – 10%	LHC – 20%
$\delta = 2$	$\tau_{\text{iso}} \leq 0.8 \text{ fm/c}$	$\tau_{\text{iso}} \leq 1.2 \text{ fm/c}$	$\tau_{\text{iso}} \leq 0.26 \text{ fm/c}$	$\tau_{\text{iso}} \leq 0.4 \text{ fm/c}$
$\delta = 2/3$	$\tau_{\text{iso}} \leq 5 \text{ fm/c}$	$\tau_{\text{iso}} \leq 18 \text{ fm/c}$	$\tau_{\text{iso}} \leq 1.6 \text{ fm/c}$	$\tau_{\text{iso}} \leq 6.2 \text{ fm/c}$

Table 5.1.: Bounds on  $\tau_{\text{iso}}$  imposed by requiring either a 10% or 20% bound on percentage entropy (particle number) generation from our fixed initial condition interpolating models. To convert to physical scales we have used  $\tau_0 = 0.3 \text{ fm/c}$  for RHIC and  $\tau_0 = 0.1 \text{ fm/c}$  for LHC.

only hydrodynamic expansion from the formation time. As we will show in the results section, for fixed initial conditions, this results in an enhancement in high-energy dilepton production; however, compared to the free-streaming case the effect is reduced due to the lower effective temperatures obtained by the collisionally-broadened plasma. We also note that in the case of collisionally-broadened expansion the magnitude of  $\xi$  is significantly reduced as compared to the free-streaming case. As can be seen from the rightmost panel of Fig. 5.4, even if one assumes a large isotropization time,  $\tau_{\text{iso}} = 18 \tau_0$ , the amount of momentum space anisotropy generated is small with  $\xi_{\text{max}} \sim 2.5$  for  $\gamma = 2$  and  $\xi_{\text{max}} \sim 1.5$  for  $\gamma = 0.5$ .

### 5.2.5. Space-Time Interpolating Models with Fixed Final Multiplicity

In the previous subsection we constructed models which allow one to interpolate between an initially non-equilibrium plasma to an isotropic equilibrium one assuming that the initial conditions are held fixed. One problem with this procedure is that given fixed initial conditions these interpolating models will result in generation of particle number during the transition from  $\delta \in \{2, 2/3\}$  to zero. One can derive an expression for the amount by which the number density is increased by starting

from the general expression for the particle number density  $n(\tau)/n_0 = (p_{\text{hard}}/T_0)^3 (1 + \xi(\tau))^{-1/2}$  and using the expression for  $p_{\text{hard}}$  derived in the previous section (5.36c) to obtain

$$\frac{n(\tau)}{n_0} = \frac{\bar{\mathcal{U}}(\tau)}{\sqrt{1 + \xi(\tau)}}. \quad (5.38)$$

Taking the limit  $\tau \gg \tau_{\text{iso}}$  we obtain

$$\lim_{\tau \gg \tau_{\text{iso}}} \frac{n(\tau)}{n_0} = \frac{\tau_{\text{iso}}}{\tau} \left( \frac{\tau_{\text{iso}}}{\tau_0} \right)^{\delta/2-1} \left[ \mathcal{R} \left( (\tau_{\text{iso}}/\tau_0)^\delta - 1 \right) \right]^{3/4}. \quad (5.39)$$

Translating this into a statement about the entropy generation using  $S(\tau) = \tau n(\tau)$  gives

$$\lim_{\tau \gg \tau_{\text{iso}}} \frac{S(\tau)}{S_0} = \left( \frac{\tau_{\text{iso}}}{\tau_0} \right)^{\delta/2} \left[ \mathcal{R} \left( (\tau_{\text{iso}}/\tau_0)^\delta - 1 \right) \right]^{3/4}. \quad (5.40)$$

When either  $\delta \rightarrow 0$  or  $\tau_{\text{iso}} \rightarrow \tau_0$ ,  $\Delta S \equiv (S_{\text{final}} - S_0)/S_0$  goes to zero and there is no entropy generation; however, entropy generation increases monotonically with  $\delta$ . In the limit of large  $\tau_{\text{iso}}/\tau_0$  we find

$$\lim_{\tau_{\text{iso}} \rightarrow \infty} \frac{\Delta S}{S_0} = \left( \frac{\tau_{\text{iso}}}{\tau_0} \right)^{\frac{\delta}{8}} - 1. \quad (5.41)$$

Again we see that in the limit that either  $\delta \rightarrow 0$  or  $\tau_{\text{iso}} \rightarrow \tau_0$  then there is no entropy generation.

The requirement of bounded entropy generation can be used to constrain non-equilibrium models of the QGP [163]. In Fig. 5.5 we plot the entropy generation (particle number generation) resulting from our models using Eq. (5.40) for  $\delta \in \{2, 2/3\}$  along with bounds at 10% and 20%. In the free-streaming interpolating model ( $\delta = 2$ ) with fixed initial conditions, requiring that the percentage entropy generation be less than each of these bounds requires  $\tau_{\text{iso}} \leq 2.6 \tau_0$  for the 10% bound and  $\tau_{\text{iso}} \leq 4 \tau_0$  for the 20% bound. In the collisionally-broadened interpolating model ( $\delta = 2/3$ ) with fixed initial conditions we obtain similarly  $\tau_{\text{iso}} \leq 17 \tau_0$  for the 10% bound and  $\tau_{\text{iso}} \leq 62 \tau_0$  for the 20% bound. We summarize our results in Table 5.1. As can be seen from Table 5.1, requiring the listed bounds on entropy generation the values of  $\tau_{\text{iso}}$  allowed in our free-streaming interpolating model become highly constrained. However, in the case of the collisionally-broadened interpolating model the upper-bounds imposed on  $\tau_{\text{iso}}$  are much larger due to the much lower entropy generation required to transition from collisionally-broadened evolution to hydrodynamic evolution.

One problem with our fixed initial condition family of models is that due to the fact that they generate additional particles the multiplicity of final particles is not independent of the assumed value of  $\tau_{\text{iso}}$ . Because most of the experimental results for dilepton spectra are binned with respect to a fixed final multiplicity this means that we should also construct models which always result in a fixed final number density. In the following subsection we will show how this can be accomplished.

### Enforcing Fixed Final Multiplicity

We will now construct interpolating models which have a fixed final entropy (multiplicity). In order to accomplish this, the initial conditions will have to vary as a function of the assumed isotropization time. We will show that, as a result, for finite  $\tau_{\text{iso}}$  one must lower the initial ‘‘temperature’’ in both the free-streaming and collisionally-broadened interpolating models. To accomplish this requires only a small modification to the definition of  $\bar{\mathcal{U}}$  in Eq. (5.37)

$$\bar{\mathcal{U}}(\tau) \equiv \mathcal{U}(\tau) / \mathcal{U}(\tau_{\text{iso}}^+), \quad (5.42a)$$

$$\mathcal{U}(\tau_{\text{iso}}^+) \equiv \lim_{\tau \rightarrow \tau_{\text{iso}}^+} \mathcal{U}(\tau) = \left[ \mathcal{R} \left( (\tau_{\text{iso}}/\tau_0)^\delta - 1 \right) \right]^{3/4} \left( \frac{\tau_{\text{iso}}}{\tau_0} \right). \quad (5.42b)$$

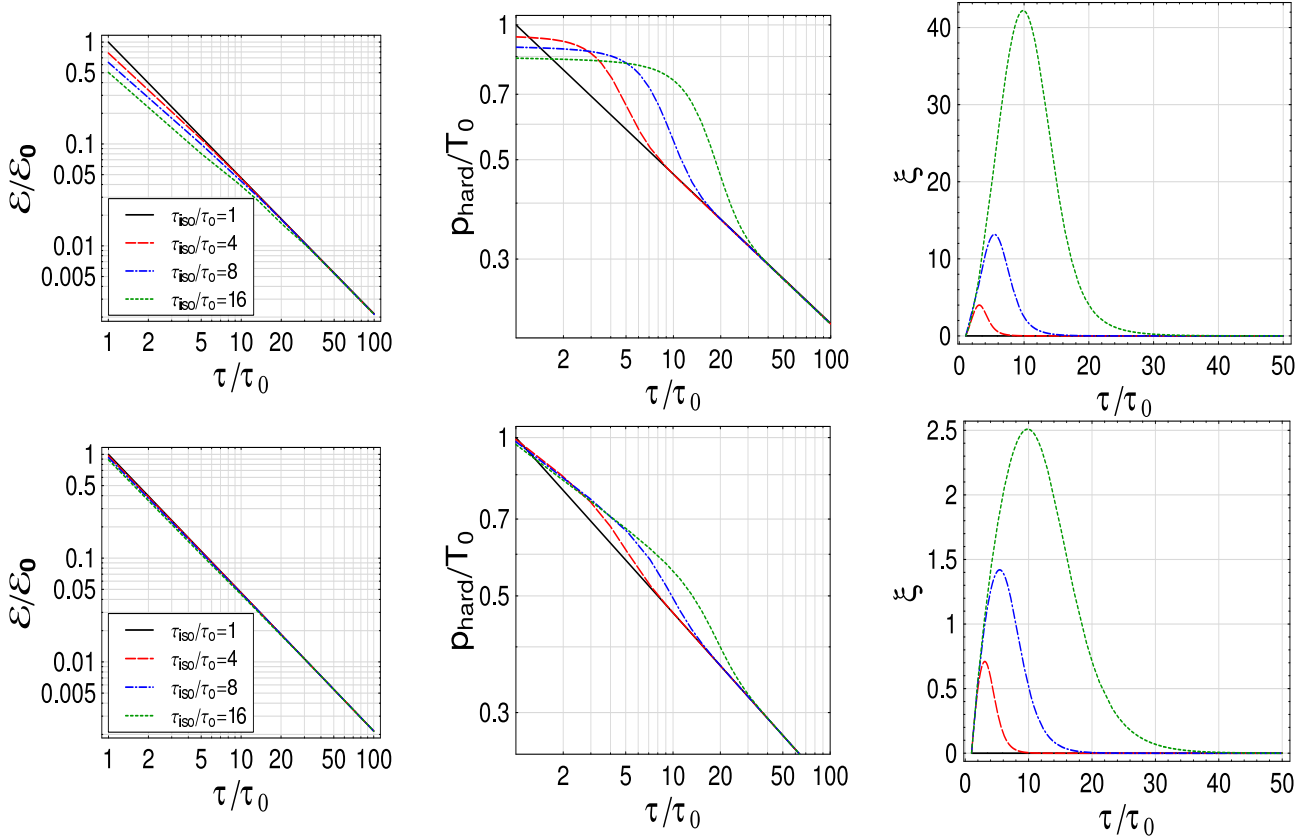


Figure 5.6.: Temporal evolution using our fixed final multiplicity interpolating models for the energy density (left column), hard momentum scale (middle column), and anisotropy parameter (right column) for four different isotropization times  $\tau_{\text{iso}} \in \{1, 4, 6, 18\} \tau_0$ . Top row is the free-streaming interpolation model ( $\delta = 2$ ) and bottom row is the collisionally-broadening interpolation model ( $\delta = 2/3$ ). To convert to physical scales use  $\tau_0 \sim 0.3$  fm/c for RHIC and  $\tau_0 \sim 0.1$  fm/c for LHC.

As a consequence of this modification, the initial energy density and hence initial “temperature” will depend on the assumed value for  $\tau_{\text{iso}}$ . There is no modification required for the temporal evolution of  $\xi$ . We demonstrate this in Fig. 5.6 where we plot the time-dependence of  $\mathcal{E}$ ,  $p_{\text{hard}}$ , and  $\xi$  for  $\gamma = 2$  and (top)  $\delta = 2$  and (bottom)  $\delta = 2/3$ .

In the remainder of this work we present our final results for dilepton yields using both approaches, i.e. fixed initial conditions using Eqs. (5.36) with (5.37) or fixed final multiplicity through Eq. (5.36) with (5.42). We mention that in both cases, dilepton production is affected in the presence of anisotropies in momentum-space, however, one anticipates that the effect will be larger when the initial conditions are held fixed due to the larger particle number generation. We will come back to this issue in the conclusions and discussion.

### 5.2.6. Results of high energy dileptons in the central rapidity region

In this section we will present the expected  $e^+e^-$  yields resulting from a central Au-Au collision at RHIC full beam energy,  $\sqrt{s}=200$  GeV and from a Pb-Pb collision at LHC full beam energy,  $\sqrt{s}=5.5$  TeV. In all figures in this section we will present the prediction for RHIC energies in the left panel and LHC energies in the right panel.

Before presenting our results we first explain the setup, numerical techniques used, and parameters chosen for our calculations. Because the differential dilepton rate  $dR^{l^+l^-}/d^4P$  given in Eq. (5.8) is independent of the assumed space-time model, we first evaluated it numerically using double-exponential integration with a target precision of  $10^{-9}$ . The result for the rate was then tabulated on a uniformly-spaced 4-dimensional grid in  $M$ ,  $p_T$ ,  $y$ , and  $\log_{10} \xi : M/p_{\text{hard}}, p_T/p_{\text{hard}} \in \{0.1, 25\}$ ,  $y \in \{-3, 3\}$ ,  $\log_{10} \xi \in \{-6, 4\}$ . This table was then used to build a four-dimensional interpolating function which was valid at continuous values of these four variables. We then boosted this rate from the local reference frame to center-of-mass frame and evaluated the remaining integrations over space-time ( $\tau$  and  $\eta$ ) and transverse momentum or invariant mass appearing in Eqs. (5.11) using quasi-Monte Carlo integration with  $\tau \in \{\tau_0, \tau_f\}$ ,  $\eta \in \{-2.5, 2.5\}$  and, depending on the case, restrict the integration to any cuts specified in  $M$  or  $p_T$ . Our final integration time,  $\tau_f$ , was set by solving numerically for the point in time at which the temperature in our interpolating model is equal to the critical temperature, i.e.  $p_{\text{hard}}(\tau_f) = T_C$ . We will assume that when the system reaches  $T_C$ , all medium emission stops. We are not taking into account the emission from the mixed/hadronic phase at late times since the kinematic regime we study (high  $M$  and  $p_T$ ) is dominated by early-time high-energy dilepton emission [156, 82].

For RHIC energies we take an initial temperature  $T_0 = 370$  MeV, at a formation time of  $\tau_0 = 0.26$  fm/c, and use  $R_T = 6.98$  fm. For LHC energies, we use  $\tau_0 = 0.088$  fm/c,  $T_0 = 845$  MeV and  $R_T = 7.1$  fm. In both cases, the critical temperature  $T_C$  is taken as 160 MeV and the spectra are calculated at central rapidity region  $y = 0$ . Any cuts in transverse momentum or invariant mass will be indicated along with results. Note that the precise numerical value of the parameters above were chosen solely in order to facilitate straightforward comparisons with previous works [146] from which we have obtained predictions for Drell Yan, heavy quark, jet-fragmentation, and jet-thermal dilepton yields.

Finally we note that below we will use  $K$ -factors to adjust for next-to-leading order corrections to the dilepton rate. These  $K$ -factors are determined by computing the ratio of the next-to-leading order prediction of [137, 146] with our leading order prediction in the case of ideal-hydrodynamic expansion. We therefore assume that the  $K$ -factors are independent of the assumed thermalization time. This is an approximation which, in the future, one would like to relax by computing the full next-to-leading order dilepton rate in the presence of momentum-space anisotropies.

### 5.2.7. Dilepton production with fixed initial conditions

We now present the results of dilepton production assuming the time dependence of the energy density, the hard momentum scale and the anisotropy parameter are given by Eqs. (5.36) and (5.37) with  $\delta \in \{2, 2/3\}$ .

#### Free streaming interpolating model

In Fig. 5.7, we show our predicted dilepton mass spectrum for RHIC and LHC energies assuming the time dependence of the energy density, the hard momentum scale and the anisotropy parameter are given by Eqs. (5.36) and (5.37) with  $\delta = 2$ . This corresponds to our free-streaming interpolating model. This model will serve as an upper-bound on the possible effect of momentum-space anisotropies on dilepton yields. From Fig. 5.7 we see that for both RHIC or LHC energies, there is a significant enhancement of up to one order of magnitude in the medium dilepton yield when we vary the isotropization time from  $\tau_0$  to 2 fm/c. This enhancement is due to the fact that in 0+1 dimensional free streaming, the system preserves more transverse momentum as can be seen from Fig. 5.3. For fixed initial conditions this results in a larger effective temperature than would be obtained if the system underwent locally-isotropic (hydrodynamical) expansion throughout its evolution.

Nevertheless, as Fig. 5.7 shows, as a function of invariant mass, the other contributions to high-energy dilepton yields (Drell-Yan, jet-thermal, and jet-fragmentation) are all of the same order of magnitude as the medium contribution. This, coupled with the large background coming from

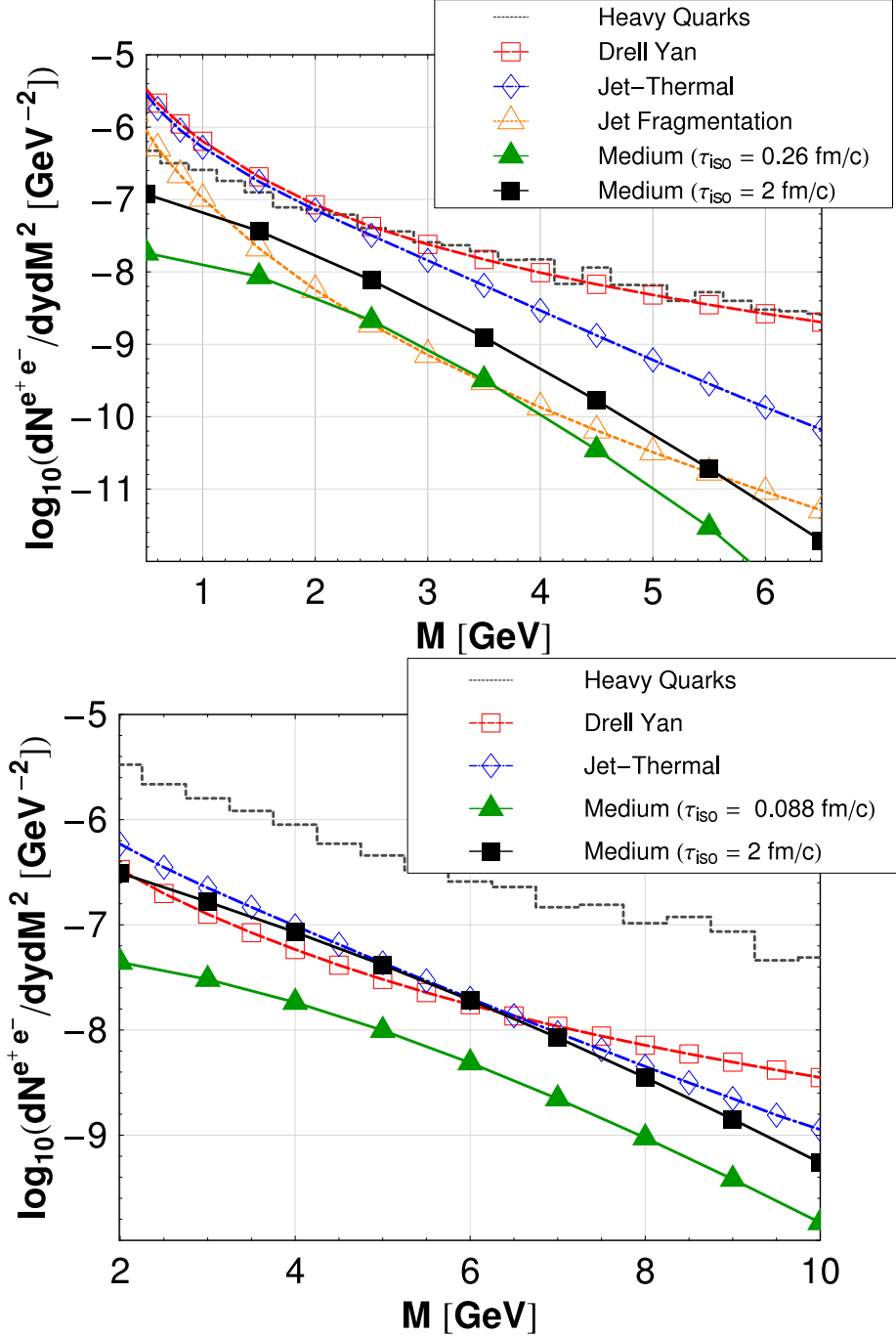


Figure 5.7.: Free-streaming interpolating model dilepton yields as a function of invariant mass in central Au+Au collisions at RHIC (top) and Pb+Pb at the LHC (bottom), with a cut  $p_T \geq 4$  (8)  $\text{GeV}$  and rapidity  $y=0$ . For medium dileptons we use  $\gamma=2$  and  $\tau_{\text{iso}}$  is taken to be either 0.26 (0.088)  $\text{fm/c}$  or 2  $\text{fm/c}$  for RHIC (LHC) energies with fixed initial conditions. A  $K$ -factor of 1.5 was applied to account for NLO corrections. Dilepton yields from Drell Yan, Heavy Quarks, Jet-Thermal and Jet-Fragmentation were obtained from Ref. [146].

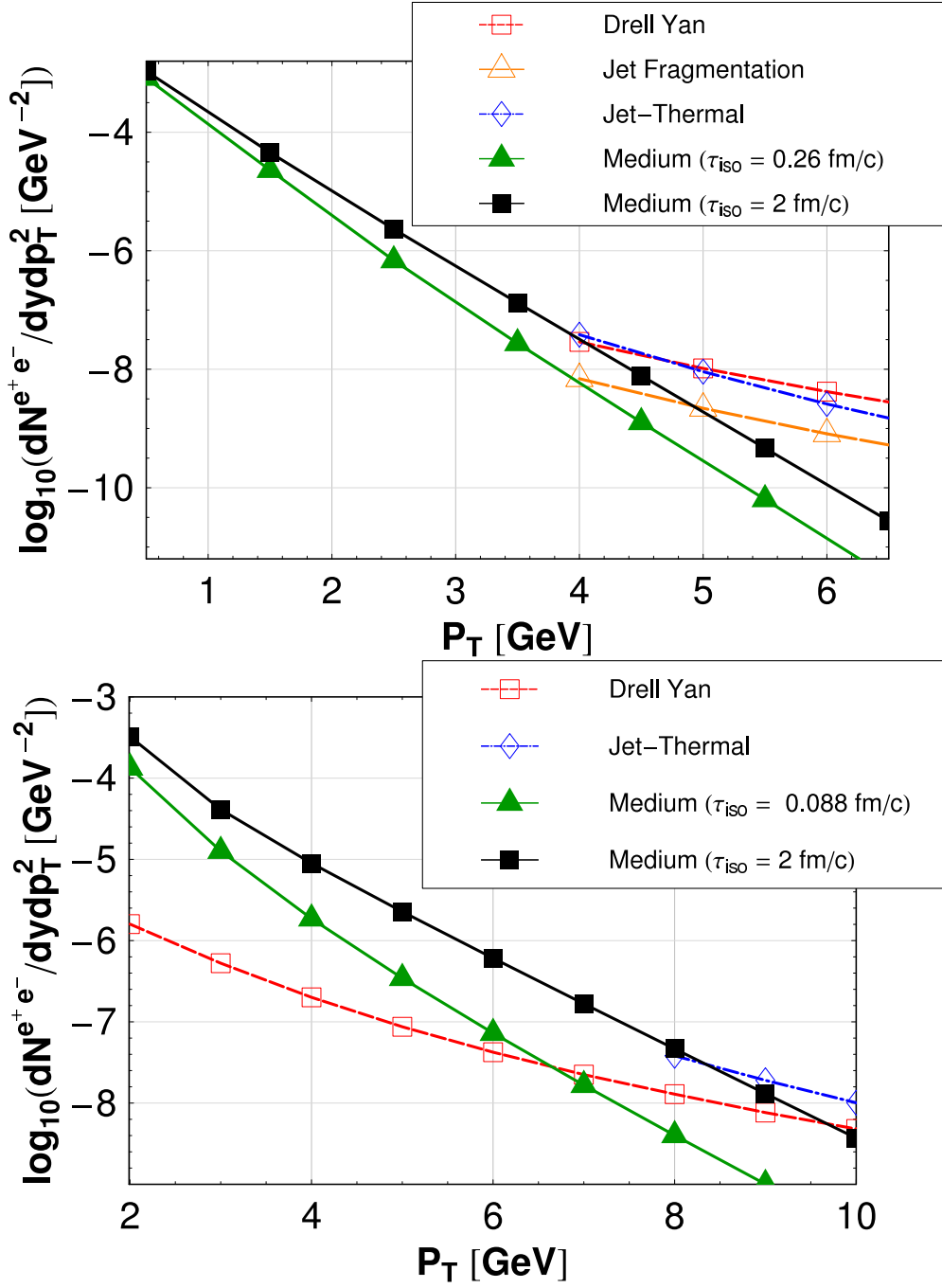


Figure 5.8.: Free-streaming interpolating model dilepton yields as a function of transverse momentum in central Au+Au collisions at RHIC (top) and Pb+Pb at the LHC (bottom), with a cut  $0.5 \leq M \leq 1$  GeV and rapidity  $y=0$ . For medium dileptons we use  $\gamma=2$  and  $\tau_{\text{iso}}$  is taken to be either 0.26 (0.088) fm/c or 2 fm/c for RHIC (LHC) energies with fixed initial conditions. A  $K$ -factor of 6 was applied to account for NLO corrections. Dilepton yields from Drell Yan, Jet-Thermal and Jet-Fragmentation were obtained from Ref. [146].

semileptonic heavy quarks decays, would make it extremely difficult for experimentalists to extract a clean medium dilepton signal from the invariant mass spectrum. For this reason it does not look very promising to determine plasma initial conditions from the dilepton invariant mass spectrum. For this reason we will not present our predictions for the invariant mass spectrum for the intermediate models detailed below and only return to the invariant mass spectrum at the end of this section for completeness.

The good news is, however, that as a function of transverse momentum, see Fig. 5.8, the production of medium dileptons is expected to dominate other production mechanisms for  $p_T \lesssim 4$  (6) GeV in the case of RHIC (LHC). In addition to this, we see that for the free-streaming interpolating model that there is a significant enhancement of medium dileptons for both RHIC and LHC energies.

In order to quantify the effect of time-dependent pre-equilibrium emissions we define the ‘‘dilepton enhancement’’,  $\phi(\tau_{\text{iso}})$ , as the ratio of the dilepton yield obtained with an isotropization time of  $\tau_{\text{iso}}$  to that obtained from an instantaneously thermalized plasma undergoing only 0+1 hydrodynamical expansion, ie.  $\tau_{\text{iso}} = \tau_0$ .

$$\phi(\tau_{\text{iso}}) \equiv \left( \frac{dN^{e^+e^-}(\tau_{\text{iso}})}{dydp_T^2} \right) \bigg/ \left( \frac{dN^{e^+e^-}(\tau_{\text{iso}} = \tau_0)}{dydp_T^2} \right) \quad (5.43)$$

Using this criterion we find for the free streaming interpolating model with fixed initial conditions the dilepton enhancement at  $\tau_{\text{iso}} = 2$  fm/c can be as large as 10. However, as mentioned above we expect that the actual enhancement will be lower due to the fact that parton interactions such as collisional-broadening will modify the free-streaming  $\xi = \tau^2/\tau_0^2 - 1$  to something growing slower in proper time, bringing the system closer to equilibrated expansion. In addition, as we will discuss below when using fixed initial conditions and  $\delta = 2$  there is significant entropy generation which, when properly normalized to fixed final multiplicity, results in reduced  $\phi$ . Therefore, we expect  $\phi \sim 10$  obtained from the free streaming interpolation model with fixed initial conditions to be an upper-bound on the effect of pre-equilibrium emissions. Some of our results fixing initial conditions are related with recent work on dilepton production from a viscous QGP [164].

### Collisionally-broadened interpolating model

In Fig. 5.9, we show our predicted dilepton transverse momentum spectrum for RHIC and LHC energies assuming the time dependence of the energy density, the hard momentum scale and the anisotropy parameter are given by Eqs. (5.36) and (5.37) with  $\delta = 2/3$ . This corresponds to our collisionally-broadened interpolating model with fixed initial conditions. From Fig. 5.9 we see that for both RHIC or LHC energies, there is dilepton enhancement in the kinematic range shown; however, compared to the free streaming case the enhancement is reduced. This is due to the fact that the collisionally-broadened interpolating model is always closer to locally-isotropic expansion than the free-streaming ( $\delta = 2$ ) model, see Figs. 5.3 and 5.4.

In Fig. 5.10 we show the dilepton enhancement,  $\phi$ , as function of transverse momentum for  $\tau_{\text{iso}} = 2$  fm/c at (top) RHIC energies (bottom) LHC energies. The invariant mass cut is the same as in Fig. 5.9 ( $0.5 \leq M \leq 1$  GeV). As can be seen from Fig. 5.10 using fixed initial conditions there is a rapid increase in  $\phi$  between 1 and 3 GeV at RHIC energies and 1 and 4 GeV at LHC energies. The precise value of the enhancement depends on the assumed width  $\gamma^{-1}$  and in Fig. 5.10 we show  $\phi$  for  $\gamma^{-1} \in \{0.1, 0.5, 2\}$ . As can be seen from this figure both sharp and smooth transitions from early-time collisionally-broadened expansion to ideal hydrodynamic expansion result in a 40-70% enhancement of medium dilepton yields at RHIC energies and 60-100% at LHC energies. We will return to this in the results summary at the end of this section.



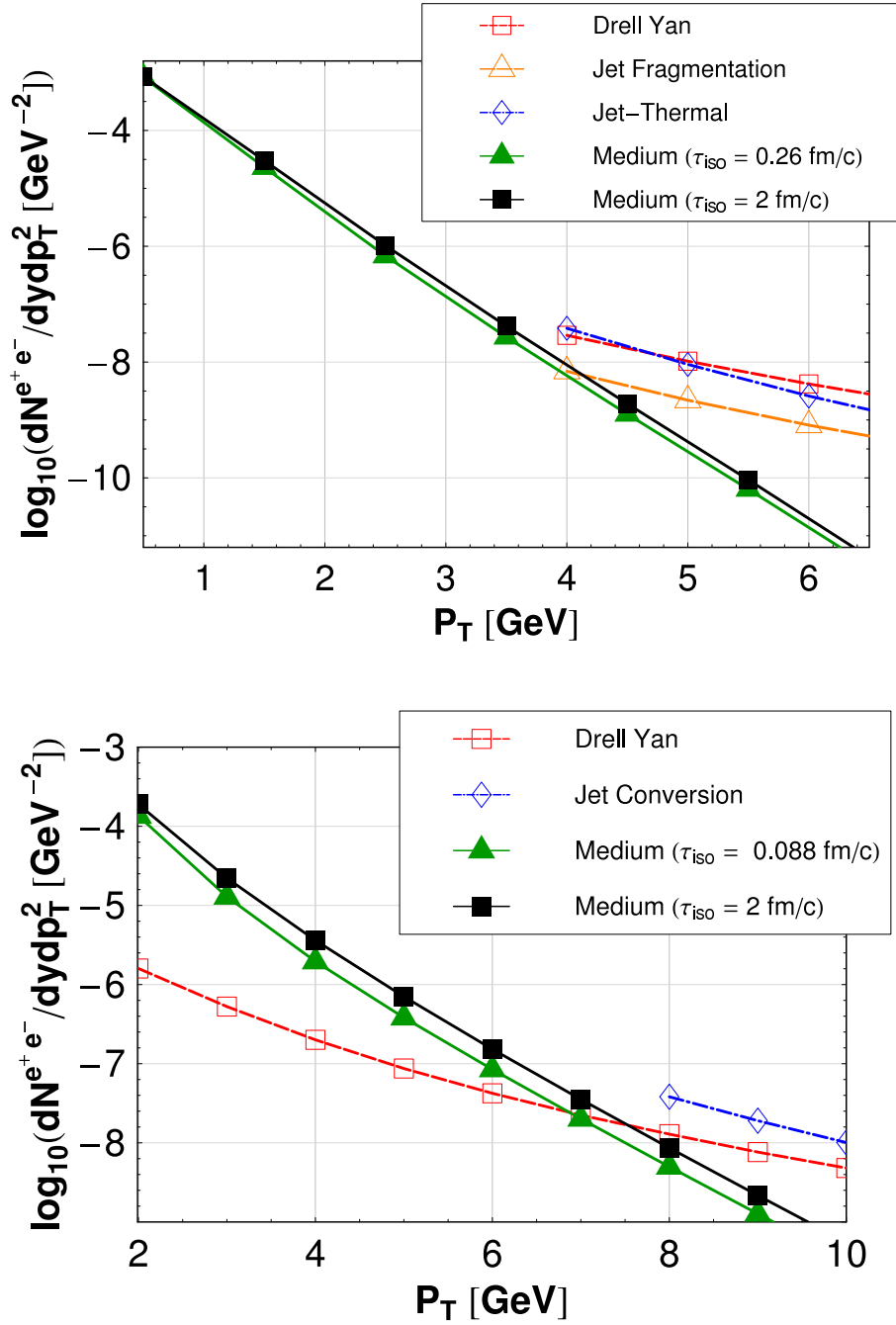


Figure 5.9.: Collisionally-broadened interpolating model dilepton yields including collisional broadening as a function of transverse momentum in central Au+Au collisions at RHIC (top) and Pb+Pb at the LHC (bottom), with a cut  $0.5 \leq M \leq 1$  GeV and rapidity  $y=0$ . For medium dileptons we use  $\gamma=2$  and  $\tau_{\text{iso}}$  is taken to be either 0.26 (0.088) fm/c or 2 fm/c for RHIC (LHC) energies with fixed initial conditions. A  $K$ -factor of 6 was applied to account for NLO corrections. Dilepton yields from Drell Yan, Jet-Thermal and Jet-Fragmentation were obtained from Ref. [146].

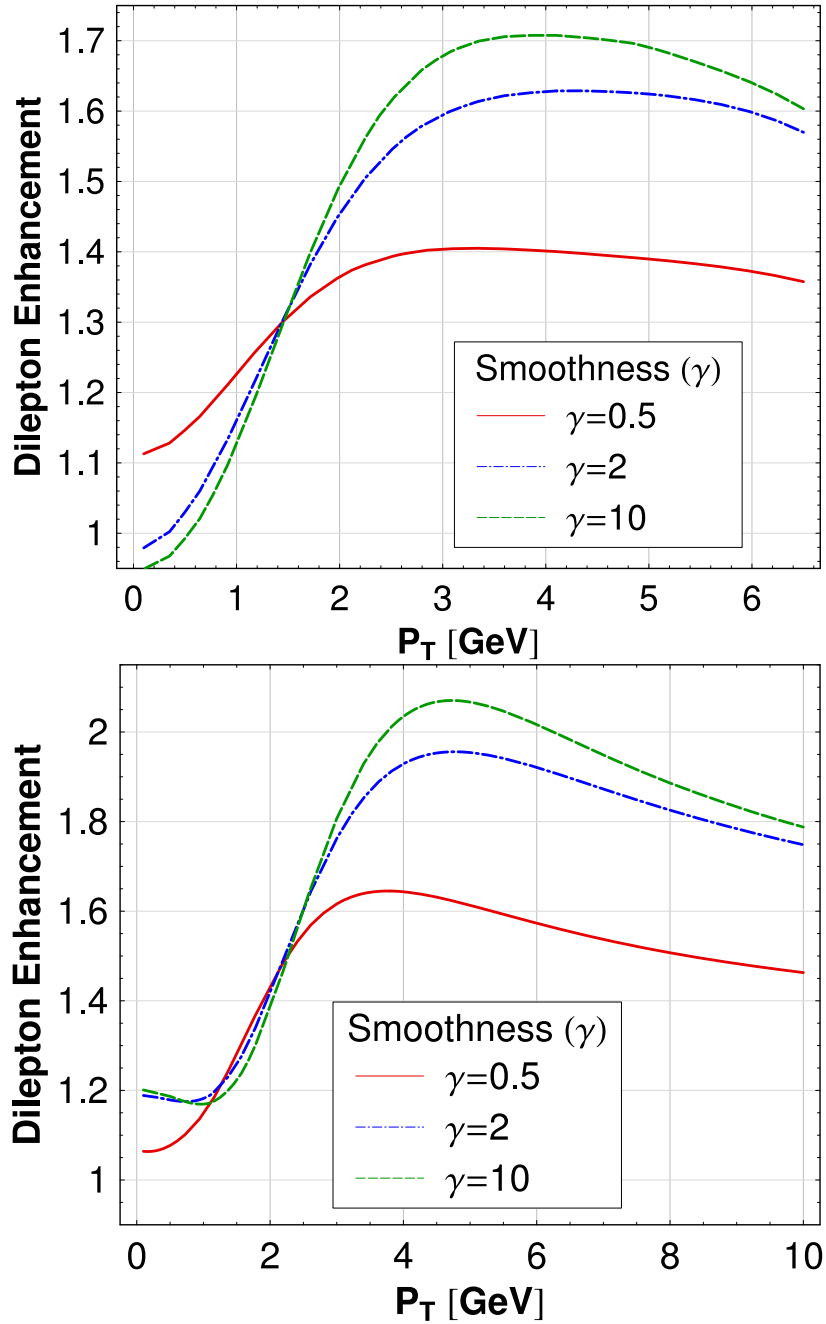


Figure 5.10.: Dilepton enhancement,  $\phi$ , as defined in Eq. (5.43) resulting from our collisionally-broadened interpolating model ( $\delta = 2/3$ ) with fixed initial conditions and  $\tau_{\text{iso}} = 2$  fm/c. The result shown here are for RHIC energies (top) and for LHC energies (bottom). The invariant mass cut used was  $0.5 \leq M \leq 1$  GeV and rapidity  $y=0$ . Lines show expected pre-equilibrium dilepton enhancements for different values of transition width  $\gamma$  corresponding to sharp or smooth transitions between pre-equilibrium and equilibrium behavior.

### 5.2.8. Dilepton production with fixed final multiplicity

We now present the results of the dilepton production assuming the time dependence of the energy density, the hard momentum scale and the anisotropy parameter are given by Eqs. (5.36) and (5.42) with  $\delta \in \{2, 2/3\}$ .

#### Free streaming interpolating model

In Fig. 5.11, we show our predicted dilepton transverse momentum spectrum for RHIC and LHC energies assuming the time dependence of the energy density, the hard momentum scale and the anisotropy parameter are given by Eqs. (5.36) and (5.42) with  $\delta = 2$ . This corresponds to our free-streaming interpolating model with fixed final multiplicity. From Fig. 5.11 we see that for both RHIC or LHC energies, there is dilepton enhancement in the kinematic range shown; however, when fixing on final multiplicity the effect of a free-streaming pre-equilibrium phase is reduced. In fact, for small and large  $p_T$  the free-streaming interpolating model with fixed final multiplicities predicts a suppression of dileptons. This is due to the fact that in order to maintain fixed final multiplicity for  $\tau_{\text{iso}} = 2$  fm/c the free-streaming model initial energy density has to be reduced by  $\sim 50\%$  (see top row of Fig. 5.6).

#### Collisionally-broadened interpolating model

In Figs. 5.12 and 5.13, we show our predicted dilepton invariant mass and transverse momentum spectrum for RHIC and LHC energies assuming the time dependence of the energy density, the hard momentum scale and the anisotropy parameter are given by Eqs. (5.36) and (5.42) with  $\delta = 2/3$ . This corresponds to our collisionally-broadened interpolating model with fixed final multiplicity. In Fig. 5.14 we show the dilepton enhancement,  $\phi$ , as function of transverse momentum for  $\tau_{\text{iso}} = 2$  fm/c at (top) RHIC energies (bottom) LHC energies. The invariant mass cut is the same as in Fig. 5.13 ( $0.5 \leq M \leq 1$  GeV). As can be seen from Fig. 5.14 similar to the case of fixed initial conditions there is a rapid increase in  $\phi$  between 1 and 3 GeV at RHIC energies and 1 and 4 GeV at LHC energies. However, compared to the case of the collisionally-broadened interpolating model with fixed initial condition (Fig. 5.10) the maximum enhancement is reduced slightly and we see a more pronounced peak in  $\phi$  as a function of transverse momentum appearing. As can be seen from this figure both sharp and smooth transitions from early-time collisionally-broadened expansion to ideal hydrodynamic expansion result in a 20-40% enhancement of medium dilepton yields at RHIC energies, and 30-50% at LHC energies.

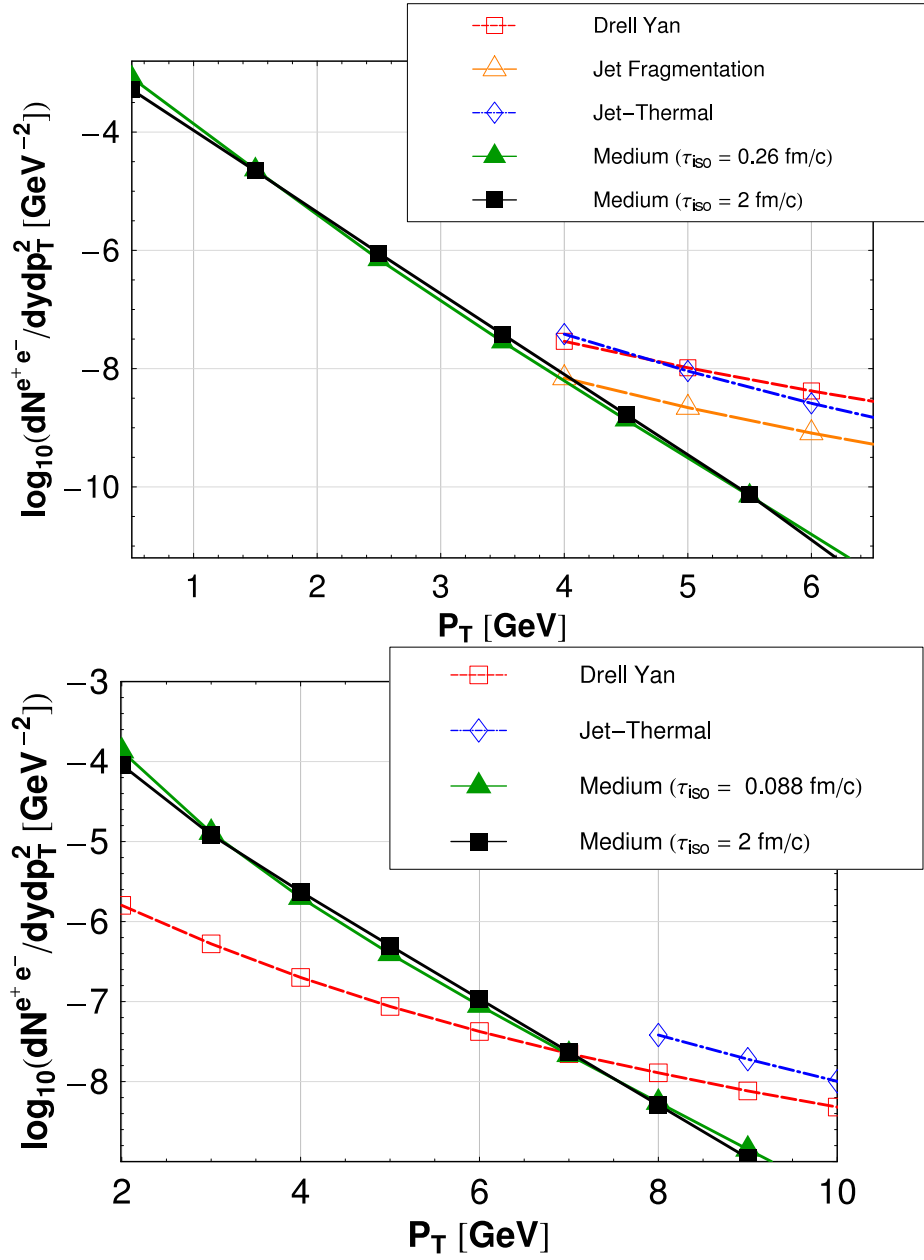


Figure 5.11.: Free streaming interpolating model dilepton yields as a function of transverse momentum in central Au+Au collisions at RHIC (top) and Pb+Pb at the LHC (bottom), with a cut  $0.5 \leq M \leq 1$  GeV and rapidity  $y=0$ . For medium dileptons we use  $\gamma=2$  and  $\tau_{\text{iso}}$  is taken to be either 0.26 (0.088) fm/c or 2 fm/c for RHIC (LHC) energies and fixed final multiplicity. A  $K$ -factor of 6 was applied to account for NLO corrections and rapidity  $y=0$ . Dilepton yields from Drell Yan, Jet-Thermal and Jet-Fragmentation were obtained from Ref. [146].

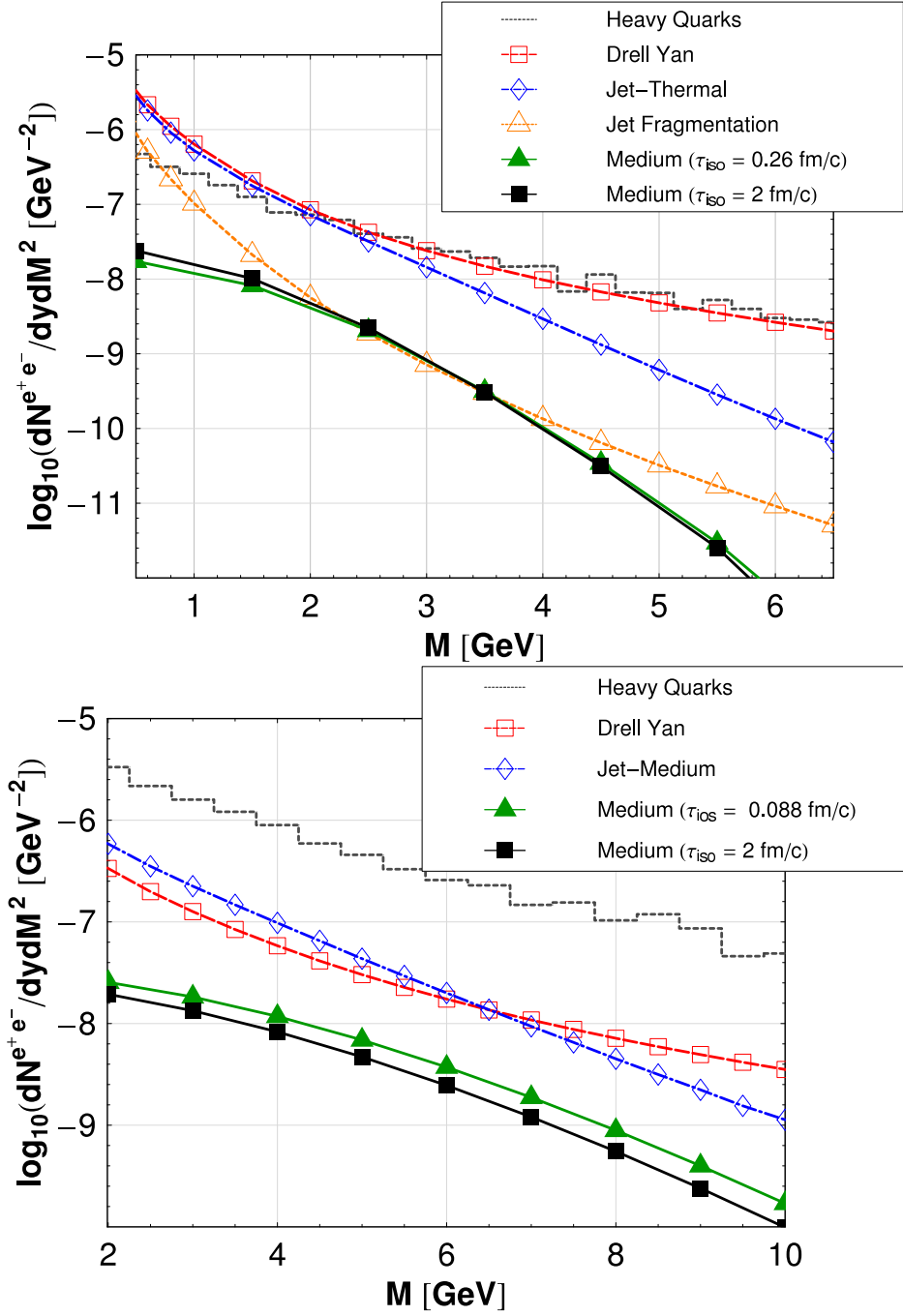


Figure 5.12.: Collisionally-broadened interpolating model dilepton yields as a function of invariant mass in central Au+Au collisions at RHIC (left) and Pb+Pb at the LHC (right), with a cut  $p_T \geq 4$  (8) GeV and rapidity  $y=0$ . For medium dileptons we use  $\gamma=2$  and  $\tau_{\text{iso}}$  is taken to be either 0.26 (0.088) fm/c or 2 fm/c for RHIC (LHC) energies and fixed final multiplicity. A  $K$ -factor of 1.5 was applied to account for NLO corrections. Dilepton yields from Drell Yan, Heavy Quarks, Jet-Thermal and Jet-Fragmentation were obtained from Ref. [146].

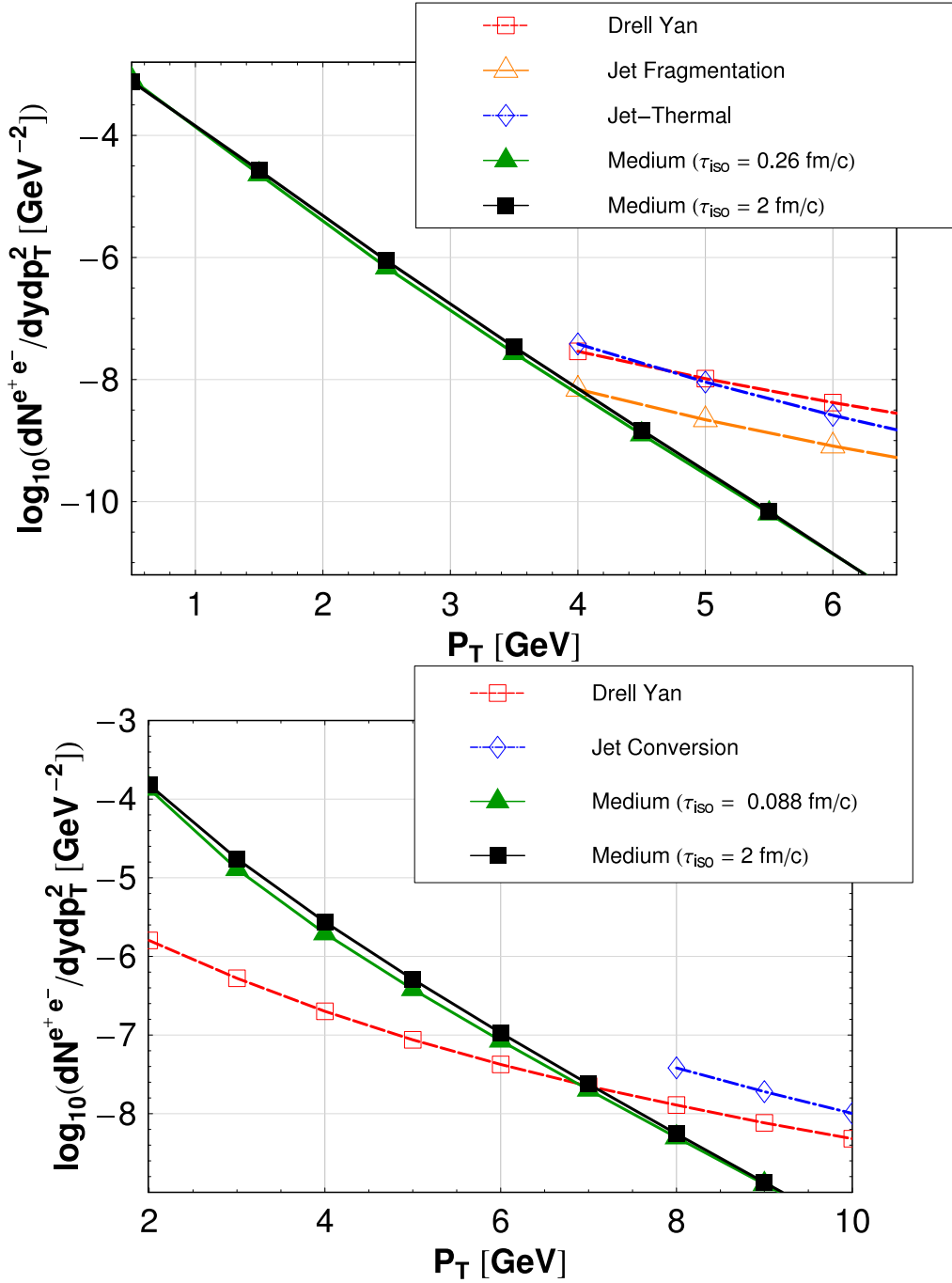


Figure 5.13.: Collisionally-broadened interpolating model dilepton yields as a function of transverse momentum in central Au+Au collisions at RHIC (left) and Pb+Pb at the LHC (right), with a cut  $0.5 \leq M \leq 1 \text{ GeV}$  and rapidity  $y=0$ . For medium dileptons we use  $\gamma=2$  and  $\tau_{\text{iso}}$  is taken to be either 0.26 (0.088) fm/c or 2 fm/c for RHIC (LHC) energies and fixed final multiplicity. A  $K$ -factor of 6 was applied to account for NLO corrections. Dilepton yields from Drell Yan, Jet-Thermal and Jet-Fragmentation were obtained from Ref. [146].

### 5.2.9. Summary of Results

Based on the figures presented in the previous sections we see that the best opportunity for measuring information about plasma initial conditions is from the  $M < 2$  GeV dilepton transverse momentum spectra between  $1 < p_T < 6$  GeV at RHIC and  $2 < p_T < 8$  GeV at LHC. This is due to the fact that medium dilepton yields dominate other mechanisms in that kinematic range and hence give the cleanest possible information about plasma initial conditions. In all cases shown above dilepton production is enhanced by pre-equilibrium emissions with the largest enhancements occurring when assuming fixed initial conditions and the free-streaming interpolating model. As we have mentioned above, this model sets the upper-bound for the expected dilepton enhancement. Our most physically realistic model is the collisionally-broadened interpolating model with fixed final multiplicity so we will use it for our final predictions of expected dilepton enhancement. For this model, as can be seen from Fig. 5.14, assuming  $\tau_{\text{iso}} = 2$  fm/c we find a 20-40% enhancement in dilepton yields at RHIC and 30-50% at LHC.

In addition we have calculated the dilepton enhancement for different assumed values for  $\tau_{\text{iso}}$ . This is shown for RHIC energies (left) and LHC energies (right) in Fig. 5.15 where we have fixed  $\gamma = 2$  and varied  $\tau_{\text{iso}}$  to see the effect of varying the assumed isotropization time. As can be seen from this figure the effect of reducing  $\tau_{\text{iso}}$  is to shift the peak in  $\phi$  to larger  $p_T$  while at the same time reducing the overall amplitude of the peak. This feature seems generic at both RHIC and LHC energies. Therefore, in order to see the difference between an instantaneously thermalized QGP with  $\tau_{\text{iso}} = \tau_0$  and one with a later thermalization time requires determining the medium dilepton spectra between  $1 < p_T < 6$  GeV at RHIC and  $2 < p_T < 8$  GeV at LHC with high precision so that one could measure the less than 50% variation resulting from pre-equilibrium emissions.

Finally, we point out that in Fig. 5.15 we have chosen an invariant mass cut of  $0.5 < M < 1$  GeV. Since our model predicts the full yields versus  $M$  and  $p_T$  it is possible to take other cuts (invariant mass and/or transverse momentum). This could be coupled with fits to experimental data, allowing one to fix  $\tau_{\text{iso}}$  and  $\gamma$  via a “multiresolution” analysis. To demonstrate the dependence of  $\phi$  on the mass cut in Fig. 5.16 we show the dilepton enhancement,  $\phi$ , using a mass cut of  $1 < M < 2$  GeV. As can be seen from this Figure the qualitative features of our model’s predictions are similar to the lower mass cut presented in Fig. 5.15; however, for this mass cut we see that there is a stronger suppression of dilepton production at low and high invariant masses if there is late thermalization,  $\tau_{\text{iso}} \gtrsim 2$  fm/c. Such features can be used to constrain the model further when confronted with experimental data.

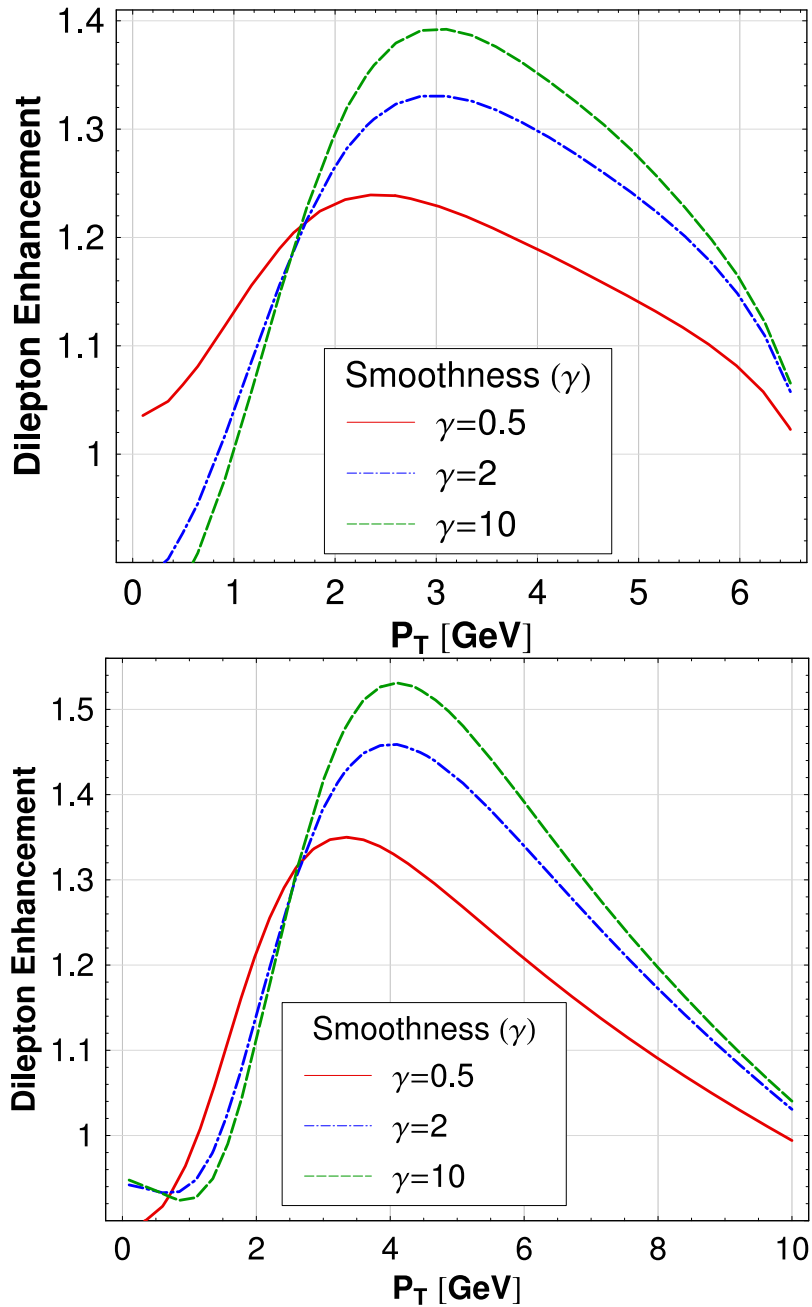


Figure 5.14.: Dilepton enhancement,  $\phi$ , as defined in Eq. (5.43) resulting from our collisionally-broadened interpolating model ( $\delta = 2/3$ ) with fixed final multiplicity and  $\tau_{\text{iso}} = 2 \text{ fm}/c$ . Here we show the results for RHIC energies (top) and for LHC energies (bottom). The invariant mass cut used was  $0.5 \leq M \leq 1 \text{ GeV}$  and rapidity  $y=0$ . Lines show expected pre-equilibrium dilepton enhancements for different values of the transition width  $\gamma$  corresponding to sharp or smooth transitions between pre-equilibrium and equilibrium behavior.



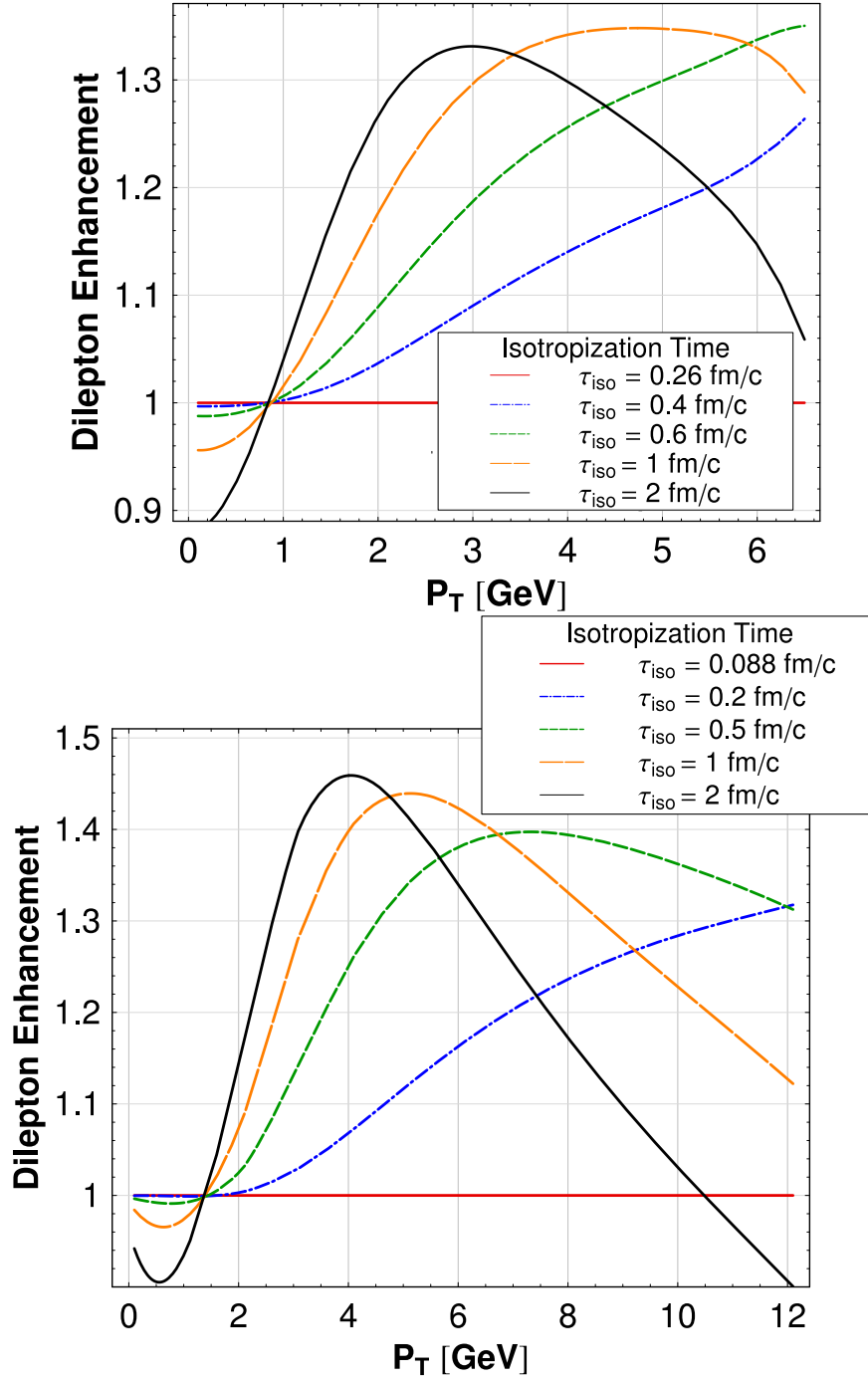


Figure 5.15.: Dilepton enhancement,  $\phi$ , as defined in Eq. (5.43) resulting from our collisionally-broadened interpolating model ( $\delta = 2/3$ ) with fixed final multiplicity and  $\gamma = 2$ . Here we show the results for RHIC energies (top) and for LHC energies (bottom). The invariant mass cut used was  $0.5 \leq M \leq 1$  GeV and rapidity  $y=0$ . Lines show expected pre-equilibrium dilepton enhancements for different values of the assumed plasma isotropization time,  $\tau_{\text{iso}}$ .

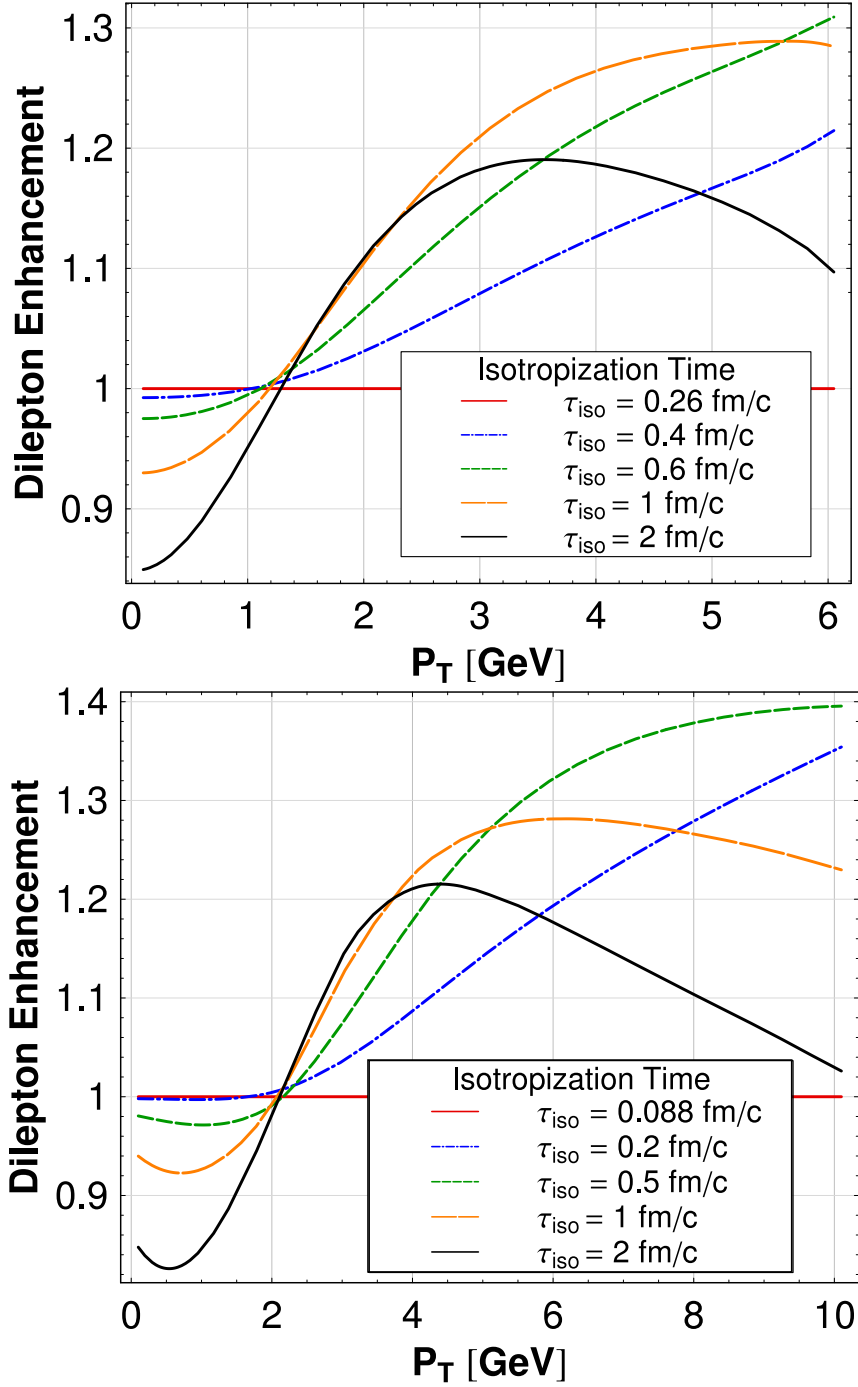


Figure 5.16.: Dilepton enhancement,  $\phi$ , as defined in Eq. (5.43) resulting from our collisionally-broadened interpolating model ( $\delta = 2/3$ ) with fixed final multiplicity and  $\gamma = 2$ . Here we show the results for RHIC energies (top) and for LHC energies (bottom). The invariant mass cut used was  $1 \leq M \leq 2$  GeV and rapidity  $y=0$ . Lines show expected pre-equilibrium dilepton enhancements for different values of the assumed plasma isotropization time,  $\tau_{\text{iso}}$ .

### 5.3. Dilepton yields from the pre-equilibrated stage: forward rapidity region

Our previous calculations considered high-energy dileptons in the central rapidity region. In this section, we extend our approach by considering the impact of the momentum-space anisotropies on the full rapidity dependence of medium dilepton production. We find that at LHC energies, dilepton yields are suppressed by a factor of 3 around  $y \sim 9$  if one chooses  $\tau_{\text{iso}} = 2$  fm/c. Dilepton production in the forward rapidity region has been studied before in relativistic heavy ion collisions [165, 166, 167, 168, 169, 170]<sup>3</sup>. Here we propose to use forward dileptons to experimentally determine the time of the onset of locally isotropic hydrodynamic expansion and the degree of the anisotropy created at early-times in high-energy nucleus-nucleus collisions.

We consider the space-time dependence of  $p_{\text{hard}}$  and  $\xi$ . In Sect. 5.2 the expansion of the plasma was limited to be boost invariant. The inclusion of rapidity dependence breaks down this condition, and in a realistic non-boost-invariant system  $p_{\text{hard}}$  will depend of the rapidity on the quark and anti-quark and hence the differential dilepton rate (5.8) will depend not only on the difference of  $y - \eta$  but also on  $\eta$  itself. Here we improve the proposed models presented in Sect. 5.2 including the rapidity dependence of  $p_{\text{hard}}$  (see Sect. 5.3.1).

Once the space-time dependence of  $p_{\text{hard}}$  and  $\xi$  is modeled, the final rapidity spectra of high-energy dileptons are obtained as follows

$$\frac{dN^{l^+l^-}}{dy} = \pi R_T^2 \int dM^2 d^2 p_T \int_{\tau_0}^{\tau_f} \int_{-\infty}^{\infty} \frac{dR^{l^+l^-}}{d^4 P} \tau d\tau d\eta, \quad (5.44)$$

where  $R_T = 1.2 A^{1/3}$  fm is the radius of the nucleus in the transverse plane. Similar to the case of the central rapidity region, this expression is evaluated in the center-of-mass (CM) frame while the differential dilepton rate is calculated in the local rest frame (LR) of the emitting region. Then, the dilepton pair energy has to be understood as  $E_{LR} = p_T \cosh(y - \eta)$  in the differential dilepton rate  $dR^{l^+l^-}/d^4 P$ . Substituting the differential dilepton rate Eq. (5.8) into Eq. (5.44), we obtain the dilepton spectrum as a function of the rapidity including the effect of a time-dependent momentum anisotropy.

One can be worried if either transverse expansion or mixed/hadronic phases in Eq. (5.44) will affect the production of high-energy dileptons presented here. Fortunately, in the kinematic region studied here this is not the case and these effects turn out to be negligible (1-2% effect) compared with the longitudinal expansion [82].

#### 5.3.1. Space-time interpolating models with the rapidity dependence

We model the space-time evolution of the energy density ( $p_{\text{hard}}$ ) by assuming that its functional form is the product of two functions: one indicates the temporal evolution and the other one is associated with the rapidity dependence. To take into account the temporal dependence that interpolates from early-time pre-equilibrated plasma to late-time ideal hydrodynamical expansion, we use the interpolating model for fixed final multiplicity introduced already in Sect. 5.2.8 [83]. For the rapidity dependence we use the prescription described in [171] (see explanation below). The space-time evolution of the energy density, the hard momentum scale and the anisotropy parameter for general  $\delta$  is given by

$$\xi(\tau, \delta) = (\tau/\tau_0)^{\delta(1-\lambda(\tau))} - 1, \quad (5.45a)$$

$$\mathcal{E}(\tau, \eta) = \mathcal{E}_0 \mathcal{R}(\xi) \bar{U}^{4/3}(\tau) F^4(\eta), \quad (5.45b)$$

$$p_{\text{hard}}(\tau, \eta) = T_0 \bar{U}^{1/3}(\tau) F(\eta), \quad (5.45c)$$

<sup>3</sup>The author thanks to Prof.Dr. Mihai Petrovici for pointing out many of these references.

with  $\mathcal{R}(\xi)$  defined in Eq. (5.14). For fixed final multiplicity, we have

$$\begin{aligned} \mathcal{U}(\tau) &\equiv \left[ \mathcal{R}\left(\left(\tau_{\text{iso}}/\tau_0\right)^\delta - 1\right) \right]^{3\lambda(\tau)/4} \left(\frac{\tau_{\text{iso}}}{\tau}\right)^{1-\delta(1-\lambda(\tau))/2}, \\ \bar{\mathcal{U}}(\tau) &\equiv \mathcal{U}(\tau)/\mathcal{U}(\tau_{\text{iso}}^+), \end{aligned} \quad (5.46a)$$

$$\mathcal{U}(\tau_{\text{iso}}^+) \equiv \lim_{\tau \rightarrow \tau_{\text{iso}}^+} \mathcal{U}(\tau) = \left[ \mathcal{R}\left(\left(\tau_{\text{iso}}/\tau_0\right)^\delta - 1\right) \right]^{3/4} \left(\frac{\tau_{\text{iso}}}{\tau_0}\right). \quad (5.46b)$$

$\delta = 2 (2/3)$  for the case of 1d free streaming (collisionally broadened) expansion interpolating to 1d ideal hydrodynamic expansion. In Eq. 5.45,  $\lambda(\tau, \tau_{\text{iso}}, \gamma)$  is the smeared step function introduced in Sect. 5.2.1 (Eq. 5.35)

$$\lambda(\tau, \tau_{\text{iso}}, \gamma) \equiv \frac{1}{2} \left( \tanh \left[ \frac{\gamma(\tau - \tau_{\text{iso}})}{\tau_{\text{iso}}} \right] + 1 \right).$$

where  $\gamma^{-1}$  sets the width of the transition between non-equilibrium and hydrodynamical evolution in units of  $\tau_{\text{iso}}$ .

Compared with the interpolating model described in Sect. 5.2.1, our main goal with the modification of the energy density  $p_{\text{hard}}$  is to explore the phenomenological consequences in the forward rapidity region where the effect of early-time anisotropies is expected to be maximal. We are not attempting to describe the physics of the forward rapidity region from first principles,<sup>4</sup> instead, we implement a Gaussian fit profile for the rapidity dependence which successfully describes experimentally observed pion rapidity spectra from AGS to RHIC energies [176, 177, 178, 179, 171] and use this to extrapolate to high energies

$$F(\eta) = \exp\left(-\frac{\eta^2}{2\sigma_\eta^2}\right), \quad (5.47)$$

with

$$\sigma_\eta^2 = \frac{8}{3} \frac{c_s^2}{(1 - c_s^4)} \ln(\sqrt{s_{NN}}/2m_p), \quad (5.48)$$

where  $c_s$  is the sound velocity and  $m_p$  is the proton mass.

Note that once the rapidity dependence in the parton momentum distribution functions is implemented, boost invariance along the longitudinal axis breaks down. This procedure leads to a violation of the conservation laws expressed by hydrodynamics unless a finite baryon chemical potential is introduced [180]. It is possible to demonstrate that for a longitudinal scaling expansion,  $\partial\mathcal{P}(T, \mu)/\partial\eta=0$ , where  $\mathcal{P}$  is the pressure and  $T$  is the temperature. This condition is equivalent to [110]<sup>5</sup>

$$\mathcal{S} \frac{\partial T}{\partial \eta} + n \frac{\partial \mu}{\partial \eta} = 0, \quad (5.49)$$

where  $\mathcal{S}$  and  $n$  denote the entropy density and particle number density, respectively. In the present context we don't have to worry about the presence of finite chemical potentials since we are considering high-energy dilepton production and  $E/T \gg \mu/T$  is satisfied. Therefore, in the differential dilepton rate  $dR/d^4P$ , Eq.(5.8), the product of the distribution functions  $f_q(\mathbf{p}_q, +\mu) f_{\bar{q}}(\mathbf{p}_{\bar{q}}, -\mu) \approx f_q(\mathbf{p}_q) f_{\bar{q}}(\mathbf{p}_{\bar{q}})$ .

In Fig. 5.17, the temporal evolution of the anisotropy parameter  $\xi(\tau)$  is plotted using Eq. (5.45a). In Fig. 5.18, we show the time and rapidity dependence of  $p_{\text{hard}}(\tau, \eta)$  (right and left panel, respectively) using Eq. (5.45c).

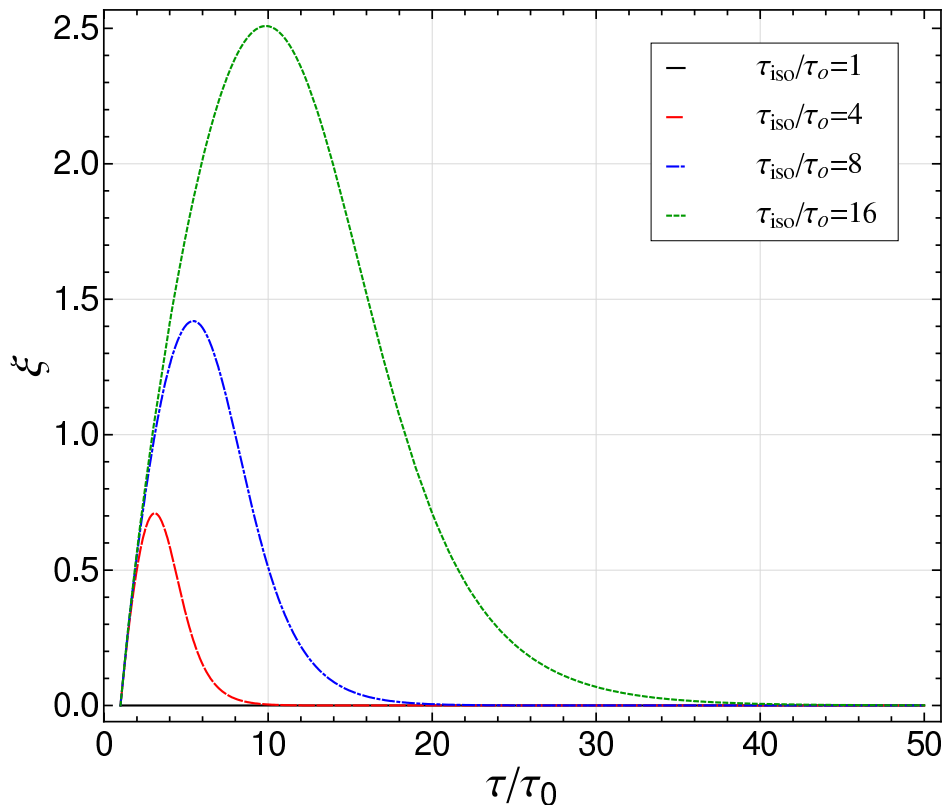


Figure 5.17.: Temporal evolution of the plasma anisotropy parameter using our collisionally-broadened interpolating model for four different isotropization times  $\tau_{\text{iso}} \in \{1, 4, 6, 18\} \tau_0$ . The transition width is taken to be  $\gamma = 2$ . To convert to physical scales use  $\tau_0 \sim 0.1$  fm/c for LHC energies.

### 5.3.2. Results of high-energy dileptons in the forward rapidity region

In this section, we will present our predicted dilepton yields as a function of the rapidity from a Pb-Pb collision at LHC full beam energy,  $\sqrt{s_{NN}} = 5.5$  TeV. At this center-of-mass energy we use  $\tau_0 = 0.088$  fm/c,  $T_0 = 845$  MeV,  $R_T = 7.1$  fm and the critical temperature  $T_c = 160$  MeV. The kinematic cuts in the transverse momentum and invariant mass of the dilepton yields are indicated in the corresponding results. Also, we use  $c_s^2 = 1/3$  and  $m_p = 0.938$  GeV in Eq. (5.48).

Before presenting our results we first explain the numerical procedure used for our calculations. Because the differential dilepton rate  $dR^{l^+l^-}/d^4P$  given in Eq. (5.8) is independent of the assumed space-time model, we first evaluate it numerically using double-exponential integration with a target precision of  $10^{-9}$ . The result for the rate was then tabulated on a uniformly-spaced 4-dimensional grid in  $M$ ,  $p_T$ ,  $y$ , and  $\xi$ :  $M/p_{\text{hard}}, p_T/p_{\text{hard}} \in \{0.1, 20\}$ ,  $y \in \{-10, 10\}$  and  $\xi \in \{0, 5\}$ . This table was then used to build a four-dimensional interpolating function which was valid at continuous values of these four variables. We then boosted this rate from the local reference frame to center-of-mass frame and evaluated the remaining integrations over space-time ( $\tau$  and  $\eta$ ), transverse momentum and invariant mass appearing in Eq. (5.44) using quasi-Monte Carlo integration with  $\tau \in \{\tau_0, \tau_f\}$ ,

<sup>4</sup>Some proposals have been mentioned in the literature, see Ref. [172, 173, 174, 175]

<sup>5</sup>Partial derivatives with respect to  $\eta$  are performed at constant  $\tau$ .

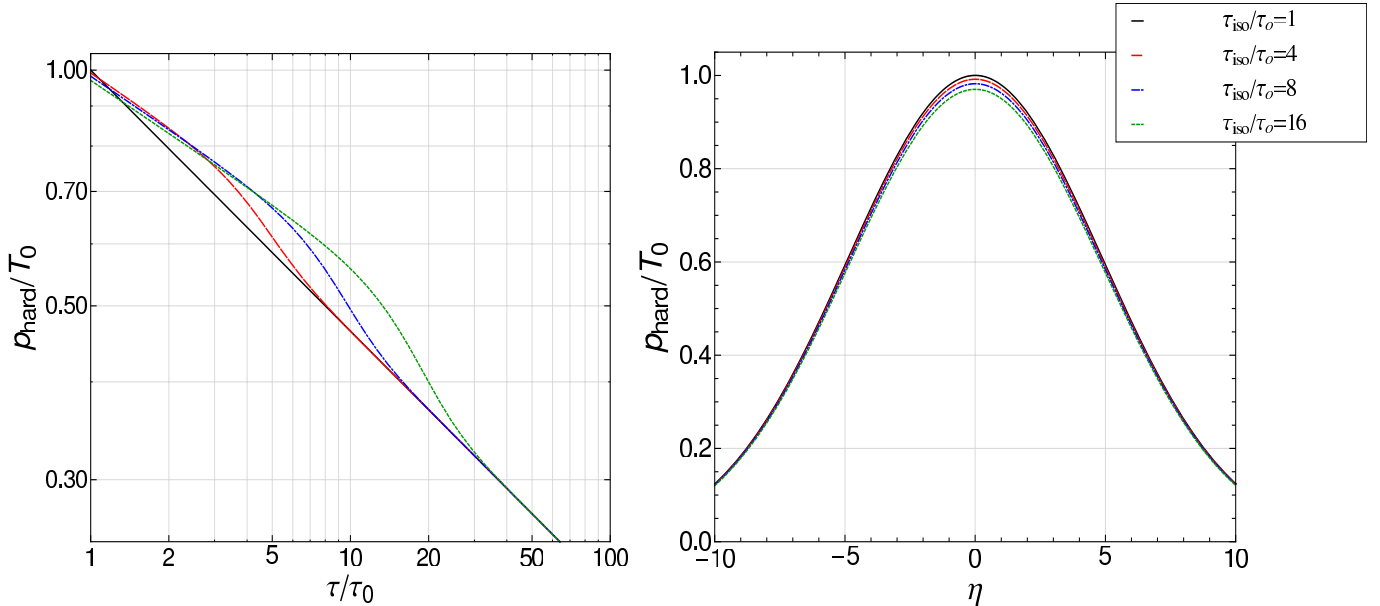


Figure 5.18.: Temporal evolution (left panel) and rapidity dependence (right panel) of the hard momentum scale,  $p_{\text{hard}}$  using our fixed final multiplicity collisionally-broadened interpolating model for the hard momentum scale for four different isotropization times  $\tau_{\text{iso}} \in \{1, 4, 8, 16\} \tau_0$ . The transition width is taken to be  $\gamma = 2$ . To convert to physical units use  $\tau_0 \sim 0.1 \text{ fm}/c$  for LHC energies. For the rapidity dependence of  $p_{\text{hard}}$  (right panel) we used a constant value of  $\tau \sim 0.1 \text{ fm}/c$  and the width  $\sigma_\eta^2 \sim 8$ .

$\eta \in \{-10, 10\}$  and, depending on the case, restricted the integration to any cuts specified in  $M$  or  $p_T$ .

Our final integration time,  $\tau_f$ , was set by solving numerically for the point in time at which the temperature in our interpolating model is equal to the critical temperature, i.e.  $p_{\text{hard}}(\tau_f, \eta) = T_C$ . We will assume that when the system reaches  $T_C$ , all medium emission stops. Note that due to the fact that  $p_{\text{hard}}$  depends on the parton rapidity, the plasma lifetime now depends on which rapidity slice you are in, with higher rapidities having a shorter lifetime due to their lower initial “temperature”. We are not taking into account the emission from the mixed/hadronic phase at late times since the kinematic regime we study (high  $M$  and  $p_T$ ) is dominated by early-time high-energy dilepton emission [82, 156].

We show our predicted dilepton spectrum as a function of the pair rapidity,  $y$ , for LHC energies using our model described by Eqs. (5.45) in Fig. 5.19. From this, we see that for LHC energies there is a suppression when we vary the isotropization time from  $\tau_0$  to  $2 \text{ fm}/c$ . This suppression can be explained qualitatively by two mechanisms. The first one, the anisotropic nature of the distribution function as a consequence of the rapid expansion implies that dileptons with larger values of longitudinal momentum are reduced compared with the case of an isotropic distribution function. The suppression will depend on the maximum amount of momentum-space anisotropy achieved at early times and also on the time dependence of the anisotropy parameter  $\xi$ . Here we consider a realistic scenario for a collisionally-broadened plasma. The other source of rapidity dependence of the final dilepton spectra is related to the fact that the hard momentum scale (“temperature”) depends explicitly on the rapidity  $\eta$ , even in the case of instantaneous thermalization. To generate Fig. 5.19 we have applied a cut  $M \geq 2 \text{ GeV}$  and  $P_T \geq 100 \text{ MeV}$ . As can be seen from this figure an isotropization time of  $\tau_{\text{iso}} = 2 \text{ fm}/c$  results in fewer dileptons as compared to “instantaneous”

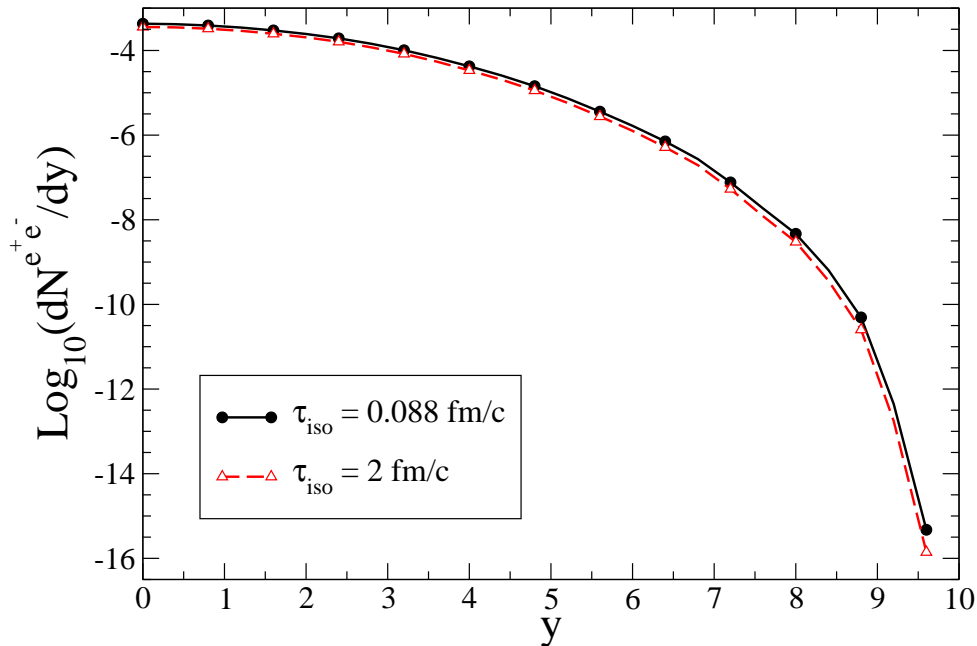


Figure 5.19.: Fixed final multiplicity condition collisionally-broadened interpolating model dilepton yields as a function of rapidity in Pb-Pb collisions at LHC, with a cut  $M \geq 2$  GeV and  $P_T \geq 100$  MeV. For medium dileptons we use  $\gamma = 2$  and  $\tau_{\text{iso}}$  to be either 0.088 or 2 fm/c for LHC energies.

isotropization  $\tau_{\text{iso}} = 0.088$  fm/c. This suppression is enhanced at forward rapidities.

In order to quantify the effect of the pre-equilibrium emission we define the “dilepton modification” factor as the ratio of the dilepton yield obtained with an isotropization time of  $\tau_{\text{iso}}$  to that obtained from an instantaneously thermalized plasma undergoing only 0+1 hydrodynamical expansion, i.e.  $\tau_{\text{iso}} = \tau_0$

$$\Phi(\tau_{\text{iso}}) \equiv \left( \frac{dN^{e^+e^-}(\tau_{\text{iso}})}{dy} \right) \bigg/ \left( \frac{dN^{e^+e^-}(\tau_{\text{iso}} = \tau_0)}{dy} \right). \quad (5.50)$$

This ratio measures how large the effect of early-time momentum anisotropies are on medium dilepton production. In the case of instantaneous isotropization,  $\Phi(\tau_{\text{iso}})$  is unity, and for  $\tau_{\text{iso}} > \tau_0$  any deviation from unity indicates a modification of medium dilepton production due to pre-equilibrium emissions.

In Fig. 5.20 we show our prediction for the rapidity dependence of the high-energy dilepton modification factor,  $\Phi(\tau_{\text{iso}})$ , for three different assumed plasma isotropization times,  $\tau_{\text{iso}} \in \{0.1, 1, 2\}$  fm/c. To generate this figure we have applied a cut  $M \geq 2$  GeV and  $P_T \geq 100$  MeV. As can be seen from this figure a isotropization time of  $\tau_{\text{iso}} = 2$  fm/c results in fewer dileptons as compared to “instantaneous” isotropization  $\tau_{\text{iso}} = 0.088$  fm/c. This suppression is enhanced at forward rapidities and reaches a maximum suppression of a factor of 3 at extremely forward rapidities.

Using the dilepton modification factor as our criterion we find that for our collisionally-broadened interpolating model with fixed final multiplicity, the dilepton yields as a function of the rapidity at  $\tau_{\text{iso}} = 2$  fm/c can be suppressed up to  $\sim 20\%$  for  $0 < y \lesssim 4$ . The suppression of dilepton yields is more dramatic at rapidity values around  $y \sim 9$  and can be as large as a factor of 3. With

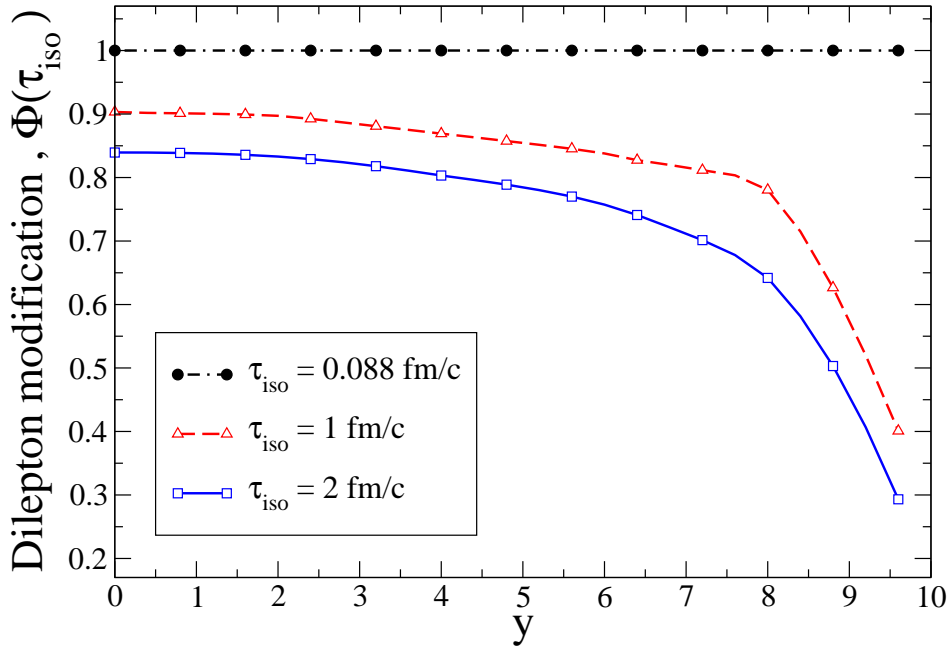


Figure 5.20.: Predicted dilepton modification factor,  $\Phi(\tau_{\text{iso}})$ , for three different assumed plasma isotropization times,  $\tau_{\text{iso}} \in \{0.1, 1, 2\}$  fm/c. Cuts are the same as in Fig. 5.19.

sufficiently accurate experimental results this could give an experimental method for determining the isotropization time of a quark gluon plasma as formed in an ultrarelativistic nuclear collision.

## 5.4. Conclusions

In this chapter we show that dilepton yields are a sensitive observable for determining early-time momentum space anisotropies. We proposed two models that take into account the evolution of the space-time momentum anisotropy of the parton distribution functions. Our phenomenological models interpolate from 0+1 pre-equilibrium expansion (free streaming and collisionally broadening) at early times to 0+1 ideal hydrodynamics. To do that, we included the proper-time dependence of the parton hard momentum scale,  $p_{\text{hard}}$ , and the anisotropy parameter of the QGP plasma,  $\xi$ . We generalized our models by including the rapidity dependence of  $p_{\text{hard}}$ .

In the central region, dilepton production as a function of the transverse momentum is a promising observable to obtain information about  $\tau_{\text{iso}}$  at RHIC and LHC energies. High  $p_T$  dileptons are sensitive to the assumed value  $\tau_{\text{iso}}$ . Our calculations indicate that high  $p_T$  dileptons are enhanced at RHIC energies in the kinematic range  $1 < p_T < 6$  GeV and at LHC energies,  $2 < p_T < 8$  GeV. Additionally, it may be possible to estimate the maximum amount of momentum-space anisotropy achieved during the lifetime of the QGP using the phenomenological model presented here. The effect of varying  $\tau_{\text{iso}}$  is also large in the dilepton spectra vs invariant mass but Drell-Yan and jet conversion production can be on the same order (or even larger) than medium dilepton production, thus making it difficult to measure a clean medium dilepton signal. In the forward rapidity region we find that forward dilepton production is suppressed; for  $0 < y \lesssim 4$ , forward dileptons can be 20% suppressed compared with an ‘instantaneous’ equilibrated QGP plasma whereas for  $y \sim 9$  the suppression factor can be up to a factor of 3.



---

Future work on dilepton production will incorporate the possibility of late-time persistent anisotropies (finite viscosity), NLO order corrections and finite chemical potentials. In addition, the proposed interpolating models can be used to assess the impact of momentum-space anisotropies on other observables such as jet-medium-induced electromagnetic radiation, photon production and heavy-quark transport.

In the next chapter we will construct a method for matching early-time pre-equilibrium dynamics to 2nd order viscous hydrodynamics and discuss constraints which can be placed on the matching time and matched values.



## 6. Constraining the onset of relativistic viscous hydrodynamics

But he also recognized that knowledge never stayed still, and that today's certainties might become tomorrow's superstitions. Therefore the intellectual duty to continue looking never ceased.

---

*Arthur & George  
Julian Barnes.*

Historically, in order to make phenomenological predictions for experimental observables, fluid hydrodynamics has been used to model the space-time evolution and non-equilibrium properties of the expanding matter. The validity of hydrodynamics relies on the assumption that the mean free path is small compared with the size of the system. However, the hot and dense matter created in the collisions between heavy ions expands at almost the speed of light, thus casting doubt on the applicability of fluid hydrodynamics to ultrarelativistic heavy ion collisions.

After the first results of RHIC, it was somewhat of a surprise that ideal hydrodynamics could reproduce the hadron transverse momentum spectra in central and semi-peripheral collisions. Ideal hydrodynamical models were fairly successful in describing the dependence of  $v_2$  on the hadron rest mass for transverse momenta up to about 1.5-2 GeV/c [22, 23, 24, 25]. This observation led to the conclusion that the QGP formed at RHIC could have a short thermalization time ( $\tau_{\text{hydro}} \lesssim 1 \text{ fm}/c$ ) and a low shear viscosity.<sup>1</sup> As a result, it was posited that the matter created in the experiment behaves like a nearly perfect fluid starting at very early times after the collision. However, recent results from viscous hydrodynamical simulations which include all 2nd-order transport coefficients consistent with conformal symmetry [1] have shown that estimates of the thermalization time are rather uncertain due to poor knowledge of the proper initial conditions, details of plasma hadronization, subsequent hadronic cascade, etc. As a result, it now seems that thermalization times of up to  $\tau_{\text{hydro}} \sim 2 \text{ fm}/c$  are not completely ruled out by RHIC data.

One of the key ingredients necessary to perform any numerical simulation using fluid hydrodynamics is the proper choice of initial conditions at the initially simulated time ( $\tau_{\text{hydro}}$ ). These initial conditions include the initial fluid energy density  $\epsilon$ , the initial components of the fluid velocity  $u^\mu$  and the initial shear tensor  $\Pi^{\mu\nu}$ . Once the set of initial conditions is known, it is “simple” to follow the subsequent dynamics of the fluid equations in simulations. At the moment there is no first principles calculation that allows one to determine the initial conditions necessary. Two different approaches are currently used for numerical simulations of fluids in heavy-ion collisions: Glauber type [181] or Color Glass Condensate (CGC) initial conditions [182]. The selection of either of these models as the initial state of hydrodynamics introduces theoretical uncertainties. For example, in the analysis of charged hadron elliptic flow data from the STAR experiment based on conformal viscous hydrodynamical model, Luzum and Romatschke [1] found an allowed range  $0 < \eta/S < 0.1$  for Glauber and  $0.08 < \eta/S < 0.2$  for CGC initial conditions. The difference of the extracted values of  $\eta/S$  between both models is a consequence of the initial values of the eccentricity, with the

---

<sup>1</sup>In Chapter 5, we introduced  $\tau_{\text{iso}}$  as the time when the system is almost completely isotropic in momentum-space and therefore, ideal hydrodynamical behavior is an appropriate model to describe it.  $\tau_{\text{iso}}$  should not be confused with  $\tau_{\text{hydro}}$ . Here  $\tau_{\text{hydro}}$  is the time when one considers that the matter is close to local equilibrium, and viscous hydrodynamics can be used as a tool to model the dynamics of the expansion of the fireball.

CGC model allowing approximately  $\sim 30\%$  larger initial eccentricities than the Glauber Model [183]. Moreover, the values of the components of the shear tensor  $\Pi^{\mu\nu}$  at  $\tau_{\text{hydro}}$  are also affected by the choice of either CGC or Glauber initial conditions (see discussion in Sect. 4 of Ref. [184]). In the case of Glauber initial conditions the shear tensor is completely unconstrained. In the case of CGC initial conditions there is a prescription for calculating the initial shear; however, with CGC initial conditions the longitudinal pressure is zero due to the assumption of exact boost invariance and the subsequent thermalization of the system could completely change the initial shear obtained in the CGC approximation. Therefore, in both cases it would seem that the initial shear is completely unconstrained. Given these uncertainties it would be useful to have a method which can help to constrain the allowed initial conditions used in hydrodynamical simulations. In this chapter we focus on this issue.

Firstly, we present two criteria that impose lower bounds on the initial time  $\tau_{\text{hydro}}$ . By requiring that during all the simulated times, the solutions of viscous hydrodynamics satisfy: (1) positivity of the effective longitudinal pressure  $\mathcal{P}_L \geq 0$ , and (2) the size of all the components of the shear viscous tensor  $\Pi^{\mu\nu}$  to be small compared with the isotropic pressure  $\mathcal{P}$ , e.g.,  $|\Pi^{\mu\nu}| \leq \alpha\mathcal{P}$ , where  $\alpha$  is an arbitrary but not large number, i.e.,  $0 \leq \alpha \leq 1$ . We find that by imposing these requirements over the solutions of the viscous hydrodynamical behavior, the allowed  $\tau_{\text{hydro}}$  is non-trivially related with the initial condition of the shear tensor  $\Pi_{\text{hydro}}$  and the initial energy density  $\mathcal{E}_{\text{hydro}}$ . We show this by solving 0+1 dimensional 2nd-order conformal viscous hydrodynamics [125, 103].

In the last part of this chapter, we demonstrate how to match pre-equilibrium dynamics of a 0+1 dimensional quark gluon plasma to 2nd-order viscous hydrodynamical evolution. The matching allows us to specify the initial values of the energy density and shear tensor at the initial time of hydrodynamical evolution as a function of the lifetime of the pre-equilibrium period. We compare two models for the pre-equilibrium quark-gluon plasma, longitudinal free streaming and collisionally-broadened longitudinal expansion, and present analytic formulas which can be used to fix the necessary components of the energy-momentum tensor. The resulting dynamical models can be used to assess the effect of pre-equilibrium dynamics on quark-gluon plasma observables. Additionally, we investigate the dependence of entropy production on pre-equilibrium dynamics and discuss the limitations of the standard definitions of the non-equilibrium entropy.

This chapter is based on the following publications:

1. Mauricio Martinez and Michael Strickland, *Constraining relativistic viscous hydrodynamical evolution*, Phys. Rev. C **79**: 044903, 2009 [121].
2. Mauricio Martinez and Michael Strickland, *Matching pre-equilibrium dynamics and viscous hydrodynamics*, arXiv:0909.0264 [hep-ph] [122], accepted for publication in PRC.

## 6.1. 0+1 Dimensional Conformal 2nd-Order Viscous Hydrodynamics

From the conservation of the energy momentum tensor,  $\partial_\mu T^{\mu\nu} = 0$ , and the formalism of 2nd-order conformal viscous hydrodynamics explained in Section 3.2.3, the equations of motion for the energy density, flow velocity and shear viscous tensor are respectively,

$$D\mathcal{E} + (\mathcal{E} + \mathcal{P})\partial_\mu u^\mu - \Pi^{\mu\nu}\nabla_{(\mu}u_{\nu)} = 0, \quad (6.1a)$$

$$(\mathcal{E} + \mathcal{P})Du^\alpha - \nabla^\alpha\mathcal{P} + \Delta_\mu^\alpha\partial_\nu\Pi^{\mu\nu} = 0, \quad (6.1b)$$

$$\begin{aligned} \Pi^{\mu\nu} = & \eta\nabla^{\langle\mu}u^{\nu\rangle} - \tau_\pi \left[ \Delta_\alpha^\mu\Delta_\beta^\nu D\Pi^{\alpha\beta} + \frac{4}{3}\Pi^{\mu\nu}(\nabla_\alpha u^\alpha) \right] + \frac{\kappa}{2} [R^{\langle\mu\nu\rangle} + 2u_\alpha R^{\alpha\langle\mu\nu\rangle\beta}u_\beta] \\ & - \frac{\lambda_1}{2\eta^2}\Pi^{\langle\mu}_\lambda\Pi^{\nu\rangle\lambda} - \frac{\lambda_2}{2\eta}\Pi^{\langle\mu}_\lambda\Omega^{\nu\rangle\lambda} - \frac{\lambda_3}{2}\Omega^{\langle\mu}_\lambda\Omega^{\nu\rangle\lambda}. \end{aligned} \quad (6.1c)$$

Due to the different couplings of the hydrodynamical degrees of freedom, this set of coupled partial differential equations are highly nonlinear and solving them analytically is not an appropriate approach, so the best method for obtaining solutions of these equations is to perform numerical simulations. For 2+1 dimensions, such calculations have been already studied and applied to RHIC results at  $\sqrt{s}=200$  GeV [1] and predictions of the integrated elliptic flow coefficient  $v_2$  in  $\sqrt{s}=5.5$  TeV Pb-Pb and  $\sqrt{s}=14$  TeV proton-proton collisions at the LHC [185].

We solve Eqs. (6.1) for 0+1 dimensional case by considering a system expanding in a boost invariant manner along the longitudinal (beamline) direction with a uniform energy density along the transverse plane. For this simplest heavy-ion collision model, it is enough to consider expansion in a flat space. Because of these assumptions, there is no fluid vorticity and the energy density and the shear viscous tensor only depend on proper time  $\tau$ . For this 0+1 dimensional model the 2nd-order viscous hydrodynamic equations (6.1) are rather simple in the Milne coordinates,  $\tau = \sqrt{t^2 - z^2}$ , and space-time rapidity,  $\zeta = \text{arctanh}(z/t)$ , which are expressed in terms of the  $(t, z)$  [125, 103]

$$\partial_\tau \mathcal{E} = -\frac{\mathcal{E} + \mathcal{P}}{\tau} + \frac{\Pi}{\tau}, \quad (6.2a)$$

$$\partial_\tau \Pi = -\frac{\Pi}{\tau_\pi} + \frac{4\eta}{3\tau_\pi\tau} - \frac{4}{3\tau}\Pi - \frac{\lambda_1}{2\tau_\pi\eta^2}\Pi^2, \quad (6.2b)$$

where  $\mathcal{E}$  is the fluid energy density,  $\mathcal{P}$  is the fluid pressure,  $\Pi \equiv \Pi_\zeta^\zeta$  is the  $\zeta\zeta$  component of the fluid shear tensor,  $\eta$  is the fluid shear viscosity,  $\tau_\pi$  is the shear relaxation time, and  $\lambda_1$  is a coefficient which arises in complete 2nd-order viscous hydrodynamical equations either in the strong [103, 104] or weakly coupled limit [135, 136, 125, 138, 105]. The Navier-Stokes limit is recovered upon taking  $\tau_\pi \rightarrow 0$  and  $\lambda_1 \rightarrow 0$  in which case one obtains  $\Pi_{\text{NS}} = 4\eta/(3\tau)$ .

These coupled differential equations are completed by a specification of the equation of state which relates the energy density and the pressure through  $\mathcal{P} = \mathcal{P}(\mathcal{E})$  and initial conditions. For 0+1 dimensional dynamics one must specify the energy density and  $\Pi$  at the initial time,  $\mathcal{E}_{\text{hydro}} \equiv \mathcal{E}(\tau_{\text{hydro}})$  and  $\Pi_{\text{hydro}} \equiv \Pi(\tau_{\text{hydro}})$ , where  $\tau_{\text{hydro}}$  is the proper-time at which one begins to solve the differential equations.

### 6.1.1. Specification of equation of state and dimensionless variables

In the following analysis we will assume an ideal equation of state, in which case we have

$$\mathcal{P} = \frac{N_{\text{dof}} \pi^2}{90} T^4, \quad (6.3)$$

where for quantum chromodynamics with  $N_c$  colors and  $N_f$  quark flavors,  $N_{\text{dof}} = 2(N_c^2 - 1) + 7N_c N_f/2$  which for  $N_c = 3$  and  $N_f = 2$  is  $N_{\text{dof}} = 37$ . The general method used below, however, can easily be extended to a more realistic equation of state.

In the conformal limit the trace of the four-dimensional stress tensor vanishes requiring  $\mathcal{E} = 3\mathcal{P}$  which, using Eq. (6.3), allows us to write compactly

$$\mathcal{E} = (T/\gamma)^4, \quad \text{with} \quad \gamma \equiv \left( \frac{30}{\pi^2 N_{\text{dof}}} \right)^{1/4}. \quad (6.4)$$

Likewise we can simplify the expression for the equilibrium entropy density,  $\mathcal{S}$ , using the thermodynamic relation  $T\mathcal{S} = \mathcal{E} + \mathcal{P}$  to obtain  $\mathcal{S} = 4\mathcal{E}/3T$  or equivalently

$$\mathcal{S} = \frac{4}{3\gamma} \mathcal{E}^{3/4}. \quad (6.5)$$

Note that for a system out of equilibrium the full non-equilibrium entropy is modified compared to (6.5). Using kinetic theory it is possible to show that the entropy current receives corrections

Transport coefficient	Weakly-coupled QCD	Strongly-coupled $\mathcal{N} = 4$ SYM
$\bar{\eta} \equiv \eta/\mathcal{S}$	$\sim 1/(g^4 \log g^{-1})$	$1/(4\pi)$
$\tau_\pi$	$6\bar{\eta}/T$	$2(2 - \log 2)\bar{\eta}/T$
$\lambda_1$	$(4.1 \rightarrow 5.2)\bar{\eta}^2\mathcal{S}/T$	$2\bar{\eta}^2\mathcal{S}/T$

Table 6.1.: Typical values of the transport coefficients for a weakly-coupled QGP [138, 135, 136] and a strongly coupled  $\mathcal{N} = 4$  SYM plasma [103, 104].

at second order in gradients [102]. In the original approach of Israel and Stewart [126, 119], the non-equilibrium entropy is expanded in a series in deviations from equilibrium and higher order corrections are neglected. The Israel-Stewart (IS) ansatz for the non-equilibrium entropy is

$$\mathcal{S}_{\text{noneq}}^{\text{IS}} = \mathcal{S} - \frac{\beta_2}{2T} \Pi_{\mu\nu} \Pi^{\mu\nu}, \quad (6.6)$$

where  $\beta_2$  is an a priori unknown function which determines the importance of second-order modifications to the entropy current. The IS ansatz satisfies the second law of thermodynamics  $\partial^\mu \mathcal{S}_\mu^{\text{IS}} \geq 0$  and for massless particles described by a Boltzmann distribution function one finds  $\beta_2 = \tau_\pi/(2\eta)$ . Recent analyses have shown that, including all relevant structures in the gradient expansion, the non-equilibrium entropy contains additional terms not present in the simple IS definition of the non-equilibrium entropy [106, 186, 187, 188, 189, 190].

When solving Eqs. (6.2a) and (6.2b) it is important to recognize that the transport coefficients depend on the temperature of the plasma and hence on proper-time. We summarize in Table 6.1 the values of the transport coefficients in the strong [103, 104] and weak coupling limits [138, 135, 136]. We point out that in both cases the transport coefficients do not satisfy universal relations and therefore, their values can only be taken as estimates. In the weakly coupled case the QCD transport coefficients depend on the renormalization scale. In addition, higher order corrections to some transport coefficients from finite-temperature perturbation theory show poor convergence [191, 192]. At strong coupling, it has been shown recently that there are corrections for finite 'tHooft coupling [193, 194, 195, 196, 197]. We take the above estimates in both coupling limits in order to get a qualitative understanding of what to expect in each regime.

From Table 6.1, the reader should note that in the strong and weak coupling limit the coefficients  $\tau_\pi$  and  $\lambda_1$  are proportional to  $\tau_\pi \propto \bar{\eta}/T$  and  $\lambda_1 \propto \bar{\eta}^2\mathcal{S}/T$ , respectively. This fact suggests that we can parametrize both coefficients as

$$\tau_\pi = \frac{c_\pi \bar{\eta}}{T}, \quad (6.7a)$$

$$\lambda_1 = c_{\lambda_1} \bar{\eta}^2 \left( \frac{\mathcal{S}}{T} \right), \quad (6.7b)$$

where we have introduced the scaled shear viscosity

$$\bar{\eta} \equiv \eta/\mathcal{S}. \quad (6.8)$$

In our analysis we assume that  $\bar{\eta}$  is independent of time.

The dimensionless numbers  $\bar{\eta}$ ,  $c_\pi$  and  $c_{\lambda_1}$  carry all of the information about the particular coupling limit we are considering. Using the ideal gas equation of state (Eqs. (6.4) and (6.5)), the parametrization (6.7) of  $\tau_\pi$  and  $\lambda_1$  can be rewritten in terms of the energy density  $\mathcal{E}$

$$\tau_\pi = \frac{c_\pi \bar{\eta}}{\gamma \mathcal{E}^{1/4}}, \quad (6.9a)$$

$$\lambda_1 = \frac{4}{3\gamma^2} c_{\lambda_1} \bar{\eta}^2 \mathcal{E}^{1/2}. \quad (6.9b)$$

To remove the dimensionful scales and rewrite the fluid equations in a more explicit form we define the following dimensionless variables

$$\bar{\mathcal{E}} \equiv \mathcal{E}/\mathcal{E}_{\text{hydro}}, \quad (6.10a)$$

$$\bar{\Pi} \equiv \Pi/\mathcal{E}_{\text{hydro}}, \quad (6.10b)$$

$$\bar{\tau} \equiv \tau/\tau_{\text{hydro}}, \quad (6.10c)$$

After replacing the dimensionless variables (6.10) in the parametrization (6.9) and Eqs. (6.2a) and (6.2b), we rewrite the fluid equations

$$\bar{\tau} \partial_{\bar{\tau}} \bar{\mathcal{E}} + \frac{4}{3} \bar{\mathcal{E}} - \bar{\Pi} = 0, \quad (6.11a)$$

$$\bar{\Pi} + \frac{c_{\pi} \bar{\eta}}{\gamma k \bar{\mathcal{E}}^{1/4}} \left[ \partial_{\bar{\tau}} \bar{\Pi} + \frac{4 \bar{\Pi}}{3 \bar{\tau}} \right] - \frac{16 \bar{\eta}}{9 \gamma k} \frac{\bar{\mathcal{E}}^{3/4}}{\bar{\tau}} + \frac{3 c_{\lambda_1}}{8} \frac{\bar{\Pi}^2}{\bar{\mathcal{E}}} = 0, \quad (6.11b)$$

where  $k \equiv \tau_{\text{hydro}} \mathcal{E}_{\text{hydro}}^{1/4}$ . Note that in terms of (6.10) the initial conditions are specified at  $\bar{\tau} = 1$  where  $\bar{\mathcal{E}}(\bar{\tau} = 1) = 1$  and  $\bar{\Pi}(\bar{\tau} = 1) = \bar{\Pi}_{\text{hydro}}$  which is a free parameter. When the hydrodynamical equations are written in the form given above [Eq. (6.11)] all information about the initial proper-time and energy density is encoded in the parameter  $k$  and all information about the equation of state is encoded in the parameter  $\gamma$ .

### 6.1.2. Strong coupling estimates of the transport coefficients

Motivated and guided by the AdS/CFT correspondence[132], Baier et. al [103] and the Tata group [104] have recently shown that new transport coefficients arise in a complete theory of second order relativistic viscous hydrodynamics. They also estimate their values at infinite t'Hooft coupling for  $\mathcal{N} = 4$  SYM theory at finite temperature. Different calculations for a finite t'Hooft coupling within the same theory have been carried out [198, 199, 200, 201, 202, 203]. A remarkable aspect is that, while at first the strong t'Hooft coupling limit of the transport coefficients was expected to be universal [204, 205], there is now evidence that these coefficients receive higher order contributions [193, 194, 195, 196, 197]. Faced with this complication one is forced to make a choice as to which dual theory to consider. Here we will consider the values obtained in  $\mathcal{N} = 4$  SYM at infinite t'Hooft coupling as used in [103, 104] as our typical strong coupling values. One can expect that these coefficients change in strongly-coupled QCD compared to  $\mathcal{N} = 4$  SYM theory in the infinite t'Hooft coupling limit. Nevertheless, we take these values over from strongly-coupled  $\mathcal{N} = 4$  SYM in order to get a feeling for what to expect in this regime.

Expressed in terms of the dimensionless transport coefficients defined above (6.9), typical values of the strongly coupled transport coefficients are

$$\bar{\eta} = \frac{1}{4\pi}, \quad c_{\pi} = 2(2 - \log 2), \quad c_{\lambda_1} = 2. \quad (6.12)$$

### 6.1.3. Weak coupling estimates of the transport coefficients

Contrary to the case of  $\mathcal{N} = 4$  SYM at infinite coupling, in the case of QCD, where there is a running coupling and inherent scale dependence, the various transport coefficients are not fixed numbers but instead depend on the renormalization scale. In this limit the transport coefficients necessary have been calculated completely to leading order [135, 136, 138]. Higher order corrections to some transport coefficients from finite-temperature perturbation theory show poor convergence [192, 191] which is similar to the case for the thermodynamical potential; however, resummation techniques can dramatically extend the range of convergence of finite-temperature perturbation theory in the case of static quantities and can, in the future, also be applied to dynamical quantities<sup>2</sup>. Until

<sup>2</sup>See Ref. [206, 207] and references therein.

such resummation schemes are carried out for dynamical quantities, the values of the leading-order weak-coupling transport coefficients in Table 6.1 can only be considered as rough guides to the values expected phenomenologically. Using this rough guide the value of  $\bar{\eta}$  from finite-temperature QCD calculations [135, 136] is  $\eta/s \sim 0.5 \rightarrow 1$  at realistic couplings ( $g \sim 2 \rightarrow 3$ ). In this work we will assume a typical value of  $\bar{\eta} = 10/(4\pi)$  in the weakly-coupled limit in order to compare with the results obtained in the strong coupling limit. In our analysis for the weak coupling limit, we will use

$$\bar{\eta} = \frac{10}{4\pi}, \quad c_\pi = 6, \quad c_{\lambda_1} = \frac{9}{2}. \quad (6.13)$$

#### 6.1.4. Momentum space anisotropy

We introduce the dimensionless parameter,  $\Delta$ , which measures the pressure anisotropy of the fluid as follows

$$\Delta \equiv \frac{\mathcal{P}_T}{\mathcal{P}_L} - 1, \quad (6.14)$$

where  $\mathcal{P}_T = (T^{xx} + T^{yy})/2$  and  $\mathcal{P}_L = T^{zz} = -T_\zeta^\zeta$  are the effective transverse and longitudinal pressures, respectively. If  $\Delta = 0$ , the system is locally isotropic. If  $-1 < \Delta < 0$  the system has a local prolate anisotropy in momentum space and if  $\Delta > 0$  the system has a local oblate anisotropy in momentum space. In the 0+1 dimensional model of viscous hydrodynamics one can express the effective transverse pressure as  $\mathcal{P}_T = \mathcal{P} + \Pi/2$  and the effective longitudinal pressure as  $\mathcal{P}_L = \mathcal{P} - \Pi$ . Using these definitions for  $\mathcal{P}_T$  and  $\mathcal{P}_L$  and the ideal equation of state, Eq. (6.14) can be rewritten in terms of our dimensionless variables

$$\begin{aligned} \Delta(\tau) &= \frac{9}{2} \left( \frac{\Pi(\tau)}{\mathcal{E}(\tau) - 3\Pi(\tau)} \right), \\ &= \frac{9}{2} \left( \frac{\bar{\Pi}}{\bar{\mathcal{E}} - 3\bar{\Pi}} \right). \end{aligned} \quad (6.15)$$

The last expression has different limits

$$\lim_{\Pi \ll \mathcal{E}} \Delta(\tau) \approx \frac{9}{2} \frac{\Pi(\tau)}{\mathcal{E}(\tau)} = \frac{9}{2} \frac{\bar{\Pi}}{\bar{\mathcal{E}}}, \quad (6.16a)$$

$$\lim_{\Pi \rightarrow -2\mathcal{E}/3} \Delta(\tau) \approx -1, \quad (6.16b)$$

$$\lim_{\Pi \rightarrow \mathcal{E}/3} \Delta(\tau) \approx \infty. \quad (6.16c)$$

At the initial time,  $\Delta_{\text{hydro}} \equiv \Delta(\tau = \tau_{\text{hydro}})$  can be expressed in terms of the dimensionless variables as

$$\begin{aligned} \Delta_{\text{hydro}} &= \frac{9}{2} \left( \frac{\Pi_{\text{hydro}}}{\mathcal{E}_{\text{hydro}} - 3\Pi_{\text{hydro}}} \right), \\ &= \frac{9}{2} \left( \frac{\bar{\Pi}_{\text{hydro}}}{1 - 3\bar{\Pi}_{\text{hydro}}} \right). \end{aligned} \quad (6.17)$$

Positivity of the longitudinal pressure requires  $\Delta \neq \infty$  at any time during the evolution of the plasma. Note that requiring positivity is a *weak constraint* on the magnitude of  $\Delta$  since the formal justification for applying viscous hydrodynamical approximations neglecting large gradients and higher-order nonlinear terms. This requires that  $\Pi$  be small compared to the pressure,  $\mathcal{P}$ , i.e.  $|\Pi| \ll \mathcal{P}$ . This can be turned into a quantitative statement by requiring that  $-\alpha\mathcal{P} < \Pi < \alpha\mathcal{P}$ , where  $\alpha$  is a positive phenomenological constant which is less than or equal to 1, i.e.  $0 \leq \alpha \leq 1$ . The



limit  $\alpha \rightarrow 1$  gives the weak constraint of  $-3/4 \leq \Delta < \infty$  and for general  $\alpha$  requires  $\Delta_- \leq \Delta \leq \Delta_+$  where

$$\Delta_{\pm} \equiv \pm \frac{3}{2} \left( \frac{\alpha}{1 \mp \alpha} \right). \quad (6.18)$$

For example, requiring  $\alpha = 1/3$  we would find the constraint  $-3/8 \leq \Delta_{\alpha} \leq 3/4$ .

In Sec. 6.3.1, we show how the  $\Delta$  parameter defined above is related with the microscopic anisotropy parameter  $\xi$  which quantifies the degree of local plasma isotropy.

### 6.1.5. Approximate Analytic Solution of 0+1 Conformal Hydrodynamics

In this section we present an approximate analytic solution to the 0+1 dimensional conformal 2nd-order hydrodynamical evolution equations. The approximation used will be to first exactly integrate the differential equation for the energy density (6.11a), thereby expressing the energy density as an integral of the shear. We then insert this integral relation into the equation of motion for shear itself (6.11b) and expand in  $\bar{\eta}$ . Explicitly, the solution obtained from the first step is

$$\bar{\mathcal{E}}(\bar{\tau}) = \bar{\tau}^{-4/3} \left[ 1 + \int_1^{\bar{\tau}} d\bar{\tau}' (\bar{\tau}')^{1/3} \bar{\Pi}(\bar{\tau}') \right]. \quad (6.19)$$

We then solve the second differential equation for  $\bar{\Pi}$  approximately by dropping the second term in Eq. (6.19) and inserting this into the second equation of (6.11) to obtain

$$27 c_{\lambda_1} \gamma k \bar{\tau}^{10/3} \bar{\Pi}^2 + 72 c_{\pi} \bar{\tau}^{7/3} \partial_{\bar{\tau}} \bar{\Pi} + (72 \gamma k \bar{\tau}^2 + 96 c_{\pi} \bar{\tau}^{4/3}) \bar{\Pi} = 128 \bar{\eta}. \quad (6.20)$$

This differential equation has a solution of the form

$$\begin{aligned} \bar{\Pi} = & \left( \frac{4}{3 c_{\lambda_1} \bar{\tau}^{4/3}} \right) \\ & \times \frac{\mathcal{C} \left[ 2 {}_1F_1 \left( \begin{matrix} 1-b \\ 2 \end{matrix} \middle| -a \bar{\tau}^{2/3} \right) + a(b-1) \bar{\tau}^{2/3} {}_1F_1 \left( \begin{matrix} 2-b \\ 3 \end{matrix} \middle| -a \bar{\tau}^{2/3} \right) \right] + 2 G_{1,2}^{2,0} \left( a \bar{\tau}^{2/3} \middle| \begin{matrix} b \\ 0,0 \end{matrix} \right)}{a \mathcal{C} \bar{\tau}^{2/3} {}_1F_1 \left( \begin{matrix} 1-b \\ 2 \end{matrix} \middle| -a \bar{\tau}^{2/3} \right) - G_{1,2}^{2,0} \left( a \bar{\tau}^{2/3} \middle| \begin{matrix} b+1 \\ 0,1 \end{matrix} \right)}, \end{aligned} \quad (6.21)$$

where  ${}_1F_1$  is a confluent hypergeometric function,  $G$  is the Meijer G function,  $a = 3\gamma k/(2c_{\pi})$ ,  $b = c_{\lambda_1} \bar{\eta}/c_{\pi}$ , and  $\mathcal{C}$  is an integration constant which is fixed by the initial condition for  $\bar{\Pi}$  at  $\bar{\tau} = 1$ . Requiring  $\bar{\Pi}(\bar{\tau} = 1) = \bar{\Pi}_{\text{hydro}}$  fixes  $\mathcal{C}$  to be

$$\mathcal{C} = \frac{8 G_{1,2}^{2,0} \left( a \middle| \begin{matrix} b \\ 0,0 \end{matrix} \right) + 3 c_{\lambda_1} \bar{\Pi}_{\text{hydro}} G_{1,2}^{2,0} \left( a \middle| \begin{matrix} b+1 \\ 0,1 \end{matrix} \right)}{[3 a c_{\lambda_1} \bar{\Pi}_{\text{hydro}} - 8] {}_1F_1 \left( \begin{matrix} 1-b \\ 2 \end{matrix} \middle| -a \right) - 4 a (b-1) {}_1F_1 \left( \begin{matrix} 2-b \\ 3 \end{matrix} \middle| -a \right)}. \quad (6.22)$$

To obtain the proper-time evolution of the energy density one must integrate (6.19) using (6.21). This is possible to do analytically but the answer is rather unwieldy and hence not very useful to list explicitly. Below we will use this approximate analytic solution as a cross check for our numerics. In the limit  $\bar{\eta} \rightarrow 0$  this solution becomes an increasingly better approximation and hence represents the leading correction to ideal hydrodynamical evolution in that limit.

Note that in the limit  $c_{\lambda_1} \rightarrow 0$  and  $c_{\pi} \rightarrow 0$  the differential equation above (6.20) reduces to an algebraic equation

$$\bar{\Pi}_{\text{NS}} = \frac{16\bar{\eta}}{9\gamma k \bar{\tau}^2}, \quad (6.23)$$

which, when converted back to dimensionful variables, corresponds to the Navier-Stokes (NS) solution under the assumption that  $\bar{\mathcal{E}} = \bar{\tau}^{-4/3}$ . Finally we note that in the large time limit Eq. (6.21) simplifies to

$$\lim_{\bar{\tau} \rightarrow \infty} \bar{\Pi} = \bar{\Pi}_{\text{NS}} + \mathcal{O} \left( e^{-a \bar{\tau}^{-2/3}} \right). \quad (6.24)$$

## 6.2. Lower bounds on the initial time from the viscous hydrodynamical equations

In this section we present our results of numerical integration of Eq. (6.11) and present consistency checks obtained by comparing these results with the approximate analytic solution presented in the previous section.

### 6.2.1. Time Evolution of $\Delta$

Below we present numerical results for the time evolution of the plasma anisotropy parameter  $\Delta$ . For purpose of illustration we will hold the initial temperature fixed at  $T_{\text{hydro}} = 350$  MeV and vary the starting time  $\tau_{\text{hydro}}$ . This will allow us to probe different values of  $k = \tau_{\text{hydro}} \mathcal{E}_{\text{hydro}}^{1/4} = \tau_{\text{hydro}} T_{\text{hydro}} / \gamma$  in a transparent manner. Note that, by doing this, each curve corresponds to a different initial entropy density; however, this is irrelevant for the immediate discussion since we are concerned only with the general mathematical properties of the system of differential equations as one varies the fundamental parameters. Phenomenological studies of entropy generation during the non-equilibrated phase of the QGP are presented in Sect. 6.5. In Secs. 6.2.3 and 6.2.4 we will present the general results as a function of the dimensionless parameter  $k$ .

#### Strong Coupling

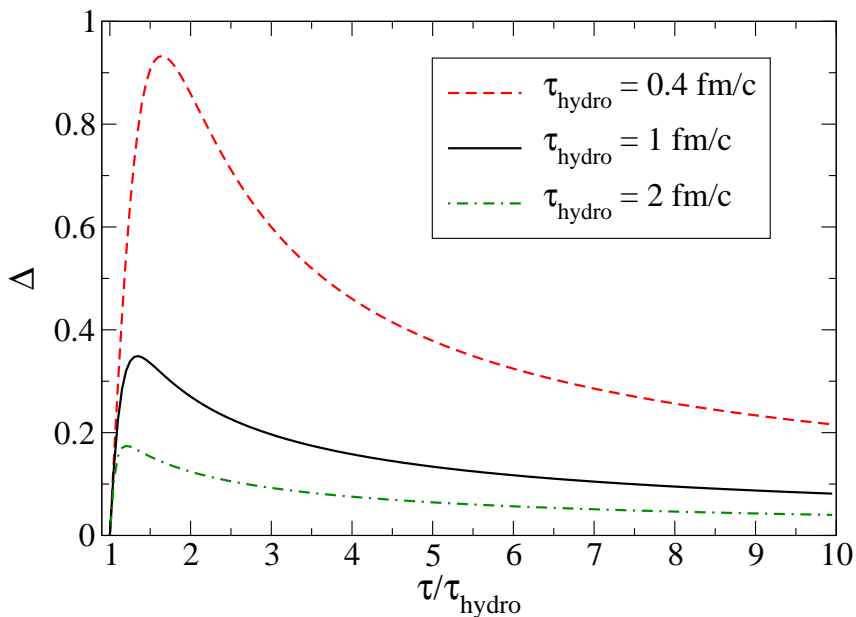


Figure 6.1.: Result for the proper-time evolution of  $\Delta$  obtained by numerical integration of Eq. (6.11). Long-dashed, solid, and short-dashed lines correspond  $\tau_{\text{hydro}} = \{0.4, 1, 2\}$  fm/c, respectively. Transport coefficients were the typical strong coupling values given in Eq. (6.12). The initial temperature,  $T_{\text{hydro}}$ , is held fixed at  $T_{\text{hydro}} = 350$  MeV and it is assumed that  $\Delta_{\text{hydro}} = 0$  for this example.

In Fig. 6.1 we show our result for the proper-time evolution of the pressure anisotropy parameter,  $\Delta$ , obtained by numerical integration of Eq. (6.11). The transport coefficients in this case are the typical strong coupling values given in Eq. (6.12). For purpose of illustration we have chosen the

initial temperature,  $T_{\text{hydro}}$ , to be held fixed at  $T_{\text{hydro}} = 350$  MeV and assumed that the initial pressure anisotropy,  $\Delta_{\text{hydro}}$ , vanishes, i.e.  $\Delta_{\text{hydro}} = 0$ .

As can be seen from this figure, when the initial value of the pressure anisotropy is taken to be zero it does not remain so. A finite oblate pressure anisotropy is rapidly established due to the intrinsic longitudinal expansion of the fluid. Depending on the initial time at which the hydrodynamic evolution is initialized,  $\Delta$  peaks in the range  $0.2 \lesssim \Delta \lesssim 1$ .

### Weak Coupling

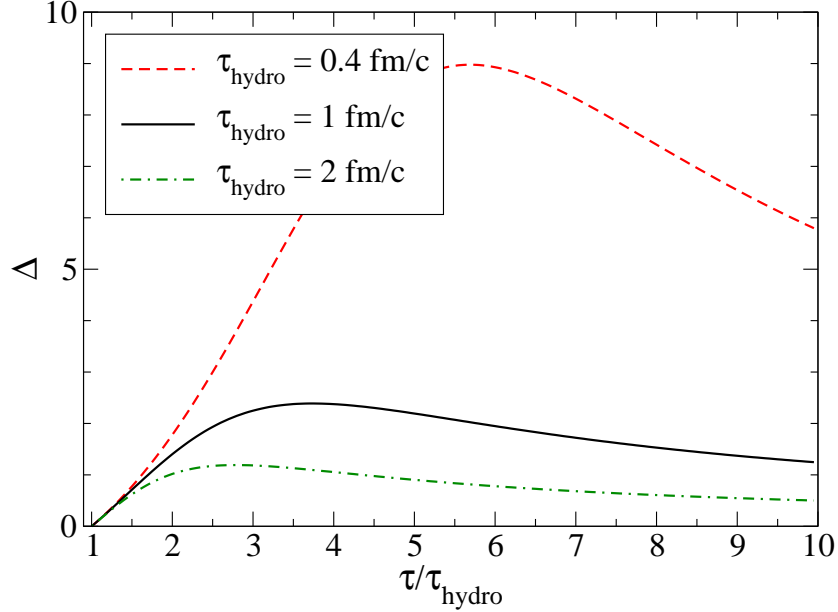


Figure 6.2.: Result for the proper-time evolution of  $\Delta$  obtained by numerical integration of Eq. (6.11). Long-dashed, solid, and short-dashed lines correspond  $\tau_{\text{hydro}} = \{0.4, 1, 2\}$  fm/c, respectively. Transport coefficients in this case are the typical weak coupling values given in Eq. (6.13). The initial temperature,  $T_{\text{hydro}}$ , is held fixed at  $T_{\text{hydro}} = 350$  MeV and it is assumed that  $\Delta_{\text{hydro}} = 0$  for this example.

In Fig. 6.2 we show our result for the proper-time evolution of the pressure anisotropy parameter,  $\Delta$ , obtained by numerical integration of Eq. (6.11). The transport coefficients in this case are the typical weak coupling values given in Eq. (6.13). For purpose of illustration we have chosen the initial temperature,  $T_{\text{hydro}}$ , to be held fixed at  $T_{\text{hydro}} = 350$  MeV and assumed that the initial pressure anisotropy,  $\Delta_{\text{hydro}}$ , vanishes, i.e.  $\Delta_{\text{hydro}} = 0$ .

As can be seen from this figure, as in the strongly coupled case, a finite oblate pressure anisotropy is rapidly established due to the intrinsic longitudinal expansion of the fluid. In the case of weak coupling transport coefficients a larger pressure anisotropy develops. Depending on the initial time at which the hydrodynamic evolution is initialized,  $\Delta$  peaks in the range  $1 \lesssim \Delta \lesssim 9$ .

As can be seen from the  $\tau_{\text{hydro}} = 0.4$  fm/c result, if the initial simulation time is assumed to be small, then very large pressure anisotropy can develop. In that case, in dimensionful units, the peak of the  $\Delta$  evolution occurs at a time of  $\tau \sim 2.3$  fm/c. Such large pressure anisotropies would cast doubt on the applicability of the 2nd-order conformal viscous hydrodynamical equations, since

nonconformal 2nd-order terms and higher-order non-linear terms corresponding to 3rd- or higher-order expansions could become important [105, 186]. If, in the weakly coupled case, the initial simulation time  $\tau_{\text{hydro}}$  is taken to be 0.2 fm/c one would find that  $\Delta$  would become infinite during the simulation. This divergence is due to the fact that the longitudinal pressure goes to zero and then becomes negative during some period of the time evolution.

### Comparison with analytic approximation

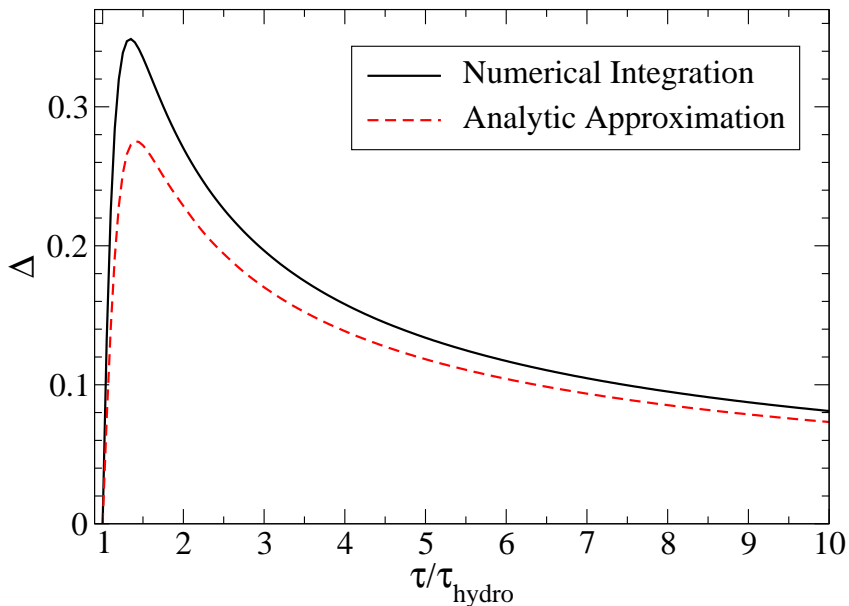


Figure 6.3.: Comparison of result for  $\Delta$  as a function of proper time using numerical integration of Eq. (6.11) and the approximate analytic solution given via Eqs. (6.21) and (6.19). Transport coefficients in this case are the typical strong coupling values given in Eq. (6.12). The initial temperature,  $T_{\text{hydro}}$ , is taken to be  $T_{\text{hydro}} = 350$  MeV, the initial time,  $\tau_{\text{hydro}}$ , is taken to be  $\tau_{\text{hydro}} = 1$  fm/c and it is assumed that  $\Delta_{\text{hydro}} = 0$  for this example.

As a cross check of our numerical method, in Fig. 6.3 we compare the result for  $\Delta$  obtained via direct numerical integration of Eq. (6.11) and the approximate analytic solution given via Eqs. (6.21) and (6.19). As can be seen from the figure the analytic solution provides a reasonable approximation to the true time-evolution of the plasma anisotropy. The parameter  $\Delta$  is a particularly sensitive quantity to compare. If one compares the analytic and numerical solutions for the energy density, for example, in the strongly-coupled case there is at most a 1% deviation between the analytic approximation and our exact numerical integration during the entire 10 fm/c of simulation time. Of course, for larger viscosity the analytic approximation becomes more suspect but for the weakly-coupled case we find that there is at most a 8% deviation between the energy densities obtained using our analytic approximation and the exact numerical result. In the limit that  $\bar{\eta}$  goes to zero, the analytic treatment and our numerical integration agree to arbitrarily better precision. Based on the agreement between the two approaches we are confident in our numerical integration of the coupled differential equations.

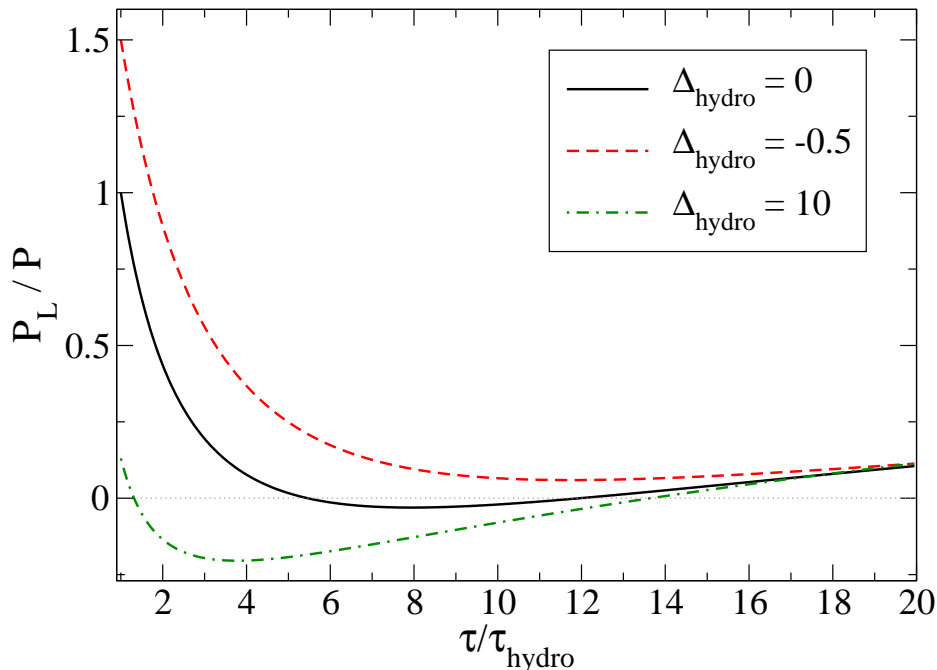


Figure 6.4.: Result for the proper-time evolution of the ratio of the longitudinal pressure over the pressure,  $\mathcal{P}_L/\mathcal{P}$ , obtained by numerical integration of Eq. (6.11). Solid, long-dashed, and short-dashed lines correspond  $\Delta_{\text{hydro}} = \{0, -0.5, 10\}$ , respectively. Transport coefficients in this case are the typical weak coupling values given in Eq. (6.13). The initial temperature,  $T_{\text{hydro}}$ , is held fixed at  $T_{\text{hydro}} = 350$  MeV and it is assumed that  $\tau_{\text{hydro}} = 0.2$  fm/c for this example. The dotted grey line indicates  $\mathcal{P}_L = 0$  in order to more easily identify the point in time where the longitudinal pressure becomes negative.

### 6.2.2. Negativity of Longitudinal Pressure

In order to explicitly demonstrate the possibility that  $\Delta$  diverges, in Fig. 6.4 we have plotted the evolution the longitudinal pressure over the isotropic pressure ( $\mathcal{P} = \mathcal{E}/3$ ),  $\mathcal{P}_L/\mathcal{P}$ , obtained by numerical integration of Eq. (6.11) for different assumed initial pressure anisotropies. The transport coefficients in this case are the typical weak coupling values given in Eq. (6.13). The initial temperature,  $T_{\text{hydro}}$ , is held fixed at  $T_{\text{hydro}} = 350$  MeV and it is assumed that  $\tau_{\text{hydro}} = 0.2$  fm/c for this example.

As this figure shows, if the initial simulation time is too early, the longitudinal pressure of the system can become negative. The exact point in time at which it becomes negative depends on the assumed initial pressure anisotropy. As the initial pressure anisotropy becomes more prolate, the time over which the longitudinal pressure remains positive is increased. For initially extremely prolate distributions the longitudinal pressure can remain positive during the entire simulation time. In the opposite limit of extremely oblate distributions, the longitudinal pressure can become negative very rapidly and remain so throughout the entire lifetime of the plasma. We note that in the Navier-Stokes limit the initial shear would be  $(\bar{\Pi}_{\text{hydro}})_{\text{Navier-Stokes}} = 16\bar{\eta}/(9\tau_{\text{hydro}}T_{\text{hydro}})$  which, using the initial conditions indicated in Fig. 6.4, gives  $\bar{\mathcal{P}}_{L,0}/\mathcal{P} = -11.1$ . This means that if one

were to use Navier-Stokes initial conditions the system would start with an extremely large negative longitudinal pressure. Using  $\tau_{\text{hydro}} = 1 \text{ fm}/c$  and  $T_{\text{hydro}} = 350 \text{ MeV}$  improves the situation somewhat; however, even in that case the initial Navier-Stokes longitudinal pressure remains negative with  $\mathcal{P}_{L,0}/\mathcal{P} = -1.4$ .

What does a negative longitudinal pressure indicate? From a transport theory point of view it indicates that something is unphysical about the simulation since in transport theory the pressure components are obtained from moments of the momentum-squared over the energy, e.g. for the longitudinal pressure

$$\mathcal{P}_L = \int \frac{d^3p}{(2\pi)^3} \frac{p_z^2}{p^0} f(\mathbf{p}), \quad (6.25)$$

where  $f(\mathbf{p})$  is the one-particle phase-space distribution function. Therefore, in transport theory all components of the pressure are positive definite. It is possible to generate negative longitudinal pressure in the case coherent fields as in the case of the early-time evolution of the quark-gluon plasma [48, 208, 209, 51]; however, such coherent fields are beyond the scope of hydrodynamical simulations which describe the time evolution of a locally color- and charge-neutral fluid.

This fundamental issue aside, the negativity of the longitudinal pressure indicates that the expansion which was used to derive the hydrodynamical equations themselves is breaking down. This expansion implicitly relies on the perturbation described by  $\Pi$  being small compared to the isotropic pressure  $\mathcal{P}$ . The point at which the longitudinal pressure goes to zero is the point at which the perturbation,  $\Pi$ , is equal in magnitude to the background around which one is expanding. This means that the perturbation is no longer a small correction to the system's evolution and that higher order corrections could become important. Therefore negative longitudinal pressure signals regions of parameter space where one cannot trust 2nd-order viscous hydrodynamical solutions. In the following two subsections we will make this statement quantitative and extract constraints on the initial conditions which allow for 2nd-order viscous hydrodynamical simulation.

### 6.2.3. Determining the critical line in initial condition space

For a fixed set of transport coefficients given by  $\{\bar{\eta}, c_\pi, c_{\lambda_1}\}$  the only remaining freedom in the hydrodynamical evolution equations (6.11) comes from the coefficient  $\gamma$  (using the assumed ideal equation of state) and from the initial conditions through the dimensionless coefficient  $k = \tau_{\text{hydro}} \mathcal{E}_{\text{hydro}}^{1/4}$  and the initial shear  $\bar{\Pi}_{\text{hydro}}$ . In the next section we will vary these two parameters and determine for which values one obtains a solution that, at any point during the evolution, has a negative longitudinal pressure. For a given  $\bar{\Pi}_{\text{hydro}}$  we find that for  $k$  below a certain value, the system exhibits a negative longitudinal pressure. We will define this point in  $k$  as the ‘‘critical’’ value of  $k$ . Above the critical value of  $k$  the longitudinal pressure is positive definite at all times.

#### Strong Coupling

In Fig. 6.5 we plot the critical boundary in  $k$  ( $k_{\text{critical}}$ ) as a function of the initial value of the shear,  $\bar{\Pi}_{\text{hydro}}$ . Since  $k$  is proportional to the assumed initial simulation time  $\tau_{\text{hydro}}$  increasing  $k$  with fixed initial energy density corresponds to increasing  $\tau_{\text{hydro}}$ . Assuming fixed initial temperature, for an initially prolate distribution, one can start the simulation at earlier times. For an initially oblate distribution, one must start the simulation at later times in order to remain above the critical value of  $k$ . In general,  $k = \tau_{\text{hydro}} \mathcal{E}_{\text{hydro}}^{1/4}$  and our result can be used to set a bound on this product.

In the case of typical strong coupling transport coefficients, the critical value of  $k$  at  $\bar{\Pi}_{\text{hydro}} = 0$  is  $k_{\text{critical}}(\bar{\Pi}_{\text{hydro}} = 0) = 0.26$ . In the case of an ideal QCD equation of state and assuming  $\bar{\Pi}_{\text{hydro}} = 0$ , the constraint is that  $\tau_{\text{hydro}} T_{\text{hydro}} > \gamma k_{\text{critical}}$ , which is numerically  $\tau_{\text{hydro}} T_{\text{hydro}} > 0.14$ . Assuming an initial temperature of  $T_{\text{hydro}} = 0.35 \text{ GeV}$  this implies that  $\tau_{\text{hydro}} > 0.08 \text{ fm}/c$ . For other initial values of  $\bar{\Pi}_{\text{hydro}}$  one can use Fig. 6.5 to determine the constraint [121].

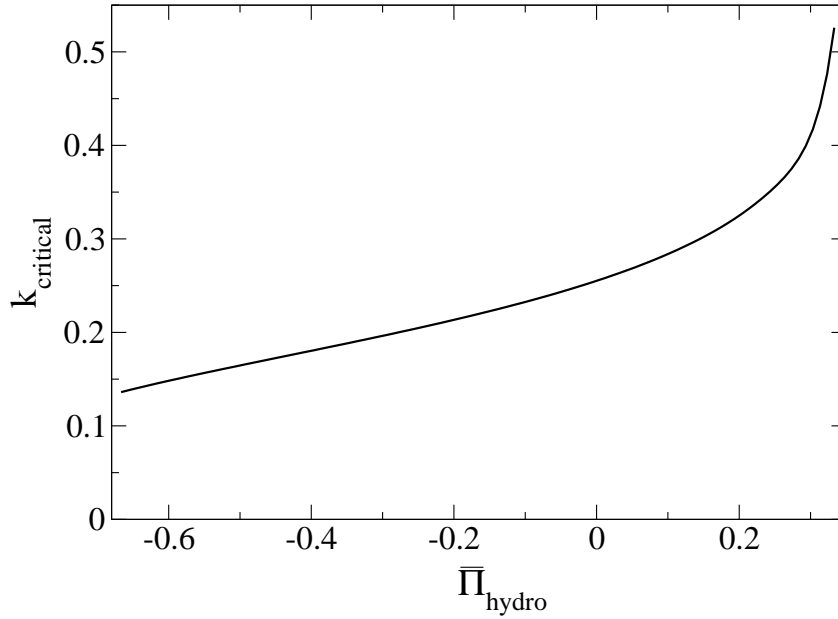


Figure 6.5.: Critical boundary in  $k$  ( $k_{\text{critical}}$ ) as a function of the initial shear,  $\bar{\Pi}_{\text{hydro}}$ . Above this line solutions have positive longitudinal pressure at all times. Below this line solutions have negative longitudinal pressure at some point during the evolution. Transport coefficients in this case are the typical strong coupling values given in Eq. (6.12). Left limit of plot region corresponds to  $\Delta_{\text{hydro}} = -1$  and right to  $\Delta_{\text{hydro}} = \infty$ .

### Weak Coupling

In Fig. 6.6 we plot the critical boundary in  $k$  ( $k_{\text{critical}}$ ) as a function of the initial value of the shear,  $\bar{\Pi}_{\text{hydro}}$ . Since  $k$  is proportional to the assumed initial simulation time  $\tau_{\text{hydro}}$  increasing  $k$  with fixed initial energy density corresponds to increasing  $\tau_{\text{hydro}}$ . As in the case of strong coupling, for an initially prolate distribution, one can start the simulation at earlier times. For an initially oblate distribution, one must start the simulation at later times in order to remain above the critical value of  $k$ .

In the case of typical weak coupling transport coefficients the critical value of  $k$  at  $\bar{\Pi}_{\text{hydro}} = 0$  is  $k_{\text{critical}}(\bar{\Pi}_{\text{hydro}} = 0) = 0.74$ . In the case of an ideal QCD equation of state and assuming  $\bar{\Pi}_{\text{hydro}} = 0$ , the constraint is that  $\tau_{\text{hydro}} T_{\text{hydro}} > \gamma k_{\text{critical}}$ , which is numerically,  $\tau_{\text{hydro}} T_{\text{hydro}} > 0.40$ . Assuming an initial temperature of  $T_{\text{hydro}} = 0.35$  GeV this implies that  $\tau_{\text{hydro}} > 0.23$  fm/c. For other initial values of  $\bar{\Pi}_{\text{hydro}}$  one can use Fig. 6.6 to determine the constraint [121].

### 6.2.4. Determining the convergence line in initial condition space

As mentioned in Sec. 6.1.4 the requirement that the longitudinal pressure is positive during the simulated time only gives a weak constraint in the sense that it merely requires that  $|\Pi| < \mathcal{P}$ . A stronger constraint can be obtained by requiring instead  $-\alpha \mathcal{P} \leq \Pi \leq \alpha \mathcal{P}$  and then using this to constrain the possible initial time and energy density which can be used in hydrodynamical simulations. In the following subsections we will fix  $\alpha = 1/3$  as our definition of what is a “large” correction. For this value of  $\alpha$  the initial values of  $\bar{\Pi}_{\text{hydro}}$  are constrained to be between  $-1/9 \leq \bar{\Pi}_{\text{hydro}} \leq 1/9$ . For a given  $\bar{\Pi}_{\text{hydro}}$  in this range we find that for  $k$  below a certain value we cannot satisfy the stronger constraint at all simulated times. We will define this point in  $k$  as the “convergence” value of  $k$  or

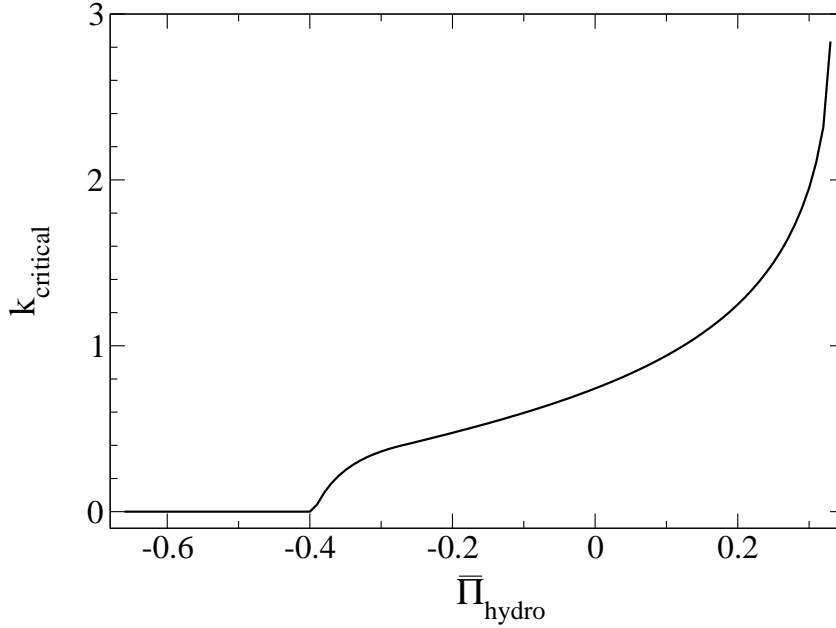


Figure 6.6.: Critical boundary in  $k$  ( $k_{\text{critical}}$ ) as a function of the initial shear,  $\bar{\Pi}_{\text{hydro}}$ . Above this line solutions have positive longitudinal pressure at all times. Below this line solutions have negative longitudinal pressure at some point during the evolution. Transport coefficients in this case are the typical weak coupling values given in Eq. (6.13). Left limit of plot region corresponds to  $\Delta_{\text{hydro}} = -1$  and right to  $\Delta_{\text{hydro}} = \infty$ .

$k_{\text{convergence}}$ . Above this value of  $k = k_{\text{convergence}}$  the shear satisfies the constraint  $-\bar{\mathcal{P}}/3 \leq \bar{\Pi} \leq \bar{\mathcal{P}}/3$  at all simulated times and therefore represents a “reasonable” simulation.

### Strong Coupling

In Fig. 6.7 we plot the “convergence boundary” in  $k$  ( $k_{\text{convergence}}$ ) as a function of the initial shear,  $\bar{\Pi}_{\text{hydro}}$ . In the case of typical strong coupling transport coefficients the convergence value of  $k$  at  $\bar{\Pi}_{\text{hydro}} = 0$  is  $k_{\text{convergence}}(\bar{\Pi}_{\text{hydro}} = 0) = 1.58$ . In the case of an ideal QCD equation of state and assuming  $\bar{\Pi}_{\text{hydro}} = 0$ , the constraint is that  $\tau_{\text{hydro}} T_{\text{hydro}} > \gamma k_{\text{convergence}}$ , which is numerically  $\tau_{\text{hydro}} T_{\text{hydro}} > 0.85$ . Assuming an initial temperatures of  $T_{\text{hydro}} = 0.35$  GeV this implies that  $\tau_{\text{hydro}} > 0.49$  fm/c. For other initial values of  $\bar{\Pi}_{\text{hydro}}$  one can use Fig. 6.7 to determine the constraint [121].

### Weak Coupling

In Fig. 6.8 we plot the “convergence boundary” in  $k$  ( $k_{\text{convergence}}$ ) as a function of the initial shear,  $\bar{\Pi}_{\text{hydro}}$ . In the case of typical weak coupling transport coefficients the convergence value of  $k$  at  $\bar{\Pi}_{\text{hydro}} = 0$  is  $k_{\text{convergence}}(\bar{\Pi}_{\text{hydro}} = 0) = 10.9$ . In the case of an ideal QCD equation of state and assuming  $\bar{\Pi}_{\text{hydro}} = 0$ , the constraint is that  $\tau_{\text{hydro}} T_{\text{hydro}} > \gamma k_{\text{convergence}}$ , which is numerically  $\tau_{\text{hydro}} T_{\text{hydro}} > 5.9$ . Assuming an initial temperature of  $T_{\text{hydro}} = 0.35$  GeV this implies that  $\tau_{\text{hydro}} > 3.37$  fm/c. For other initial values of  $\bar{\Pi}_{\text{hydro}}$  one can use Fig. 6.8 to determine the constraint.



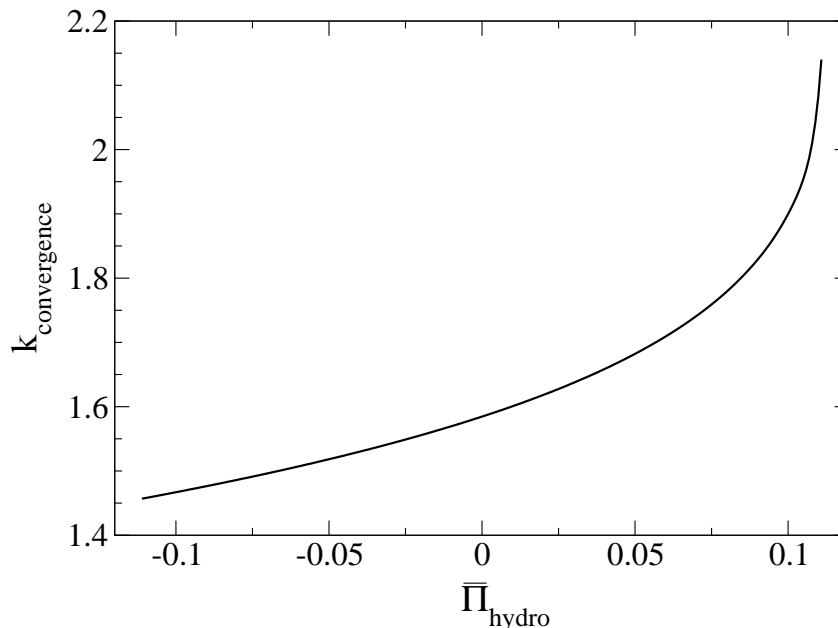


Figure 6.7.: Convergence boundary in  $k$  ( $k_{\text{convergence}}$ ) as a function of the initial shear,  $\bar{\Pi}_{\text{hydro}}$ . Above this line solutions satisfy the convergence constraint. Transport coefficients in this case are the typical strong coupling values given in Eq. (6.12).

### 6.2.5. Implications for higher dimensional hydrodynamical simulations

If one proceeds to more realistic simulations in higher dimensional boost invariant treatments, e.g. 1+1 and 2+1, the spatial variation of the initial conditions and time evolution in the transverse plane have to be taken into account. In addition, new freedoms such as the initial fluid flow field and additional transport coefficients arise; however, to first approximation one can treat these higher dimensional systems as a collection of 0+1 dimensional systems with different initial conditions at each point in the transverse plane. Within this approximation one would quickly find that there are problems with the hydrodynamic treatment at the transverse edges of the simulated region.

This happens because as one goes away from the center of the hot and dense matter, the energy density (temperature) drops and, assuming a fixed initial simulation time  $\tau_{\text{hydro}}$ , one would find that at a finite distance from the center the condition  $k > k_{\text{critical}}$  would be violated by the initial conditions. In these regions of space, hydrodynamics would then predict an infinitely large anisotropy parameter,  $\Delta$ , casting doubt on the reliability of the hydrodynamic assumptions. Even worse is that at a smaller distance from the center one would cross the “convergence boundary” in  $k$ ,  $k_{\text{convergence}}$ , and therefore not fully trust the analytic approximations used in deriving the hydrodynamic equations (conformality, truncation at 2nd order, etc.).

Of course, an approximation by uncoupled 0+1 systems with different initial conditions would not generate any radial or elliptic flow; however, we find empirically that the picture above holds true in higher-dimensional simulations, justifying the basic logic. For example, using strongly-coupled transport coefficients and assuming an initially isotropic plasma ( $\bar{\Pi}_{\text{hydro}} = 0$ ), we found in Sec. 6.2.3 that  $k_{\text{critical}} = 0.26$ . In terms of the initial temperature this predicts that when starting a simulation with  $T_{\text{hydro}} = 0.35$  GeV, one will generate negative longitudinal pressures for any initial time  $\tau_{\text{hydro}} \lesssim 0.08$  MeV.

We will now compare this prediction with results for the longitudinal pressure extracted from the 2+1 dimensional code of Luzum and Romatschke [1, 185]. In Fig. 6.9 we show fixed  $\tau$  snapshots of

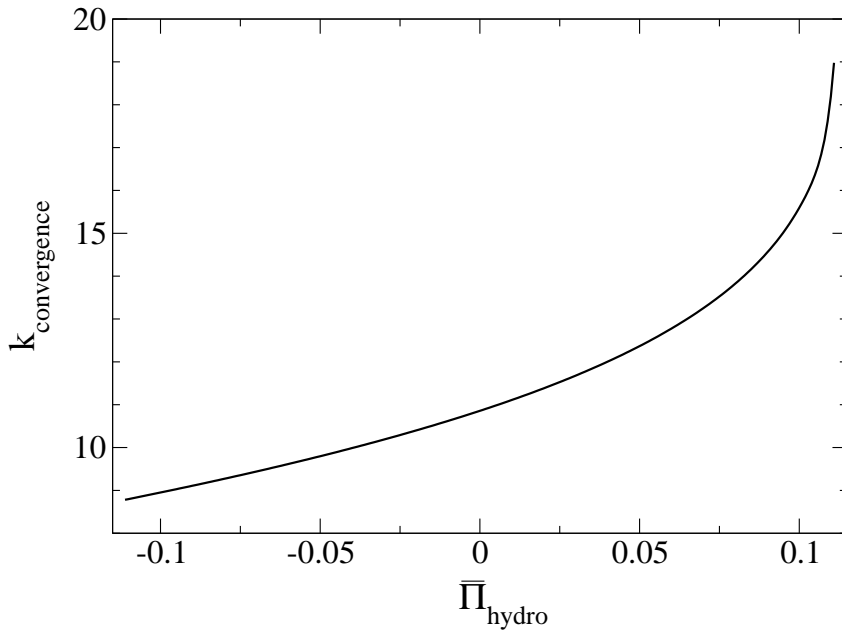


Figure 6.8.: Convergence boundary in  $k$  ( $k_{\text{convergence}}$ ) as a function of the initial shear,  $\bar{\Pi}_{\text{hydro}}$ . Above this line solutions satisfy the convergence constraint. Transport coefficients in this case are the typical weak coupling values given in Eq. (6.13).

the longitudinal pressure. The runs shown in Fig. 6.9 were performed on a  $69^2$  transverse lattice with a lattice spacing of  $2 \text{ GeV}^{-1}$  using Glauber initial conditions starting at  $\tau_{\text{hydro}}=1 \text{ fm}/c$ , an initial central temperature of  $T_{\text{hydro}} = 350 \text{ MeV}$ , zero initial shear and zero impact parameter. For these runs we have used the realistic QCD equation of state used in Ref. [1]. In the top panel of Fig. 6.9 the transport coefficients were set to the typical strong coupling values given in Eq. (6.12), except with  $c_{\lambda_1} = 0$  due to the fact that the code used did not include this term in the hydrodynamic equations. Based on the initial transverse temperature profile and our estimated critical initial temperature, in the strong-coupling case we expect negative longitudinal pressures to be generated at transverse radius  $r \gtrsim 10 \text{ fm}$ . As can be seen from the left panel of Fig. 6.9, at the edge of the simulated region the longitudinal pressure becomes negative starting already at very early times. The transverse radii at which this occurs is in good agreement with our estimate based on the 0+1 dimensional critical value detailed above.

Based on our convergence criterium detailed in Sec. 6.2.4 we found, in the strong-coupling case, that  $k_{\text{convergence}}(\bar{\Pi}_{\text{hydro}} = 0) = 1.58$ . Assuming  $\tau_{\text{hydro}} = 1 \text{ fm}/c$  this translates into a minimum initial temperature of  $167 \text{ MeV}$ . Based on the transverse temperature profile used in the run shown in the left panel of Fig. 6.9 this results in a maximum transverse radius  $r \sim 6.8 \text{ fm}$ . At radii larger than this value it is possible that higher order corrections are large and therefore the applicability of 2nd-order viscous hydrodynamics becomes questionable. Since this temperature is greater than the typical freeze-out temperature used,  $T_f \sim 150 \text{ MeV}$ , this means that in the strong coupling limit it is relatively safe to use hydrodynamical simulations. However, one should be extremely careful with the transverse edges.

The situation, however, is not as promising in the weak-coupling case. To see this explicitly, in the bottom panel of Fig. 6.9 we show the longitudinal pressure resulting from a run with weak coupling transport coefficients (6.13). Based on the initial transverse temperature profile and our estimated critical initial temperature, in the weak-coupling case we expect negative longitudinal pressures to

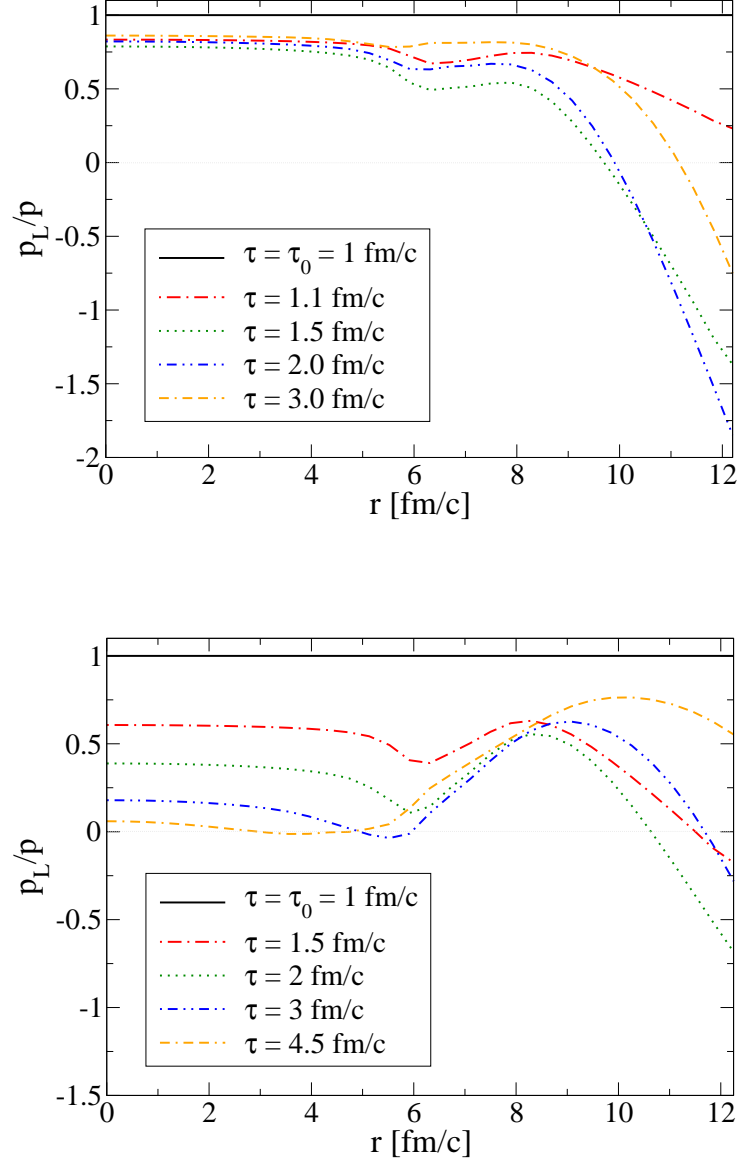


Figure 6.9.: Evolution of the longitudinal pressure in proper-time obtained from the 2+1 dimensional viscous hydrodynamics code of Ref. [1, 185]. Horizontal axis is the distance from the center of the simulated region. In the top panel we show the result obtained using the typical strong coupling values given in Eq. (6.12) but with  $c_{\lambda_1} = 0$ . In the bottom panel we show the result obtained using the typical weak coupling values given in Eq. (6.13) but with  $c_{\lambda_1} = 0$ . The runs shown used Glauber initial conditions with an initial central temperature of  $T_{\text{hydro}} = 350$  MeV, initial time  $\tau_{\text{hydro}} = 1$  fm/c and  $\Pi'_{\mu}(\tau_{\text{hydro}}) = 0$ .

be generated at transverse radius  $r \gtrsim 8$  fm. Comparing this prediction to the results shown in the right panel of Fig. 6.9 we see that the situation is even worse than expected. By the final time of 4.5 fm/c the entire central region has very low or negative longitudinal pressure. We note that at that time the radius at which the temperature has dropped below the freeze-out temperature is around 7.3 fm so the region where the longitudinal pressure is negative (or almost negative) is still in the QGP phase.

In terms of convergence, we remind the reader that based on our convergence criterium detailed in Sec. 6.2.4 we found that in the weakly-coupled case  $k_{\text{convergence}}(\bar{\Pi}_{\text{hydro}} = 0) = 10.9$ . Assuming  $\tau_{\text{hydro}} = 1$  fm/c we found that the initial central temperature should be greater than 1.16 GeV. As can be seen in Fig. 6.9 the corrections to ideal hydrodynamics are sizable so this again points to the possibility that there are large corrections to the 2nd-order hydrodynamic equations. Based on this, it would be questionable to ever apply 2nd-order viscous hydrodynamics to a weakly-coupled quark-gluon plasma generated in relativistic heavy-ion collisions. At the very least one would need to include nonconformal 2nd-order terms and 3rd-order terms in order to assess their impact [105, 186].

### 6.3. Matching pre-equilibrium dynamics and viscous hydrodynamics

In the previous sections we derived two general criteria that can be used to constrain the initial time of onset of 2nd-order conformal viscous hydrodynamics in relativistic heavy-ion collisions. We imposed those requirements explicitly over the solutions of 0+1 dimensional viscous hydrodynamics and discussed how to extend the constraint to higher dimensions. When we integrate the viscous hydrodynamical equations 6.2, we fix by ‘hand’ the initial values of the energy density, shear viscous tensor and initial time. In the rest of the chapter we demonstrate how to determine the initial energy density  $\mathcal{E}$  and shear  $\Pi$  in a 0+1 dimensional model by introducing a pre-equilibrium period, in which the system develops a local momentum-space anisotropy due to the longitudinal expansion of the matter. After this period we evolve the system using 2nd-order viscous hydrodynamics with initial conditions consistent with the pre-equilibrium evolution of the matter. To frame the discussion we introduce two proper time scales: (1) the parton formation time,  $\tau_0$ , which is the time after which coherence effects in the nuclear wave function for the hadrons can be ignored and partons can be thought of as liberated; and (2) the time at which one starts modeling the system using viscous hydrodynamics,  $\tau_{\text{hydro}}$ . During the pre-equilibrium stage,  $\tau_0 < \tau < \tau_{\text{hydro}}$ , the longitudinal expansion of the matter along the beam axis makes the system colder along the longitudinal direction than in the transverse direction,  $\langle p_L^2 \rangle < \langle p_T^2 \rangle$  [26] corresponding to a non-vanishing plasma shear  $\Pi$ .

This approach can be seen as an extension of the pre-equilibrium interpolating models presented in Chapter 5. We used such models to calculate the dependence of high energy dilepton on the plasma isotropization time [82, 83, 84]. In these previous analyses the pre-equilibrium stage was matched at late times to isotropic ideal hydrodynamical expansion. Here we show how to determine the shear  $\Pi$  and energy density  $\mathcal{E}$  at a proper-time  $\tau_{\text{hydro}}$  given a model for the evolution of the microscopic anisotropy of the plasma,  $\xi = \frac{1}{2} \langle p_T^2 \rangle / \langle p_L^2 \rangle - 1$ , where  $p_T$  and  $p_L$  are the transverse and longitudinal momenta of the particles in the plasma, respectively. This is done by matching to the corresponding pressure anisotropy  $\Delta \equiv \mathcal{P}_T / \mathcal{P}_L - 1$  (Eq. 6.14), and energy density,  $\mathcal{E}$ . Once this matching is performed one can solve the 2nd-order viscous hydrodynamical differential equations to determine the further time evolution of the system.

In Fig. 6.10 we show the time evolution of the pressure anisotropy and energy density assuming  $\tau_{\text{hydro}} = 1$  fm/c resulting from the models described herein. As can be seen from Fig. 6.10 (left) the magnitude of  $\Delta$  is larger in the weakly-coupled case starting from the same initial pressure anisotropy at  $\tau = 1$  fm/c. In Fig. 6.10 (right) we show the typical time evolution of the energy density using our matching. As can be seen from this figure in the weakly-coupled case the 0+1 dimensional plasma lifetime is increased due to the larger shear viscosity. In the body of the text we show how such

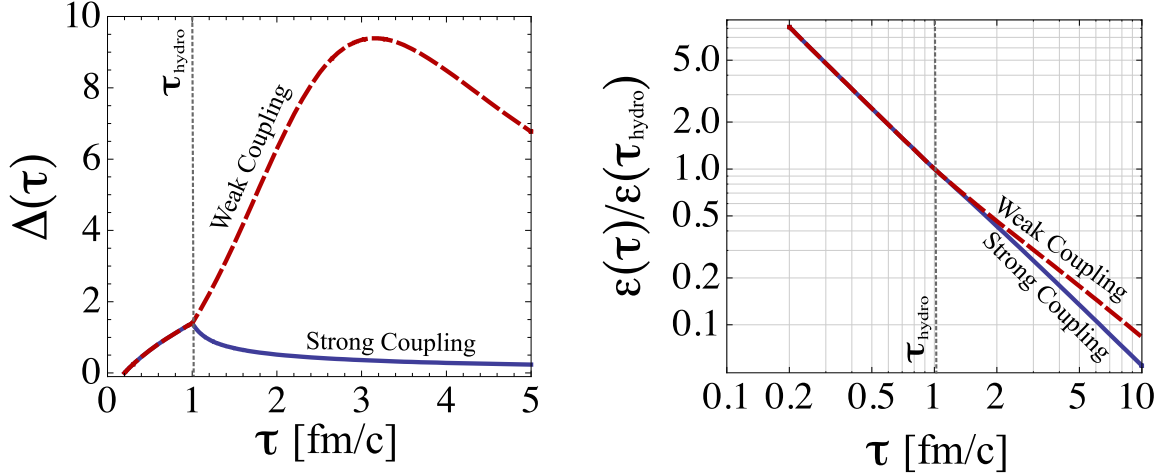


Figure 6.10.: Time evolution of the pressure anisotropy  $\Delta$  (left) and energy density (right) for the case of collisionally broadened pre-equilibrium dynamics. In this plot we have fixed  $\tau_{\text{hydro}} = 1$  fm/c. The red dashed line is the case of weakly-coupled transport coefficients and the solid blue line is the case of strongly-coupled transport coefficients.

models are derived and how, specifically, the matching at  $\tau_{\text{hydro}}$  is performed. The resulting models can be used as input to predict the effect of the pre-equilibrium period on QGP observables such as dilepton and photon production, heavy quark screening, etc.

### 6.3.1. 0+1 dimensional model for a pre-equilibrium QGP

In this section we present two models for 0+1 dimensional nonequilibrium time evolution of the QGP: 0+1 dimensional free-streaming and 0+1 dimensional collisionally-broadening expansion. In each case below we will be required to specify a proper time dependence of the hard-momentum scale,  $p_{\text{hard}}$ , and the microscopic anisotropy parameter,  $\xi$ , introduced in Ref. [2]. Before proceeding, however, it is useful to note some general relations. A similar approach was implemented in Chapter 5 to model the evolution of the fireball in the presence of anisotropies in the momentum-space. We will assume that during the pre-equilibrated evolution, the system is described by the anisotropic distribution function with the following parameterization

$$f_{\text{aniso}}(\mathbf{p}, \xi, p_{\text{hard}}) = f_{\text{iso}}(\sqrt{\mathbf{p}^2 + \xi(\mathbf{p} \cdot \hat{\mathbf{n}})^2}, p_{\text{hard}}), \quad (6.26)$$

where  $p_{\text{hard}}$  is the hard momentum scale,  $\hat{\mathbf{n}}$  is the direction of the anisotropy<sup>3</sup> and  $-1 < \xi < \infty$  is a parameter that reflects the strength and type of anisotropy. In general,  $p_{\text{hard}}$  is related to the average momentum in the partonic distribution function. The microscopic plasma anisotropy parameter  $\xi$  is related to the average longitudinal and transverse momentum of the plasma partons via the relation [82, 83, 84, 210]

$$\xi = \frac{\langle p_T^2 \rangle}{2\langle p_L^2 \rangle} - 1. \quad (6.27)$$

From this expression, one can see that for an oblate plasma  $\langle p_T^2 \rangle > 2\langle p_L^2 \rangle$  then  $\xi > 0$ . In an isotropic plasma one has  $\xi = 0$  and, in this case,  $p_{\text{hard}}$  can be identified with the plasma temperature  $T$ .

We now show how to derive a general formula for the time evolution of the microscopic plasma anisotropy  $\xi$  which allows for a non-vanishing anisotropy of the plasma at the formation time followed

<sup>3</sup>Hereafter, we will use  $\hat{\mathbf{n}} = \hat{\mathbf{e}}_z$ , where  $\hat{\mathbf{e}}_z$  is a unit vector along the beamline direction.

by subsequent dynamical evolution. This is a straightforward extension of the treatment presented in Chapter 5 where it was assumed that the plasma was isotropic at the formation time [83].

In most phenomenological approaches to QGP dynamics it is assumed that the distribution function at  $\tau \sim \tau_0$  is isotropic, i.e.  $\xi(\tau = \tau_0) = 0$ . There is no clear justification for this assumption. In fact, in the simplest form of the Color Glass Condensate (CGC) model [62] the longitudinal momentum would initially be zero. This configuration corresponds to an extreme anisotropy with  $\xi$  (or  $\Delta$ ) being infinite in the initial state. In the CGC framework in order to generate a non-zero longitudinal pressure it is necessary to include the next-to-leading-order corrections to gluon production taking into account the effect of rapidity fluctuations and full three-dimensional gauge field dynamics. There has been progress towards the solution of this problem; however, it is still an open question (for recent advances in this area see Ref. [182, 51] and references therein). We also note that, taking into account the finite longitudinal width of the nuclei, studies have shown that it may even be possible for the initial plasma anisotropy to be prolate at the formation time [32].

Here we will assume, quite generally, that the microscopic anisotropy parameter,  $\xi$ , at the formation time takes on an arbitrary value between -1 and  $\infty$  given by  $\xi_0$ . The initial anisotropy  $\xi_0$  can be evaluated using Eq. (6.27) giving

$$\xi_0 = \frac{1}{2} \frac{\langle p_T^2 \rangle_0}{\langle p_L^2 \rangle_0} - 1. \quad (6.28)$$

Writing the longitudinal momentum as

$$\langle p_L^2 \rangle = \langle p_L^2 \rangle_0 + \langle \delta p_L^2 \rangle, \quad (6.29)$$

and using the fact that, in the case of 0+1 dynamics, the average transverse momentum is constant

$$\langle p_T^2 \rangle = \langle p_T^2 \rangle_0, \quad (6.30)$$

we can rewrite the general expression for  $\xi$  given in Eq. (6.27) as

$$\xi = \frac{\xi_0 + 1}{1 + \frac{\langle \delta p_L^2 \rangle}{\langle p_L^2 \rangle_0}} - 1. \quad (6.31)$$

Finally we can parametrize the time-dependence of the average longitudinal momentum squared of the plasma as

$$\langle p_L^2 \rangle \sim \langle p_L^2 \rangle_0 \left( \frac{\tau_0}{\tau} \right)^\delta.$$

Comparing with (6.29), we obtain

$$\frac{\langle \delta p_L^2 \rangle}{\langle p_L^2 \rangle_0} = \left( \frac{\tau_0}{\tau} \right)^\delta - 1 \quad (6.32)$$

Inserting this into (6.31), we have

$$\xi(\xi_0, \tau, \tau_0) = (\xi_0 + 1) \left( \frac{\tau}{\tau_0} \right)^\delta - 1 \quad (6.33)$$

This expression holds for any of the 0+1 dimensional pre-equilibrium scenarios studied in this work. In this chapter we just consider two particular models of pre-equilibrated expansion, longitudinal free streaming where  $\delta = 2$  and in collisional broadening we have  $\delta = 2/3$ .<sup>4</sup> As it was pointed out in Chapter 5, there are other possibilities for the values of this exponent associated with the bending caused by growth of the chromoelectric and chromomagnetic fields at early times of the collision [83].

<sup>4</sup>Due to the assumption of no dynamics in the transverse plane, collisional broadening can only increase the longitudinal momentum in 0+1 dimensions.

In a comoving frame, the energy density and pressure components can be determined by evaluating the components of the stress-energy tensor

$$T^{\mu\nu} = \int \frac{d^3\mathbf{p}}{(2\pi)^3} \frac{p^\mu p^\nu}{p^0} f(\mathbf{p}, p_{\text{hard}}). \quad (6.34)$$

Using the ansatz (6.26) for the anisotropic distribution function and making an appropriate change of variables, one can show that the local energy density  $\mathcal{E}$  and the transverse and longitudinal pressures,  $\mathcal{P}_T$  and  $\mathcal{P}_L$ , are

$$\mathcal{E}(p_{\text{hard}}, \xi) = T^{00} = \frac{1}{2} \left( \frac{1}{1+\xi} + \frac{\arctan \sqrt{\xi}}{\sqrt{\xi}} \right) \mathcal{E}_{\text{iso}}(p_{\text{hard}}), \quad (6.35a)$$

$$= \mathcal{R}(\xi) \mathcal{E}_{\text{iso}}(p_{\text{hard}}),$$

$$\mathcal{P}_T(p_{\text{hard}}, \xi) = \frac{1}{2} (T^{xx} + T^{yy}), \quad (6.35b)$$

$$= \frac{3}{2\xi} \left( \frac{1 + (\xi^2 - 1)\mathcal{R}(\xi)}{\xi + 1} \right) \mathcal{P}_T^{\text{iso}}(p_{\text{hard}}),$$

$$\mathcal{P}_L(p_{\text{hard}}, \xi) = T^{zz}, \quad (6.35c)$$

$$= \frac{3}{\xi} \left( \frac{(\xi + 1)\mathcal{R}(\xi) - 1}{\xi + 1} \right) \mathcal{P}_L^{\text{iso}}(p_{\text{hard}}),$$

where  $\mathcal{P}_T^{\text{iso}}(p_{\text{hard}})$  and  $\mathcal{P}_L^{\text{iso}}(p_{\text{hard}})$  are the isotropic transverse and longitudinal pressures and  $\mathcal{E}_{\text{iso}}(p_{\text{hard}})$  is the isotropic energy density.<sup>5</sup> The function  $\mathcal{R}(\xi)$  is given by

$$\mathcal{R}(\xi) = \frac{1}{2} \left[ \frac{1}{1+\xi} + \frac{\arctan \sqrt{\xi}}{\sqrt{\xi}} \right], \quad (6.36)$$

and in (6.35) it is understood that  $p_{\text{hard}} = p_{\text{hard}}(\xi_0, \tau, \tau_0, \delta)$  and  $\xi = \xi(\xi_0, \tau, \tau_0, \delta)$ .

Note that for a conformal system the tracelessness of the stress-energy tensor  $T^\mu_\mu = 0$  implies  $\mathcal{E} = 2\mathcal{P}_T + \mathcal{P}_L$ . This condition is satisfied by Eqs. (6.35) for any anisotropic distribution function (6.26) since for an isotropic conformal state  $\mathcal{P}_{T,L}^{\text{iso}} = \mathcal{E}_{\text{iso}}/3$ .

The temporal evolution of  $\xi$ ,  $p_{\text{hard}}$  and  $\mathcal{E}$  for the case of 0+1 pre-equilibrated expansion is [122]

$$\xi(\tau) = (1 + \xi_0) (\tau/\tau_0)^\delta - 1, \quad (6.37a)$$

$$p_{\text{hard}}(\tau) = (p_{\text{hard}})_0 (\tau_0/\tau)^{(1-\delta/2)/3}, \quad (6.37b)$$

$$\mathcal{E}(\tau) = \mathcal{R}(\xi) \left( \frac{p_{\text{hard}}}{\gamma} \right)^4, \quad (6.37c)$$

where  $\delta = \{2, 2/3\}$  for free streaming and collisionally broadening expansion respectively.

### Relation between $\Delta$ and $\xi$

In this section, we derive the relation between the pressure anisotropy parameter,  $\Delta$ , introduced in Sec. 6.1.4 and the microscopic anisotropy parameter,  $\xi$ . Combining Eqs. (6.35b) and (6.35c) and using  $\mathcal{P}_T^{\text{iso}} = \mathcal{P}_L^{\text{iso}} = \mathcal{E}_{\text{iso}}/3$ , we obtain the following expression for  $\Delta$

$$\begin{aligned} \Delta(\xi) &= \frac{\mathcal{P}_T(\xi)}{\mathcal{P}_L(\xi)} - 1, \\ &= \frac{1}{2} (\xi - 3) + \xi \left( (1 + \xi) \frac{\arctan \sqrt{\xi}}{\sqrt{\xi}} - 1 \right)^{-1}. \end{aligned} \quad (6.38)$$

<sup>5</sup>We point out that in general, one cannot identify  $\mathcal{P}_T^{\text{iso}}(p_{\text{hard}})$ ,  $\mathcal{P}_L^{\text{iso}}(p_{\text{hard}})$  and  $\mathcal{E}_{\text{iso}}(p_{\text{hard}})$  with their equilibrium counterparts, unless one implements the Landau matching conditions.

The evolution of  $\Delta$  during the pre-equilibrium stage will depend on the kind of model for that stage, i.e. either free streaming or collisionally-broadened expansion. For small and large values of  $\xi$

$$\lim_{\xi \rightarrow 0} \Delta = \frac{4}{5}\xi + \mathcal{O}(\xi^2), \quad (6.39a)$$

$$\lim_{\xi \rightarrow \infty} \Delta = \frac{1}{2}\xi + \mathcal{O}(\sqrt{\xi}). \quad (6.39b)$$

If one uses Eq. (6.16a) together with Eq. (6.39a),  $\xi$  can be related with the shear viscous tensor during the viscous regime as

$$\xi = \frac{45}{8} \frac{\Pi}{\mathcal{E}} + \mathcal{O}(\Pi^2). \quad (6.40)$$

Note that if one uses the Navier-Stokes value of the shear tensor  $\Pi_{\text{NS}} = 4\eta/(3\tau)$  in the last relation, the anisotropy parameter can be expressed as [211]

$$\xi_{\text{NS}} = \frac{10}{T\tau} \frac{\eta}{\mathcal{S}} + \mathcal{O}(\Pi_{\text{NS}}^2). \quad (6.41)$$

### Matching the initial conditions

We will now match the general evolution of  $\xi$  from Eq. (6.33) at an intermediate  $\tau_{\text{hydro}}$  and use this to fix the initial shear tensor which should be used in the viscous evolution. From Eq. (6.33), the anisotropy parameter takes a non-vanishing value at  $\tau = \tau_{\text{hydro}}$ ,

$$\xi_{\text{hydro}} \equiv \xi(\tau = \tau_{\text{hydro}}) = (1 + \xi_0) \left( \frac{\tau_{\text{hydro}}}{\tau_0} \right)^\delta - 1. \quad (6.42)$$

Once  $\xi_{\text{hydro}}$  is known, the initial pressure anisotropy  $\Delta_{\text{hydro}}$  and initial energy density  $\mathcal{E}_{\text{hydro}}$  can be determined using Eqs. (6.38) and (6.35a) respectively. It is then straightforward to determine  $\Pi_{\text{hydro}} \equiv \Pi(\tau = \tau_{\text{hydro}})$  due to the relation (6.17), i.e.

$$\Pi_{\text{hydro}} \equiv \Pi(\tau = \tau_{\text{hydro}}) = \frac{2}{3} \left( \frac{\Delta_{\text{hydro}}}{3 + 2\Delta_{\text{hydro}}} \right) \mathcal{E}_{\text{hydro}}. \quad (6.43)$$

This expression together with  $\mathcal{E}_{\text{hydro}}$  gives the full set of initial conditions necessary to solve the 0+1 dimensional viscous hydrodynamics equations (6.2). Notice that by construction, the initial conditions do not depend on the particular coupling regime we are interested in. This is due to the fact that at leading order the coupling constant cancels out in the case of a collisionally-broadened expansion and in the case of free-streaming it is assumed that there is only free expansion. As a result  $\Pi_{\text{hydro}}$  and  $\mathcal{E}_{\text{hydro}}$  only depend on the type of pre-equilibrium scenario considered through the exponent  $\delta$ .

### 6.3.2. Temporal evolution including pre-equilibrium dynamics

In Fig. 6.11, we show the complete temporal evolution of the pressure anisotropy  $\Delta(\tau)$ , starting from a pre-equilibrium period and matching at  $\tau_{\text{hydro}}$  to viscous hydrodynamical evolution. In the plot we show three different assumed values of  $\tau_{\text{hydro}}$ . The initial conditions for the strong and weak coupling cases are assumed to be the same in both panels. During the pre-equilibrium case  $\tau_0 \leq \tau < \tau_{\text{hydro}}$ ,  $\Delta(\tau)$  is determined via its relation to  $\xi(\tau)$  specified in Eq. (6.38). In this figure we have shown the case that  $\xi$  evolves in the collisionally broadened scenario, i.e.  $\delta = 2/3$ . The matching from pre-equilibrium dynamics to viscous evolution occurs at  $\tau_{\text{hydro}}$ , where, due to the longitudinal expansion of the plasma, a non-vanishing value of  $\xi$  is generated. Using Eqs. (6.35a), (6.38), and (6.43) we use the value of  $\xi(\tau_{\text{hydro}})$  to determine the initial values of the energy density and shear necessary for the integration of the viscous hydrodynamical differential equations. From  $\tau_{\text{hydro}} \leq \tau \leq \tau_{\text{fo}}$ ,  $\Delta$



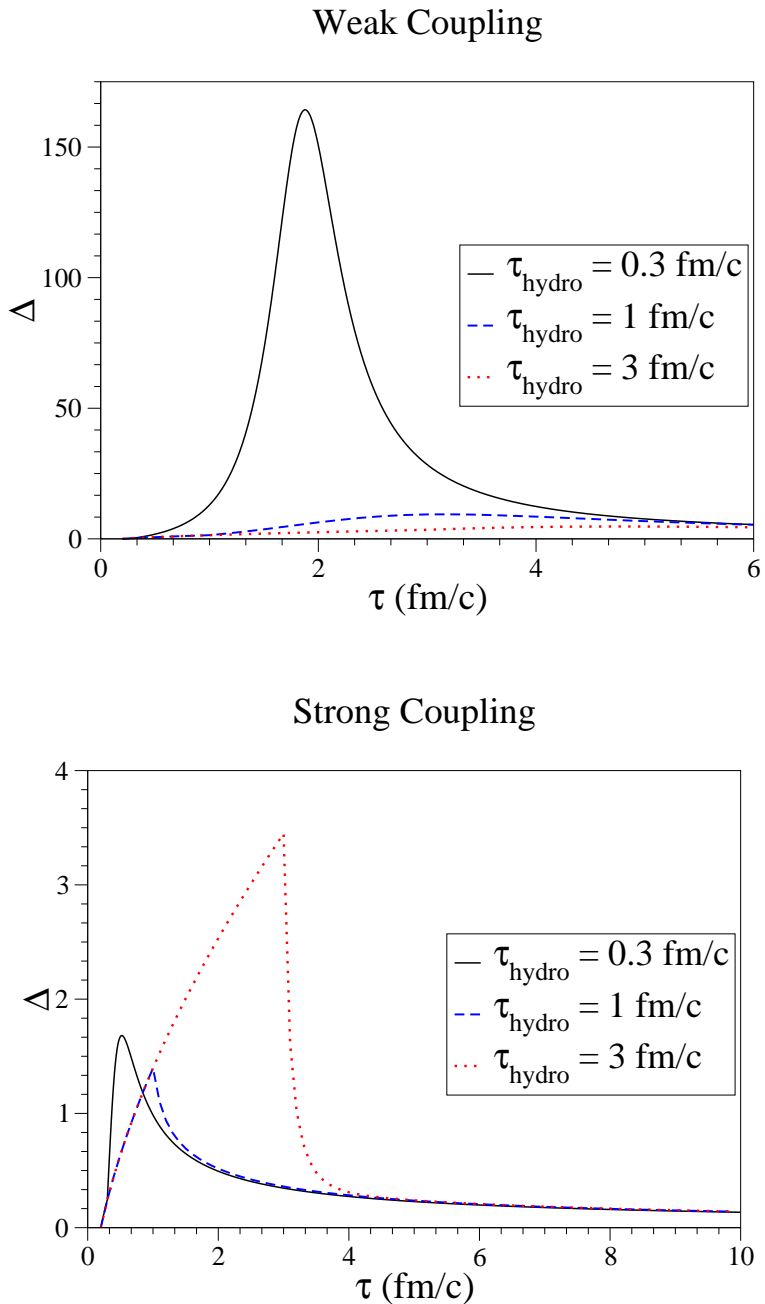


Figure 6.11.: Temporal evolution of the pressure anisotropy parameter  $\Delta$  for three different values of  $\tau_{\text{hydro}} \in \{0.3, 1, 3\}$  fm/c. We use  $\tau_0 = 0.3$  fm/c and the initial temperature at the parton formation time  $p_{\text{hard}} = T_{\text{hydro}} = 0.35$  GeV. All the plots assume the collisionally-broadened scenario and the transport coefficients during the viscous period correspond to weak coupling (top panel) and strong coupling (bottom panel) regime.

is determined using Eq. (6.15). It should be understood that during this period of the evolution the energy density and shear are the solutions of the viscous hydrodynamical differential equations, Eqs. (6.2). In both the weak and strong coupling cases the late time evolution of  $\Delta$  is given by the

Navier-Stokes solution with  $\Pi_{\text{NS}} = 4\eta/(3\tau)$ . Also note that if the pre-equilibrium evolution results in an anisotropy which is different than  $\Delta_{\text{NS}}(\tau_{\text{hydro}})$ , then the system relaxes to the Navier-Stokes solution within a time on the order of  $\tau_\pi$ .

As can be seen in Fig. 6.11 the initial value of  $\Delta$  depends on the assumed matching time. As  $\tau_{\text{hydro}}$  increases,  $\Delta_{\text{hydro}}$  and  $\Pi_{\text{hydro}}$  increase. If the assumed value of  $\tau_{\text{hydro}}$  is too large, then one sees an unreasonably fast relaxation to the Navier-Stokes solution. This is true in the collisionally broadened scenario depicted in Fig. 6.11 and also in the free-streaming scenario,  $\delta = 2$ , which we do not explicitly plot. In the free-streaming scenario the longitudinal momentum space anisotropies generated during the pre-equilibrium period are even larger.

Another issue which arises is that if the initial shear generated by the pre-equilibrium evolution becomes too large, it can become comparable to the equilibrium pressure  $\mathcal{P}$ . If this is the case, then it is suspect to apply viscous hydrodynamical evolution. However, this is not the only possible way to generate unreasonably large shear. Once the hydrodynamical evolution begins it is possible to generate large shear during the integration of the hydrodynamical differential equations. This effect is larger in the weakly-coupling case since the values of  $\bar{\eta}$  and  $\tau_\pi$  are approximately 10 and 30 times larger than in the strong coupling case, respectively. This is why in Fig. 6.11 we do not see large values of  $\Delta$  generated in the case of strong coupling, whereas we do in the weak-coupling case. One other possibility which arises is that the initial value of the shear computed from  $\xi$  will result in the initial condition being ‘‘critical’’, meaning that, when the differential equations are integrated, unphysical behavior such as negative longitudinal pressures are generated [121, 212]. In our results, we check to see if the generated initial conditions are critical and indicate if this happens in the corresponding results tables.

The evolution shown in Fig. 6.11 is typical of the time evolution of  $\Delta$  in our model. Of course, one can vary the assumed value of  $\xi$  at the formation time and also consider the free-streaming case. For the sake of brevity we will not present plots showing these possibilities since the analytic formulas required, Eqs. (6.33), (6.35a), (6.38), and (6.43), are simple enough for the reader to implement on their own. These four equations can be used to generate the time evolution of the plasma anisotropy for use in phenomenological applications. In Sect. 6.4, we will demonstrate how to use the resulting model and calculate entropy generation using it.

### Landau matching conditions

To determine the isotropic equilibrium energy density  $\mathcal{E}_{\text{eq}}(T)$  from a non-equilibrium single particle distribution function, it is necessary to implement the Landau matching conditions

$$\mathcal{E}(T) = u_\mu T_{(0)}^{\mu\nu} u_\nu, \quad (6.44a)$$

$$u_\mu \delta N^\mu = 0, \quad (6.44b)$$

$$u_\mu \delta T^{\mu\nu} u_\nu = 0, \quad (6.44c)$$

where  $T_{(0)}^{\mu\nu}$  is the energy-momentum tensor computed with the equilibrium distribution function  $f_{\text{eq}}(x, p)$  and  $\delta T^{\mu\nu}$  involves non-equilibrium corrections to the energy-momentum tensor. In the 14 Grad’s method this constraint is immediately satisfied by construction. In the case of the anisotropic Boltzmann distribution, the first constraint (6.44a) requires

$$\int \frac{d^3\mathbf{p}}{(2\pi)^3 p^0} (u \cdot p)^2 \exp[-\sqrt{\mathbf{p}^2 + \xi p_z^2} / p_{\text{hard}}] = \int \frac{d^3\mathbf{p}}{(2\pi)^3 p^0} (u \cdot p)^2 \exp[-p/T]. \quad (6.45)$$

Performing the integrals on both sides, we find that

$$p_{\text{hard}} = (\mathcal{R}(\xi))^{-1/4} T. \quad (6.46)$$

Now, we expand the anisotropic distribution function to second order in  $\xi$  and making use of the last expression, we have <sup>6</sup>

$$\begin{aligned} f_{\text{aniso}}(\mathbf{p}, \xi, T) &= \exp\left[-\sqrt{\mathbf{p}^2 + \xi p_z^2} / p_{\text{hard}}\right] \\ &= \exp\left[-\frac{p}{T}(\mathcal{R}(\xi))^{1/4} \sqrt{1 + \xi \cos^2 \theta}\right] \\ &\approx e^{-p/T} (1 + \xi f_{(1)} + \xi^2 f_{(2)}), \end{aligned} \quad (6.47)$$

where we use explicitly  $p_z = p \cos \theta$ . The functions  $f_{(1)}$  and  $f_{(2)}$  are given by

$$f_{(1)} = \frac{p}{6T} (1 - 3 \cos^2 \theta) \quad (6.48a)$$

$$f_{(2)} = \frac{p}{360T^2} [5p - 39T + 30(T - p) \cos^2 \theta + 45(T + p) \cos^4 \theta]. \quad (6.48b)$$

Replacing the expansion of the anisotropic distribution until  $\mathcal{O}(\xi)$  in the Landau condition (6.44b)

$$\begin{aligned} u_\mu \delta N^\mu &= \xi \int \frac{d^3 p}{(2\pi)^3} e^{-p/T} f_{(1)} \\ &= \frac{1}{(2\pi)^2} \frac{1}{6T} \int_0^\infty \int_0^\pi dp d(\cos \theta) p^3 e^{-p/T} (1 - 3 \cos^2 \theta) \\ &= 0. \end{aligned} \quad (6.49)$$

To  $\mathcal{O}(\xi)$ , the Landau condition (6.44b) is satisfied. Notice that this condition is not expected to hold at all orders because the particle number density is proportional to the entropy density. The only way to hold both the energy density and particle number density is by introducing a chemical potential.

When one expands the anisotropic distribution to  $\mathcal{O}(\xi^2)$  in the Landau condition (6.44c), we have

$$u_\mu \delta T^{\mu\nu} u_\nu = \int \frac{d^3 p}{(2\pi)^3} p e^{-p/T} (\xi f_{(1)} + \xi^2 f_{(2)}), \quad (6.50)$$

where  $f_{(1)}$  and  $f_{(2)}$  are given by Eqs. (6.48). Explicitly, we have

$$\xi \int \frac{d^3 p}{(2\pi)^3} p e^{-p/T} f_{(1)} = \frac{\xi}{(2\pi)^3 6T} \int d^3 p p^2 e^{-p/T} (1 - 3 \cos^2 \theta) \quad (6.51)$$

$$\begin{aligned} &= \frac{\xi}{(2\pi)^2 6T} \int dp p^4 e^{-p/T} \int d(\cos \theta) (1 - 3 \cos^2 \theta) \\ &= 0, \end{aligned} \quad (6.52)$$

$$\begin{aligned} \xi^2 \int \frac{d^3 p}{(2\pi)^3} p e^{-p/T} f_{(2)} &= \frac{\xi^2}{(2\pi)^3 360 T^2} \int d^3 p p^2 e^{-p/T} (5p - 39T \\ &\quad + 30(T - p) \cos^2 \theta + 45(p + T) \cos^4 \theta) \\ &= \frac{\xi^2}{(2\pi)^2 360 T^2} \left( 8 \int_0^\infty dp p^5 e^{-p/T} - 40 T \int_0^\infty dp p^4 e^{-p/T} \right) \\ &= 0. \end{aligned} \quad (6.53)$$

Therefore, up to second order in  $\xi$ , the anisotropic distribution function with  $p_{\text{hard}}$  given by Eq. (6.46) satisfies the Landau condition (6.44c).

<sup>6</sup>For practical purposes we expand until second order in  $\xi$  since we are considering viscous hydrodynamics until second order in gradient expansion.

## 6.4. Entropy and kinetic theory

In transport theory, the entropy current is defined as [102]

$$\mathcal{S}^\mu(x) = - \int \frac{d^3p}{(2\pi)^3} \frac{p^\mu}{p^0} f(x, \mathbf{p}) \{ \log[f(x, \mathbf{p})] - 1 \}. \quad (6.54)$$

Contracting the entropy current  $\mathcal{S}^\mu$  with the velocity fluid  $u^\mu$ , we obtain the entropy density  $\mathcal{S} \equiv u_\mu \mathcal{S}^\mu$ . Non-equilibrium corrections are usually computed by expanding the distribution function around the equilibrium [102]. For the anisotropic distribution function (6.26), the entropy density can be calculated analytically in the local fluid rest frame using a change of variables giving

$$\mathcal{S}(p_{\text{hard}}, \xi) = \frac{\mathcal{S}_{\text{iso}}(p_{\text{hard}})}{\sqrt{1 + \xi}}, \quad (6.55)$$

which, unlike typical expressions for the non-equilibrium entropy, is accurate to all orders in  $\xi$ . We note, importantly, that our ansatz (6.26) does not fall into the class of distribution functions describable using the 14 Grad's ansatz since, when expanded around equilibrium, (6.26) has momentum-dependent coefficients. Therefore, the entropy production from our anisotropic distribution will differ from the 14 Grad's method and IS ansatz as we show below.

### 6.4.1. Entropy from 14th Grad's Method

We can evaluate the entropy from the kinetic theory definition using the 14th Grad's approximation for the non-equilibrium distribution function

$$f(x, p) = f_{\text{eq}}(1 + \delta f), \quad (6.56)$$

The dependence of  $\delta f$  is assumed to be a function of the hydrodynamic degrees of freedom  $\mathcal{E}, \mathcal{P}, u^\mu, g^{\mu\nu}$  and  $\pi^{\mu\nu}$  expanded in a Taylor series

$$\delta f(x^\mu, p^\mu) = \epsilon_0 + \epsilon_\mu p^\mu + \epsilon_{\mu\nu} p^\mu p^\nu + \mathcal{O}(p^3). \quad (6.57)$$

By demanding that  $\delta f$  vanishes in equilibrium, one finds that in the Landau frame and assuming massless Boltzmann particles,  $\delta f$  is given by [126]

$$\delta f(x^\mu, p^\mu) = \frac{1}{2T^2 (\mathcal{E}(T) + \mathcal{P}(T))} \pi_{\mu\nu} p^\mu p^\nu + \mathcal{O}(p^3). \quad (6.58)$$

Expanding the expression of the entropy

$$\begin{aligned} \mathcal{S} &= - \int \frac{d^3p}{(2\pi)^3} f_{\text{eq}}(1 + \delta f) [\log(f_{\text{eq}}(1 + \delta f)) - 1], \\ &\approx \mathcal{S}_{(0)} + \mathcal{S}_{(1)} + \mathcal{S}_{(2)}. \end{aligned} \quad (6.59)$$

where

$$\mathcal{S}_{(0)} = - \int \frac{d^3p}{(2\pi)^3} f_{\text{eq}} [\log(f_{\text{eq}}) - 1], \quad (6.60a)$$

$$\mathcal{S}_{(1)} = - \int \frac{d^3p}{(2\pi)^3} f_{\text{eq}} \delta f \log(f_{\text{eq}}), \quad (6.60b)$$

$$\mathcal{S}_{(2)} = - \frac{1}{2} \int \frac{d^3p}{(2\pi)^3} f_{\text{eq}} (\delta f)^2. \quad (6.60c)$$

After replacing the 14 Grad's ansatz in the last expressions, these integrals can be calculated analytically if one rewrites them as moments of the equilibrium distribution function. Here, we

demonstrate this for a Boltzmann distribution  $f_{\text{eq}}(x^\mu, p^\mu) = e^{-p/T}$ . After a lengthy calculation, we find:

$$\mathcal{S}_{(0)} = \frac{1}{T} \left( \frac{3T^4}{\pi^2} + \frac{T^4}{\pi^2} \right) \equiv \frac{1}{T} (\mathcal{E}(T) + \mathcal{P}(T)), \quad (6.61a)$$

$$\mathcal{S}_{(1)} = 0, \quad (6.61b)$$

$$\mathcal{S}_{(2)} = -\frac{3}{8} \frac{\pi_{\mu\nu} \pi^{\mu\nu}}{T \mathcal{P}(T)}. \quad (6.61c)$$

Using the ideal equation of state, the non-equilibrium entropy is

$$\mathcal{S}_{\text{noneq}} = \frac{4}{3T} \mathcal{E}(T) - \frac{3}{8} \frac{\pi_{\mu\nu} \pi^{\mu\nu}}{T \mathcal{P}(T)}. \quad (6.62)$$

Comparing this expression with the IS ansatz for the non-equilibrium entropy, Eq. (6.6), we find a well-known result for a Boltzmann gas

$$\beta_2 = \frac{3}{4 \mathcal{P}(T)}. \quad (6.63)$$

For 0+1 dimensional case, where  $\pi_{\mu\nu} = \text{diag}(0, \Pi/2, \Pi/2, -\Pi)$ , the non-equilibrium entropy (6.62) is

$$\mathcal{S}_{\text{noneq}} = \frac{4}{3T} \mathcal{E}(T) - \frac{3}{4} \frac{\beta_2}{T} \Pi^2. \quad (6.64)$$

### 6.4.2. Entropy from the anisotropic distribution ansatz

Using the kinetic theory framework, we can calculate the entropy from the anisotropic distribution ansatz (6.26) by expanding in a Taylor series in terms of the anisotropy parameter  $\xi$  (Eqs. 6.48). Since the Landau matching conditions are satisfied by the anisotropic distribution function if Eq. (6.46) is imposed, one can write the shear tensor to first order in  $\xi$  as

$$\begin{aligned} \Pi^{\mu\nu} &= \int \frac{d^3 p}{(2\pi)^3 p^0} p^\mu p^\nu f_{\text{eq}} \delta f, \\ &= \frac{\xi}{6T} \int \frac{d^3 p}{(2\pi)^3} p^\mu p^\nu e^{-p/T} (1 - 3 \cos^2 \theta), \end{aligned} \quad (6.65)$$

where we use explicitly the first order correction to the anisotropic distribution function (6.48a). We are interested in the 0+1 dimensional case, where there is just one independent component of the shear tensor  $\Pi^{zz} = -\Pi$ . Calculating the  $zz$  component from the last expression, we have

$$\begin{aligned} \pi^{zz} \equiv -\Pi &= \frac{\xi}{6T} \int \frac{d^3 p}{(2\pi)^3} p_z^2 e^{-p/T} (1 - 3 \cos^2 \theta), \\ &= \frac{\xi}{(2\pi)^2 6T} \int_0^\pi d(\cos \theta) \cos^2 \theta (1 - 3 \cos^2 \theta) \int_0^\infty dp p^4 e^{-p/T}, \\ &= -\frac{8}{15} \frac{T^4}{\pi^2} \xi, \\ &= -\frac{8}{45} \mathcal{E}(T) \xi. \end{aligned} \quad (6.66)$$

This expression coincides with Eq. (6.40).

Expanding the entropy to second order in  $\xi$

$$\begin{aligned} \mathcal{S}_{\text{noneq}} &= - \int \frac{d^3 p}{(2\pi)^3} f_{\text{eq}} [1 + \xi f_{(1)} + \xi^2 f_{(2)}] [\log [f_{\text{eq}} (1 + \xi f_{(1)} + \xi^2 f_{(2)})] - 1], \\ &\approx \mathcal{S}_{(0)} + \mathcal{S}_{(1)} + \mathcal{S}_{(2)}. \end{aligned} \quad (6.67)$$

where

$$\mathcal{S}_{(0)} = - \int \frac{d^3p}{(2\pi)^3} f_{\text{eq}} [\log f_{\text{eq}} - 1], \quad (6.68)$$

$$\mathcal{S}_{(1)} = -\xi \int \frac{d^3p}{(2\pi)^3} f_{(1)} f_{\text{eq}} \log f_{\text{eq}}, \quad (6.69)$$

$$\mathcal{S}_{(2)} = -\xi^2 \int \frac{d^3p}{(2\pi)^3} f_{\text{eq}} \left( \frac{(f_{(1)})^2}{2} + f_{(2)} \log f_{\text{eq}} \right). \quad (6.70)$$

After replacing  $f_{(1)}$  and  $f_{(2)}$  (Eqs. (6.48)) in the last expressions and  $f_{\text{eq}} = e^{-p/T}$ , we have

$$\mathcal{S}_{(0)} = \frac{1}{T} \left( \frac{3T^4}{\pi^2} + \frac{T^4}{\pi^2} \right) \equiv \frac{1}{T} (\mathcal{E}(T) + \mathcal{P}(T)) \quad (6.71)$$

$$\mathcal{S}_{(1)} = 0 \quad (6.72)$$

$$\begin{aligned} \mathcal{S}_{(2)} &= -\frac{2}{15T} \frac{T^4}{\pi^2} \xi^2 \\ &= -\frac{2}{45} \frac{\mathcal{E}(T)}{T} \xi^2. \end{aligned} \quad (6.73)$$

Using the ideal equation of state, the non-equilibrium entropy can be written as

$$\begin{aligned} \mathcal{S}_{\text{noneq}} &= \frac{4}{3} \frac{\mathcal{E}(T)}{T} - \frac{2}{45} \frac{\mathcal{E}(T)}{T} \xi^2 \\ &= \frac{4}{3} \frac{\mathcal{E}(T)}{T} \left( 1 - \frac{\xi^2}{30} \right) \\ &= \frac{4}{3} \frac{\mathcal{E}(T)}{T} \left( 1 - \frac{135}{128} \left( \frac{\Pi}{\mathcal{E}(T)} \right)^2 \right). \end{aligned} \quad (6.74)$$

If one compares this result with the IS ansatz for the non-equilibrium entropy in the 0+1 dimensional case, Eq. (6.64), the term  $\beta_2$  for the anisotropic distribution ansatz can be fixed as

$$\beta_2 = \frac{5}{8} \frac{1}{\mathcal{P}(T)} \quad (6.75)$$

Notice that the difference of the values between Eqs. (6.63) and the last expression comes from the fact that the anisotropic distribution is incompatible with the 14 Grad's ansatz. This is due to the fact that at small  $\xi$  the linear term coming from the ansatz (6.26) cannot be expressed in the form  $a_{42} p_\mu \Pi^{\mu\nu} p_\nu$ , with  $a_{42}$  being a momentum-independent quantity. In the case of (6.26) the corresponding coefficient of  $p_\mu \Pi^{\mu\nu} p_\nu$  is momentum dependent and hence (6.26) does not fall in the class of distribution functions describable using the 14 Grad's ansatz.

## 6.5. Entropy generation

In both the pre-equilibrium and viscous hydrodynamical periods we use (6.55) to calculate the percentage entropy generation  $\Delta S/S_0$ . We define

$$\frac{\Delta S}{S_0} = \frac{\tau_{\text{fo}} \mathcal{S}(\tau_{\text{fo}}) - \tau_0 \mathcal{S}(\tau_0)}{\tau_0 \mathcal{S}(\tau_0)} \equiv \frac{S_f - S_0}{S_0} \quad (6.76)$$

where  $S_f$  and  $S_0$  are the entropy per unit rapidity evaluated at  $\tau = \tau_{\text{fo}}$  and  $\tau = \tau_0$ , respectively.

Note that the two models for pre-equilibrium evolution, free-streaming and collisionally-broadened expansions, generate no entropy during the pre-equilibrium period. In the case of free-streaming it

is obvious that there can be no entropy generation. In the case of collisionally broadened expansion there is an implicit assumption that there are no inelastic processes. Therefore, in both cases there is no entropy generation. This can be checked analytically by using Eq. (6.37) and computing either the entropy density or the number density, in which case one finds that both drop like  $\tau^{-1}$  [83, 26].<sup>7</sup> Of course, these models are an idealization and one expects inelastic processes to contribute to entropy production during the pre-equilibrium period in a more realistic model; however, this is beyond the scope of the current work.

The entropy produced during the expansion can be used to constrain nonequilibrium models of the QGP [163]. The produced entropy depends on the values of the transport coefficients and is sensitive to the assumed value of  $\eta/\mathcal{S}$ . Based on the fact that our pre-equilibrium models do not generate entropy, one naively expects that if the viscous hydrodynamical period starts later, then less entropy is produced. However, this is only true if during the viscous period we have control over the gradient expansion, i.e.  $|\Pi/\mathcal{P}| \ll 1$ . Additionally, for fixed  $p_{\text{hard}}$ , the factor of  $\sqrt{1+\xi}$  in (6.55) causes the entropy to monotonically decrease as  $\xi \rightarrow \infty$ . The competing effects of  $p_{\text{hard}}$  and  $\xi$  can cause the naive expectation described above to be violated, as we will discuss below.

In all of the calculations shown below, the parton formation time,  $\tau_0$ , is chosen to be 0.2 fm/c and the initial temperature,  $T_{\text{hydro}}$ , at that time is taken as 0.35 GeV. We use a freeze-out temperature of  $T_{\text{fo}} = 0.16$  GeV. The values of the transport coefficients are summarized in Eqs. (6.12) and (6.13). In what follows, we show the results for entropy production when one fixes the initial conditions at the formation time.

### 6.5.1. Free streaming model

In Fig. 6.12, we show the entropy percentage as a function of  $\tau_{\text{hydro}}$  in the strong (bottom panel) and weak (top panel) coupling limits when one uses free streaming as the pre-equilibrium scenario. In both figures after a certain time, which we will call  $\tau_c$ , there is no entropy generation in our model. This is due to the fact that for  $\tau_{\text{hydro}} > \tau_c$  the system freezes out while still in the pre-equilibrium period of evolution. For the free streaming model this time is approximately  $\tau_c = 3.6$  fm/c.

From Fig. 6.12, we see that the entropy production depends on the values of the transport coefficients. In the strong coupling case, we see that  $\Delta S/S_0$  increases between  $0.5 \lesssim \tau_{\text{hydro}} \lesssim 3$  fm/c and it goes to zero after  $\tau_c$ . The increase in entropy production is due to the rapidly increasing value of  $\Pi_{\text{hydro}}$  in the free-streaming case. In the weak coupling case, there is a similar behaviour but the effect is less pronounced. Again the increase in entropy production can be understood if one considers the values of the initial conditions  $\Pi_{\text{hydro}}$  and  $\mathcal{E}_{\text{hydro}}$  obtained from the pre-equilibrium free streaming expansion. For the free-streaming model, for example, the anisotropy parameter  $\xi$  increases as  $\tau^2$ . As a consequence, one can obtain large initial values for the shear. In fact, one should take care since the size of  $\Pi_{\text{hydro}}/\mathcal{P}_{\text{hydro}}$  can be of  $O(1)$  making the use of a viscous hydrodynamical description after  $\tau_{\text{hydro}}$  suspect. Therefore, it is necessary to check the relative size of  $\Pi$  and  $\mathcal{P}$  at the matching time to assess the trustworthiness of the hydrodynamical evolution. The constraint on  $\tau_{\text{hydro}}$  is stronger if one requires instead a more stringent convergence criterium,  $|\Pi| \leq \mathcal{P}/3$ , during the hydrodynamical evolution [121]. Here we do not apply this stronger condition but mention this in order to make the reader aware of this caveat.

### 6.5.2. Collisionally broadened model

In Fig. 6.13, we show the entropy percentage  $\Delta S/S_0$  in the strong (bottom panel) or weak coupling (top panel) cases as a function of  $\tau_{\text{hydro}}$ . In the collisionally-broadened case we find  $\tau_c = 2.2$  fm/c which is shorter than the corresponding time in the case of free streaming. This is due to the fact

<sup>7</sup>Only if you use the exact expression given by Eq. (6.55) does one find this result. If you use the Israel-Stewart or 14 Grad's expression for the non-equilibrium entropy you will find that, even assuming a free-streaming plasma, entropy is generated during the pre-equilibrium evolution. This is obviously incorrect so we use Eq. (6.55) in all cases.

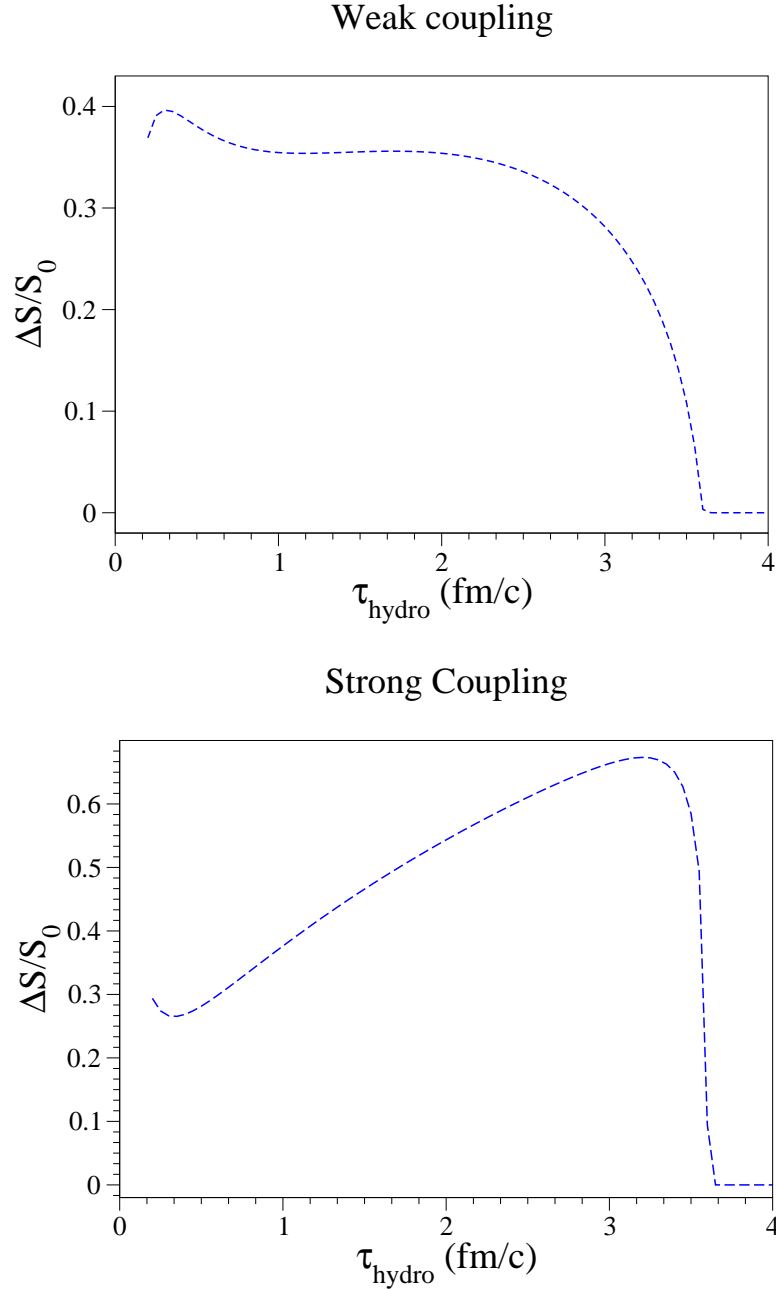


Figure 6.12.: Entropy percentage as a function of  $\tau_{\text{hydro}}$  for a free streaming pre-equilibrium scenario in the weak (top panel) and strong coupling (bottom panel) regime. We use  $\tau_0 = 0.2$  fm/c and the initial temperature at the parton formation time  $T_{\text{hydro}} = 0.35$  GeV.

than in the collisionally broadened case, the energy density decreases more quickly ( $\mathcal{E}_{\text{c.b.}} \sim \tau^{-11/9}$ ) compared with the free streaming case ( $\mathcal{E}_{\text{f.s.}} \sim \tau^{-1}$ ).

In Fig. 6.13, we see that, contrary to the case of free streaming, the entropy percentage as  $\tau_{\text{hydro}}$  is now a monotonically decreasing function of  $\tau_{\text{hydro}}$ . This is due to the fact that the anisotropies developed during the pre-equilibrium period are smaller for the collisionally-broadened case than the free-streaming case [83]. We note that we also observe that the entropy percentage as a function



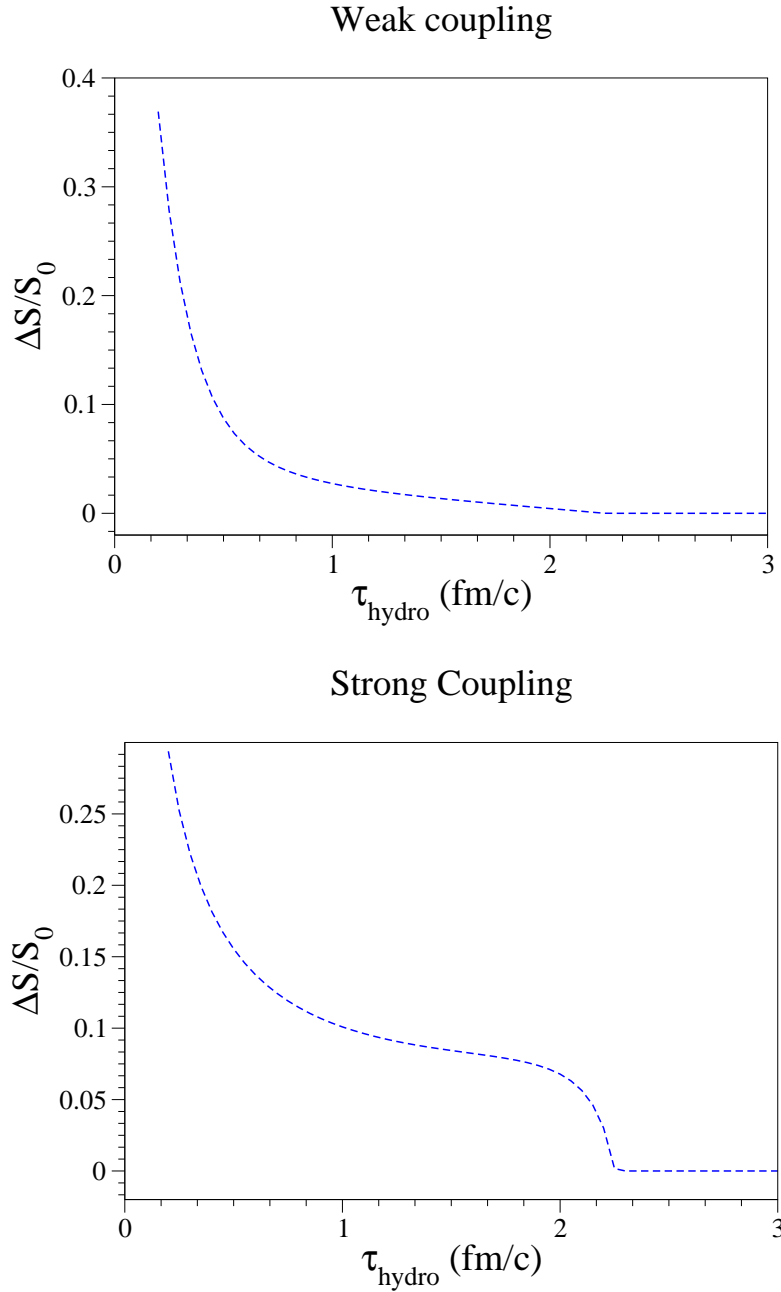


Figure 6.13.: Entropy percentage as a function of  $\tau_{\text{hydro}}$  for a collisionally broadening pre-equilibrium scenario in the weak (top panel) and strong coupling (bottom panel) regime. We use  $\tau_0 = 0.2$  fm/c and the initial temperature at the parton formation time  $T_{\text{hydro}} = 0.35$  GeV.

of  $\tau_{\text{hydro}}$  drops more quickly in the weak coupling regime compared with the strong coupling case. This is a consequence of Eq. (6.55) which shows that for fixed  $p_{\text{hard}}$  as  $\xi$  increases, less entropy is produced. As we pointed out in Sect. 6.3.2, the value of the anisotropy in momentum-space is larger in the weak-coupling case than in the strong-coupling case during the viscous period (see comparison in Fig. 6.11).

### 6.5.3. Including initial anisotropies at the formation time

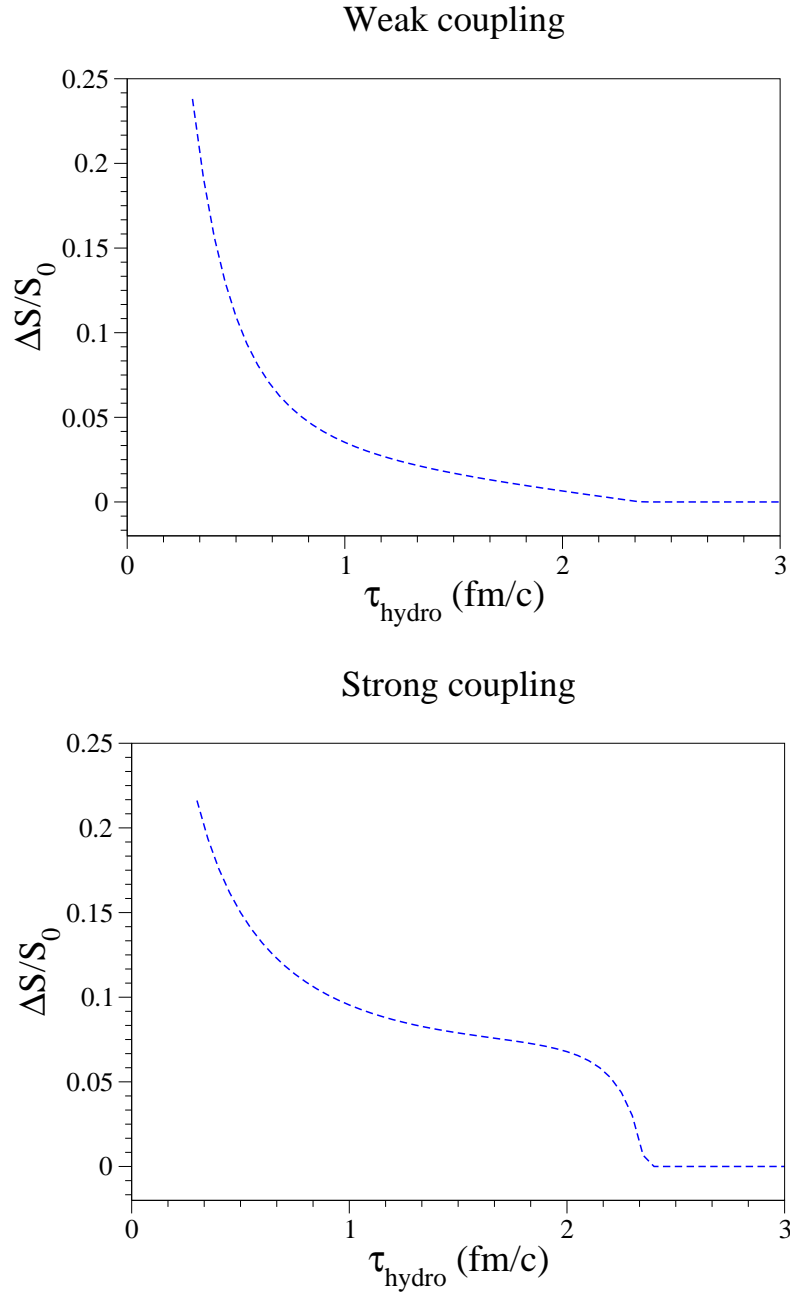


Figure 6.14.: Entropy percentage as a function of  $\tau_{\text{hydro}}$  for a collisionally broadening pre-equilibrium scenario and  $\xi_0 = -0.1$ , in the strong (bottom panel) and weak coupling (top panel) regime. We use  $\tau_0 = 0.2$  fm/c and the initial temperature at the parton formation time  $T_{\text{hydro}} = 0.35$  GeV.

In the previous subsections we showed results for the case that at the formation time there was no momentum-space anisotropy, i.e.  $\xi_0 = 0$ . In this subsection we will relax this assumption. In Fig. 6.14, we show the result for entropy production for a prolate initial distribution with  $\xi_0 = -0.1$  in

$\Delta S/S_0 \leq 10\%$			$\Delta S/S_0 \leq 20\%$		
$\xi_0$	Weak coupling	Strong coupling	$\xi_0$	Weak coupling	Strong coupling
-0.5	$\tau_{\text{hydro}} \geq 0.65 \text{ fm/c}$	$\tau_{\text{hydro}} \geq 0.75 \text{ fm/c}$	-0.5	Non determined	Non determined
0	$\tau_{\text{hydro}} \geq 0.45 \text{ fm/c}$	$\tau_{\text{hydro}} \geq 0.9 \text{ fm/c}$	0	$\tau_{\text{hydro}} \geq 0.3 \text{ fm/c}$	$\tau_{\text{hydro}} \geq 0.35 \text{ fm/c}$
10	Non determined	$\tau_{\text{hydro}} \geq 0.75 \text{ fm/c}$	10	Non determined	$\tau_{\text{hydro}} \geq 0.65 \text{ fm/c}$

Table 6.2.: Bounds on  $\tau_{\text{hydro}}$  imposed by requiring either a 10% (left panel) or 20% (right panel) bound on percentage entropy when one considers different values of  $\xi_0$  and transport coefficients. We fix the initial conditions through 0+1 collisionally broadening expansion.  $\tau_0 = 0.2 \text{ fm/c}$  and  $T = 350 \text{ MeV}$ .

the collisionally-broadened scenario. In both coupling cases,  $\Delta S/S_0$  is decreasing as  $\tau_{\text{hydro}}$  increases. Since the initial value of the anisotropy is close to zero, generally speaking, the behaviour of the entropy percentage is similar to the case we have an isotropic initial state ( $\xi_0 = 0$ ).

For larger values of  $\xi_0$ , the situation becomes more complicated because we do not have control of the size of  $\Pi/\mathcal{P}$  and the system can become “critical”. Therefore, for extreme initial anisotropies, it is not possible to determine  $\tau_{\text{hydro}}$  based on entropy constraints. In Table 6.2, we summarize the bounds on  $\tau_{\text{hydro}}$  obtained by varying  $\xi_0$  in the strong and weak coupling regime when one fixes the initial conditions using collisionally broadened expansion. The cases which have “Non determined” are cases in which the initial anisotropies were so extreme as to cause the system to begin generating negative longitudinal pressure. In those cases viscous hydrodynamics is unreliable. The striking conclusion from this table is that, in all cases, we find that the lower bound on  $\tau_{\text{hydro}}$  due solely to entropy considerations is larger in weak-coupling case than in the strong coupling case. This is due to a competing effect between increasing anisotropy and dropping temperature in Eq. (6.55) and can be seen already in the fact that the entropy production decreases more rapidly in the weak-coupling panels of Figs. 6.13 and 6.14. We point out that these estimates are lower bounds on the minimum  $\tau_{\text{hydro}}$  since our models have no entropy generation during the pre-equilibrium period. In a more realistic scenario there would also be entropy generation during the pre-equilibrium period which would add to all curves presented in this section.

In closing we emphasize that the bounds in Table 6.2 do not factor in the constraint that the shear should be small compared to the isotropic pressure. As shown in Ref. [83] requiring  $\Pi/\mathcal{P} < 1/3$  as a convergence criteria for viscous hydrodynamics and assuming an initially isotropic plasma (i.e.,  $\Pi_{\text{hydro}} = 0$ ) results in a constraint  $\tau_{\text{hydro}} > 5.9 T_{\text{hydro}}^{-1}$  in the case of a weakly-coupled plasma and  $\tau_{\text{hydro}} > 0.85 T_{\text{hydro}}^{-1}$  in the case of a strongly-coupled plasma. Assuming an initial temperature of 350 MeV this gives  $\tau_{\text{hydro}} > 3.3 \text{ fm/c}$  in the case of a weakly-coupled plasma and  $\tau_{\text{hydro}} > 0.6 \text{ fm/c}$  in the case of a strongly-coupled plasma. Therefore, assuming an initially isotropic plasma, the convergence constraint can be a stronger constraint than the constraint implied by entropy production. In general one must compare both constraints to determine which results in a stronger condition.

## 6.6. Summary of results

The validity of viscous hydrodynamics at early-times is not totally reliable since at early times the dissipative corrections can be large. In this chapter we studied how to constrain viscous hydrodynamics at early-times of the evolution of the collision.

We present two criteria that impose lower bounds on  $\tau_{\text{hydro}}$  by requiring that during all the simulated times, the solutions of viscous hydrodynamics satisfy: (1) positivity of the effective longitudinal pressure  $P_L$ , and (2) that the shear tensor  $\Pi$  to be small compared with the isotropic pressure  $\mathcal{P}$ , e.g.,  $|\Pi| \leq \mathcal{P}/3$ . As a result, the allowed  $\tau_{\text{hydro}}$  is non-trivially related with the initial condition of the shear tensor  $\Pi_{\text{hydro}}$  and the initial energy density  $\mathcal{E}_{\text{hydro}}$ . We show this by solving 0+1 dimensional 2nd-order conformal viscous hydrodynamics and studying if, for a given set of initial conditions

$\{\mathcal{E}_{\text{hydro}}, \Pi_{\text{hydro}}, \tau_{\text{hydro}}\}$ , the solution satisfies the required criteria [121].

We find that for certain values of  $\Pi_{\text{hydro}}$ , the system exhibits negative values of  $P_L$ , which indicates that one cannot trust on the validity of viscous hydrodynamics in certain kinematic regions. By requiring positivity of the longitudinal pressure, we find that if  $T_{\text{hydro}}=0.35$  GeV and the system is isotropic at  $\tau = \tau_{\text{hydro}}$ , (i.e.,  $\Pi_{\text{hydro}}=0$ ), for strong coupling  $\tau_{\text{hydro}} > 0.08$  fm/c while in weak coupling  $\tau_{\text{hydro}} > 0.23$  fm/c [121]. The last constraint is considered ‘weak’ in the sense that, the value of the shear viscous tensor can be on the same order as the isotropic pressure and therefore, the assumption of small departures from equilibrium is not completely satisfied. By imposing on the solution the stronger convergence criteria  $|\Pi| \leq P/3$ ,  $T_{\text{hydro}}=0.35$  GeV and  $\Pi_0=0$ , we find that for strong coupling  $\tau_{\text{hydro}} > 0.49$  fm/c whereas for weak coupling  $\tau_{\text{hydro}} > 3.37$  fm/c [121].

We presented a model that allows us to match 0+1 pre-equilibrium dynamics and 0+1 2nd-order conformal viscous hydrodynamics at a specified proper-time  $\tau_{\text{hydro}}$ . The pre-equilibrium evolution is modeled by either free-streaming or collisionally-broadening expansion. We derived a relation between the microscopic anisotropy parameter  $\xi$  and the pressure anisotropy of the fluid  $\Delta$ . This relation allowed us to determine the initial conditions for the shear  $\Pi$  and energy density  $\mathcal{E}$  at the assumed matching time. The initial values of  $\mathcal{E}$  and  $\Pi$  depend on the kind of pre-equilibrium model considered and also on the interval of time over which pre-equilibrium dynamics is assumed to take place. As a particular application here we studied entropy generation as a function of  $\tau_{\text{hydro}}$ . We derived an exact expression for the non-equilibrium entropy and then used this to determine the percentage entropy generation. We showed that due to the reduction of the entropy by a factor of  $\sqrt{1+\xi}$  compared to the isotropic case that it is possible to have more entropy generation in the strongly-coupled case. We summarized our results for entropy generation by presenting bounds on  $\tau_{\text{hydro}}$  which result from requiring the percentage entropy generation to be less than 10% or 20% in Table 6.2. We also mention that these results can be generalized to higher dimensions and in order to match all components of the energy momentum tensor and fluid four-velocity. However, it is necessary to better quantify the effect of transverse expansion during the pre-equilibrium period and its impact on the anisotropy developed at early times. One way to approach this problem is to make use of 3d parton cascade models [28, 29, 213] or 3d Boltzmann-Vlasov-Yang-Mills simulations [50]. Short of this, one can investigate simple analytic models such as 3d free-streaming or 3d collisionally-broadened expansion and develop analytic models which can be used to determine the necessary initial conditions self-consistently.

## 7. Conclusions and outlook

Fue entonces cuando comprendio que una historia no tiene dueño, que no es de uno hasta que se la conoce en su perfecta totalidad, hasta que se adivina el perfil con los ojos cerrados de una habitación a oscuras.

---

*Historia argentina*  
Rodrigo Fresán.

In this work we studied phenomenological consequences of an anisotropic QGP. Due to the different expansion rates along the longitudinal and transverse direction of the collision, the hot and dense matter is anisotropic in momentum-space. We investigated the impact of momentum-anisotropies in ultrarelativistic heavy ion collisions.

We have presented models which allow one to smoothly interpolate between early-time non-equilibrium 0+1 dimensional expansion to late-time isotropic equilibrium 0+1 dimensional hydrodynamic expansion. To accomplish this we introduced two parameters:  $\tau_{\text{iso}}$ , which is the time at which the system begins to expand hydrodynamically and  $\gamma$  which sets the width of the transition. Using these models we integrated the leading order rate for dilepton production in an anisotropic plasma over our modeled space-time evolution.

Based on our numerical results for the variation of dilepton yields with the assumed values of  $\tau_{\text{iso}}$  we find that the best opportunity to determine information about the plasma isotropization time in the central rapidity region is by analyzing the high transverse momentum ( $1 < p_T < 6$  GeV at RHIC and  $2 < p_T < 8$  GeV at LHC) dilepton spectra using relatively low pair invariant mass cuts ( $M \lesssim 2$  GeV). Based on these  $p_T$  spectra we introduced the “dilepton enhancement” factor  $\phi(\tau_{\text{iso}})$  which measures the ratio of yields obtained from a plasma which isotropizes at  $\tau_{\text{iso}}$  to one which isotropizes at the formation time,  $\tau_0$ . We showed that for our most extreme model, the free-streaming interpolating model ( $\delta = 2$ ) with fixed initial conditions, that the resulting enhancement  $\phi$  can be as large as 10; however, this extreme model probably overestimates the amount of anisotropy in the plasma. Additionally, this model results in a large amount of entropy generation during the transition from the free-streaming  $\tau^{-1}$  asymptotic behavior to hydro  $\tau^{-4/3}$  asymptotic behavior. As we discussed this greatly constrains the maximum isotropization times  $\tau_{\text{iso}}$  which are consistent with experimental indications of low (10-20%) entropy generation. In order to construct a more realistic model we then included collisional-broadening of the initial pre-equilibrium parton distribution functions ( $\delta = 2/3$ ). In this more realistic model there is much less entropy generation and the system is always closer to ideal 0+1 hydrodynamic expansion than in the free-streaming interpolating model. As a result the dilepton enhancement due to pre-equilibrium emissions is lower than the free-streaming case. We find that when fixing final multiplicity at RHIC energies there is a 20-40% enhancement in the high-transverse momentum dileptons and at LHC energies it is 30-50% when one assumes an isotropization time of  $\tau_{\text{iso}} = 2$  fm/c. The amplitude of the enhancement and position of the peak in the enhancement function,  $\phi$ , varies with the assumed value of  $\tau_{\text{iso}}$  which, given sufficiently precise data, would provide a way to determine the plasma isotropization time experimentally. We presented our predictions for the dilepton enhancement,  $\phi$ , as a function of  $\tau_{\text{iso}}$  for two different invariant mass cuts, demonstrating that our model can be constrained by a multiresolution analysis which should give higher statistics and further constrain the two model parameters at our disposal.

To study the dilepton production rapidity dependence, we have parametrized the rapidity dependence of  $p_{\text{hard}}$  using a Gaussian profile which is consistent with experimental observations of final

pion spectra from AGS through RHIC energies. We have applied the proposed model to study high-energy dilepton yields as a function of the pair rapidity and find that this observable is sensitive to the chosen value of  $\tau_{\text{iso}}$ . This suppression can be explained as a consequence of the combined effect of the anisotropy in momentum-space achieved at early-times due to expansion and the rapidity dependence of the hard momentum scale which explicitly breaks longitudinal boost invariance. We find that with the resulting dilepton modification factor,  $\Phi(\tau_{\text{iso}}=2 \text{ fm}/c)$ , shows suppressed dilepton yields in the forward rapidity region which can be up to 20% for  $0 < y \lesssim 4$  and up to a factor of 3 at  $y \sim 9$ . The amplitude of the suppression of  $\Phi(\tau_{\text{iso}})$  could help us to experimentally constrain  $\tau_{\text{iso}}$  given sufficiently precise data in the forthcoming LHC experiments. In this way forward dileptons would provide a way to determine the plasma isotropization time experimentally.

One shortcoming of our approach is that we have not included NLO corrections to dilepton production from an anisotropic QGP. At low invariant mass these corrections would become important. As a next step one must undertake a calculation of the rate for dilepton pair production at NLO in an anisotropic plasma. This is complicated by the presence of plasma instabilities that render some expressions like  $\langle AA \rangle$  correlators formally divergent and hence analytically meaningless. However, when combined with numerical solution of the long-time behavior of a plasma subject to the chromo-Weibel instability it may be possible to extract finite correlators. This is a daunting but doable task. Absent such a calculation, phenomenologically speaking it is probably a very good approximation to simply take existing NLO calculations and apply the enhancement function  $\phi$  as calculated at LO. We leave this for future work. Another uncertainty comes from our implicit assumption of chemical equilibrium. If the system is not in chemical equilibrium (too many gluons and/or too few quarks) early time quark chemical potentials, or fugacities, will affect the production of lepton pairs.

Next, we have studied momentum-anisotropies in the context of viscous hydrodynamics. Under the presence of the shear viscous tensor, the effective transverse and longitudinal pressures differ from each other as the system expands. We have derived two general criteria that can be used to assess the applicability of 2nd-order conformal viscous hydrodynamics to relativistic heavy-ion collisions. We did this by simplifying to a 0+1 dimensional system undergoing boost invariant expansion and then (a) requiring the longitudinal pressure to be positive during the simulated time or (b) requiring a convergence criterium that  $|\Pi| < \mathcal{P}/3$  during the simulated time. We showed that these requirements lead to a non-trivial relation between the different values of the energy density, shear viscous tensor and initial time when one starts to run numerical simulations. In particular, we found lower bounds on the initial time after imposing these requirements on the solutions of 0+1 2nd-order conformal viscous hydrodynamical equations. The constraints derived here were then shown to provide guidance for where one might expect 2nd-order viscous hydrodynamics to be a good approximation in higher-dimensional cases.

Finally, we presented a model that allows us to match 0+1 pre-equilibrium dynamics and 0+1 2nd-order conformal viscous hydrodynamics for a given initialization time. We find that the anisotropy parameter  $\xi$  can be related with the pressure anisotropy of the fluid  $\Delta$ . Using this relation we can find the values of the initial energy density and shear viscous tensor as a function of the initialization time. We derived a relation between the microscopic anisotropy parameter  $\xi$  and the pressure anisotropy of the fluid  $\Delta$ . This relation allowed us to determine the initial conditions for the shear tensor and energy density at the assumed matching time. The initial conditions for 0+1 viscous hydrodynamics depend on the kind of pre-equilibrium model considered and also on the interval of time over which pre-equilibrium dynamics is assumed to take place. As a particular application here we studied entropy generation as a function of the initial time. We derived an exact expression for the non-equilibrium entropy and then used this to determine the percentage entropy generation. We also discussed the limitations of the definitions of the non-equilibrium entropy and we concluded that these studies can be extended to higher dimensions in order to match all components of the energy momentum tensor and fluid four-velocity. To do this it is necessary to specify information about the transverse expansion during the pre-equilibrium period and how this impacts the anisotropy at early times. Short of this, one can investigate simple analytic models such as 3d free-streaming or 3d collisionally-broadened expansion and develop analytic models which can be used to determine

the necessary initial conditions self consistently.





# Appendices



## A. Useful relations of the moments of the Boltzmann distribution function

In this appendix we derive some of coefficients of the moments of the Boltzmann distribution function. The  $n$ -th moment of the equilibrated distribution function is defined as the  $n$  rank tensor

$$I^{\mu_1 \mu_2 \dots \mu_n}(x) = \int d\Gamma p^{\mu_1} p^{\mu_2} \dots p^{\mu_n} f_{\text{eq}}(x, p). \quad (\text{A.1})$$

This  $n$  rank tensor can be decomposed in a tensorial basis as [119, 120]

$$I^{\mu_1 \mu_2 \dots \mu_n} = \sum_{k=0}^{(n/2)} a_{nk} \Delta^{(2k)} u^{n-2k}, \quad (\text{A.2})$$

where

$$\Delta^{(2k)} u^{n-2k} = \frac{2^k! k! (n-2k)!}{n!} \times \sum_{\text{permutations}} \Delta^{\mu_1 \mu_2} \dots \Delta^{\mu_{2k-1} \mu_{2k}} u^{\mu_{2k+1}} \dots u^{\mu_n}, \quad (\text{A.3})$$

where  $\Delta^{\mu\nu} = g^{\mu\nu} - u^\mu u^\nu$  and  $u^\mu$  is the flow velocity of the fluid. The coefficients  $a_{nk}$  are found by contracting both sides of Eq. (A.2) with a tensor of the form (A.3).

For Boltzmann distribution function  $e^{-u_\mu p^\mu/T}$ , notice that one correlates its  $(n+1)$ -th moment with the  $n$ -th moment through the iterative relation

$$\begin{aligned} \frac{d}{dT} I^{\mu_1 \mu_2 \dots \mu_n} &= \frac{d}{dT} \left( \int d\Gamma p^{\mu_1} p^{\mu_2} \dots p^{\mu_n} e^{-u_\mu p^\mu/T} \right) \\ &= \frac{u_\delta}{T^2} \left( \int d\Gamma p^{\mu_1} p^{\mu_2} \dots p^{\mu_n} p^\delta e^{-u_\mu p^\mu/T} \right) \\ &\equiv \frac{1}{T^2} u_{\mu_{n+1}} I^{\mu_1 \mu_2 \dots \mu_{n+1}}. \end{aligned} \quad (\text{A.4})$$

Using Eq. (A.2), the 2nd moment of the Boltzmann distribution function can be written as

$$I^{\mu\nu} = \int d\Gamma p^\mu p^\nu f_{\text{eq}}(x, p) \equiv a_{20} u^\mu u^\nu + a_{21} \Delta^{\mu\nu}. \quad (\text{A.5})$$

For a Boltzmann distribution function, the coefficients  $a_{20}$  and  $a_{21}$  can be calculated after contracting with  $u_\mu u_\nu$  and  $\Delta_{\mu\nu}$ , respectively

$$a_{20} = \int d\Gamma p^2 e^{-p/T} = \frac{3}{\pi^2} T^4, \quad (\text{A.6a})$$

$$a_{21} = -\frac{1}{3} \int d\Gamma p^2 e^{-p/T} = -\frac{1}{\pi^2} T^4 = -\frac{a_{20}}{3}, \quad (\text{A.6b})$$

Using the Eq. (A.2) for  $n = 3$ , the 3rd moment of the Boltzmann distribution function can be decomposed as

$$I^{\alpha\beta\gamma} = a_{30} u^\alpha u^\beta u^\gamma + a_{31} [\Delta^{\alpha\beta} u^\gamma + \Delta^{\alpha\gamma} u^\beta + \Delta^{\gamma\beta} u^\alpha]. \quad (\text{A.7})$$

We need to calculate  $a_{31}$ . By contracting the last expression with  $u_\alpha \Delta_{\beta\gamma}$  we obtain

$$a_{31} = \frac{1}{3} u_\alpha \Delta_{\beta\gamma} I^{\alpha\beta\gamma}. \quad (\text{A.8})$$

Using Eq. (A.4) for  $n = 2$ , we conclude that:

$$\begin{aligned} a_{31} &= T^2 \frac{d}{dT} \left( \frac{1}{3} \Delta_{\alpha\beta} I^{\alpha\beta} \right), \\ &= T^2 \frac{d}{dT} a_{21}, \\ &= -\frac{4}{\pi^2} T^5, \\ &= -T (\mathcal{E} + \mathcal{P}), \end{aligned} \quad (\text{A.9})$$

where we explicitly use the tensor decomposition (A.5) for  $I^{\alpha\beta}$  and the fact that  $\Delta_{\alpha\beta} I^{\alpha\beta} = 9a_{21}$ .

According to Eq. (A.2) for  $n = 4$ , the fourth moment of the Jünter distribution function is decomposed in a tensorial basis as follows

$$\begin{aligned} I^{\mu\nu\alpha\beta} &= a_{40} u^\mu u^\nu u^\alpha u^\beta + a_{41} (u^\mu u^\nu \Delta^{\alpha\beta} + \text{permutations}) \\ &+ a_{42} (\Delta^{\mu\nu} \Delta^{\alpha\beta} + \Delta^{\mu\alpha} \Delta^{\nu\beta} + \Delta^{\mu\beta} \Delta^{\nu\alpha}). \end{aligned} \quad (\text{A.10})$$

The coefficient  $a_{42}$  is obtained by contracting the last expression with  $\Delta_{\mu\nu} \Delta_{\alpha\beta}$

$$a_{42} = \frac{1}{15} \Delta_{\mu\nu} \Delta_{\alpha\beta} I^{\mu\nu\alpha\beta}. \quad (\text{A.11})$$

Contracting the definition of  $I^{\mu\nu\alpha\beta}$  for  $n = 4$  in Eq. (A.1) with  $\Delta_{\mu\nu} \Delta_{\alpha\beta}$

$$\begin{aligned} \Delta_{\mu\nu} \Delta_{\alpha\beta} I^{\mu\nu\alpha\beta} &= \Delta_{\mu\nu} \Delta_{\alpha\beta} \int d\Gamma p^\mu p^\nu p^\alpha p^\beta e^{-u_\mu p^\mu / T}, \\ &= \Delta_{\mu\nu} \int d\Gamma p^\mu p^\nu (p^\delta p_\delta - (u \cdot p)^2) e^{-u_\mu p^\mu / T}, \\ &= -\Delta_{\mu\nu} u_\alpha u_\beta \int d\Gamma p^\mu p^\nu p^\alpha p^\beta e^{-u_\mu p^\mu / T}, \\ &= -u_\alpha (\Delta_{\mu\nu} u_\beta I^{\mu\nu\alpha\beta}), \\ &= -T^2 \frac{d}{dT} (u_\gamma \Delta_{\alpha\beta} I^{\alpha\beta\gamma}), \\ &= -3T^2 \frac{d}{dT} a_{31}. \end{aligned} \quad (\text{A.12})$$

In the fifth line we contract the iterative relation (A.4) for  $n = 3$  with  $\Delta_{\mu\nu} \Delta_{\alpha\beta}$  and in the sixth line we use explicitly Eq. (A.8). By comparing Eqs. (A.11) with (A.12) and using Eqn. (A.9) we conclude

$$\begin{aligned} a_{42} &= -\frac{1}{5} T^2 \frac{d}{dT} a_{31}, \\ &= \frac{4}{\pi^2} T^6, \\ &= T^2 (\mathcal{E} + \mathcal{P}). \end{aligned} \quad (\text{A.13})$$

Consider the tensor decomposition of  $I^{\mu\nu\alpha\beta\rho}$  based on Eq. (A.2) for  $n = 5$

$$\begin{aligned} I^{\mu\nu\alpha\beta\rho} &= a_{50} u^\mu u^\nu u^\alpha u^\beta u^\rho + a_{51} (u^\mu u^\nu u^\rho \Delta^{\alpha\beta} + \text{permutations}) \\ &+ a_{52} (\Delta^{\alpha\beta} \Delta^{\mu\nu} u^\rho + \text{permutations}). \end{aligned} \quad (\text{A.14})$$

By contracting the last expression with  $\Delta_{\alpha\beta}\Delta_{\mu\nu}u_\rho$ , the coefficient  $a_{52}$  is

$$\begin{aligned} a_{52} &= \frac{1}{15} \Delta_{\alpha\beta}\Delta_{\mu\nu}u_\rho I^{\mu\nu\alpha\beta\rho}, \\ &= \frac{1}{15} T^2 \Delta_{\alpha\beta}\Delta_{\mu\nu} \frac{d}{dT} I^{\mu\nu\alpha\beta} \end{aligned} \quad (\text{A.15})$$

where we use explicitly in the second line the Eq. (A.4) for  $n = 4$ . Using Eq. (A.11) in the last expression, we find

$$\begin{aligned} a_{52} &= T^2 \frac{d}{dT} a_{42}, \\ &= \frac{24}{\pi^2} T^7, \\ &= 6T^3(\mathcal{E} + \mathcal{P}), \end{aligned} \quad (\text{A.16})$$

where we have used relation (A.13).



## B. 2nd order conformal relativistic hydrodynamics for a 0+1 dimensional expansion

### B.1. 0+1 viscous hydrodynamical equations

The equations of motion of 2nd order conformal viscous hydrodynamics for the energy density  $\mathcal{E}$ , the fluid velocity  $u^\mu$  and the shear tensor  $\Pi^{\mu\nu}$  are given by [103, 104]

$$(\mathcal{E} + \mathcal{P})Dw^\mu = \nabla^\mu \mathcal{P} - \Delta_\alpha^\mu D_\beta \Pi^{\alpha\beta}, \quad (\text{B.1a})$$

$$D\mathcal{E} = -(\mathcal{E} + \mathcal{P})\nabla_\mu u^\mu + \frac{1}{2}\Pi^{\mu\nu}\nabla_{\langle\nu}u_{\mu\rangle}, \quad (\text{B.1b})$$

$$\begin{aligned} \Pi^{\mu\nu} = & \eta\nabla^{\langle\mu}u^{\nu\rangle} - \tau_\pi \left[ \Delta_\alpha^\mu \Delta_\beta^\nu D\Pi^{\alpha\beta} + \frac{4}{3}\Pi^{\mu\nu}(\nabla_\alpha u^\alpha) \right] \\ & + \frac{\kappa}{2} [R^{\langle\mu\nu\rangle} + 2u_\alpha R^{\alpha\langle\mu\nu\rangle\beta}u_\beta] \\ & - \frac{\lambda_1}{2\eta^2}\Pi^{\langle\mu}{}_\lambda\Pi^{\nu\rangle\lambda} + \frac{\lambda_2}{2\eta}\Pi^{\langle\mu}{}_\lambda\omega^{\nu\rangle\lambda} - \frac{\lambda_3}{2}\omega^{\langle\mu}{}_\lambda\omega^{\nu\rangle\lambda}, \end{aligned} \quad (\text{B.1c})$$

where  $D_\mu$  is the geometric covariant derivative,  $D \equiv u^\alpha D_\alpha$  is the comoving time derivative in the fluid rest frame,  $\nabla^\mu \equiv \Delta^{\mu\alpha} D_\alpha$  is the spatial derivative in the fluid rest frame,  $\omega_{\mu\nu} = -\nabla_{[\mu}u_{\nu]}$  is an antisymmetric operator that represents the fluid vorticity and  $R^{\alpha\mu\nu\beta}$  and  $R^{\mu\nu}$  are the Riemann and Ricci tensors, respectively. The coefficients  $\tau_\pi, \kappa, \lambda_1, \lambda_2$  and  $\lambda_3$  are the transport coefficients required by conformal symmetry [103, 104].

We consider a 3+1 dimensional system where there is no dependence on the transverse coordinates  $\mathbf{x}_T = (x, y)$  and the expansion along the beam line is boost invariant [19]. It is therefore convenient to work in a comoving frame described by the Milne coordinates, proper time  $\tau = \sqrt{t^2 - z^2}$  and spatial rapidity  $\zeta = \arctan(z/t)$ . In the Milne coordinates the metric  $g_{\mu\nu} = \text{diag}(1, -1, -1, -\tau^2)$  and the fluid velocity  $u^\mu = (1, 0, 0, 0)$ .

Requiring boost invariance allows some simplifications:  $\mathcal{E}, u^\mu, \Pi^{\mu\nu}$  are then independent of spatial rapidity  $\zeta$  and  $\Pi^{\mu\nu}$  is diagonal. For 0+1 dimensional viscous hydrodynamics, the orthogonality to the fluid velocity and tracelessness of  $\Pi^{\mu\nu}$  imply

$$\Pi^{\tau\nu} = 0, \quad (\text{B.2a})$$

$$\Pi_x^x + \Pi_y^y + \Pi_\zeta^\zeta = 0, \quad (\text{B.2b})$$

$$\implies \Pi_x^x = \Pi_y^y = -\frac{1}{2}\Pi_\zeta^\zeta.$$

Because of the rotational symmetry in the transverse plane, in the second line of Eq. (B.2b),  $\Pi_x^x = \Pi_y^y$ . From the last expressions, it is straightforward to conclude that in 0+1 dimensional viscous hydrodynamics there is just one independent component of the shear viscous tensor, say  $\Pi_\zeta^\zeta$ .

With these simplifications, the stress energy tensor in the presence of shear viscous corrections

takes the form [1, 121, 212, 214, 215, 125, 103, 216, 217]

$$T^{\mu\nu} = \begin{pmatrix} \varepsilon & 0 & 0 & 0 \\ 0 & p + \frac{1}{2}\Pi_\zeta^\zeta & 0 & 0 \\ 0 & 0 & p + \frac{1}{2}\Pi_\zeta^\zeta & 0 \\ 0 & 0 & 0 & p - \Pi_\zeta^\zeta \end{pmatrix}. \quad (\text{B.3})$$

In the Milne coordinates there are just three non-vanishing Christoffel symbols

$$\Gamma_{\zeta\tau}^\zeta = \Gamma_{\tau\zeta}^\zeta = \frac{1}{\tau}, \quad \Gamma_{\zeta\zeta}^\tau = \tau. \quad (\text{B.4})$$

Using these expressions, we can now derive the second order conformal viscous hydrodynamical equations for a 0+1 dimensional expansion from the general expressions given by Eqs. (B.1). Consider the term  $\Pi^{\mu\nu}\nabla_{\langle\nu}u_{\mu\rangle}$  in Eq. (B.1b):

$$\begin{aligned} \Pi^{\mu\nu}\nabla_{\langle\nu}u_{\mu\rangle} &= -\Pi_x^x\nabla_{\langle x}u_{x\rangle} - \Pi_y^y\nabla_{\langle y}u_{y\rangle} - \frac{1}{\tau^2}\Pi_\zeta^\zeta\nabla_{\langle\zeta}u_{\zeta\rangle}, \\ &= -\frac{2\Pi_x^x}{3\tau} - \frac{2\Pi_y^y}{3\tau} + \frac{4\Pi_\zeta^\zeta}{3\tau}, \\ &= \frac{2}{\tau}\Pi_\zeta^\zeta, \end{aligned} \quad (\text{B.5})$$

where we use explicitly Eq. (B.2b). Replacing the last expression in the equation of motion for the energy density (B.1b), we obtain

$$\partial_\tau\mathcal{E} = -\frac{\mathcal{E} + \mathcal{P}}{\tau} + \frac{\Pi_\zeta^\zeta}{\tau}. \quad (\text{B.6})$$

This is precisely the evolution equation for the energy density (6.2a) introduced in Chapter 6. Since we are working in flat space and we are interested in 0+1 dimensional boost invariant expansion, the Ricci scalar and the Ricci tensor vanish exactly and there is no vorticity,  $\omega_{\mu\nu} = 0$ . Therefore, we can rewrite Eq. (B.1c) for the only independent component of the shear tensor  $\Pi_\zeta^\zeta$  as

$$\Pi_\zeta^\zeta + \tau_\pi \left[ \Delta_\alpha^\zeta \Delta_\zeta^\beta D \Pi_\beta^\alpha + \frac{4}{3}\Pi_\zeta^\zeta \nabla_\alpha u^\alpha \right] + \frac{\lambda_1}{2\eta^2} \Pi_\beta^{\langle\zeta} \Pi_{\zeta\rangle}^\beta = 0. \quad (\text{B.7})$$

Now, we need to evaluate three terms,  $\Delta_\alpha^\zeta \Delta_\zeta^\beta D \Pi_\beta^\alpha$ ,  $\nabla_\alpha u^\alpha$  and  $\Pi_\beta^{\langle\zeta} \Pi_{\zeta\rangle}^\beta$ . Evaluating the first term  $\Delta_\alpha^\zeta \Delta_\zeta^\beta D \Pi_\beta^\alpha$

$$\begin{aligned} \Delta_\alpha^\zeta \Delta_\zeta^\beta D \Pi_\beta^\alpha &= \Delta_\alpha^\zeta \Delta_\zeta^\beta u^\gamma (\partial_\gamma \Pi_\beta^\alpha + \Gamma_{\gamma\delta}^\alpha \Pi_\beta^\delta - \Gamma_{\gamma\beta}^\delta \Pi_\delta^\alpha), \\ &= \partial_\tau \Pi_\zeta^\zeta + \Gamma_{\tau\zeta}^\zeta \Pi_\zeta^\zeta - \Gamma_{\tau\zeta}^\zeta \Pi_\zeta^\zeta, \\ &= \partial_\tau \Pi_\zeta^\zeta. \end{aligned} \quad (\text{B.8})$$

Calculating the term  $\nabla_\alpha u^\alpha$  we get

$$\begin{aligned} \nabla_\mu u^\mu &= \Delta_{\mu\alpha} D^\alpha u^\mu, \\ &= \partial_\mu u^\mu + \Gamma_{\mu\lambda}^\mu u^\lambda - u_\mu u^\alpha \partial_\alpha u^\mu - u_\mu u^\alpha \Gamma_{\alpha\lambda}^\mu u^\lambda, \\ &= \Gamma_{\zeta\tau}^\zeta u^\tau. \\ &= \frac{1}{\tau} \end{aligned} \quad (\text{B.9})$$



For the term  $\Pi_\beta \langle \zeta \Pi_\zeta \rangle^\beta$  we obtain

$$\begin{aligned}
 \Pi_\beta \langle \zeta \Pi_\zeta \rangle^\beta &= \left( 2 \Delta_\alpha^\zeta \Delta_{\zeta\beta} - \frac{2}{3} \Delta_\zeta^\zeta \Delta_{\alpha\beta} \right) \Pi^{\lambda\alpha} \Pi_\lambda^\beta, \\
 &= 2(\Pi_\zeta^\zeta)^2 - \frac{2}{3} \left( (\Pi_x^x)^2 + (\Pi_y^y)^2 + (\Pi_\zeta^\zeta)^2 \right), \\
 &= (\Pi_\zeta^\zeta)^2.
 \end{aligned} \tag{B.10}$$

Using the Eqs. (B.8),(B.9) and (B.10) in Eq. (B.7), we get the equation of motion for the shear component  $\Pi_\zeta^\zeta$

$$\Pi_\zeta^\zeta + \tau_\pi \left( \partial_\tau \Pi_\zeta^\zeta + \frac{4}{3\tau} \Pi_\zeta^\zeta \right) + \frac{\lambda_1}{2\eta^2} \left( \Pi_\zeta^\zeta \right)^2 = \frac{4\eta}{3\tau}. \tag{B.11}$$

This is the equation of motion for  $\Pi_\zeta^\zeta$  (6.2b) introduced in Chapter 6.



## C. Useful relations in thermal field theory

### C.1. Relation between thermal Green functions

In thermal field theory one can consider the temporal evolution of an operator  $\hat{A}(t)$  in the real-time and imaginary-time formalism as

$$\hat{A}(t) = e^{i\hat{H}t} \hat{A}(0) e^{-i\hat{H}t} \quad , \quad \text{“real time”} \quad , \quad (\text{C.1a})$$

$$\hat{A}(\tau) = e^{\hat{H}\tau} \hat{A}(0) e^{-\hat{H}\tau} \quad , \quad \text{“imaginary time”} \quad . \quad (\text{C.1b})$$

Then we define the correlators of two arbitrary bosonic operators  $\hat{A}$  and  $\hat{B}$  defined over the Hilbert space as <sup>1</sup>

$$\tilde{C}_>(p^0) \equiv \int_{-\infty}^{\infty} dt e^{ip^0 t} \langle \hat{A}(t) \hat{B}(0) \rangle \quad \text{“Advanced propagator”} \quad , \quad (\text{C.2a})$$

$$\tilde{C}_<(p^0) \equiv \int_{-\infty}^{\infty} dt e^{ip^0 t} \langle \hat{B}(0) \hat{A}(t) \rangle \quad , \quad \text{“Retarded propagator”} \quad , \quad (\text{C.2b})$$

$$\rho(p^0) \equiv \int_{-\infty}^{\infty} \langle \frac{1}{2} [\hat{A}(t), \hat{B}(0)] \rangle \quad , \quad \text{“Spectral function”} \quad , \quad (\text{C.2c})$$

$$\hat{C}_E(w_n^b) \equiv \int_0^\beta d\tau e^{iw_n^b \tau} \langle \hat{A}(\tau) \hat{B}(0) \rangle \quad , \quad (\text{C.2d})$$

with  $w_n^b = 2\pi T n$  (bosonic Matsubara frequencies).

As we show below, the following relations can be established from last definitions

$$\tilde{C}_<(p^0) = \frac{2}{e^{\beta p^0} - 1} \rho(p^0) = 2 n_B(p^0) \rho(p^0) \quad , \quad (\text{C.3a})$$

$$\tilde{C}_>(p^0) = \frac{2}{1 - e^{-\beta p^0}} \rho(p^0) = 2 e^{\beta p^0} n_B(p^0) \rho(p^0) \quad , \quad (\text{C.3b})$$

$$\rho(p^0) = \frac{1}{2i} \{ \hat{C}_E(-i[p^0 + i0^+]) - \hat{C}_E(-i[p^0 - i0^+]) \} \quad , \quad (\text{C.3c})$$

where

$$\langle \dots \rangle \equiv \text{Tr} \{ (\dots) \hat{\rho}_{\text{sys.}} \} = \frac{1}{Z_{\text{sys.}}} \text{Tr} \left\{ (\dots) e^{-\beta \hat{H}_{\text{sys.}}} \right\} .$$

The retarded and advanced propagators are related. To show this, first we rewrite the retarded propagator from its definition (C.2b)

$$\begin{aligned} \tilde{C}_<(p^0) &= \int_{-\infty}^{\infty} dt e^{ip^0 t} \frac{1}{Z} \text{Tr} [\hat{B}(0) e^{i\hat{H}t} \hat{A}(0) e^{-i\hat{H}t} e^{-\beta \hat{H}}] \quad , \\ &= \int_{-\infty}^{\infty} dt e^{ip^0 t} \frac{1}{Z} \sum_{n,m} e^{-(it+\beta)E_m} e^{itE_n} \langle n | \hat{A}(0) | m \rangle \langle m | \hat{B}(0) | n \rangle \quad , \\ &= \frac{1}{Z} \sum_{n,m} e^{-\beta E_m} (2\pi) \delta(p^0 + E_m - E_n) \langle n | \hat{A}(0) | m \rangle \langle m | \hat{B}(0) | n \rangle . \end{aligned} \quad (\text{C.4})$$

<sup>1</sup>These definitions are just for the bosonic fields and can be extended to the fermionic case. See details in Refs. [74, 75].

Now, using the definition of the advanced propagator (C.2a)

$$\begin{aligned}
\tilde{C}_>(p^0) &= \int_{-\infty}^{\infty} dt e^{ip^0 t} \frac{1}{Z} \text{Tr} [e^{i\hat{H}t} \hat{A}(0) e^{-i\hat{H}t} \hat{B}(0) e^{-\beta \hat{H}}], \\
&= \int_{-\infty}^{\infty} dt e^{ip^0 t} \frac{1}{Z} \sum_{n,m} e^{-(-it+\beta)E_n} e^{-itE_m} \langle n | \hat{A}(0) | m \rangle \langle m | \hat{B}(0) | n \rangle, \\
&= \frac{1}{Z} \sum_{n,m} e^{-\beta E_n} (2\pi) \delta(p^0 + E_n - E_m) \langle n | \hat{A}(0) | m \rangle \langle m | \hat{B}(0) | n \rangle, \\
&= e^{\beta p^0} \tilde{C}_<(p^0). \tag{C.5}
\end{aligned}$$

The last relation is known as the Kubo-Martin-Schwinger (KMS) relation. Next, using the definition of the spectral function (C.2c)

$$\rho(p^0) = \frac{1}{2} [\tilde{C}_>(p^0) - \tilde{C}_<(p^0)],$$

and the KMS relation (C.5) in the last expression, we can get (C.3a) and (C.3b) respectively

$$\rho(p^0) = \frac{1}{2} (e^{\beta p^0} - 1) \tilde{C}_<(p^0) \implies \tilde{C}_<(p^0) = \frac{2}{e^{\beta p^0} - 1} \rho(p^0) = 2 n_B(p^0) \rho(p^0), \tag{C.6a}$$

$$\rho(p^0) = \frac{1}{2} (1 - e^{-\beta p^0}) \tilde{C}_>(p^0) \implies \tilde{C}_>(p^0) = \frac{2}{1 - e^{-\beta p^0}} \rho(p^0) = 2 e^{\beta p^0} n_B(p^0) \rho(p^0). \tag{C.6b}$$

From the definition of  $\tilde{C}_E$  we have

$$\begin{aligned}
\tilde{C}_E(w_n^b) &= \int_0^\beta d\tau e^{i w_n^b \tau} \langle \hat{A}(\tau) \hat{B}(0) \rangle, \\
&= \int_{-\infty}^{\infty} \frac{dq^0}{(2\pi)} \int_0^\beta d\tau e^{i w_n^b \tau} e^{-iq^0 \tau} \tilde{C}_>(q^0) \Big|_{it \rightarrow \tau}, \\
&= \int_{-\infty}^{\infty} \frac{dq^0}{(2\pi)} \int_0^\beta d\tau e^{(i w_n^b - q^0) \tau} \frac{2}{1 - e^{-\beta p^0}} \rho(q^0), \\
&= \int_{-\infty}^{\infty} \frac{dq^0}{\pi} \frac{1}{1 - e^{-\beta p^0}} \rho(q^0) \frac{1}{i w_n^b - q^0} e^{(i w_n^b - q^0) \tau} \Big|_0^\beta, \\
&= \int_{-\infty}^{\infty} \frac{dq^0}{\pi} \frac{\rho(q^0)}{1 - e^{-\beta p^0}} \frac{1}{i w_n^b - q^0} (e^{-\beta p^0} - 1), \\
&= \int_{-\infty}^{\infty} \frac{dq^0}{\pi} \frac{\rho(q^0)}{q^0 - i w_n^b}, \tag{C.7}
\end{aligned}$$

where in the second line we use the Fourier transform of the advanced propagator  $\tilde{C}_>(q^0)$ . Now, we need to invert the last expression and in order to accomplish this, we use a well known result from complex variable theory

$$\frac{1}{\Delta \pm i0^+} = P \left( \frac{1}{\Delta} \right) \mp i\pi \delta(\Delta) \tag{C.8}$$

$$\Rightarrow \frac{1}{2i} \left( \frac{1}{q^0 - p^0 - i0^+} - \frac{1}{q^0 - p^0 + i0^+} \right) = \pi \delta(q^0 - p^0), \tag{C.9}$$

where  $P$  represents the principal part. Finally we obtain the relation (C.3c) after using in Eq. (C.7)

$$\begin{aligned}\tilde{C}_E(w_n^b) &= \int_{-\infty}^{\infty} \frac{dq^0}{\pi} \frac{\rho(q^0)}{q^0 - iw_n^b}, \\ \Rightarrow \frac{1}{2i} [\tilde{C}_E(-i[p^0 + i0^+]) - \tilde{C}_E(-i(p^0 - i0^+))] &= \rho(p^0).\end{aligned}\quad (\text{C.10})$$

## C.2. Fermionic summation formula

Let

$$\begin{aligned}G_F &= T \sum_{q_n^f} \frac{e^{iq_n^f \tau}}{(q_n^f)^2 + E^2} \\ q_n^f &= 2\pi T(n + \frac{1}{2}); \quad n \in \mathbb{Z}.\end{aligned}\quad (\text{C.11})$$

$q_n^f$  is the fermionic Matsubara frequency. Now consider the function

$$n_F(iq^0) = \frac{1}{e^{iq^0\beta} + 1}.\quad (\text{C.12})$$

This function has poles when  $q^0\beta = 2\pi(n + \frac{1}{2})$ , i.e., when  $q^0 = q_n^f$ . The residue at any pole is calculated directly

$$n_F(i[q_n^f + z]) = \frac{1}{1 - e^{iz\beta}} \approx -\frac{1}{z\beta} = iT\quad (\text{C.13})$$

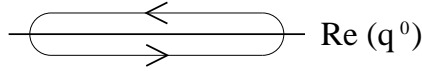


Figure C.1.: Implemented contour to perform the integral given in Eq. (C.14).

Let  $f(q^0)$  be a function which is regular on the real axis. Then,

$$\int_{\mathcal{C}} dq^0 f(q^0) n_F(iq^0) = 2\pi i (iT) \sum_{q_n^f} f(q_n^f)\quad (\text{C.14})$$

where  $\mathcal{C}$  is the contour depicted in Fig. C.1. If one chooses the function  $f(q^0)$  to be

$$f(q^0) = \frac{e^{iq^0\tau}}{(q^0)^2 + E^2}; \quad 0 < \tau < \beta,\quad (\text{C.15})$$

the relation (C.14) implies that the function  $G_F$  can be written as

$$G_F(\tau) = -\frac{1}{2\pi} \int_{\mathcal{C}} dq^0 \frac{e^{iq^0\tau}}{(q^0)^2 + E^2} n_F(q^0).\quad (\text{C.16})$$

For  $0 < \tau < \beta$ , the function  $e^{iq^0\tau} n_F(q^0)$  vanishes exponentially at infinity. This allows us to close the contour as shown in Fig. C.2 and pick up the poles at  $q^0 = \pm iE$

$$\begin{aligned}G_F(\tau) &= -\frac{1}{2\pi} (2\pi i) \left[ \frac{e^{-E\tau}}{2iE} n_F(-E) + \frac{e^{E\tau}}{-2iE} n_F(E) \right] \\ &= \frac{1}{2E} n_F(E) [e^{(\beta-\tau)E} - e^{\beta\tau}].\end{aligned}\quad (\text{C.17})$$

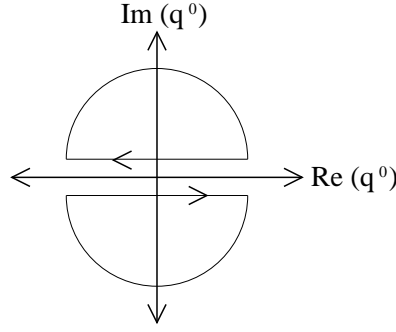


Figure C.2.: Closed contour to perform the integral C.16

### C.3. Evaluation of $\tilde{C}_{\mu\nu}(P)$ using imaginary time formalism

In general, to compute observables, it is enough to compute the imaginary Green function  $\tilde{C}_E$  and carry out an analytic continuation afterwards. One can show that the advanced and retarded propagator together with the spectral function are related with  $\tilde{C}_E$ . Here we show how to calculate the Green function  $\tilde{C}_{\mu\nu}^<(P)$  using the imaginary time formalism.

The lowest order Feynman diagram which contributes to the production of lepton pairs is shown in Fig. C.3. Therefore, the electromagnetic current-current function  $\tilde{C}_{\mu\nu}^<(P)$  can be simply expressed as  $J_\mu^q(x) = \bar{\psi}(x)\gamma_\mu\psi(x)$ . In thermal field theory, the free Feynman propagator in the imaginary time formalism is given by

$$\langle 0|T\{\psi(x)\bar{\psi}(y)\}|0\rangle = T \sum_{q_n} \int \frac{d^3\mathbf{q}}{(2\pi)^3} e^{i\tilde{Q}_f \cdot (\tilde{x}-\tilde{y})} \frac{-i\tilde{Q}_f + M}{\tilde{Q}_f^2 + M^2} \quad (\text{C.18})$$

where  $\tilde{Q}_f^2 = (q_n^f)^2 + \mathbf{q}^2$  and  $q_n^f = 2\pi T(n + 1/2)$  being the fermionic Matsubara frequencies.

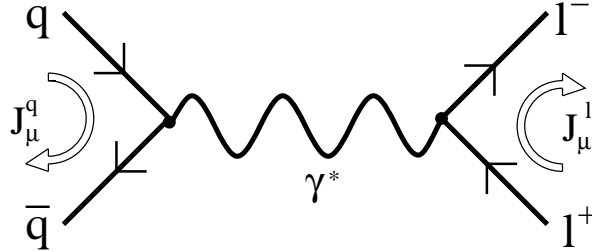


Figure C.3.: Feynman diagram for the process  $q + \bar{q} \rightarrow \gamma^* \rightarrow l^+ + l^-$ . At leading order  $\mathcal{O}(\alpha)$ , the quark current is  $\hat{J}_\mu^q(x) = \hat{\psi}(x)\gamma_\mu\hat{\psi}(x)$  and leptonic current  $\hat{J}_\mu^l(x) = \hat{l}(x)\gamma_\mu\hat{l}(x)$ .

Therefore, the imaginary current-current correlation function is

$$\begin{aligned} \tilde{C}_{\mu\nu}^E(\tilde{P}) &= \int_0^\beta d\tau \int d^3\mathbf{x} e^{i\tilde{P} \cdot \tilde{x}} \langle \bar{\psi}(\tilde{x})\gamma_\mu\psi(\tilde{x})\bar{\psi}(0)\gamma_\nu\psi(0) \rangle, \\ &= -N_C T^2 \int_0^\beta d\tau \int d^3\mathbf{x} e^{i\tilde{P} \cdot \tilde{x}} \sum_{w_n, w_m} \int d^3\mathbf{r} d^3\mathbf{q} e^{i\tilde{x} \cdot (\tilde{Q} - \tilde{R})} \\ &\quad \times \text{Tr} \left[ \tilde{\gamma}_\mu \frac{-i\tilde{Q}_f + M}{\tilde{Q}_f^2 + M^2} \tilde{\gamma}_\nu \frac{-i\tilde{R}_f + M}{\tilde{R}_f^2 + M^2} \right], \end{aligned} \quad (\text{C.19})$$

where  $\tilde{P} = (w_n^b = 2\pi nT, \mathbf{p})$ ,  $\tilde{x} = (\tau, \mathbf{x})$ ,  $\tilde{R}_f = (r_n^f, \mathbf{r})$  and  $\tilde{Q}_f = (q_m^f, \mathbf{q})$ . Performing the trace of the Dirac matrices in Euclidean space, we have <sup>2</sup>

$$\text{Tr} [\tilde{\gamma}_\mu(-i\tilde{Q}_f + M)\tilde{\gamma}_\nu(-i\tilde{R}_f + M)] = 4\{M^2\delta_{\mu\nu} - \tilde{Q}_\alpha\tilde{R}_\beta(\delta_{\mu\alpha}\delta_{\nu\beta} - \delta_{\mu\nu}\delta_{\alpha\beta} + \delta_{\mu\beta}\delta_{\nu\alpha})\} \quad (\text{C.20})$$

so in Eq. (C.19) we need just to evaluate  $\delta_{\mu\nu}\tilde{C}_{\mu\nu}^E(\tilde{P})$  since as it can be shown that  $\tilde{p}_\mu\tilde{p}_\nu\tilde{C}_{\mu\nu}^E(\tilde{P}) = 0$  (see demonstration in App. C.4). Using Eq. (C.20) together with Eq. (C.19) plus the transversality of  $\tilde{C}_{\mu\nu}^E$  we get

$$\begin{aligned} \delta_{\mu\nu}\tilde{C}_{\mu\nu}^E(\tilde{P}) &= -4N_C T^2 \sum_{\tilde{Q}_f, \tilde{R}_f} \int_0^\beta d\tau \int d^3\mathbf{x} \int d^3\mathbf{r} d^3\mathbf{q} e^{i\tau(w_m + q_n^f - r_n^f) - i\mathbf{x}\cdot(\mathbf{p} + \mathbf{q} - \mathbf{r})} \\ &\quad \times \frac{4M^2 + 2\tilde{Q}_f \cdot \tilde{R}_f}{(\tilde{Q}_f^2 + M^2)(\tilde{R}_f^2 + M^2)}, \\ &= -4N_C T^2 \int_0^\beta d\tau \sum_{q_n^f, r_n^f} e^{i(w_n + q_n^f - r_n^f)\tau} \int \frac{d^3\mathbf{q}}{(2\pi)^3} \frac{4M^2 + 2q_n^f r_n^f + 2\mathbf{p} \cdot \mathbf{q} + 2\mathbf{q}^2}{[(q_n^f)^2 + E_{\mathbf{q}}^2][(r_n^f)^2 + E_{\mathbf{q}+\mathbf{p}}^2]}, \\ &= -4N_C \frac{d^3\mathbf{q}}{(2\pi)^3} \int_0^\beta d\tau e^{iw_n\tau} \left( \sum_{q_n^f} e^{iq_n^f\tau} \right) \left( \sum_{r_n^f} e^{ir_n^f\tau} \right) \\ &\quad \times \frac{2q_n^f r_n^f + E_{\mathbf{q}}^2 + E_{\mathbf{q}+\mathbf{p}}^2 + 2M^2 - \mathbf{p}^2}{[(q_n^f)^2 + E_{\mathbf{q}}^2][(r_n^f)^2 + E_{\mathbf{q}+\mathbf{p}}^2]}, \end{aligned} \quad (\text{C.21})$$

where  $E_{\mathbf{q}} = \sqrt{\mathbf{q}^2 + M^2}$ . Next, we need to make use of the fermionic summation formula for  $0 < \tau < \beta$  (see App. C.2) [74, 75]

$$T \sum_{q_n^f} \frac{e^{\pm i q_n^f \tau}}{(q_n^f)^2 + E^2} = \frac{n_F(E)}{2E} (e^{(\beta-\tau)E} - e^{\tau E}); \quad n_F(E) = \frac{1}{e^{\beta E} + 1}, \quad (\text{C.22a})$$

$$T \sum_{q_n^f} \frac{\pm i q_n^f e^{\pm i q_n^f \tau}}{(q_n^f)^2 + E^2} = -\frac{n_F(E)}{2E} (e^{(\beta-\tau)E} + e^{\tau E}). \quad (\text{C.22b})$$

Thereby we arrive at

$$\begin{aligned} \delta_{\mu\nu}\tilde{C}_{\mu\nu}^E(\tilde{P}) &= -N_C \frac{d^3\mathbf{q}}{(2\pi)^3} \int_0^\beta d\tau e^{iw_n\tau} n_F(E_{\mathbf{q}})n_F(E_{\mathbf{q}+\mathbf{p}}) \\ &\quad \times \left\{ e^{(\beta-\tau)(E_{\mathbf{q}}+E_{\mathbf{q}+\mathbf{p}})} \left[ 2 + \frac{E_{\mathbf{q}+\mathbf{p}}^2 + E_{\mathbf{q}}^2 + 2M^2 - \mathbf{p}^2}{E_{\mathbf{q}+\mathbf{p}} E_{\mathbf{q}}} \right] \right. \\ &\quad + e^{(\beta-\tau)E_{\mathbf{q}} + \tau E_{\mathbf{q}+\mathbf{p}}} \left[ 2 - \frac{E_{\mathbf{q}+\mathbf{p}}^2 + E_{\mathbf{q}}^2 + 2M^2 - \mathbf{p}^2}{E_{\mathbf{q}+\mathbf{p}} E_{\mathbf{q}}} \right] \\ &\quad + e^{\tau E_{\mathbf{q}} + (\beta-\tau)E_{\mathbf{q}+\mathbf{p}}} \left[ 2 - \frac{E_{\mathbf{q}+\mathbf{p}}^2 + E_{\mathbf{q}}^2 + 2M^2 - \mathbf{p}^2}{E_{\mathbf{q}+\mathbf{p}} E_{\mathbf{q}}} \right] \\ &\quad \left. + e^{\tau(E_{\mathbf{q}}+E_{\mathbf{q}+\mathbf{p}})} \left[ 2 + \frac{E_{\mathbf{q}+\mathbf{p}}^2 + E_{\mathbf{q}}^2 + 2M^2 - \mathbf{p}^2}{E_{\mathbf{q}+\mathbf{p}} E_{\mathbf{q}}} \right] \right\}. \end{aligned} \quad (\text{C.23})$$

<sup>2</sup>In Euclidean space the Dirac matrices satisfy these properties

$$\tilde{\gamma}_0 = \gamma^0; \quad \tilde{\gamma}_\mu^\dagger = \tilde{\gamma}_\mu; \quad \{\tilde{\gamma}_\mu, \tilde{\gamma}_\nu\} = 2\delta_{\mu\nu}.$$

The final integral is of the form

$$\begin{aligned} \int_0^\beta d\tau e^{i w_n \tau} e^{\tau \gamma_1 + (\beta - \tau) \gamma_2} &= e^{\beta \gamma_2} \frac{1}{i w_n + \gamma_1 - \gamma_2} e^{i w_n \tau + \tau \gamma_1 - \tau \gamma_2} \Big|_0^\beta; \quad w_n = 2\pi n T, \\ &= \frac{1}{i w_n + \gamma_1 - \gamma_2} (e^{\beta \gamma_1} - e^{\beta \gamma_2}). \end{aligned} \quad (\text{C.24})$$

Finally, the analytic continuation yields

$$\begin{aligned} \rho(P) &= \frac{\delta_{\mu\nu}}{2i} [\tilde{C}_{\mu\nu}^E(-i[p^0 + i0^+], \mathbf{p}) - \tilde{C}_{\mu\nu}^E(-i[p^0 - i0^+], \mathbf{p})] \\ &= -\pi \delta(p^0 + \gamma_1 - \gamma_2) (e^{\beta \gamma_1} - e^{\beta \gamma_2}), \end{aligned} \quad (\text{C.25})$$

where we made use of the relation  $(x \pm i0^+)^{-1} = P(x^{-1}) \mp i\pi \delta(x)$ . After performing some algebra, we obtain the final expression for the spectral function

$$\begin{aligned} \rho(P) &= \pi N_C \int \frac{d^3 \mathbf{q}}{(2\pi)^3} n_F(E_{\mathbf{q}}) n_F(E_{\mathbf{q}+\mathbf{p}}) \\ &\times \left\{ \delta(p^0 - E_{\mathbf{q}} - E_{\mathbf{q}+\mathbf{p}}) (1 - e^{\beta(E_{\mathbf{q}}+E_{\mathbf{q}+\mathbf{p}})}) \left[ 2 - \frac{E_{\mathbf{q}+\mathbf{p}}^2 + E_{\mathbf{q}}^2 + 2M^2 - \mathbf{p}^2}{E_{\mathbf{q}+\mathbf{p}} E_{\mathbf{q}}} \right] \right. \\ &+ \delta(p^0 - E_{\mathbf{q}} + E_{\mathbf{q}+\mathbf{p}}) (e^{\beta E_{\mathbf{q}+\mathbf{p}}} - e^{\beta E_{\mathbf{q}}}) \left[ 2 - \frac{E_{\mathbf{q}+\mathbf{p}}^2 + E_{\mathbf{q}}^2 + 2M^2 - \mathbf{p}^2}{E_{\mathbf{q}+\mathbf{p}} E_{\mathbf{q}}} \right] \\ &+ \delta(p^0 + E_{\mathbf{q}} - E_{\mathbf{q}+\mathbf{p}}) (e^{\beta E_{\mathbf{q}}} - e^{\beta E_{\mathbf{q}+\mathbf{p}}}) \left[ 2 - \frac{E_{\mathbf{q}+\mathbf{p}}^2 + E_{\mathbf{q}}^2 + 2M^2 - \mathbf{p}^2}{E_{\mathbf{q}+\mathbf{p}} E_{\mathbf{q}}} \right] \\ &\left. + \delta(p^0 + E_{\mathbf{q}} + E_{\mathbf{q}+\mathbf{p}}) (e^{\beta(E_{\mathbf{q}}+E_{\mathbf{q}+\mathbf{p}})} - 1) \times \left[ 2 - \frac{E_{\mathbf{q}+\mathbf{p}}^2 + E_{\mathbf{q}}^2 + 2M^2 - \mathbf{p}^2}{E_{\mathbf{q}+\mathbf{p}} E_{\mathbf{q}}} \right] \right\}. \end{aligned} \quad (\text{C.26})$$

### C.3.1. Reinterpretation of $\tilde{C}^{<}(p^0)$ in terms of kinetic theory

In the last section we derived the spectral function using imaginary time formalism of thermal field theory (Eq. (C.26)). Here we simplify this expression into a physically more suggestive form.

Many of the factors of Eq. (C.26) look quite complicated but can be rearranged. First, let us factor out  $n_B(p^0) \equiv (e^{\beta p^0} - 1)^{-1}$  in some terms as follows

$$\begin{aligned} \delta(p^0 - E_{\mathbf{q}} - E_{\mathbf{q}+\mathbf{p}}) n_F(E_{\mathbf{q}}) n_F(E_{\mathbf{q}+\mathbf{p}}) (1 - e^{\beta(E_{\mathbf{q}}+E_{\mathbf{q}+\mathbf{p}})}) &= -n_B^{-1}(p^0) \delta(p^0 - E_{\mathbf{q}} - E_{\mathbf{q}+\mathbf{p}}) \\ &\times n_F(E_{\mathbf{q}}) n_F(E_{\mathbf{q}+\mathbf{p}}), \end{aligned} \quad (\text{C.27a})$$

$$\begin{aligned} \delta(p^0 - E_{\mathbf{q}} + E_{\mathbf{q}+\mathbf{p}}) n_F(E_{\mathbf{q}}) n_F(E_{\mathbf{q}+\mathbf{p}}) (e^{\beta E_{\mathbf{q}+\mathbf{p}}} - e^{\beta E_{\mathbf{q}}}) &= -n_B^{-1}(p^0) \delta(p^0 - E_{\mathbf{q}} + E_{\mathbf{q}+\mathbf{p}}) \\ &\times n_F(E_{\mathbf{q}}) [1 - n_F(E_{\mathbf{q}+\mathbf{p}})], \end{aligned} \quad (\text{C.27b})$$

$$\begin{aligned} \delta(p^0 + E_{\mathbf{q}} - E_{\mathbf{q}+\mathbf{p}}) n_F(E_{\mathbf{q}}) n_F(E_{\mathbf{q}+\mathbf{p}}) (e^{\beta E_{\mathbf{q}+\mathbf{p}}} - e^{\beta E_{\mathbf{q}}}) &= -n_B^{-1}(p^0) \delta(p^0 + E_{\mathbf{q}} - E_{\mathbf{q}+\mathbf{p}}) \\ &\times n_F(E_{\mathbf{q}+\mathbf{p}}) [1 - n_F(E_{\mathbf{q}})], \end{aligned} \quad (\text{C.27c})$$

$$\begin{aligned} \delta(p^0 + E_{\mathbf{q}} + E_{\mathbf{q}+\mathbf{p}}) n_F(E_{\mathbf{q}}) n_F(E_{\mathbf{q}+\mathbf{p}}) (e^{\beta(E_{\mathbf{q}}+E_{\mathbf{q}+\mathbf{p}})} - 1) &= -n_B^{-1}(p^0) \delta(p^0 + E_{\mathbf{q}} + E_{\mathbf{q}+\mathbf{p}}) \\ &\times [1 - n_F(E_{\mathbf{q}})] [1 - n_F(E_{\mathbf{q}+\mathbf{p}})]. \end{aligned} \quad (\text{C.27d})$$

Next, note that the integral in Eq. (C.26) is a function of  $q$  and  $q+p$  only. This allows us to rewrite



it as

$$\int \frac{d^3\mathbf{q}}{(2\pi)^3} f(q, q+p) = \int \frac{d^3\mathbf{q}}{(2\pi)^3} \frac{d^3\mathbf{r}}{(2\pi)^3} (2\pi)^3 \delta^{(3)}(\mathbf{p} + \mathbf{q} - \mathbf{r}) f(q, r), \quad (\text{C.28a})$$

$$= \int \frac{d^3\mathbf{q}}{(2\pi)^3} \frac{d^3\mathbf{r}}{(2\pi)^3} (2\pi)^3 \delta^{(3)}(\mathbf{p} + \mathbf{q} + \mathbf{r}) f(q, r), \quad (\text{C.28b})$$

$$\int \frac{d^3\mathbf{q}}{(2\pi)^3} f(q, p-q) = \int \frac{d^3\mathbf{q}}{(2\pi)^3} \frac{d^3\mathbf{r}}{(2\pi)^3} (2\pi)^3 \delta^{(3)}(\mathbf{p} - \mathbf{q} - \mathbf{r}) f(q, r), \quad (\text{C.28c})$$

$$= \int \frac{d^3\mathbf{q}}{(2\pi)^3} \frac{d^3\mathbf{r}}{(2\pi)^3} (2\pi)^3 \delta^{(3)}(\mathbf{p} - \mathbf{q} + \mathbf{r}) f(q, r). \quad (\text{C.28d})$$

Thereby, this trick will allow us to introduce Lorentz invariant Dirac delta functions in Eq. (C.26). Now, the ‘amplitudes’  $[2 \pm \dots]$  in Eq. (C.26) can be also rewritten

$$\frac{\delta^{(4)}(P - Q + R)}{E_{\mathbf{q}} E_{\mathbf{r}}} \{2E_{\mathbf{q}} E_{\mathbf{r}} + E_{\mathbf{q}}^2 + E_{\mathbf{r}}^2 + 2M^2 - \mathbf{p}^2\} = \frac{\delta^{(4)}(P - Q - R)}{E_{\mathbf{q}} E_{\mathbf{r}}} \{P^2 + 2M^2\} \quad (\text{C.29a})$$

$$\frac{\delta^{(4)}(P - Q - R)}{E_{\mathbf{q}} E_{\mathbf{r}}} \{2E_{\mathbf{q}} E_{\mathbf{r}} - E_{\mathbf{q}}^2 - E_{\mathbf{r}}^2 - 2M^2 + \mathbf{p}^2\} = \frac{\delta^{(4)}(P - Q - R)}{E_{\mathbf{q}} E_{\mathbf{r}}} \{-P^2 - 2M^2\} \quad (\text{C.29b})$$

Putting all of this together, the spectral function is rewritten as

$$\begin{aligned} \rho = & -\pi N_C \int \frac{d^3\mathbf{q}}{(2\pi)^3} \frac{d^3\mathbf{r}}{(2\pi)^3} \frac{1}{2E_{\mathbf{q}} 2E_{\mathbf{r}} n_B(P)} \left\{ \underbrace{(2\pi)^4 \delta^{(4)}(P - Q - R) n_F(E_{\mathbf{q}}) n_F(E_{\mathbf{r}})}_{(a)} \right. \\ & - \underbrace{(2\pi)^4 \delta^{(4)}(P - Q + R) n_F(E_{\mathbf{q}}) [1 - n_F(E_{\mathbf{r}})]}_{(b)} \\ & - \underbrace{(2\pi)^4 \delta^{(4)}(P + Q - R) n_F(E_{\mathbf{r}}) [1 - n_F(E_{\mathbf{q}})]}_{(c)} \\ & \left. + \underbrace{(2\pi)^4 \delta^{(4)}(P + Q + R) [1 - n_F(E_{\mathbf{q}})] [1 - n_F(E_{\mathbf{r}})]}_{(d)} \right\} \quad (\text{C.30}) \end{aligned}$$

In terms of Feynman diagrams, the spectral function can be expressed as

$$\begin{aligned} \rho = & -\pi N_C \int \frac{d^3\mathbf{q}}{(2\pi)^3} \frac{d^3\mathbf{r}}{(2\pi)^3} \frac{1}{2E_{\mathbf{q}} 2E_{\mathbf{r}} n_B(P)} \\ & \times \left( \begin{array}{c} \text{(a)} \\ \text{(b)} \\ \text{(c)} \\ \text{(d)} \end{array} \right). \quad (\text{C.31}) \end{aligned}$$

The subindex below every diagram refers to its respective integral form in Eq. (C.30). For the case of dileptons, every diagram corresponds to a different production channel. But three of these channels do not contribute to dilepton production. To understand this better, let us evaluate the Dirac delta function in the local rest frame where the momentum of the lepton pairs  $l^+ l^-$  vanishes, i.e.  $\mathbf{p}=0$ . In this frame

$$\delta^{(4)}(P - Q + R) = \delta(p^0 - E_{\mathbf{q}} + E_{\mathbf{r}}) \delta^{(3)}(-\mathbf{q} + \mathbf{r}) = \delta(p^0) \delta^3(-\mathbf{q} + \mathbf{r}), \quad (\text{C.32})$$

$$\delta^{(4)}(P + Q - R) \quad \text{similar to} \quad \delta^{(4)}(P - Q + R), \quad (\text{C.33})$$

$$\delta^{(4)}(P + Q + R) = \delta(p^0 + E_{\mathbf{q}} + E_{\mathbf{r}}) \delta^{(3)}(\mathbf{q} + \mathbf{r}) = \delta(p^0 + 2E_{\mathbf{q}}) \delta^3(\mathbf{q} + \mathbf{r}). \quad (\text{C.34})$$

Because  $\mathbf{p}=0 \Rightarrow p^0 = E_{1+} + E_{1-} > 0$  and since any of the last expressions satisfy this constraint, so their contribution to the spectral function (and hence the dilepton production rate) vanishes. The only channel that contributes to the spectral function is the diagram (a).

The retarded current-current correlation function is found using the relation  $\tilde{C}^<(p^0) = 2 n_B(p^0) \rho(p^0)$ . This completes our calculation of the retarded current-current correlation function and connects thermal field theory with kinetic theory approach.

#### C.4. Transversality of the free current-current correlator

In the last section, we calculated the current-current correlator in the imaginary time formalism. Here, we complement the calculation by showing the transversality of the current-current correlator. From the definition of the current-current correlator at leading order  $\tilde{C}_{\mu\nu}^E(\tilde{P})$  (Eq. (C.19))

$$\begin{aligned}
\tilde{P}_\mu \tilde{P}_\nu \tilde{C}_{\mu\nu}^E(\tilde{P}) &= -4N_C \tilde{P}_\mu \tilde{P}_\nu \sum_{q_n^f, r_n^f} \int \frac{d^3\mathbf{q}}{(2\pi)^3} \frac{d^3\mathbf{r}}{(2\pi)^3} (2\pi)^4 \delta(\tilde{P} - \tilde{Q}_f - \tilde{R}_f) \\
&\quad \{M^2 \delta_{\mu\nu} - \tilde{Q}_\alpha \tilde{R}_\beta (\delta_{\mu\alpha} \delta_{\nu\beta} - \delta_{\mu\nu} \delta_{\alpha\beta} + \delta_{\mu\beta} \delta_{\nu\alpha})\}, \\
&= -4N_C \sum_{q_n^f, r_n^f} \int \frac{d^3\mathbf{q}}{(2\pi)^3} \frac{d^3\mathbf{r}}{(2\pi)^3} (2\pi)^4 \delta(\tilde{P} - \tilde{Q}_f - \tilde{R}_f) \\
&\quad \times \frac{M^2 \tilde{P}^2 - 2\tilde{Q}_f \cdot \tilde{P} \tilde{R}_f \cdot \tilde{P} + \tilde{Q}_f \cdot \tilde{R} \tilde{P}^2}{(\tilde{Q}_f^2 + M^2)(\tilde{R}_f^2 + M^2)}, \\
&= -4N_C \sum_{q_n^f} \int \frac{d^3\mathbf{q}}{(2\pi)^3} \frac{M^2 \tilde{P}^2 - 2\tilde{Q}_f \cdot \tilde{P} (\tilde{P}_f + \tilde{Q}_f) \cdot \tilde{P} + \tilde{Q}_f \cdot (\tilde{P} + \tilde{Q}_f) \tilde{P}^2}{(\tilde{Q}_f^2 + M^2)[(\tilde{P} + \tilde{Q}_f)^2 + M^2]}, \\
&= -4N_C \sum_{q_n^f} \int \frac{d^3\mathbf{q}}{(2\pi)^3} \left\{ \frac{\tilde{P}^2}{(\tilde{P} + \tilde{Q}_f)^2 + M^2} - \frac{\tilde{P}^2}{2} \frac{(\tilde{P} + \tilde{Q}_f)^2 - \tilde{P}^2 - \tilde{Q}_f^2}{(\tilde{Q}_f^2 + M^2)[(\tilde{P} + \tilde{Q}_f)^2 + M^2]} \right. \\
&\quad \left. - \tilde{P} \cdot \tilde{Q} + \frac{(\tilde{P} + \tilde{Q}_f)^2 - \tilde{P}^2 - \tilde{Q}_f^2}{(\tilde{Q}_f^2 + M^2)[(\tilde{P} + \tilde{Q}_f)^2 + M^2]} \right\}, \\
&= -4N_C \sum_{q_n^f} \int \frac{d^3\mathbf{q}}{(2\pi)^3} \left\{ \frac{\tilde{P}^2}{(\tilde{P} + \tilde{Q}_f)^2 + M^2} + \frac{\tilde{P}^2}{2} \frac{1}{(\tilde{P} + \tilde{Q}_f)^2 + M^2} - \frac{\tilde{P}^2}{2} \frac{1}{\tilde{Q}_f^2 + M^2} \right. \\
&\quad \left. + \frac{\tilde{P}^4}{2} \frac{1}{(\tilde{Q}_f^2 + M^2)[(\tilde{P} + \tilde{Q}_f)^2 + M^2]} - \frac{\tilde{P} \cdot \tilde{Q}}{\tilde{Q}_f^2 + M^2} + \frac{\tilde{P} \cdot \tilde{Q}}{(\tilde{P} + \tilde{Q}_f)^2 + M^2} \right. \\
&\quad \left. + \frac{\tilde{P}^2}{2} \frac{(\tilde{P} + \tilde{Q}_f)^2 - \tilde{P}^2 - \tilde{Q}_f^2}{(\tilde{Q}_f^2 + M^2)[(\tilde{P} + \tilde{Q}_f)^2 + M^2]} \right\}, \\
&= -4N_C \sum_{q_n^f} \int \frac{d^3\mathbf{q}}{(2\pi)^3} \left\{ \frac{\tilde{P}^2}{(\tilde{P} + \tilde{Q}_f)^2 + M^2} - \frac{\tilde{P} \cdot \tilde{Q}_f}{\tilde{Q}_f^2 + M^2} + \frac{\tilde{P} \cdot \tilde{Q}_f}{(\tilde{P} + \tilde{Q}_f)^2 + M^2} \right\}, \\
&= -4N_C \sum_{q_n^f} \int \frac{d^3\mathbf{q}}{(2\pi)^3} \left\{ \frac{\tilde{P}^2}{(\tilde{P} + \tilde{Q}_f)^2 + M^2} - \frac{\tilde{P}^2}{\tilde{Q}_f^2 + M^2} \right\}. \tag{C.35}
\end{aligned}$$

The expressions in the last line vanish exactly after changing the integration variable in the first integral  $\tilde{Q}_f \rightarrow -\tilde{P} - \tilde{Q}_f$ . This proves the validity of neglecting the term  $\tilde{P}_\mu \tilde{P}_\nu \tilde{C}_{\mu\nu}^E(P)$  in Eq. (C.21). More generally, the transversality follows from a Ward identity expressing vector current conservation [74, 75].

## Bibliography

- [1] M. Luzum and P. Romatschke, *Conformal Relativistic Viscous Hydrodynamics: Applications to RHIC results at  $\sqrt{s_{NN}} = 200$  GeV*, *Phys. Rev.* **C78** (2008) 034915, [0804.4015].
- [2] P. Romatschke and M. Strickland, *Collective Modes of an Anisotropic Quark-Gluon Plasma*, *Phys. Rev.* **D68** (2003) 036004, [hep-ph/0304092].
- [3] D. J. Gross and F. Wilczek, *Ultraviolet behavior of non-abelian gauge theories*, *Phys. Rev. Lett.* **30** (1973) 1343–1346.
- [4] H. D. Politzer, *Reliable perturbative results for strong interactions?*, *Phys. Rev. Lett.* **30** (1973) 1346–1349.
- [5] I. B. Khriplovich, *Green's functions in theories with non-abelian gauge group*, *Yad. Fiz.* **10** (1969) 409–424.
- [6] V. N. Gribov, *Quantization of non-Abelian gauge theories*, *Nucl. Phys.* **B139** (1978) 1.
- [7] D. Zwanziger, *No confinement without Coulomb confinement*, *Phys. Rev. Lett.* **90** (2003) 102001, [hep-lat/0209105].
- [8] Y. L. Dokshitzer and D. E. Kharzeev, *The Gribov conception of quantum chromodynamics*, *Ann. Rev. Nucl. Part. Sci.* **54** (2004) 487–524, [hep-ph/0404216].
- [9] S. Bethke, *Determination of the QCD coupling  $\alpha_s$* , *J. Phys.* **G26** (2000) R27, [hep-ex/0004021].
- [10] L. McLerran and R. D. Pisarski, *Phases of Cold, Dense Quarks at Large  $N_c$* , *Nucl. Phys.* **A796** (2007) 83–100, [0706.2191].
- [11] Y. Hidaka, L. D. McLerran, and R. D. Pisarski, *Baryons and the phase diagram for a large number of colors and flavors*, *Nucl. Phys.* **A808** (2008) 117–123, [0803.0279].
- [12] A. Andronic *et al.*, *Hadron Production in Ultra-relativistic Nuclear Collisions: Quarkyonic Matter and a Triple Point in the Phase Diagram of QCD*, 0911.4806.
- [13] V. Koch, *Aspects of chiral symmetry*, *Int. J. Mod. Phys.* **E6** (1997) 203–250, [nucl-th/9706075].
- [14] K. Rajagopal and F. Wilczek, *The condensed matter physics of QCD*, hep-ph/0011333.
- [15] C. R. Allton *et al.*, *The equation of state for two flavor QCD at non-zero chemical potential*, *Phys. Rev.* **D68** (2003) 014507, [hep-lat/0305007].
- [16] F. Karsch, E. Laermann, and A. Peikert, *The pressure in 2, 2+1 and 3 flavour QCD*, *Phys. Lett.* **B478** (2000) 447–455, [hep-lat/0002003].
- [17] F. Karsch, *Lattice QCD at high temperature and density*, *Lect. Notes Phys.* **583** (2002) 209–249, [hep-lat/0106019].
- [18] M. Gyulassy and L. McLerran, *New forms of QCD matter discovered at RHIC*, *Nucl. Phys.* **A750** (2005) 30–63, [nucl-th/0405013].

- [19] J. D. Bjorken, *Highly Relativistic Nucleus-Nucleus Collisions: The Central Rapidity Region*, *Phys. Rev.* **D27** (1983) 140–151.
- [20] D. A. Teaney, *Viscous Hydrodynamics and the Quark Gluon Plasma*, 0905.2433.
- [21] P. Arnold, J. Lenaghan, G. D. Moore, and L. G. Yaffe, *Apparent thermalization due to plasma instabilities in quark gluon plasma*, *Phys. Rev. Lett.* **94** (2005) 072302, [nucl-th/0409068].
- [22] P. Huovinen, P. F. Kolb, U. W. Heinz, P. V. Ruuskanen, and S. A. Voloshin, *Radial and elliptic flow at RHIC: further predictions*, *Phys. Lett.* **B503** (2001) 58–64, [hep-ph/0101136].
- [23] T. Hirano and K. Tsuda, *Collective flow and two pion correlations from a relativistic hydrodynamic model with early chemical freeze out*, *Phys. Rev.* **C66** (2002) 054905, [nucl-th/0205043].
- [24] M. J. Tannenbaum, *Recent results in relativistic heavy ion collisions: From ‘ a new state of matter ’ to ‘ the perfect fluid ’*, *Rept. Prog. Phys.* **69** (2006) 2005–2060, [nucl-ex/0603003].
- [25] P. F. Kolb and U. W. Heinz, *Hydrodynamic description of ultrarelativistic heavy-ion collisions*, nucl-th/0305084.
- [26] R. Baier, A. H. Mueller, D. Schiff, and D. T. Son, *‘Bottom-up’ thermalization in heavy ion collisions*, *Phys. Lett.* **B502** (2001) 51–58, [hep-ph/0009237].
- [27] R. Baier, A. H. Mueller, D. Schiff, and D. T. Son, *Does parton saturation at high density explain hadron multiplicities at RHIC?*, *Phys. Lett.* **B539** (2002) 46–52, [hep-ph/0204211].
- [28] Z. Xu and C. Greiner, *Thermalization of gluons in ultrarelativistic heavy ion collisions by including three-body interactions in a parton cascade*, *Phys. Rev.* **C71** (2005) 064901, [hep-ph/0406278].
- [29] Z. Xu and C. Greiner, *Transport rates and momentum isotropization of gluon matter in ultrarelativistic heavy-ion collisions*, *Phys. Rev.* **C76** (2007) 024911, [hep-ph/0703233].
- [30] S. Mrowczynski, *Color collective effects at the early stage of ultrarelativistic heavy-ion collisions*, . Given at Workshop on Pre-Equilibrium Parton Dynamics in Heavy Ion Collisions, Berkeley, CA, 23 Aug - 3 Sep 1993.
- [31] S. Mrowczynski, *Plasma instability at the initial stage of ultrarelativistic heavy ion collisions*, *Phys. Lett.* **B314** (1993) 118–121.
- [32] W. Jas and S. Mrowczynski, *Evolution of Anisotropy of Parton System from Relativistic Heavy-Ion Collisions*, *Phys. Rev.* **C76** (2007) 044905, [0706.2273].
- [33] M. Strickland, *Thermalization and the chromo-Weibel instability*, *J. Phys.* **G34** (2007) S429–436, [hep-ph/0701238].
- [34] S. Mrowczynski and M. H. Thoma, *Hard loop approach to anisotropic systems*, *Phys. Rev.* **D62** (2000) 036011, [hep-ph/0001164].
- [35] J. Randrup and S. Mrowczynski, *Chromodynamic Weibel instabilities in relativistic nuclear collisions*, *Phys. Rev.* **C68** (2003) 034909, [nucl-th/0303021].
- [36] P. Arnold, J. Lenaghan, and G. D. Moore, *QCD plasma instabilities and bottom-up thermalization*, *JHEP* **08** (2003) 002, [hep-ph/0307325].
- [37] P. Romatschke and M. Strickland, *Collective modes of an anisotropic quark-gluon plasma. II*, *Phys. Rev.* **D70** (2004) 116006, [hep-ph/0406188].

- 
- [38] S. Mrowczynski, A. Rebhan, and M. Strickland, *Hard-loop effective action for anisotropic plasmas*, *Phys. Rev.* **D70** (2004) 025004, [[hep-ph/0403256](#)].
- [39] A. Rebhan, P. Romatschke, and M. Strickland, *Hard-loop dynamics of non-Abelian plasma instabilities*, *Phys. Rev. Lett.* **94** (2005) 102303, [[hep-ph/0412016](#)].
- [40] P. Arnold, G. D. Moore, and L. G. Yaffe, *The fate of non-abelian plasma instabilities in 3+1 dimensions*, *Phys. Rev.* **D72** (2005) 054003, [[hep-ph/0505212](#)].
- [41] A. Rebhan, P. Romatschke, and M. Strickland, *Dynamics of quark-gluon plasma instabilities in discretized hard-loop approximation*, *JHEP* **09** (2005) 041, [[hep-ph/0505261](#)].
- [42] P. Romatschke and R. Venugopalan, *Collective non-Abelian instabilities in a melting color glass condensate*, *Phys. Rev. Lett.* **96** (2006) 062302, [[hep-ph/0510121](#)].
- [43] B. Schenke, M. Strickland, C. Greiner, and M. H. Thoma, *A model of the effect of collisions on QCD plasma instabilities*, *Phys. Rev.* **D73** (2006) 125004, [[hep-ph/0603029](#)].
- [44] B. Schenke and M. Strickland, *Fermionic collective modes of an anisotropic quark-gluon plasma*, *Phys. Rev.* **D74** (2006) 065004, [[hep-ph/0606160](#)].
- [45] C. Manuel and S. Mrowczynski, *Chromo-hydrodynamic approach to the unstable quark-gluon plasma*, *Phys. Rev.* **D74** (2006) 105003, [[hep-ph/0606276](#)].
- [46] D. Bodeker and K. Rummukainen, *Non-abelian plasma instabilities for strong anisotropy*, *JHEP* **07** (2007) 022, [[0705.0180](#)].
- [47] P. Romatschke and R. Venugopalan, *The unstable Glasma*, *Phys. Rev.* **D74** (2006) 045011, [[hep-ph/0605045](#)].
- [48] P. Romatschke and A. Rebhan, *Plasma Instabilities in an Anisotropically Expanding Geometry*, *Phys. Rev. Lett.* **97** (2006) 252301, [[hep-ph/0605064](#)].
- [49] A. Dumitru and Y. Nara, *QCD plasma instabilities and isotropization*, *Phys. Lett.* **B621** (2005) 89–95, [[hep-ph/0503121](#)].
- [50] A. Dumitru, Y. Nara, and M. Strickland, *Ultraviolet avalanche in anisotropic non-Abelian plasmas*, *Phys. Rev.* **D75** (2007) 025016, [[hep-ph/0604149](#)].
- [51] A. Rebhan, M. Strickland, and M. Attems, *Instabilities of an anisotropically expanding non-Abelian plasma: 1D+3V discretized hard-loop simulations*, *Phys. Rev.* **D78** (2008) 045023, [[0802.1714](#)].
- [52] E. V. Shuryak, *Quark-Gluon Plasma and Hadronic Production of Leptons, Photons and Psions*, *Phys. Lett.* **B78** (1978) 150.
- [53] E. L. Feinberg, *Direct Production of Photons and Dileptons in Thermodynamical Models of Multiple Hadron Production*, *Nuovo Cim.* **A34** (1976) 391.
- [54] C. Gale and K. L. Haglin, *Electromagnetic radiation from relativistic nuclear collisions*, [hep-ph/0306098](#).
- [55] R. Chatterjee, L. Bhattacharya, and D. K. Srivastava, *Electromagnetic probes*, 0901.3610.
- [56] S. M. Carroll, *Lecture notes on general relativity*, [gr-qc/9712019](#).
- [57] E. Shuryak, *Physics of Strongly coupled Quark-Gluon Plasma*, *Prog. Part. Nucl. Phys.* **62** (2009) 48–101, [[0807.3033](#)].

- [58] E. Shuryak, *A strongly coupled quark-gluon plasma*, *J. Phys.* **G30** (2004) S1221–S1224.
- [59] P. Arnold, D. T. Son, and L. G. Yaffe, *Hot B violation, color conductivity, and  $\log(1/\alpha)$  effects*, *Phys. Rev.* **D59** (1999) 105020, [[hep-ph/9810216](#)].
- [60] P. Arnold, *Quark-Gluon Plasmas and Thermalization*, *Int. J. Mod. Phys.* **E16** (2007) 2555–2594, [[0708.0812](#)].
- [61] L. D. McLerran and R. Venugopalan, *Computing quark and gluon distribution functions for very large nuclei*, *Phys. Rev.* **D49** (1994) 2233–2241, [[hep-ph/9309289](#)].
- [62] L. D. McLerran and R. Venugopalan, *Gluon distribution functions for very large nuclei at small transverse momentum*, *Phys. Rev.* **D49** (1994) 3352–3355, [[hep-ph/9311205](#)].
- [63] L. D. McLerran and R. Venugopalan, *Green’s functions in the color field of a large nucleus*, *Phys. Rev.* **D50** (1994) 2225–2233, [[hep-ph/9402335](#)].
- [64] A. H. Mueller, *Toward equilibration in the early stages after a high energy heavy ion collision*, *Nucl. Phys.* **B572** (2000) 227–240, [[hep-ph/9906322](#)].
- [65] J. F. Gunion and G. Bertsch, *Hadronization by color bremsstrahlung*, *Phys. Rev.* **D25** (1982) 746.
- [66] L. D. Landau and I. Pomeranchuk, *Limits of applicability of the theory of bremsstrahlung electrons and pair production at high-energies*, *Dokl. Akad. Nauk Ser. Fiz.* **92** (1953) 535–536.
- [67] R. Baier, D. Schiff, and B. G. Zakharov, *Energy loss in perturbative QCD*, *Ann. Rev. Nucl. Part. Sci.* **50** (2000) 37–69, [[hep-ph/0002198](#)].
- [68] E. Braaten and R. D. Pisarski, *Soft Amplitudes in Hot Gauge Theories: A General Analysis*, *Nucl. Phys.* **B337** (1990) 569.
- [69] E. Braaten and R. D. Pisarski, *Deducing Hard Thermal Loops from Ward Identities*, *Nucl. Phys.* **B339** (1990) 310–324.
- [70] J.-P. Blaizot and E. Iancu, *The quark-gluon plasma: Collective dynamics and hard thermal loops*, *Phys. Rept.* **359** (2002) 355–528, [[hep-ph/0101103](#)].
- [71] P. F. Kelly, Q. Liu, C. Lucchesi, and C. Manuel, *Classical transport theory and hard thermal loops in the quark - gluon plasma*, *Phys. Rev.* **D50** (1994) 4209–4218, [[hep-ph/9406285](#)].
- [72] P. F. Kelly, Q. Liu, C. Lucchesi, and C. Manuel, *Deriving the hard thermal loops of QCD from classical transport theory*, *Phys. Rev. Lett.* **72** (1994) 3461–3463, [[hep-ph/9403403](#)].
- [73] B. Schenke, *Collective Phenomena in the Non-Equilibrium Quark-Gluon Plasma*, 0810.4306.
- [74] J. I. Kapusta and C. Gale, *Finite-temperature field theory: Principles and applications*, . Cambridge, UK: Univ. Pr. (2006) 428 p.
- [75] M. Le Bellac, *Thermal Field Theory*, . Cambridge University Press (2000).
- [76] A. Rebhan, *Hard loop effective theory of the (anisotropic) quark gluon plasma*, *Prog. Part. Nucl. Phys.* **62** (2009) 518–528, [[0811.0457](#)].
- [77] P. Arnold, G. D. Moore, and L. G. Yaffe, *Effective kinetic theory for high temperature gauge theories*, *JHEP* **01** (2003) 030, [[hep-ph/0209353](#)].

- 
- [78] B. Schenke, M. Strickland, A. Dumitru, Y. Nara, and C. Greiner, *Transverse momentum diffusion and jet energy loss in non-Abelian plasmas*, *Phys. Rev.* **C79** (2009) 034903, [0810.1314].
- [79] A. Dumitru, Y. Nara, B. Schenke, and M. Strickland, *Jet broadening in unstable non-Abelian plasmas*, *Phys. Rev.* **C78** (2008) 024909, [0710.1223].
- [80] A. Dumitru, Y. Guo, A. Mocsy, and M. Strickland, *Quarkonium states in an anisotropic QCD plasma*, *Phys. Rev.* **D79** (2009) 054019, [0901.1998].
- [81] B. Schenke and M. Strickland, *Photon production from an anisotropic quark-gluon plasma*, *Phys. Rev.* **D76** (2007) 025023, [hep-ph/0611332].
- [82] M. Martinez and M. Strickland, *Measuring QGP thermalization time with dileptons*, *Phys. Rev. Lett.* **100** (2008) 102301, [0709.3576].
- [83] M. Martinez and M. Strickland, *Pre-equilibrium dilepton production from an anisotropic quark-gluon plasma*, *Phys. Rev.* **C78** (2008) 034917, [0805.4552].
- [84] M. Martinez and M. Strickland, *Suppression of forward dilepton production from an anisotropic quark-gluon plasma*, *Eur. Phys. J.* **C61** (2009) 905–913, [0808.3969].
- [85] L. Bhattacharya and P. Roy, *Photons from anisotropic Quark-Gluon-Plasma*, 0809.4596.
- [86] L. Bhattacharya and P. Roy, *Measuring isotropization time of Quark-Gluon-Plasma from direct photon at RHIC*, *Phys. Rev.* **C79** (2009) 054910, [0812.1478].
- [87] L. Bhattacharya and P. Roy, *Rapidity distribution of photons from an anisotropic Quark-Gluon-Plasma*, 0907.3607.
- [88] D. Bodeker, *The impact of QCD plasma instabilities on bottom-up thermalization*, *JHEP* **10** (2005) 092, [hep-ph/0508223].
- [89] P. Arnold and G. D. Moore, *The turbulent spectrum created by non-Abelian plasma instabilities*, *Phys. Rev.* **D73** (2006) 025013, [hep-ph/0509226].
- [90] P. Arnold and G. D. Moore, *Non-Abelian Plasma Instabilities for Extreme Anisotropy*, *Phys. Rev.* **D76** (2007) 045009, [0706.0490].
- [91] S. Mrowczynski, *Chromodynamic Fluctuations in Quark-Gluon Plasma*, *Phys. Rev.* **D77** (2008) 105022, [0801.0536].
- [92] A. Majumder, B. Muller, and S. Mrowczynski, *Momentum Broadening of a Fast Parton in a Perturbative Quark-Gluon Plasma*, 0903.3683.
- [93] P. Arnold and P.-S. Leang, *Lessons from non-Abelian plasma instabilities in two spatial dimensions*, *Phys. Rev.* **D76** (2007) 065012, [0704.3996].
- [94] J. Berges, S. Scheffler, and D. Sexty, *Turbulence in nonabelian gauge theory*, *Phys. Lett.* **B681** (2009) 336–342, [0811.4293].
- [95] J. Berges, S. Scheffler, and D. Sexty, *Bottom-up isotropization in classical-statistical lattice gauge theory*, *Phys. Rev.* **D77** (2008) 034504, [0712.3514].
- [96] J. Berges, D. Gelfand, S. Scheffler, and D. Sexty, *Simulating plasma instabilities in SU(3) gauge theory*, *Phys. Lett.* **B677** (2009) 210–213, [0812.3859].
- [97] L. D. Landau, *On the multiparticle production in high-energy collisions*, *Izv. Akad. Nauk SSSR Ser. Fiz.* **17** (1953) 51–64.

- [98] **PHENIX** Collaboration, K. Adcox *et al.*, *Formation of dense partonic matter in relativistic nucleus nucleus collisions at RHIC: Experimental evaluation by the PHENIX collaboration*, *Nucl. Phys.* **A757** (2005) 184–283, [nucl-ex/0410003].
- [99] **STAR** Collaboration, J. Adams *et al.*, *Experimental and theoretical challenges in the search for the quark gluon plasma: The STAR collaboration's critical assessment of the evidence from RHIC collisions*, *Nucl. Phys.* **A757** (2005) 102–183, [nucl-ex/0501009].
- [100] B. B. Back *et al.*, *The PHOBOS perspective on discoveries at RHIC*, *Nucl. Phys.* **A757** (2005) 28–101, [nucl-ex/0410022].
- [101] **BRAHMS** Collaboration, I. Arsene *et al.*, *Quark Gluon Plasma an Color Glass Condensate at RHIC? The perspective from the BRAHMS experiment*, *Nucl. Phys.* **A757** (2005) 1–27, [nucl-ex/0410020].
- [102] S. R. De Groot, W. A. Van Leeuwen, and C. G. Van Weert, *Relativistic Kinetic Theory. Principles and Applications*, . Amsterdam, Netherlands: North-holland ( 1980) 417p.
- [103] R. Baier, P. Romatschke, D. T. Son, A. O. Starinets, and M. A. Stephanov, *Relativistic viscous hydrodynamics, conformal invariance, and holography*, *JHEP* **04** (2008) 100, [0712.2451].
- [104] S. Bhattacharyya, V. E. Hubeny, S. Minwalla, and M. Rangamani, *Nonlinear Fluid Dynamics from Gravity*, *JHEP* **02** (2008) 045, [0712.2456].
- [105] B. Betz, D. Henkel, and D. H. Rischke, *From kinetic theory to dissipative fluid dynamics*, *Prog. Part. Nucl. Phys.* **62** (2009) 556, [0812.1440].
- [106] P. Romatschke, *Relativistic Viscous Fluid Dynamics and Non-Equilibrium Entropy*, 0906.4787.
- [107] T. Hirano, N. van der Kolk, and A. Bilandzic, *Hydrodynamics and Flow*, 0808.2684.
- [108] U. W. Heinz, *Early collective expansion: Relativistic hydrodynamics and the transport properties of QCD matter*, 0901.4355.
- [109] P. Romatschke, *New Developments in Relativistic Viscous Hydrodynamics*, 0902.3663.
- [110] D. H. Rischke, *Fluid dynamics for relativistic nuclear collisions*, nucl-th/9809044.
- [111] F. Karsch, *Lattice results on QCD at high temperature and non-zero baryon number density*, *Prog. Part. Nucl. Phys.* **62** (2009) 503–511.
- [112] Z. Fodor and S. D. Katz, *The phase diagram of quantum chromodynamics*, 0908.3341.
- [113] P. Danielewicz and M. Gyulassy, *Dissipative Phenomena in Quark Gluon Plasmas*, *Phys. Rev.* **D31** (1985) 53–62.
- [114] D. T. Son and A. O. Starinets, *Hydrodynamics of R-charged black holes*, *JHEP* **03** (2006) 052, [hep-th/0601157].
- [115] H. Goldstein, C. Poole, and J. Safko, *Classical mechanics*, . 3rd. Ed., Addison-Wesley (2002).
- [116] K. Huang, *Statistical mechanics*, . 2nd. Ed., John Wiley & Sons (1987).
- [117] E. Lifshitz and L. PitaevskiiHuang, *Physical Kinetics: Volume 10 Course of Theoretical Physics*, . 1st. Ed., Pergamon Press Ltd. (1981).
- [118] L. Csernai, *Introduction to relativistic heavy ion collisions*, . John Wiley & Sons (1994).



- 
- [119] W. Israel and J. M. Stewart, *Transient relativistic thermodynamics and kinetic theory*, *Ann. Phys.* **118** (1979) 341–372.
- [120] A. Muronga, *Relativistic Dynamics of Non-ideal Fluids: Viscous and heat-conducting fluids II. Transport properties and microscopic description of relativistic nuclear matter*, *Phys. Rev.* **C76** (2007) 014910, [[nucl-th/0611091](#)].
- [121] M. Martinez and M. Strickland, *Constraining relativistic viscous hydrodynamical evolution*, *Phys. Rev.* **C79** (2009) 044903, [[0902.3834](#)].
- [122] M. Martinez and M. Strickland, *Matching pre-equilibrium dynamics and viscous hydrodynamics*, [0909.0264](#).
- [123] W. A. Hiscock and L. Lindblom, *Generic instabilities in first-order dissipative relativistic fluid theories*, *Phys. Rev.* **D31** (1985) 725–733.
- [124] W. A. Hiscock and L. Lindblom, *Linear plane waves in dissipative relativistic fluids*, *Phys. Rev.* **D35** (1987) 3723–3732.
- [125] A. Muronga, *Causal Theories of Dissipative Relativistic Fluid Dynamics for Nuclear Collisions*, *Phys. Rev.* **C69** (2004) 034903, [[nucl-th/0309055](#)].
- [126] W. Israel, *Nonstationary irreversible thermodynamics: A Causal relativistic theory*, *Ann. Phys.* **100** (1976) 310–331.
- [127] I. Muller, *Zum Paradoxon der Wärmeleitungstheorie*, *Z. Phys.* **198** (1967) 329.
- [128] W. A. Hiscock and L. Lindblom, *Stability and causality in dissipative relativistic fluids*, *Annals Phys.* **151** (1983) 466–496.
- [129] M. Grmela and H. C. Ottinger, *Dynamics and thermodynamics of complex fluids. 1. Development of a general formalism*, *Phys. Rev.* **E56** (1997) 6620–6632.
- [130] H. C. Ottinger, *General projection operator formalism for the dynamics and thermodynamics of complex fluids*, *Phys. Rev.* **E57** (1998) 1416–1420.
- [131] K. Dusling and D. Teaney, *Simulating elliptic flow with viscous hydrodynamics*, *Phys. Rev.* **C77** (2008) 034905, [[0710.5932](#)].
- [132] J. M. Maldacena, *The large  $N$  limit of superconformal field theories and supergravity*, *Adv. Theor. Math. Phys.* **2** (1998) 231–252, [[hep-th/9711200](#)].
- [133] P. Arnold, G. D. Moore, and L. G. Yaffe, *Photon emission from quark gluon plasma: Complete leading order results*, *JHEP* **12** (2001) 009, [[hep-ph/0111107](#)].
- [134] P. Arnold, G. D. Moore, and L. G. Yaffe, *Photon emission from ultrarelativistic plasmas*, *JHEP* **11** (2001) 057, [[hep-ph/0109064](#)].
- [135] P. Arnold, G. D. Moore, and L. G. Yaffe, *Transport coefficients in high temperature gauge theories: (I) Leading-log results*, *JHEP* **11** (2000) 001, [[hep-ph/0010177](#)].
- [136] P. Arnold, G. D. Moore, and L. G. Yaffe, *Transport coefficients in high temperature gauge theories. II: Beyond leading log*, *JHEP* **05** (2003) 051, [[hep-ph/0302165](#)].
- [137] P. Arnold, G. D. Moore, and L. G. Yaffe, *Photon and Gluon Emission in Relativistic Plasmas*, *JHEP* **06** (2002) 030, [[hep-ph/0204343](#)].
- [138] M. A. York and G. D. Moore, *Second order hydrodynamic coefficients from kinetic theory*, *Phys. Rev.* **D79** (2009) 054011, [[0811.0729](#)].

- [139] H. B. Meyer, *A calculation of the bulk viscosity in  $SU(3)$  gluodynamics*, *Phys. Rev. Lett.* **100** (2008) 162001, [0710.3717].
- [140] S. Sakai and A. Nakamura, *Lattice calculation of the QGP viscosities - Present results and next project -*, *PoS LAT2007* (2007) 221, [0710.3625].
- [141] R. Rapp and J. Wambach, *Chiral symmetry restoration and dileptons in relativistic heavy-ion collisions*, *Adv. Nucl. Phys.* **25** (2000) 1, [hep-ph/9909229].
- [142] E. W. Kolb and M. S. Turner, *The Early universe*, *Front. Phys.* **69** (1990) 1–547.
- [143] C. Gale and J. I. Kapusta, *Vector dominance model at finite temperature*, *Nucl. Phys.* **B357** (1991) 65–89.
- [144] L. D. McLerran and T. Toimela, *Photon and Dilepton Emission from the Quark - Gluon Plasma: Some General Considerations*, *Phys. Rev.* **D31** (1985) 545.
- [145] H. A. Weldon, *Reformulation of finite temperature dilepton production*, *Phys. Rev.* **D42** (1990) 2384–2387.
- [146] S. Turbide, C. Gale, D. K. Srivastava, and R. J. Fries, *High momentum dilepton production from jets in a quark gluon plasma*, *Phys. Rev.* **C74** (2006) 014903, [hep-ph/0601042].
- [147] M. E. Peskin and D. V. Schroeder, *An Introduction to quantum field theory*, . Reading, USA: Addison-Wesley (1995) 842 p.
- [148] R. D. Pisarski, *Scattering Amplitudes in Hot Gauge Theories*, *Phys. Rev. Lett.* **63** (1989) 1129.
- [149] C. Y. Wong, *Introduction to high-energy heavy ion collisions*, . Singapore, Singapore: World Scientific (1994) 516 p.
- [150] J.-w. Qiu and X.-f. Zhang, *Virtual photon fragmentation functions*, *Phys. Rev.* **D64** (2001) 074007, [hep-ph/0101004].
- [151] E. L. Berger, J.-w. Qiu, and X.-f. Zhang, *QCD factorized Drell-Yan cross-section at large transverse momentum*, *Phys. Rev.* **D65** (2002) 034006, [hep-ph/0107309].
- [152] M. L. Mangano, P. Nason, and G. Ridolfi, *Heavy quark correlations in hadron collisions at next-to-leading order*, *Nucl. Phys.* **B373** (1992) 295–345.
- [153] S. Jeon and G. D. Moore, *Energy loss of leading partons in a thermal QCD medium*, *Phys. Rev.* **C71** (2005) 034901, [hep-ph/0309332].
- [154] J. I. Kapusta, L. D. McLerran, and D. Kumar Srivastava, *Rates for dilepton production at RHIC and LHC between  $J/\Psi$  and  $\Upsilon$  are big*, *Phys. Lett.* **B283** (1992) 145–150.
- [155] A. Dumitru *et al.*, *Suppression of dilepton production at finite baryon density*, *Phys. Rev. Lett.* **70** (1993) 2860–2863.
- [156] M. Strickland, *Thermal photons and dileptons from nonequilibrium quark - gluon plasma*, *Phys. Lett.* **B331** (1994) 245–250.
- [157] J.-Y. Ollitrault, *Relativistic hydrodynamics*, *Eur. J. Phys.* **29** (2008) 275–302, [0708.2433].
- [158] M. H. Thoma and C. T. Traxler, *Production of energetic dileptons with small invariant masses from the quark-gluon plasma*, *Phys. Rev.* **D56** (1997) 198–202, [hep-ph/9701354].
- [159] F. Arleo *et al.*, *Photon physics in heavy ion collisions at the LHC*, hep-ph/0311131.

- 
- [160] B. Kampfer and O. P. Pavlenko, *Dilepton radiation from nonequilibrium parton matter produced in ultrarelativistic heavy ion collisions*, *Phys. Lett.* **B289** (1992) 127–131.
- [161] K. Kajantie, J. I. Kapusta, L. D. McLerran, and A. Mekjian, *Dilepton Emission and the QCD Phase Transition in Ultrarelativistic Nuclear Collisions*, *Phys. Rev.* **D34** (1986) 2746.
- [162] G. Baym, *Thermal Equilibration in Ultrarelativistic Heavy Ion Collisions*, *Phys. Lett.* **B138** (1984) 18–22.
- [163] A. Dumitru, E. Molnar, and Y. Nara, *Entropy production in high-energy heavy-ion collisions and the correlation of shear viscosity and thermalization time*, *Phys. Rev.* **C76** (2007) 024910, [0706.2203].
- [164] K. Dusling and S. Lin, *Dilepton production from a viscous QGP*, *Nucl. Phys.* **A809** (2008) 246–258, [0803.1262].
- [165] M. A. Betemps and M. B. Gay Ducati, *Relating Cronin effect and dilepton production in the color glass condensate*, [hep-ph/0505143](#).
- [166] B. Kampfer, O. P. Pavlenko, M. I. Gorenstein, A. Peshier, and G. Soff, *Rapidity dependence of thermal dileptons resulting from hadronizing quark - gluon matter with finite baryon charge*, *Z. Phys.* **A353** (1995) 71–77.
- [167] M. A. Betemps, M. B. Gay Ducati, and E. G. de Oliveira, *Dilepton distributions at backward rapidities*, *Phys. Rev.* **D74** (2006) 094010, [[hep-ph/0607247](#)].
- [168] W. Cassing, W. Ehehalt, and C. M. Ko, *Dilepton production at SPS energies*, *Phys. Lett.* **B363** (1995) 35–40, [[hep-ph/9508233](#)].
- [169] F. Gelis and J. Jalilian-Marian, *Dilepton production from the color glass condensate*, *Phys. Rev.* **D66** (2002) 094014, [[hep-ph/0208141](#)].
- [170] Z.-J. He, J.-J. Zhang, W.-Z. Jiang, X.-J. Qiu, and B. Liu, *Dilepton production in an expanding hot baryon-rich quark- gluon matter*, *Chin. Phys. Lett.* **16** (1999) 259–261.
- [171] M. Bleicher, *Evidence for the onset of deconfinement from longitudinal momentum distributions? Observation of the softest point of the equation of state*, [hep-ph/0509314](#).
- [172] T. Renk, *A dynamical model for the spacetime evolution of heavy-ion collisions at RHIC*, *Phys. Rev.* **C70** (2004) 021903, [[hep-ph/0404140](#)].
- [173] T. Hirano and Y. Nara, *Hydrodynamic afterburner for the color glass condensate and the parton energy loss*, *Nucl. Phys.* **A743** (2004) 305–328, [[nucl-th/0404039](#)].
- [174] T. Hirano, *Is early thermalization achieved only near midrapidity in Au + Au collisions at  $\sqrt{s_{NN}} = 130$  GeV?*, *Phys. Rev.* **C65** (2002) 011901, [[nucl-th/0108004](#)].
- [175] K. Morita, S. Muroya, C. Nonaka, and T. Hirano, *Comparison of space-time evolutions of hot/dense matter in  $\sqrt{s_{NN}} = 17$ -GeV and 130-GeV relativistic heavy ion collisions based on a hydrodynamical model*, *Phys. Rev.* **C66** (2002) 054904, [[nucl-th/0205040](#)].
- [176] **BRAHMS** Collaboration, I. G. Bearden *et al.*, *Charged meson rapidity distributions in central Au + Au collisions at  $\sqrt{s_{NN}} = 200$ -GeV*, *Phys. Rev. Lett.* **94** (2005) 162301, [[nucl-ex/0403050](#)].
- [177] **PHOBOS** Collaboration, I. C. Park *et al.*, *Charged particle flow measurement for  $|\eta| < 5.3$  with the PHOBOS detector*, *Nucl. Phys.* **A698** (2002) 564–567, [[nucl-ex/0105015](#)].

- [178] **PHOBOS** Collaboration, B. B. Back *et al.*, *Charged-particle pseudorapidity distributions in Au+Au collisions at  $s_{NN}^{1/2} = 62.4$ -GeV*, *Phys. Rev.* **C74** (2006) 021901, [nucl-ex/0509034].
- [179] **PHOBOS** Collaboration, G. I. Veres *et al.*, *System size, energy, centrality and pseudorapidity dependence of charged-particle density in Au+Au and Cu+Cu collisions at RHIC*, 0806.2803.
- [180] A. Dumitru *et al.*, *Thermal photons as a measure for the rapidity dependence of the temperature*, *Z. Phys.* **A353** (1995) 187–190, [hep-ph/9503347].
- [181] P. F. Kolb, U. W. Heinz, P. Huovinen, K. J. Eskola, and K. Tuominen, *Centrality dependence of multiplicity, transverse energy, and elliptic flow from hydrodynamics*, *Nucl. Phys.* **A696** (2001) 197–215, [hep-ph/0103234].
- [182] T. Lappi, *Initial conditions of heavy ion collisions and small  $x$* , *Nucl. Phys.* **A827** (2009) 365c–370c, [0901.1949].
- [183] H.-J. Drescher, A. Dumitru, A. Hayashigaki, and Y. Nara, *The eccentricity in heavy-ion collisions from color glass condensate initial conditions*, *Phys. Rev.* **C74** (2006) 044905, [nucl-th/0605012].
- [184] R. Baier and P. Romatschke, *Causal viscous hydrodynamics for central heavy-ion collisions*, *Eur. Phys. J.* **C51** (2007) 677–687, [nucl-th/0610108].
- [185] M. Luzum and P. Romatschke, *Viscous Hydrodynamic Predictions for Nuclear Collisions at the LHC*, 0901.4588.
- [186] A. El, Z. Xu, and C. Greiner, *Third-order relativistic dissipative hydrodynamics*, 0907.4500.
- [187] R. Loganayagam, *Entropy Current in Conformal Hydrodynamics*, *JHEP* **05** (2008) 087, [0801.3701].
- [188] S. Bhattacharyya *et al.*, *Local Fluid Dynamical Entropy from Gravity*, *JHEP* **06** (2008) 055, [0803.2526].
- [189] M. Lublinsky and E. Shuryak, *Improved Hydrodynamics from the AdS/CFT*, 0905.4069.
- [190] M. Lublinsky and E. Shuryak, *How much entropy is produced in strongly coupled quark-gluon plasma (sQGP) by dissipative effects?*, *Phys. Rev.* **C76** (2007) 021901, [0704.1647].
- [191] S. Caron-Huot and G. D. Moore, *Heavy quark diffusion in perturbative QCD at next-to-leading order*, *Phys. Rev. Lett.* **100** (2008) 052301, [0708.4232].
- [192] S. Caron-Huot and G. D. Moore, *Heavy quark diffusion in QCD and  $N=4$  SYM at next-to-leading order*, *JHEP* **02** (2008) 081, [0801.2173].
- [193] M. Brigante, H. Liu, R. C. Myers, S. Shenker, and S. Yaida, *Viscosity Bound Violation in Higher Derivative Gravity*, *Phys. Rev.* **D77** (2008) 126006, [0712.0805].
- [194] M. Brigante, H. Liu, R. C. Myers, S. Shenker, and S. Yaida, *The Viscosity Bound and Causality Violation*, *Phys. Rev. Lett.* **100** (2008) 191601, [0802.3318].
- [195] Y. Kats and P. Petrov, *Effect of curvature squared corrections in AdS on the viscosity of the dual gauge theory*, *JHEP* **01** (2009) 044, [0712.0743].
- [196] M. Natsuume and T. Okamura, *Causal hydrodynamics of gauge theory plasmas from AdS/CFT duality*, *Phys. Rev.* **D77** (2008) 066014, [0712.2916].

- 
- [197] A. Buchel, R. C. Myers, and A. Sinha, *Beyond  $\eta/s = 1/4\pi$* , *JHEP* **03** (2009) 084, [0812.2521].
- [198] A. Buchel, J. T. Liu, and A. O. Starinets, *Coupling constant dependence of the shear viscosity in  $N=4$  supersymmetric Yang-Mills theory*, *Nucl. Phys.* **B707** (2005) 56–68, [hep-th/0406264].
- [199] P. Benincasa and A. Buchel, *Transport properties of  $N = 4$  supersymmetric Yang-Mills theory at finite coupling*, *JHEP* **01** (2006) 103, [hep-th/0510041].
- [200] A. Buchel, *Shear viscosity of boost invariant plasma at finite coupling*, *Nucl. Phys.* **B802** (2008) 281–306, [0801.4421].
- [201] R. C. Myers, M. F. Paulos, and A. Sinha, *Quantum corrections to  $\eta/s$* , *Phys. Rev.* **D79** (2009) 041901, [0806.2156].
- [202] M. F. Paulos, *Higher derivative terms including the Ramond-Ramond five-form*, *JHEP* **10** (2008) 047, [0804.0763].
- [203] A. Buchel and M. Paulos, *Relaxation time of a CFT plasma at finite coupling*, *Nucl. Phys.* **B805** (2008) 59–71, [0806.0788].
- [204] G. Policastro, D. T. Son, and A. O. Starinets, *The shear viscosity of strongly coupled  $N = 4$  supersymmetric Yang-Mills plasma*, *Phys. Rev. Lett.* **87** (2001) 081601, [hep-th/0104066].
- [205] D. T. Son and A. O. Starinets, *Viscosity, Black Holes, and Quantum Field Theory*, *Ann. Rev. Nucl. Part. Sci.* **57** (2007) 95–118, [0704.0240].
- [206] J. O. Andersen and M. Strickland, *Resummation in Hot Field Theories*, *Ann. Phys.* **317** (2005) 281–353, [hep-ph/0404164].
- [207] J. O. Andersen, M. Strickland, and N. Su, *Gluon Thermodynamics at Intermediate Coupling*, 0911.0676.
- [208] R. J. Fries, *Early time evolution of high energy heavy ion collisions*, *J. Phys.* **G34** (2007) S851–854, [nucl-th/0702026].
- [209] Y. V. Kovchegov and A. Taliotis, *Early time dynamics in heavy ion collisions from AdS/CFT correspondence*, *Phys. Rev.* **C76** (2007) 014905, [0705.1234].
- [210] A. Dumitru, Y. Guo, and M. Strickland, *The heavy-quark potential in an anisotropic (viscous) plasma*, *Phys. Lett.* **B662** (2008) 37–42, [0711.4722].
- [211] M. Asakawa, S. A. Bass, and B. Muller, *Anomalous transport processes in anisotropically expanding quark-gluon plasmas*, *Prog. Theor. Phys.* **116** (2007) 725–755, [hep-ph/0608270].
- [212] K. Rajagopal and N. Tripuraneni, *Bulk Viscosity and Cavitation in Boost-Invariant Hydrodynamic Expansion*, 0908.1785.
- [213] P. Huovinen and D. Molnar, *The applicability of causal dissipative hydrodynamics to relativistic heavy ion collisions*, *Phys. Rev.* **C79** (2009) 014906, [0808.0953].
- [214] U. W. Heinz, H. Song, and A. K. Chaudhuri, *Dissipative hydrodynamics for viscous relativistic fluids*, *Phys. Rev.* **C73** (2006) 034904, [nucl-th/0510014].
- [215] D. Teaney, *Effect of shear viscosity on spectra, elliptic flow, and Hanbury Brown-Twiss radii*, *Phys. Rev.* **C68** (2003) 034913, [nucl-th/0301099].

- [216] R. Baier, P. Romatschke, and U. A. Wiedemann, *Dissipative hydrodynamics and heavy ion collisions*, *Phys. Rev.* **C73** (2006) 064903, [[hep-ph/0602249](#)].
- [217] R. J. Fries, B. Muller, and A. Schafer, *Stress Tensor and Bulk Viscosity in Relativistic Nuclear Collisions*, *Phys. Rev.* **C78** (2008) 034913, [[0807.4333](#)].







# Curriculum Vitae

## Personal Information

Name: Mauricio Martínez Guerrero  
 Sex: Male  
 Date of Birth: 26.03.81  
 Place of Birth: Socorro, Colombia  
 Nationality: Colombian  
 Address: Ruth-Moufang-Str. 1, D-60438  
 Frankfurt am Main, Germany.  
 E-mail Address: guerrero@fias.uni-frankfurt.de



## Education

- **PhD 2006-Present** Theoretical Physics, Helmholtz Research School for Quark Matter Studies, Goethe-Universität Frankfurt am Main, Frankfurt am Main, Germany.
- **M. Sc. 2004-2006** Theoretical Physics, Instituto de Ciencias Nucleares, Universidad Nacional Autónoma de México, México D.F., México.
- **B. Sc. 1998-2003** Physics, Universidad Nacional de Colombia, Bogotá, Colombia.

## Publications

### Journal articles

- **M. Martínez** and M. Strickland, *Matching pre-equilibrium dynamics and viscous hydrodynamics*, arXiv:0909.0264. Accepted in Phys. Rev. C.
- **M. Martínez** and M. Strickland, *Constraining relativistic viscous hydrodynamical evolution*. Phys. Rev. **C79**: 044903, 2009.
- **M. Martínez** and M. Strickland, *Suppression of forward dilepton production from an anisotropic quark-gluon plasma*. Eur. Phys. J. **C61**:905-913, 2009.
- **M. Martínez** and M. Strickland, *Pre-equilibrium dilepton production from an anisotropic quark-gluon plasma*. Phys. Rev. **C78**:034917, 2008.
- A. Ayala, **M. Martínez**, G. Paic, G. Toledo Sanchez, *Dynamical quark recombination in ultrarelativistic heavy-ion collisions and the proton-to-pion ratio*. Phys. Rev. **C77**:044901, 2008.
- **M. Martínez** and M. Strickland, *Measuring QGP thermalization time with dileptons*. Phys. Rev. Lett. **100**:102301, 2008.

## Refereed Proceedings

- **M. Martinez** and M. Strickland, *Constraining the onset of viscous hydrodynamics*. Nucl. Phys. **A830**:615c-616c, 2009. Proceedings of Quark Matter 2009 - The 21st International Conference on Ultrarelativistic Nucleus-Nucleus Collisions, Knoxville, Tennessee, USA, March 30-April 4, 2009.
- **M. Martinez**, *High-energy dileptons from an anisotropic quark-gluon plasma*. arXiv:0904.2866. To appear in the proceedings for 4th International Workshop on High- $p_T$  physics at LHC 09, Prague, Czech Republic, 4-7 February 2009.
- T. Brasoveanu, D. Kharzeev, **M. Martinez**, *In search of the QCD-Gravity correspondence*. Lect. Notes Phys. **785**:341- 369, 2010. Chapter contribution to QGP Winter School, Jaipur, India, 1-3 February 2008.
- A. Ayala, **M. Martinez**, G. Paic, G. Toledo Sanchez, *Proton to pion ratio at RHIC from dynamical quark recombination*. AIP Conf. Proc.**1026**:101-108, 2008. Proceedings of 11th Mexican Workshop on Particles and Fields 2007, Tuxtla Gutierrez, Mexico, 7-12 November 2007.
- A. Ayala, **M. Martinez**, G. Paic, G. Toledo Sanchez, *Modeling the hadronization of quark matter*. J. Phys. **G35**: 044060,2008. Proceedings of SQM 2007 - International Conference on Strangeness in Quark Matter, Levoca, Slovakia, 24-29 June 2007.
- **M. Martinez** and M. Strickland, *Dilepton production as a measure of QGP thermalization time*. J. Phys. **G35**: 104162,2008. Proceedings of Quark Matter 2008: 20th International Conference on Ultra-Relativistic Nucleus Nucleus Collisions (QM 2008), Jaipur, India, 4-10 February 2008.

## Academic Tutors

- Helmholtz Basic Lecture  
JProf. Dr. Christoph Blume      Pr. Dr. Harald Appelshäuser      Pr. Miklos Gyulassy  
Pr. Dr. Horst Stöcker      Pr. Dr. Peter Braun-Munzinger      Pr. Dr. Bengt Friman  
PD. Dr. Stefan Leupold      Dr. Henner Büsching
- ITP Lecture  
JProf. Adrian Dumitru      Pr. Dr. Igor Mishustin      PD Dr. Elena Bratkovskaya

## Acknowledgements

First, I want to thank my mother Angélica and my sister Shadia. Their love has always been my biggest source for inspiration and strength, without it my life would be completely different. Gracias mami y hermanita.

I am also grateful with my grandparents for their love, I feel happy they are accompanying me. To my uncle Octavio and his family, my aunts Mery, Nelsi, Miriam, Adela and her family. Thanks for the continuous support to Mrs. Mary Molano, Carlos Ayala and his family.

I would like to express my gratitude to my external advisor Michael Strickland for being the Obi-Wan Jedi Master along all last three years as his young Skywalker. His guidance, patience, continuous support and generosity of his knowledge were crucial during my PhD work. I really enjoyed so much our discussions about physics of anisotropic plasmas and related issues. Special thanks to Adrian Dumitru for the greatest discussions about physics, it was really healthy to listen his critics and suggestions to my research project.

I want to thank to Carsten Greiner for accepting me as his student one and a half year before of concluding my PhD studies. His support and interest of my work was important in order to continue my research project with Mike when he left Frankfurt.

During last three and half years, I had great discussions about different topics of relativistic heavy ion collisions with different professors, postdoctoral fellows and students. Thanks to all of them. I enjoyed so much to talk continuously with the “unstable” group in Frankfurt: Björn Schenke, Nan Su, Yun Guo and Fritz Kretschmar. Moreover, I thank to J. Noronha, J. Noronha-Hostler, P. Huovinen, D. Rischke, A. Rebhan, M. Gyulassy, P. Romatschke, A. El, G. Denicol, S. Jeon, H. Appelshäuser, T. Koide, H. Petersen, B. Betz, I. Sagert and S. Vogel. All of them helped me to improve my research work with different ideas and suggestions. I cannot avoid to thank the organizers of the conferences which I attended during my PhD, they helped me with financial and logistic support in order to participate in important scientific events.

To Nadia and Fernando, the mexican side of my life. To the folks from Colombia for their friendship during years: Carlos Célimo, Robinson, Nancy, German, Ricardo, Milton, Fernando Blanco, Bibi, Nandre, Teyo, Adrianita, Gela, Angélica, Andreita, Carlos Alirio and Eduardo. To my mexican friends. To the persons who had an influence during my early years as student in Colombia: Carlos Nuñez, Leonardo Castañeda, Alvaro Villamil (RIP), Flor Martínez, Alfonso Castellanos, and Manuel Guillermo Rojas. To Peter Hess for the great discussions about physics and life in general, I have enjoyed so much to talk with him since we met in Mexico. To Alejandro Ayala for introducing me to this research field.

As it is known, life as a PhD student is not easy and to deal with different situations can be really hard if one does not have good friends around. During certain stage of my PhD, personal issues affected me more than what I expected. It was at that time when I started to meet many persons whom rapidly became my friends. Thanks Maca, Vicky, Saskia, Paco, Maria, Benny, Alexa, Danni, Max, Andreita, Dana, Philipp, Raphaele, Carola, Dimitrije, Sascha, Selim, Graziela, Jorge, Sophie, Basil, Hossein, Veronica, Irina, Hermes, Nora, Barbara, Yun, Volodya, Fritz, Nan, Felix, Joshi, Michael Hauer and the fellows of the HQM program. Of course, I have to mention the triathlon team “Radioactive Men”, thanks guys for your patience when I was not able to conclude on time our trainings. Thanks to all this people for the healthy distractions which made my PhD life more comfortable. I feel very fortunate that I met so many folks in Frankfurt, a city which I consider nowadays my second home.

I am grateful with the people of FIAS for the friendly environment at the institute. I am indebted with Frau Bergmann, Gaby, Eike, A. Achenbach, Denise Meixler for all their help with administrative

issues. Without them, life of students at ITP and FIAS would be really complicated. I want to thank to Henner Büsching for his friendship and the excellent organization of the Helmholtz Research Program.

Finally, I want to thank the financial support of the Helmholtz Association through the program Helmholtz Research School for Quark Matter Studies. Moreover, the Otto Stern School (nowadays known as GRADE) for the excellent workshops offered along last three years.